OPTOELECTRONICS
INTO A POWERFUL ECONOMY

Book of proceedings

October 20 - 23, 2020

OPTOELECTRONICS INTO A POWERFUL ECONOMY.
Book of Proceedings

Copyright and Reprint Permission.
For print or republication permission,
email to INOE Copyrights Manager
at *inoe@inoe.ro*
All rights reserved. Copyright ©2020 by INOE 2000.

Editor: Rădvan Roxana
Design & DTP: Medeleanu Adrian Constantin

ISBN: 978-973-720-822-4

AGIR Publishing House
www.edituraagir.ro

E-mail: *editura@agir.ro*
Tel./Fax: 4021-3168992

This publication was supported within the project PRO INSTITUTIO - 19 PFE / 2018, funded by the Ministry of Research and Innovation through Program I - Development of the National Research and Development System, Subprogram 1.2 - Institutional Performance - Projects for Financing Excellence in RDI, Contract No. 19 PFE / 17.10.2018.

OPTOELECTRONICS

INTO A POWERFUL ECONOMY

Table of Contents

Chapter IV

Optoelectronics: materials, sensors and products

Chapter V

Optoelectronics in Heritage Science

Foreword

Optoelectronics is the field that increasingly meets the requirements of the modern society, as it did in the first decades of the 21st century. We cannot fail to recognize the performances achieved in modern medicine with the help of hyperspectral imaging, in monitoring and evaluating environmental conditions, or pollution using laser remote sensing, solutions for controlled surface processing for high-tech industrial fields, contributions to civil engineering, real-time characterization of the state of conservation of cultural heritage, authentication or restoration of heritage. The enumeration can continue and should not be limited to the results obtained and validated by capitalization. Certainly, the challenges of the coming decades are those whose solutions are today's research topics. The researchers and collaborators of the National Institute for Research-Development in Optoelectronics INOE 2000 are the ones who present in this volume some of their activities.

Wishing success to all authors in ongoing projects, we also add the invitation to collaborate!

Roxana Rădvan

Scientific commitee

Mariana Braic, INOE 2000

Viorel Braic, INOE 2000

Mihaela Călin, INOE 2000

Elfrida Cârstea, INOE 2000

Monica Dinu, INOE 2000

Luminița Ghervase, INOE 2000

Cristiana E. A. Grigorescu, INOE 2000

Wolfgang Kautek, University of Vienna

Gabriela Matache, IHP

Vadim Parfenov, St. Petersburg

Electrotechnical University

Roxana Rădvan, INOE 2000

Doina Nicolae, INOE 2000

Cecilia Roman, ICIA

Dan Savastru, INOE 2000

Roxana Savastru, INOE 2000

Cătălin Vițelaru, INOE 2000

Organising commitee

Laurențiu Angheluță, INOE 2000

Laurențiu Bașchir, INOE 2000

Mihai Boldeanu, INOE 2000

Alexandru Chelmuș, INOE 2000

Mircea Chintoanu, ICIA

Ioana Cortea, INOE 2000

Cătălin Dumitrescu, IHP

Victor Nicolae, INOE 2000

Lucian Ratoiu, INOE 2000

Claudia Stancu, INOE 2000

CHAPTER I

Optoelectronics in Environment and Climate research

Climatology of the Universal Thermal Climate Index for Europe between 1979–2019

B. ANTONESCU*, L. MĂRMUREANU, J. VASILESCU,
C. MARIN, S. ANDREI, M. BOLDEANU, A. ȚILEA
National Institute of Research and Development for Optoelectronics INOE2000, Măgurele, Ilfov, Romania.

Abstract: The bioclimatology of thermal stress over Europe between 1979-2019 was analyzed using the Universal Thermal Climate Index (UTCI) derived from ERA5-Heat reanalysis. The annual number of hours with heat stress (UTCI > 32°C) increased significantly during the study period for all the Köpper-Geiger climate sub-classes analyzed. The highest percentage of hours (20% of all hours) with cold stress (UTCI < -13°C) occur over northern Europe. A significant increasing trend (> 0.05 hours yr^{-1}) in the number of hours with heat stress was observed for 23 out of 32 analyzed European cities analyzed.

Keywords: UTCI, heat stress, European bioclimate.

1. Introduction

Climate change, as shown in the latest IPCC report [1], is expected to have profound effects on weather patterns and temperatures worldwide in the coming decades, with a significant impact on public health [2]. During the last two decades of the 21st Century, Europe experienced exceptionally prolonged episodes of heat waves with record-breaking temperatures in many regions. A formal classification of top 10 heat waves in Europe that occurred between 1950–2015, indicated that 6 out of the 10 most important episodes occurred in the last 15 years [3]. For example, the summer of 2003 over western and central Europe, considered being one of the hottest European summers since CE 1500 [4], resulted in more than 70,000 fatalities [5].
An analysis at the global scale using gridded daily temperature data [6] showed that the frequency, intensity, and duration of warms spells and heat waves increased between 1950–2011 [7]. In particular, the warm spell trends in Eurasia increased with at least 0.9\% per decade, with slightly higher trends of up to 1.5\% per decade over western Europe. Koffi and Koffi [8] have investigated the changes in the frequency, duration and intensity of heat wave events that occurred between the 20th and 21st Centuries in Europe based on simulations using different regional climate models. The simulated heat waves for 2071–2100 will be more frequent across Europe, more severe and they will last longer. In particular, the intensity and frequency of heat waves will be increased by a factor of

at least 3, depending on season and location, compared with 1961–1990. More recently, [9] showed that the frequency of hot extremes in representative European cities has doubled or tripled in the last three decades compared to the previous ones. Thus, the European population is currently facing an increase in the heat stress [10].

Prolonged exposure to extreme temperatures can lead to thermal stress-related illnesses [11]. The thermo-regulation is a vital function of the autonomic nervous system in response to thermal stress (i.e., cold and heat stress) to keep the body temperature between certain limits when the environmental weather conditions are changing. Heat stress occurs when the human thermoregulatory mechanism is disrupted (i.e., the body produces more heat than it dissipates) and the core body temperature and the heart rate are increasing. As the body continues to store heat, it can lead to discomfort, fainting, and sometimes can cause death [12]. Cold stress can lead to hypothermia, which is defined as a core temperature below 35°C. Hypothermia can lead to shivering, respiratory depression, cardiac dysrhythmias, impaired mental function, mydriasis, hypotension, and muscle dysfunction, which can progress to cardiac arrest or coma [11].

Assessing the societal impact of thermal stress is a crucial issue, especially because the intensity of heat waves in Europe is forecast to increase in the futures [*e.g.*, 13].

Thus, in this article, we explore the ERA5-HEAT (Human thErmAL comforT) dataset, a global hourly gridded historical dataset (i.e., 1979–2019) of human thermal comfort indices derived from ERA5 reanalysis [14]. Because UTCI describes the response of the human body to different atmospheric conditions (i.e., temperature, humidity, wind and radiation), the index can be employed to understand the bioclimatology of different regions. Thus, the aim of this article is twofold. First, a baseline bioclimatology of thermal stress in Europe is constructed. Second, the variations and trends in UTCI and thus the changes in the thermal stress for different European regions and cities between 1979–2019 were assessed. This is the first study, to our knowledge, is analyzing heat- and cold-related bioclimatology from a pan-European perspective using ERA5-based hourly data over 41 years.

2. Universal Climate Thermal Index

The Universal Thermal Climate Index is derived from the UTCI-Fiala model [15] of the human physiological response (e.g., mean skin and face temperature, skin blood flow, shivering, sweat rate, rectal temperature, cardiac output) under different meteorological conditions (i.e., air temperature, humidity, wind, radiation). The UTCI-Fiala model is coupled with the UTCI-clothing model [16] to determine the insulation and vapour resistance over a range of air temperatures of the clothing worn for different body segments. For the physiological response the COST Action 730 (Towards a Universal Thermal Climate Index UTCI for Assessing the Thermal Environment of the Human Being) agreed on a reference activity level equivalent with walking at 4 km h^{-1} and metabolic heat production constant at 2.3 MET (i.e., 135 W m^{-2}) [17]. For the meteorological variables, the reference values considered by the COST Action 730 were 1) wind speed of 0.5 m s^{-1} (at 10 m AGL), 2) no thermal irradiation, and 3) relative humidity of 50% or constant vapour pressure of 12 hPa (for air temperature >29°C the reference humidity was considered as a constant vapour pressure of 20 hPa). UTCI is then defined as the air temperature of a reference outdoor environment that would elicit the same UTCI-Fiala model physiological response in the human body as the actual environmental temperature [18]. Brode *et al.* [19] derived UTCI based on more than 100,000 thermo-physiological responses from the UTCI-Fiala model coupled the UTCI-clothing model with input meteorological variables covering a relevant range of values (e.g., air temperature between -50°C and 50°C) and defined ten thermal stress categories.

The comparison between UTCI and other biometeorological indices – *e.g.*, PET (Physiologically Equivalent Temperature [20]), PHS (Predicted Heat Strain, [21]) – showed that UTCI represents specific climates and depicts temporal variability of thermal conditions much better than other indices [22]. Pappenberger *et al.* [23] showed that there is a linear dependency of UTCI on the air temperature, solar elevation angle, and solar and thermal radiation. UTCI shows also sensitivity to wind and humidity which represents the added values of this index as a heat stress indicator [24].

The UTCI dataset was obtained from ERA5-Heat reanalysis which is provided by the Copernicus Climate Change Service [25]. The UTCI was computed based on ERA5 data, the fifth global reanalysis produced by the European Centre for Medium-Range Weather Forecasts (ECWMF) [26]. First, the solar and thermal radiation fluxes at the surface of the Earth extracted from ERA5 were used to calculate the mean radiant temperature [MRT, 14]. Second, MRT, 2-m air temperature and relative humidity at 2-m AGL, wind speed at 10 m AGL also from ERA5 were used as input into a multi-variable equation to compute UTCI. The output is global (except for Antarctica) with 1-h temporal resolution on 0.25° spatial grid between 1979–2019. Only the values corresponding to the European domain defined as 25°N–75°N and 24°W–60°E, were considered in this article.

3. Köppen–Geiger climate classification

The European domain considered in this article was divided into eight subdomains to understand the changes and the trends in thermal stress for different regions. The subdomains were derived from Köppen–Geiger climate classification [27] updated by [28] and [29]. Previously the Köppen–Geiger classification was used by [10] to assess the heat-related health risk in Europe during the summer months for major European cities. According to the Köppen–Geiger classifications, the climate can be divided into five main groups: tropical, arid, temperate, continental, and polar, based on temperature, except for the arid class that is classified according to with the dryness criteria. All these five classes are then classified into 30 sub-classes, derived from the seasonal patterns of temperature, precipitations and vegetation types. Vegetation is considered a result of climatic conditions, being used for the biome distributions

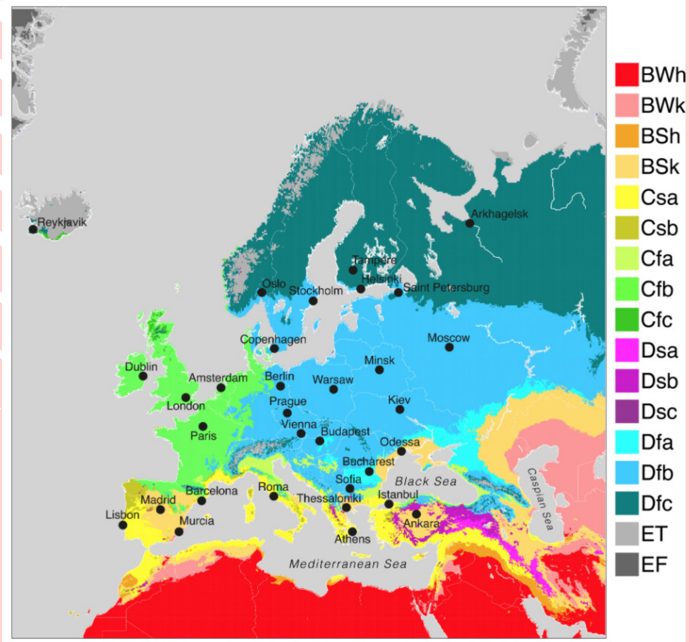

Fig. 1. Köppen--Geiger climate classification present-day map (1980–2016) for Europe. The color scheme was adopted from [28]. Represented on the map are the cities selected for analysis.

[30]. In this article, the global map of the climate classification constructed by [29] was used. This new map has a 1-km resolution for the recent period (*i.e.*, 1980–2016) and was obtained from four topographically-corrected climatic maps. The study domain analyzed contains 4 out the 5 main Köppen–Geiger climate classes and 17 out the 30 climate sub-classes (Fig. 1). Based on the area covered (*i.e.*, >2% from the total number of pixels) across Europe, eight of Köppen–Geiger climate sub-classes have been selected for analysis BWk (6.89%), BSk (8.71%), CSa (5.17%), Cfb (6.33%), Dfa (2.1%), Dfb (22.36%), Dfc (19.04%), ET (3.3%). To attribute a UTCI pixel to a certain Köppen–Geiger sub-class, the Köppen–Geiger map was regridded at the same spatial resolution as the ERA5-Heat grid.
All the pixels with the center in a certain Köppen–Geiger sub-class were attributed to that sub-class.

4. Results

4.1 Spatial distribution of thermal stress in Europe

There is a clear latitudinal increase towards the south in the percentage of hours with heat stress (Fig. 2a). A large number of days with heat stress (*i.e.*, 5–20%), compared with other regions of Europe, occurs over southern Europe, especially around the Mediterranean coast. Similar values are observed over parts of western (e.g., southern France), central (*e.g.*, western Croatia, Hungary, northern Serbia) and eastern Europe (*e.g.*, southern Romania, southern Moldova). Plain regions south of the Pyrenees, the Alps, and the Carpathian Mountains are also hot spots for heat stress. For example, over Romania, only the southern part (*i.e.*, north of the Danube river) present a higher percentage of heat stress (*i.e.*, 5–10\%) compared with other regions of Romania. Heat stress has a very low impact (*i.e.*, < 0.1%) over most central Europe and in northern Europe.

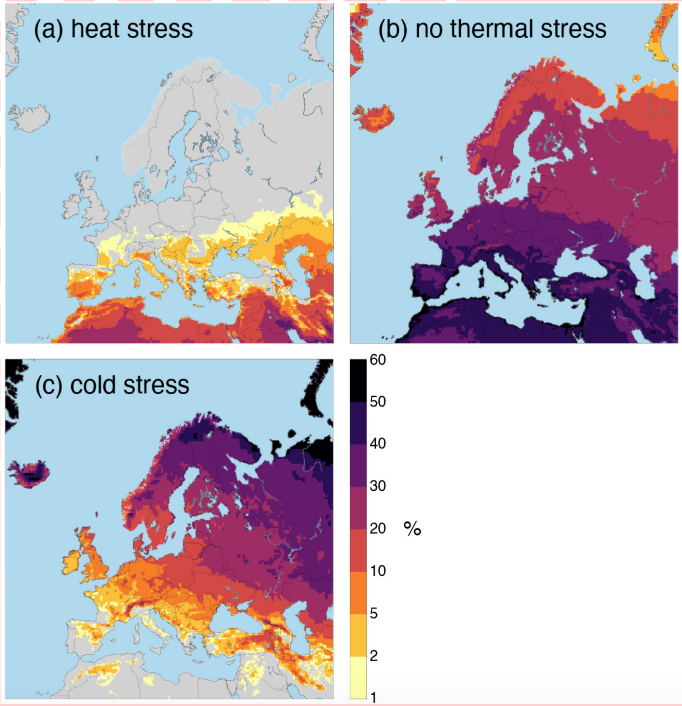

Fig. 2. The percentage from the total number of hours for each grid cell between 1979–2019 of the number of hours with (a) strong, very strong, and extreme heat stress (UTCI > 32°C), (b) no thermal stress (9°C < UTCI < 26°C), and (c) strong, very strong and extreme cold stress (UTCI < -13°C) shaded according to the scale. Note that the interval represented on the scale are not all equal Percentages lower than 0.1% are shaded in gray.

No thermal stress conditions occurred more frequently (*i.e.*, >30% of the total number of hours) over a region stretching from Portugal and Spain over most parts of western and central Europe (including southern Ireland and the United Kingdom) to Ukraine and southwestern Russia (Fig. 2b). The Mediterranean and Black Sea coasts are associated with the highest percentage of days with no thermal stress (*i.e.*, > 40%). The highest percentage of hours with cold stress (*i.e.*, 20%) occurred over northern Europe (i.e., Iceland, northern Scandinavia, Russia) (Fig. 2c). The only other regions characterized partially by a percentage of the number of hours with cold stress between 30–40% are the Alps and the Great Caucasus Mountains. The cold stress is very low (*i.e.*, < 0.1%) in the Mediterranean basin, Portugal, and southern France.

4.2. Thermal stress trends for Köppen–Geiger sub-classes

The annual number of hours with heat stress increased significantly between 1979–2019 for all the Köpper–Geiger climate sub-classes analyzed in this article, except for Dfc sub-region (Fig. 3). The highest magnitude of these increasing trends was observed over Dfa sub-class (+5.245 hours yr^{-1}, Fig. 3e), *i.e.*, over southern Romania, southern Ukraine, southern Russia and around the shores of the Azov Sea. High values were also observed over the northern and eastern shores of the Caspian Sea (BWk, +5.055 hours yr^{-1}, Fig. 3a), the Mediterranean shores (CSa, +4.761 hours yr^{-1}, Fig. 3c), and eastern Europe (i.e., Russia, southern Ukraine, southeastern Romania) (BSk, +4.740 h yr^{-1}, Fig. 3b). For the other regions, the magnitude of the statistically significant trends was < 1.6 hours yr^{-1} (Fig.~\ref{fig3}). Over Scandinavia, northern Russia (i.e., Dfc), and tundra areas (i.e., ET) there were no significant

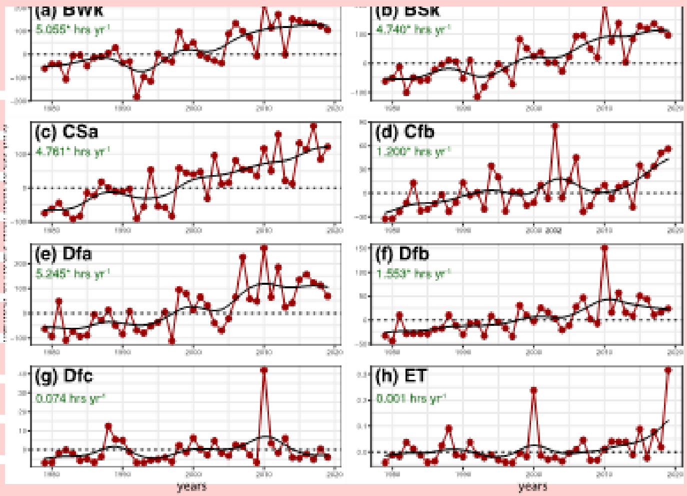

Fig. 3. The mean annual number of hours with heat stress anomalies relative to 1981–2010 for eight Köpper–Giger sub-classes between 1979–2019 (red line and dots). To highlight the multidecadal variability, a 11-years Gaussian low-pass filter was applied (black line). The trend (hours yr^{-1}) calculated using the Theil–Sen slope estimator is indicated in green for each sub-class. Statistical significance at $p < 0.05$ using the Mann–Kendall trend test is indicated by an asterisk. Note that the y-axis is different for each sub-class.

trend in number of hours with heat stress (Figs. 3g and h). The heat wave of 2003, that resulted in more than 70,000 heat-related fatalities over western and central Europe [31, 32], is indicated by the large value of the anomaly in the number of hours with heat stress for Cfb sub-class (Fig. 3d). Similarly, the 2010 heat wave that affected Russia (with about 55,000 heat-related fatalities) and eastern Europe [33] is reflected in the maximum values of the anomalies of the number of hours with heat stress over BWk, BSk, Dfa, Dfb, and Dfc (Figs. 3a,b,e,f, and g).

4.3. Thermal stress trends for European cities

For 23 of the selected cities, there was a significant increasing trend (i.e., 0.05 hours yr^{-1}) in the number of hours with heat stress observed each year during the study period (Fig. 4). Strong and statistically significant trends in the number of hours with heat stress characterized Thessaloniki (7.5 hours yr^{-1}), Odessa (7.0 hours yr^{-1}), Rome (6.8 hours yr^{-1}), and Bucharest (6.6 hours yr^{-1}). Positive anomalies in the number of hours with heat stress during the same year and for multiple cities were associated with heat waves. For example, the majority (i.e., 90.6%) of the analyzed cities showed a positive anomaly in 2010 associated European heat wave that affected Eastern Europe (anomalies >220 hours yr^{-1} were observed for Kiev, Odessa, and Moscow). Similarly, the European heat waves from 1994 (across Europe, especially over Germany and Poland), 2006 (central Europe and parts of northern Europe), 2018, and 2019

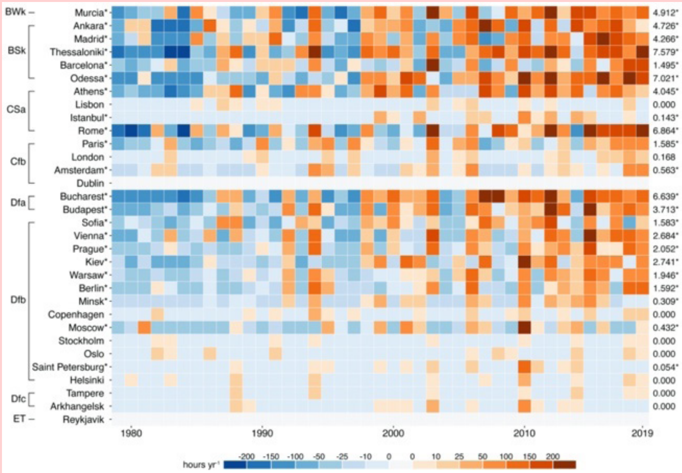

Fig. 4. Annual number of hours with heat stress anomalies (hours, relative to 1981–2010, shaded according to the scale) for 32 European cities. The Köpper–Geiger sub-class for each city is indicated on the le ft. The trend (hours yr^{-1}) calculated using the Theil-Sen slope estimator for each city is shown on the right. Statistical significance at $p < 0.05$ using the Mann–Kendall trend test is indicated by an asterisk.

(across Europe) are also emphasized in Fig. 4 [3, 34]. No trend was observed for Copenhagen, Stockholm, Oslo, Helsinki, Tampere, Arkhangelsk (latitude >55.5°N), and Lisbon (latitude 38.7°N), while during the study period, there were no hours with heat stress in Dublin and Reykjavik. Previously, [35] studied thermal stress based on UTCI for 15 European cities between 1991–2000 (only January and July). Their results indicated a lower frequency of heat stress for a coastal city (i.e., Barcelona) and lower frequency of cold stress for cities near the Atlantic Ocean (i.e., London and Dublin).

The thermal regimes of the coastal cities are influenced by the cooling effect of the nearby water bodies. This effect is less obvious for Odessa (on the Black Sea shore), Thessaloniki, Athens, Barcelona and Murcia (on the Mediterranean Sea shores) which show a high percentage of hours with heat stress and strong and statistically significant trends (Figs. 2a and 4). Both the Mediterranean Sea and the Black Sea are inland seas for which recent studies indicated an increasing trend in SST (sea surface temperature) of 0.36°C decade^{-1} [36], and 0.51°C decade^{-1} respectively [37]. Thus, there is a possible but not certain relationship between the SST and UTCI.

5. Conclusions

This study focuses on the bioclimatology and trends of thermal stress in Europe. The bioclimatology was constructed based on the Universal Thermal Climate Index (UTCI)derived from hourly ERA5-Heat reanalysis data between 1979–2019. The trends in thermal stress were analyzed for different Köppen–Geiger climate classes and cities across Europe. The main conclusions are as follows. A large number of days with heat stress (i.e., 5–20% of all days during the study period) were found mainly over southern Europe. The bioclimatic characteristics of heat stress are not fully modelled by Köppen–Geiger sub-classes. For example, there is an

increase in the number of hours with heat stress over the plain regions in northern Italy (Cfa) and southern Romania (Dfa) south of the Alps, and the Carpathian Mountains respectively. The largest values for the magnitude of significantly increasing trends in the number of hours with heat stress were observed over Romania, Ukraine and Russia (i.e, 5.245 hours yr^{-1}) and northern and eastern shores of Caspian Sea (i.e., 5.055 hours yr^{-1}). To highlight the impact on the population, ananalysis was made of the most important cities in Europe in terms of population and some in terms of the number of tourists. The most affected cities by heat stress are Thessaloniki, Rome, and Bucharest, where the average trend in the number of hours with heat stress was 7.03 hours yr^{-1}. Also, the positive anomaly of the heat stress in 2010 observed for over 90% of the analyzed cities is associated with the European heat wave, that affected eastern Europe (anomalies >220 hours yr^{-1}).
Future work will explore in more details the impact of thermal stress by including data on population growth, migration and mortality.

Acknowledgements

This work was supported by the Romanian Ministry of Research and Innovation through the Program I-Development of 288 the National Research Development System, Subprogram 1.2–Institutional Performance-Projects of Excellence Financing in 289 RDI, Contract No.19 PFE/17.10.2018, by the Romanian National Core Program Contract No.18N/2019, and by the European 290 Regional Development Fund through the Competitiveness Operational Programme 2014–2020, POC-A.1-A.1.1.1-F–2015, 291 project Research Centre for Environment and Earth Observation CEO-Terra, SMIS code 108109, contract No. 152/2016.

References

[1] IPCC. “Global Warming of 1.5◦C”. Masson-Delmotte, V. *et al.*, Eds., Cambridge University Press, 630 pp (2019).
[2] N. Seltenrich. Environmental health perspectives, **123**(11), A275–80 (2015).
[3] S. Russo, J. Sillmann, and E.M. Fischer. Environ. Res. Lett., **10**:124003 (2015).
[4] W. Lass, A. Haas, and C. Jaeger.. Int J Disaster Risk Sci, **2:398**, 1–14 (2011).
[5] J.-M. Robine, S.L.K. Cheung, S. Le Roy, H. Van Oyen, C. Griffiths, J.-P. Michel, and F.R. Herrmann. CR Biol., **331**, 171–178 (2008).
[6] J. Caesar, L. Alexander, and R. Vose. J. Geophys. Res., **111**:D05101 (2006).
[7] S. E. Perkins, L. V. Alexander, and J. R. Nairn. Geophys. Res. Lett., **39**:L20714 (2012).
[8] B. Koffi and E. Koffi. Clim. Res., **36**:153–168 (2008).
[9] D.and F. Pierros Founda, G. Katavoutas, and I. Keramitsoglou. Atmosphere, **10**:436 (2019).
[10] C. Di Napoli, F. Pappenberger, and H. L. Cloke. Int. J. Biometeorol, 62:1155–1165 (2018).
[11] W.P. Chesire Jr. Basic Clin., **196**:91–104 (2016).

[12] C. Di Napoli, F. Pappenberger, and H. L. Cloke. J. Appl. Meteor. Climatol., **58**:1177–1194 (2019).
[13] M. Collins, R. Knutti, J. Arblaster, J.-L. Dufresne, T. Fichefet, P. Friedlingstein, X. Gao, W. Gutowski, T. Johns, G. Krinner, M. Shongwe, C. Tebaldi, A. Weaver, and M. Wehner. In T. F. Stocker, D. Qin, G.-K. Plattner, M. Tignor, S. K. Allen, J. Boschung, A. Nauels, Y. Xia, V. Bex, and P. M. Midgley, editors, Climate Change 2013: "The Physical Science Basis. Contribution of Working Group I to the Fifth Assessment Report of the Intergovernmental Panel on Climate Change", 1029–1136. Cambridge, UK and New York, NY: Cambridge University Press (2013).
[14] C. Di Napoli, C. Barnard, C. Prudhomme, H.L. Cloke, and F. Pappenberger, Geosci. Data J., **00**:1–9 (2020).
[15] D. Fiala, G. Havenith, P. Bröde, B. Kampmann, and G. Jendritzky, Int. J. Biometeor., **56**:429–441 (2012).
[16] G. Havenith and D. Fiala, In R. Terjung, editor, In "Comprehensive Physiology", 255–302. Biomed, Ljubljana (2015).
[17] P. Bröde, K. Błazejczyk, D. Fiala, G. Havenith, I. Holmér I, G. Jendritzky, and B. Kampmann, Ind. Health, **51**:16–24 (2013).
[18] G. Jendritzky, R. de Dear, and G. Havenith. Int. J. Biometeor., **56**:421–428, (2012).
[19] P. Bröde, K. Błazejczyk, D. Fiala, G. Havenith, I. Holmér I, G. Jendritzky, and B. Kampmann, Ind. Health, **51**:16–24 (2013).
[20] P. Höppe. Int. J. Biometeor., **43**:71–75 (1999).
[21] J. Malchaire, A. Piette, B. Kampmann, P. Mehnert, H.J. Gebhardt, G. Havenith, and E. Den Hartog, Ann. Occup. Hyg., **45**:123–135 (2001).
[22] K. Błazejczyk, Y. Epstein, G. Jendritzky, H. Staiger, and B. Tinz Int. J. Biometeor., **56**:515–535 (2012).
[23] F. Pappenberger, G. Jendritzky, H. Staiger, E. Dutra, F. Di Giuseppe, D. S. Richardson, and H. L. Cloke. Int. J. Biometeorol., **59**: 311–323, (2015).
[24] C. Di Napoli, F. Pappenberger, and H. L. Cloke, Int. J. Biometeorol, **62**:1155–1165 (2018).
[25] C3S. Copernicus Climate Change Service Climate Data Store (2020).
[26] H Hersbach, W. Bell, P. Berrisford, A. Horányi, J. M. Sabater, J. Nicolas, R. Radu, D. Schepers, A. Simmons, C. Soci, and D. Dee, ECMWF Newsletter, **159**:17–24, (2020).
[27] W. Köppen. "Das geographische System der Klimate" (The Geographical System of the Climate). In W. Köppen and R. Geiger, editors, Handbuch der Klimatologie (Handbook of Climatology), pages 1–44. Borntraeger, Berlin (1936).
[28] M. C. Peel, B. L. Finlayson, and T. A. McMahon, Hydrol. Earth Syst. Sci., **11**:1633–1644 (2007).
[29] H.E. Beck, N.E. Zimmermann, T.R. McVicar, N. Vergopolan, A. Berg, and E.F. Wood, Scientific Data, **5**:180214 (2018).
[30] R.J. Huggett. "Fundamental of Biogeography" 2 edition, Routledge, 456 pp (2004)
[31] J. Luterbacher, D. Dietrich, E. Xoplaki, M. Grosjean, and H. Wanner, Science, **303**(5663):1499–1503 (2004).
[32] R. García-Herrera, J. Díaz, R. M. Trigo, J. Luterbacher, and E. M. Fischer, Critical Reviews in Environmental Science

and Technology, **40**:267–306 (2010).
[33] D. Barriopedro, E.M. Fischer, J. Luterbacher, R.M. Trigo, and R.García-Herrera, Science, **332**(6026):220–224 (2011).
[34] P Xu, L. Wang, Y. Liu, W. Chen, and P. Huang. Atmos Sci Lett., **21**:e964 (2020).
[35] Błazejczyk, P. Bröde, D. Fiala, G. Havenith, I. Holmér, G. Jendritzky, B. Kampmann, and A. Kunert, Misc. Geogr., **14**:91–102 (2010).
[36] F. Pastor, J. A. Valiente, and J. L. Palau, Pure Appl. Geophys., **175**:4017–4029 (2018).
[37] M. Shaltout and A. Omstedt, Oceanologia, **56**: 411–443, 2014.

*Corresponding author: Dr. Bogdan Antonescu (bogdan.antonescu@inoe.ro)

Estimating ground level concentrations of PM2.5 using satellite AOD and WRF-Chem model data

M. BOLDEANU [1], A. NEMUC[1], D. NICOLAE[1],
I. STACHLEWSKA[2], N. AJTAI[3], R. DUMITRACHE[4]
1. National Institute of R&D for Optoelectronics
2. Institute of Geophysics, Faculty of Physics, University of Warsaw
3. Faculty of Environmental Science and Engineering, Babeș-Bolyai University
4. National Meteorology Administration

Abstract: The rise of industrialization in Europe has increased the quantity of particulate matter that citizens are exposed to, on a daily basis. This event has given rise to increases in pulmonary conditions and an increased cancer risk. The goal of this study is to create an algorithm that increases the coverage of particulate matter information over Europe by using remote sensing satellites and weather and climate models.

Our main goal: to describe and verify the algorithm with an open-source code developed to estimate surface and tropospheric PM2.5 concentration on the near real-time obtained satellite AOD retrieved at 1 km resolution.

Keywords: PM2.5, satellite data, WRF-Chem.

1. Introduction

Particle matter is an umbrella term for a wide range of aerosols that have an aerodynamic diameter of less than 10 microns. This term refers to mixture of solid and liquid particles suspended in the air. The small size of these aerosols has the consequence of having a high fly-time which in turn allows the aerosols to be transported over large areas [1]. Particle matter with an aerodynamic diameter smaller than 2.5 microns is known as PM2.5.

PM 2.5 is one of the great killers of the last hundred years. The urbanization of developed countries and the industrialization of developing countries has had a major influence on the quantity of particulate matter in the air worldwide. This trend has come with an increase in respiratory problems [2] and mortality rates [3].

The World Health Organization has released a number of guidelines and goals for improving the quality of the air. For PM2.5 the target is 10 $\mu g/m^3$ as an annual mean and 25 $\mu g/m^3$ as a daily mean [4].

These recommendations are a good start but without national and international monitoring they are unenforceable. For this task a great number of in-situ PM2.5 monitoring sites have been deployed. But this still leaves a big part of the world with little information because of the lack of infrastructure or the lack of proper reporting. A different approach is to use the increasing availability of satellite data to get a better and more complete spatial and temporal coverage of information regarding aerosol concentrations.

The existing methods using AOD are still limited to the resolution of the instrument's aerosol product retrieval algorithm. Fortunately, the spatial resolutions of satellite aerosol products have improved dramatically since their inception.

2. Methods

The idea of developing a conversion algorithm that uses satellite data to obtain particle matter at ground level is as old as the first satellite based AOD retrieval.

The focus has been on mathematical/statistical approaches. This way of estimating particulate matter concentrations at ground level have been made by using linear regression [6-10]. The major disadvantage of this way of estimating PM2.5 concentrations is that it is dependent on existing infrastructure so that a linear regression can be applied to the satellite data. Also, a good correlation is obtained but only for the specific region and at a specific time of the year. These issues cannot be overcome by just using mathematical models and a physics model should be used.

This paper is an attempt at a physical based conversion algorithm from AOD to PM 2.5. This approach was chosen because of the need for a general-purpose conversion algorithm that is not dependent on the existing infrastructure of the region where the data is measured, needed for a regression approach.

The algorithm is based on the vertically integrated mass column formula to which a factor was added to obtain the concentration in the Planetary Boundary Layer and with the assumption that the PBL is well mixed we can use it as an approximation of the ground level concentration [13]. In the formula qualitative information about the mixture is specified as the effective density, radius and extinction efficiency while quantitative information the mixture is taken from the vertical distribution and the AOD intensity.

$$PM = \frac{4 \times \rho \times r_{eff}}{3 \times Q_{ext}} \times \frac{f_{PBL}}{H_{PBL}} \times AOD \quad (1)$$

PM - the ground level PM 2.5 estimation
ρ - density of the mixture
r_eff - effective radius of the mixture
Q_ext - extinction coefficient of the mixture
f_PBL - fraction of AOD in PBL
H_PBL - height of the PBL
AOD - the satellite retrieved AOD

2.1. Data sources

In this study data was used from three main sources:
OPAC [11] or the Optical Properties of Aerosols and Clouds was used as a starting point for the micro-physical properties of four classes of aerosols that are relevant for Europe: black carbon (SOOT), water soluble (WASO), water insoluble (INSO) and sulfates (SUSO). Starting from the pure aerosols a script was made to compute the density, radius and

complex refractive index of mixtures from these main types. The information for each mixture was propagated thru the T-matrix FORTRAN code to compute optical properties such as extinction efficiency and extinction [12].
WRF-Chem model [14] was used to approximate the mass mixing ratios of the four different aerosols. The model was run for the period of September 2014 over the whole of Europe but sub-domains where selected Poland, Romania and the Czech Republic. Seviri AOD data [15]

2.2. Algorithm overview

This sub-section is an overview of the architecture of the algorithm and a description of the dataflow.
Figure 3. Diagram of the AOD to PM 2.5 conversion algorithm
The conversion algorithm uses a modified version of Mishchenko's T-matrix method for calculating the optical parameters of a mixture starting from the micro-physical ones.
Computational limitation of T-matrix
Even though the T-matrix code is highly optimized it is rather slow on a normal computer with an average run time of 3 seconds for a mixture. This is a problem when working with large datasets as is the case for satellite data. A back of the napkin estimation gives a computation time of about 24 hours for a map with 200 X 150 pixels. This is an issue when the goal is to create a real-time or near real-time system.
To overcome this constraint the conversion from micro-physical properties to optical properties was pre-computed. This was saved in the form of a look-up table with the mass mixing ratio as a key and the extinction efficiency as the returned value.
For each of the four main aerosol types the following properties were extracted from OPAC. The effective radius, the density, the complex refractive index and the variance of the log-normal distribution of particle sizes. These were used to compute the micro-physical properties of the mixtures. The aerosol particle radius was calculated with the following equation:

$$r_p = \sqrt[3]{\sum_j \mu_j \cdot (r_j^{\mathrm{mod}})^3} \quad ; \; j = \overline{1,N} \qquad (2)$$

where is the radius of the component j with respect to humidity. The real and imaginary part of the complex refractive index was determined with the Lorentz-Lorentz model:

$$\frac{m_p^2 - 1}{m_p^2 + 2} = \sum_j \mu_j \cdot \frac{m_j^2 - 1}{m_j^2 + 2} ; \; j = \overline{1,N} \qquad (3)$$

For each of the resulting mixture the T-matrix method was used to compute the extinction effective cross section (Cext). Using this the extinction efficiency (Qext) and extinction coefficient were computed.
The keys for the look-up table are the ratios (eg:0.005;0.04;0.85;0.105) of the four types of aerosols that where considered important for this study. This list of mixtures was created with different step sizes for the aerosols

taking into account the sensitivity of the calculation based on the aerosol properties.

In the figure below a graphical representation of a slice of the 4-dimensional look-up table is represented.

Four such look-up tables were created using the microphysical properties at different relative humidity levels. So, the algorithm first computes the relative humidity at a certain point and using this information it selects the corresponding look-up table. To estimate the uncertainty of the retrieved value from the look-up table the Euclidean distance of the point to the selection from the table is calculated. This is

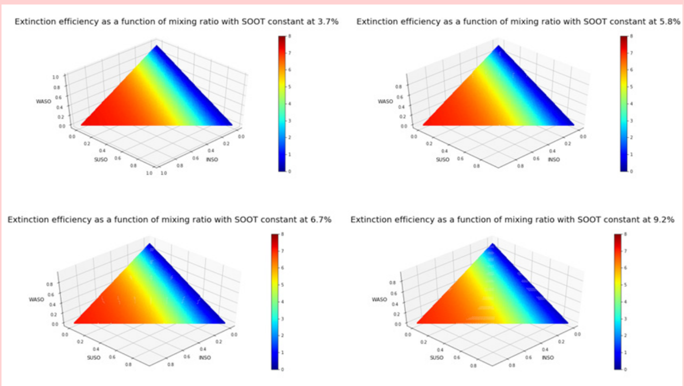

Figure 1. Look-up table visualization

propagated with the uncertainties from the AOD retrieval to get an uncertainty for the PM2.5 estimation.

With this approximation method the run-time was greatly lowered to under 5 minutes for a map of similar size. Also, by comparing neighbor values in the look-up table the error introduced by this method is just over 1% and this was further propagated as an uncertainty.

Algorithm description

The near-real time PM2.5 estimation algorithm has the following steps:

- Check if the input files
- Read the data from both files
- Compute the 4 aerosol types mass mixing ratios
- Compute the relative humidity
- Select the appropriate look-up table
- Select the appropriate value from look-up table
- Compute the vertically integrated mass column
- Estimate the ground values of PM2.5 by using the fraction of AOD in the PBL and the PBL height

Checking the input file time stamps is important because the AOD data has a temporal resolution of 15 minutes and the WRF-Chem output files are created only once per hour. This can be used to do a mean for the AOD data to overcome some of the problems of lack of data caused by the presence of clouds.

Data is read from the WRF-Chem model output files. The variables that are extracted are used to compute on one hand the relative humidity at all point of the modeled layers and on the other the mass concentrations of the four types of aerosols.

After the relative humidity and mass mixing ratios are calculated the look-up tables are queried and the results are used to compute the vertically integrated mass column.
To get the fraction of AOD in PBL parameter, an estimation of the AOD is computed from the WRF-Chem file. This is done for the entire column and for the column up to the PBL height. The ratio of these two estimated AODs is fraction of AOD in PBL.

3. Results

Thanks to the high temporal resolution of the SEVIRI AOD data that can be obtained over Europe. The result of this algorithm can make estimations for large areas several times a day. This is an improvement over other systems that provide a daily estimation.
In the following sub-sections, the generated estimation maps will be presented along with the uncertainties and the validation steps taken.

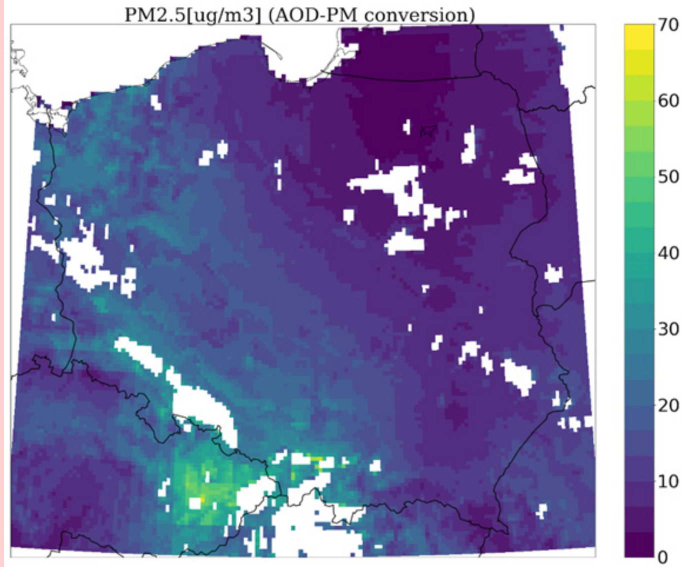

Figure 2. In this figure the output of the algorithm is presented. These maps are of Poland with missing values being caused by the lack off AOD data

3.1 Maps

3.2 Validation with ground-based measurements

For validation the work started with identifying ground-based stations that had data for the period of 2014 that was of interest for this study. For the three domains studied a total of 79 stations where found. The stations over two of the domains, Poland and Czech Republic, have hour averaged measurements while the stations over the third domain, Romania, only had daily means.
For Poland a total of 35 stations that are classified as traffic, industrial and background. In Figure 3 the spatial distribution of the stations is presented.

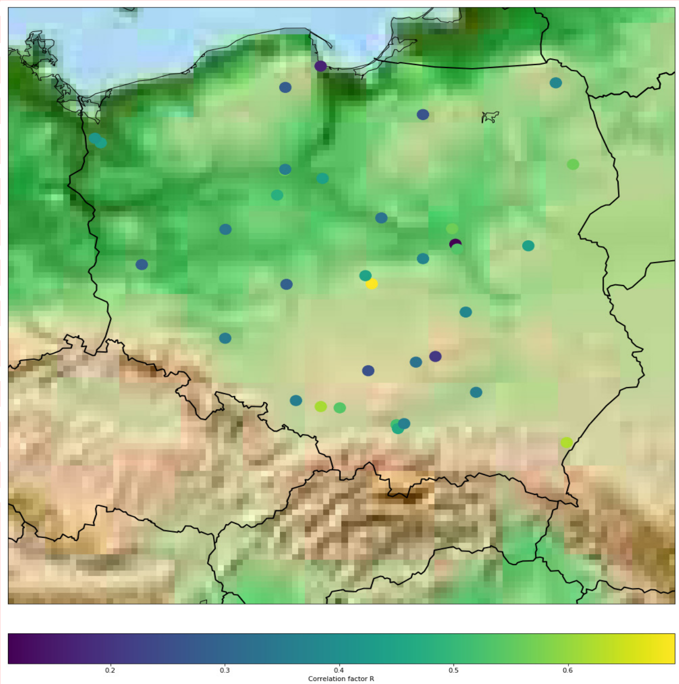

Figure 3. The spatial distribution of ground station over Poland with Color representing the R-value for each station.

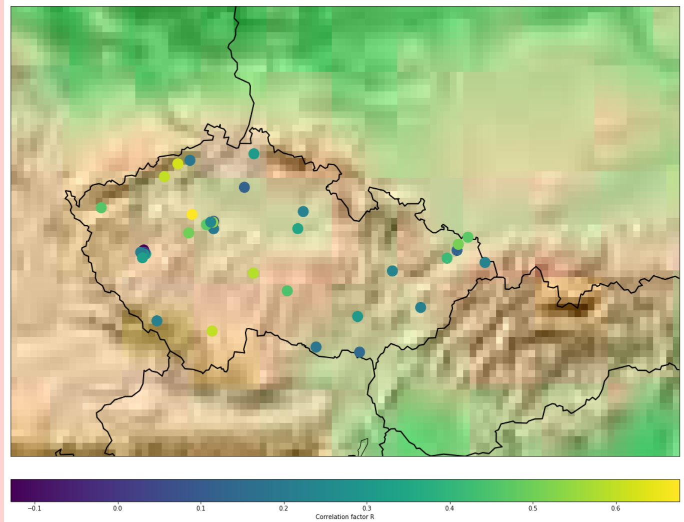

Figure 4. The spatial distribution of ground stations over the Czech Republic with color representing the R-value for each station.

For the Czech Republic a total of 35 stations that are classified as traffic, industrial and background. In Figure 4 the spatial distribution of the stations is presented.
The validation was done station by station and over an entire domain. The high range of R values (0.1-0.7) is mostly attributed to the positioning of stations in the AOD pixel.

This is the reason a selection has been made from the total number of ground-based stations by considering the position of the station in the pixel but also the geographic position of the stations.

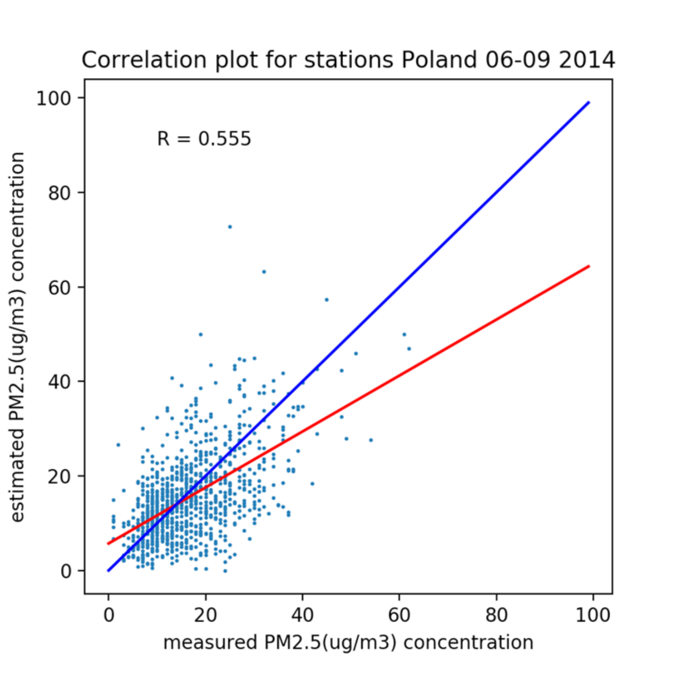

Figure 5. Plot of the ground measured versus estimated PM2.5 over Poland for the period of June – September 2014. The blue line represents y=x, and the red line is the line fit calculated with polynomial regression of degree 1.

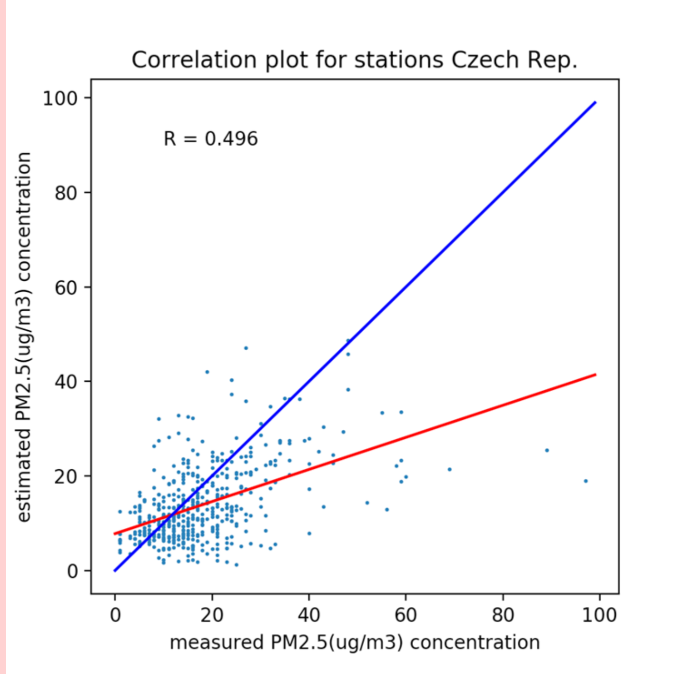

Figure 6. Plot of the ground measured versus estimated PM2.5 over Czech Republic for the period of June – September 2014. The blue line represents y=x, and the red line is the line fit calculated with polynomial regression of degree 1.

4. Conclusions

In this study we present the algorithm implemented for the conversion of the AOD satellite measurement to PM 2 5 concentration at ground level Preliminary results for a limited interval (June September 2014 and area (Czech Republic, Poland and Romania) showed correlation The low correlation could be attributed to several factors including

• Planetary boundary layer height from the model not being very representative

• A small number of humidity levels considered

• The aerosols model accounts only for the major types found

in continental Europe
• Local variability not visible in satellite pixel
• The position of the ground stations in relation
to the satellite pixel

These are just some of the possible explanations for the discrepancies between the
estimations and the ground-based measurements
Data fusion products improve on air pollution forecasts from model alone. This method could improve air quality monitoring in areas where installing ground stations for PM monitoring is difficult. The limiting factor is still the AOD map pixel size of the satellite data and the lack of data when we have cloud.

Acknowledgements

This study has been supported by SAMIRA project financed by ESA contract number ESRIN 4000117393/16/I NB Part of the work performed for this study was funded by the Ministry of Research and Innovation through Program I Development of the national research development system, Subprogram 1.2 Institutional Performance Projects of Excellence Financing in RDI, Contract No.19PFE / 17.10.2018, by Romanian National Core Program Contract No.18N/2019. Participation in this training course is partially supported by the joint organizations of The European Space Agency (ESA), the European Organisation for the Exploitation of Meteorological Satellites (EUMETSAT), and the Copernicus Atmosphere Monitoring Service (CAMS).

References

1. World Health Organization regional office for Europe (2013) Health Effects of Particulate Matter.
ISBN 978 92 890 0001 7

2. Yu-Fei Xing, Yue-Hua Xu, Min-Hua Shi and Yi-Xin Lian (2016) The impact of PM2.5 on the human respiratory system. Journal of Thoracic Disease, doi: 10.3978/j.issn.2072-1439.2016.01.19 10.3978

3. N.A.H.Janssena, P.Fischera, M.Marraa, C.Amelinga, F.R.Cassee (2013) Short-term effects of PM2.5, PM10 and PM2.5–10 on daily mortality in the Netherlands. Science of The Total Environment Volumes 463–464, 1 October 2013,
Pages 20-26

4. World Health Organization (2014) Ambient (outdoor) air quality and health. Retrieved from: https://web.archive.org/web/20160104165807/http://www.who.int/mediacentre/factsheets/fs313/en/

5. http://aqicn.org/map/world/
Applied Remote Sensing Training Retrieved (2016) Theoretical Basis for Converting Satellite Observations to Ground-Level PM2.5 Concentrations. Retrieved from: https://arset.gsfc.nasa.gov/sites/default/files/airquality/workshops/BAQ16/P8.pdf

6. Applied Remote Sensing Training Retrieved (2016) Converting AOD to PM2.5: A Statistical Approach. Retrieved from: https://arset.gsfc.nasa.gov/sites/default/files/airquality/workshops/BAQ16/P9.pdf

7. Short Tianning Su, Jing Li, Chengcai Li, Alexis Kai-Hon Lau, Dongwei Yang, Chuanyang Shen (2017) An intercomparison of AOD-converted PM2.5 concentrations using different approaches for estimating aerosol vertical distribution. Atmospheric Environment, Volume 166, October 2017, Pages 531-542

8. Su, Tianning & Li, Jing & Li, Chengcai & Lau, Alexis & Yang, Dongwei & Shen, Chuanyang. (2017). An intercomparison of AOD-converted PM 2.5 concentrations using different approaches for estimating aerosol vertical distribution. Atmospheric Environment. 166. 10.1016/j.atmosenv.2017.07.054.

9. Naresh Kumar, Allen Chu and Andrew Foster (2007) An empirical relationship between PM2.5 and aerosol optical depth in Delhi Metropolitan. Atmospheric Environment Volume 41, Issue 21, July 2007, Pages 4492-4503

10. Hess, M., Koepke, P. and Schult, I. (1998) Optical Properties of Aerosols and Clouds: The Software Package OPAC. Bulletin of the American Meteorological Society, 79, 831-844.

11. Mishchenko, M.I., and L.D. Travis, (1998): Capabilities and limitations of a current FORTRAN implementation of the T-matrix method for randomly oriented, rotationally symmetric scatterers. J. Quant. Spectrosc. Radiat. Transfer, 60, 309-324, doi:10.1016/S0022-4073(98)00008-9.

12. Koelemeijer, R.B.A., Homan, C.D. and Matthijsen, J. (2006) Comparison of spatial and temporal variations of aerosol optical thickness and particulate matter over Europe. Atmospheric Environment, 40, 5304-5315.

13. Peckham, S., G. A. Grell, S. A. McKeen, M. Barth, G. Pfister, C. Wiedinmyer, J. D. Fast, W. I. Gustafson, R. Zaveri, R. C. Easter, J. Barnard, E. Chapman, M. Hewson, R. Schmitz, M. Salzmann, S. Freitas, 2011: WRF-Chem Version 3.3 User's Guide. NOAA Technical Memo., 98 pp.

14. Zawadzka, O.; Markowicz, K.M. Retrieval of aerosol optical depth from optimal interpolation approach applied to SEVIRI data. Remote Sens. 2014, 6, 7182–7211

15. Weber, S.; Engel-Cox, J.; Hoff, R.; Parados, A.; Zhang, H. An improved method for estimating surface fine particle concentrations using seasonally adjusted satellite aerosol optical depth. J. Air Waste Manag. Assoc. 2010, 60, 574–585.

16. Franklin, M.; Kalashnikova, O.V.; Garay, M.J.; Fruin, S. Characterization of Subgrid-Scale Variability in Particulate Matter with Respect to Satellite Aerosol Observations. Remote Sens. 2018, 10, 623

17. Mishchenko, M.I.; Travis, L.D.; Mackowski, D.W. T-matrix computations of light scattering by nonspherical particles: A review. J. Quant. Spectrosc. Radiat. Transf. 1996, 55, 535–575.

*Corresponding author: M. BOLDEANU
mihai.boldeanu@inoe.ro

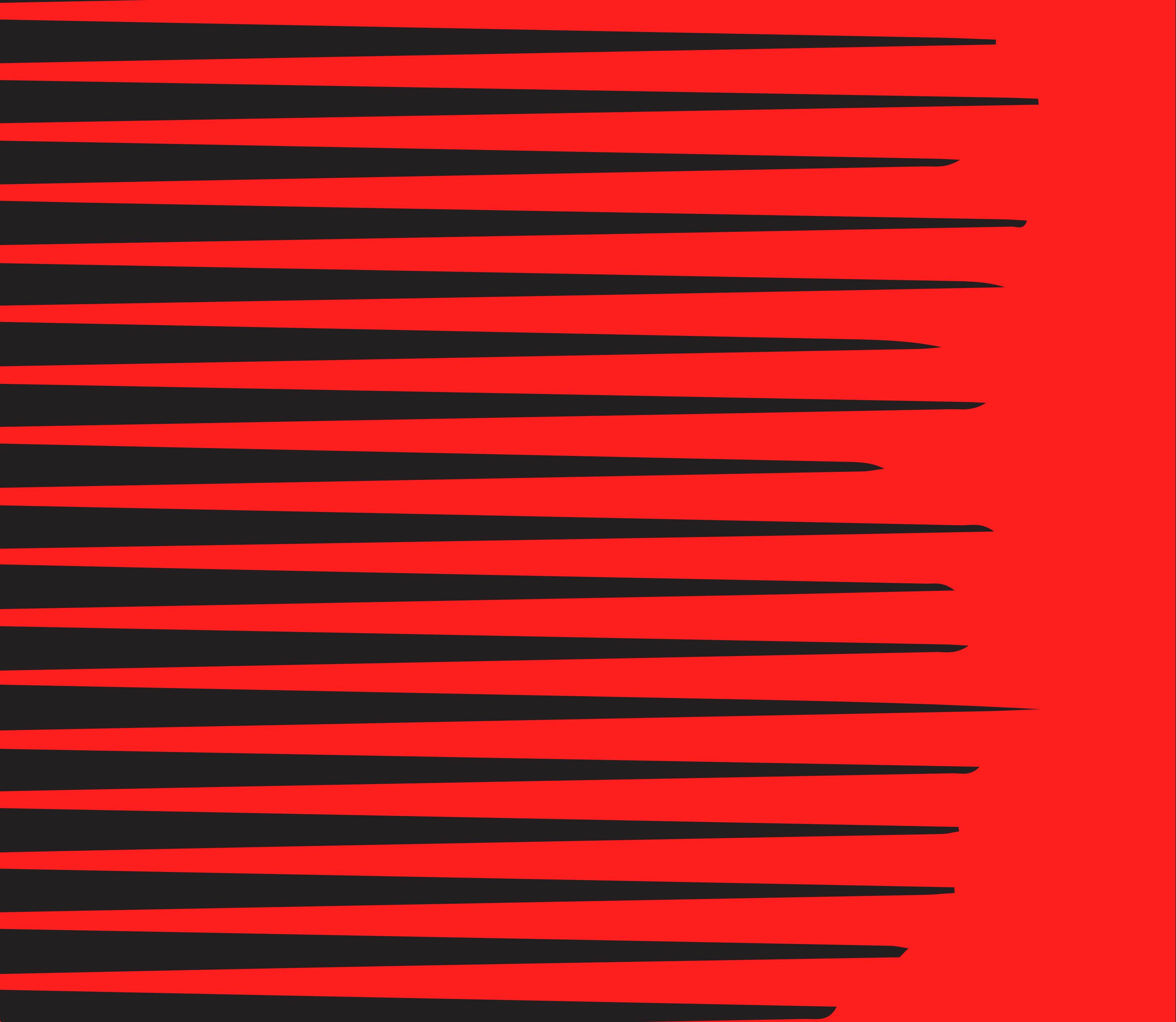

Desert dust characterization from remote sensing during Pre-TECT

V. AMIRIDIS[a], E. MARINOU[a,b], K.A. VOUDOURI[c], A. GIALITAKI[a], I. TSIKOUDI[a], E. DRAKAKI[a], A. KAMPOYRI[a], A. TSEKERI[a], D. NICOLAE[d], L. BELEGANTE[d], H. STEFANIE[d],

[a]*National Observatory of Athens, Greece*
[b]*German Aerospace Center, Germany*
[c]*Aristotle University of Thessaloniki, Greece*
[d]*National Institute for Research and Development for Optoelectronics, Romania*

Abstract: The irregular shape of mineral dust provides a strong signature on active and passive polarimetric remote sensing observations. Nowadays, advanced lidar systems operating in the framework of ACTRIS are capable of providing quality assured, calibrated multi-wavelength linear particle depolarization ratio measurements, while new developments will provide us elliptical polarization recordings in the near future. Passive polarimeters are already part of ACTRIS and their integration in operational algorithms is expected in the near future. This wealth of new information combined with updated scattering databases and sophisticated inversion schemes provide the means towards an improved characterization of desert dust in the future, towards better assessment of its climatic impact. Examples of this advanced characterization are given here, based on data collected during the Pre-TECT experiment in Crete, Greece.

Keywords: Desert dust, Lidar.

1. Introduction

Mineral dust is one of the most important aerosol types in terms of mass and optical depth and therefore significantly impacts radiation, while it also interacts with liquid or ice clouds modifying their optical properties and lifetimes, affecting in addition precipitation processes. Once dust particles are deposited at the surface, they provide micro nutrients to the ocean or to land ecosystems. For these reasons, the recent report of the IPCC identified mineral dust and its impacts on weather, climate and biogeochemistry as key topics for future research (see also Figure 1).
Existing atmospheric measurement techniques provide information about the content and type of aerosols in the atmospheric column, but not about the exact dust content. Pure dust is difficult to be detected and measured, except in very specific areas close to deserts. In export regions, mineral dust is found in external mixtures with other particles like smoke or sea salt and pollution. Accurate speciation is a main observational need to efficiently characterize desert dust abundances and intensive properties so as to assess the exact impact on climate, weather and biogeochemistry.
Despite the limitations on speciation, remote sensing has been applied from both ground and space to describe

the global distribution and characteristics of atmospheric dust. The most important parameter for assessing the dust abundances is the Dust Aerosol Optical Depth (DOD). Even though remote sensing is capable of retrieving the total Aerosol Optical Depth (AOD), there are methodologies capable of directly measuring dust.
Currently, in order to discriminate between dust and other aerosol types with existing remote sensors, typical features of dust are used such as: (1) dust dominated coarse mode that affects the Angstrom exponent values (a threshold that can be applied in spectral measurements); (2) dust particle non-sphericity that provides a clear signature in polarization or multi-angle measurements (a threshold can be applied on polarimeters, depolarization lidar or multi-angle sensors).

2. The Pre-TECT experimental campaign

PRE-TECT is an atmospheric experiment organized by the National Observatory of Athens (NOA) with the collaboration of the National Institute for Research and Development for Optoelectronics (INOE). The experiment took place from 1st to 30th of April 2017 at the Greek atmospheric observatory of Finokalia in Crete, aiming to advance desert dust microphysical characterization from ground-based remote sensing, employing sophisticated inversion techniques capable of retrieving aerosol microphysics. In order to validate the ground-based remote sensing retrievals, airborne in-situ measurements are of paramount importance. For that reason, the European Fleet for Airborne Research (EUFAR) has awarded two Transnational Access projects (DoGMA, ClIMA) that helped fulfilling the ACTRIS scientific objectives. This was a great example of collaboration between the two Research Infrastructures, aiming to advance our knowledge on aerosol microphysics and their impact on

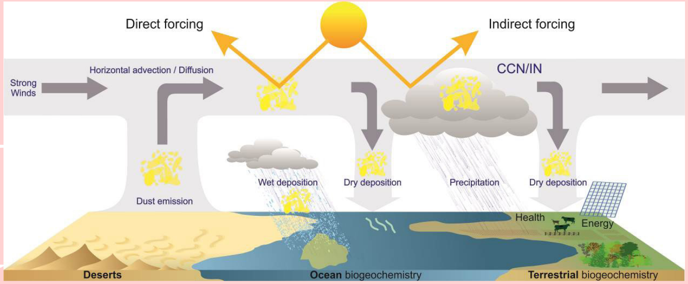

Figure 1. Schematic of long-range dust transport and its impacts on climate and biogeochemistry

Figure 2. The Falcon research aircraft of DLR that implemented the EUFAR TNs.

radiation and cloud formation. The flights were performed by the research aircraft FA20 of the German Aerospace Center (DLR), in synergy with the A-LIFE ERC project (University of Vienna). The FA20 performed 8 EUFAR flights which were coordinated with the ground-based measurements in Finokalia. The research aircraft was equipped with an extended in-situ aerosol payload, a wind lidar and meteorological sensors. PRE-TECT has been framed by synergistic experiments that were implemented during the same period in Mediterranean. Specifically, the following projects and initiatives contributed in PRE-TECT:

(1) The D-TECT ERC project, aiming to assess the impact of particle electrification on desert dust dynamics and long-range transport. During PRE-TECT, new sensors for atmospheric electricity have been tested in order to combine with the advanced ACTRIS aerosol products.

(2) The ECARS TWINNING EU project, aiming to boost INOE's research capacity in the domain of atmospheric remote sensing and create a pole of excellence in East Europe. The scientists of PRE-TECT organized a summer school for ECARS, aiming to introduce young researchers in a large-scale atmospheric cal/val exercise, focusing on the evaluation of aerosol and cloud satellite products employing ground-based and airborne sensors. During the summer school, the students were exposed on dedicated hands-on training activities.

(3) The A-LIFE ERC project, aiming to provide fundamental new understanding on the properties of absorbing aerosols and its impact on dynamics (in particular mineral dust – black carbon mixtures).

(4) The CyCARE campaign, a common initiative between the Cyprus University of Technology, Limassol and TROPOS, aiming to fill the gap in the global understanding of aerosol-cloud interactions. These investigations will help answering the question how rain patterns will develop in future and what the effect of climate change on arid regions might be.

(5) The GEO-CRADLE project, aiming to coordinate Earth Observation Activities in the regions of North Africa, Middle East, and Balkans in order to develop links with GEO. Two pilots and their services have been evaluated using the PRE-TECT dataset, the dust forecast service of the ACC pilot (Adaptation to Climate Change) and the SENSE energy system for the determination of solar energy field in the Eastern Mediterranean.

Pre-TECT experiment provided the atmospheric conditions for studying desert dust and its characterization. Multi-wavelength and continues lidar observations provide the basis for further analysis of the aerosol conditions, including interactions with clouds that can be revealed from the synergy of the lidar measurements performed by NOA with the cloud radar measurements performed by CNR-IMAA and the Microwave Radiometer measurements performed by INOE.

An overview of the aerosol and cloud air masses observed during PRE-TECT is shown in Figure 3. During the experiment, multiple dust events were observed above the station in attitudes up to 8 km, with clouds formed on top of them. Additionally, continental aerosols from long range transport were observed in altitudes up to 3 km. Falcon collected aerosol profiles above the station 3 days, and 2 of the samples were under dust presence.

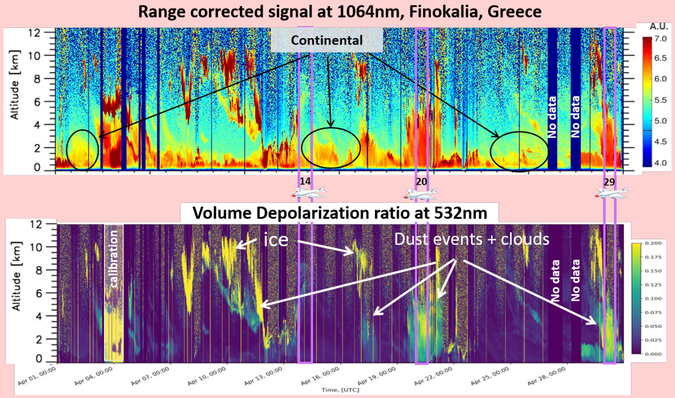

Figure 3. The PRE-TECT lidar observations of range corrected signal at 1064nm (top) and volume depolarization ratio at 532nm (bottom) between 1 to 30 of April 2017. Highlighted are the time periods of the Falcon flights above the station.

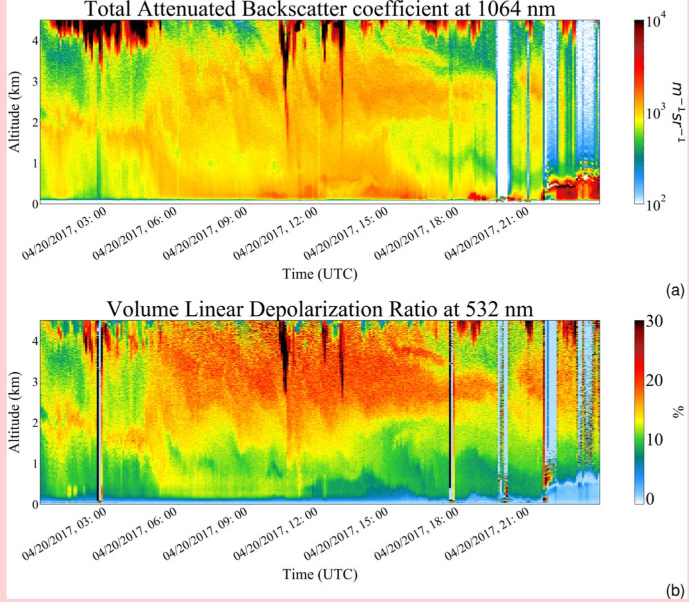

Figure 4. Lidar total attenuated backscatter at 1064nm (a) and volume depolarization ration at 532nm (b) above Finokalia station on 20/4/2017.

3. Experimental results

3.1. Dust optical and microphysical characterization

The multi-wavelength and continues PollyXT-NOA lidar observations (Baars et al., 2016; Engelmann et al., 2016) enable the retrieval of vertical profiles of the particle backscatter coefficients (at 355, 532, and 1064 nm), the extinction coefficients (at 355 and 264532 nm), the depolarization ratio at 355 and 532 nm (Freudenthaler et al., 2009) and the water vapor mixing ratio at 407 nm (Dai et al., 2018). The combined use of two receivers, a near and a far-range telescope, enables the retrieval of aerosol optical properties from the upper troposphere down to complex boundary layer structures.

Figure 4 shows the time evolution of the attenuated backscatter coefficient at 1064 nm (top) and the volume depolarization ratio at 532 nm (bottom) for a case where dust were advected above the station and clouds were formed on top of the dust layer at around 4km.

The AERONET measurements are used to provide

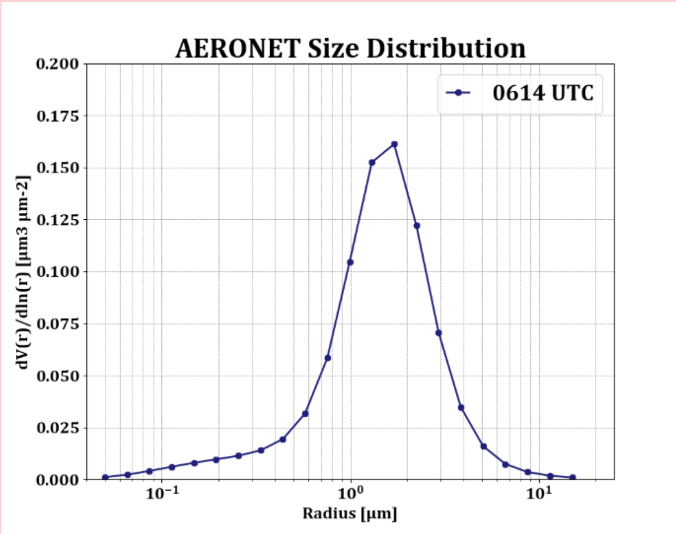

Figure 5. AERONET size distribution above Finokalia on 20 April 2017 at 06:14 UTC.

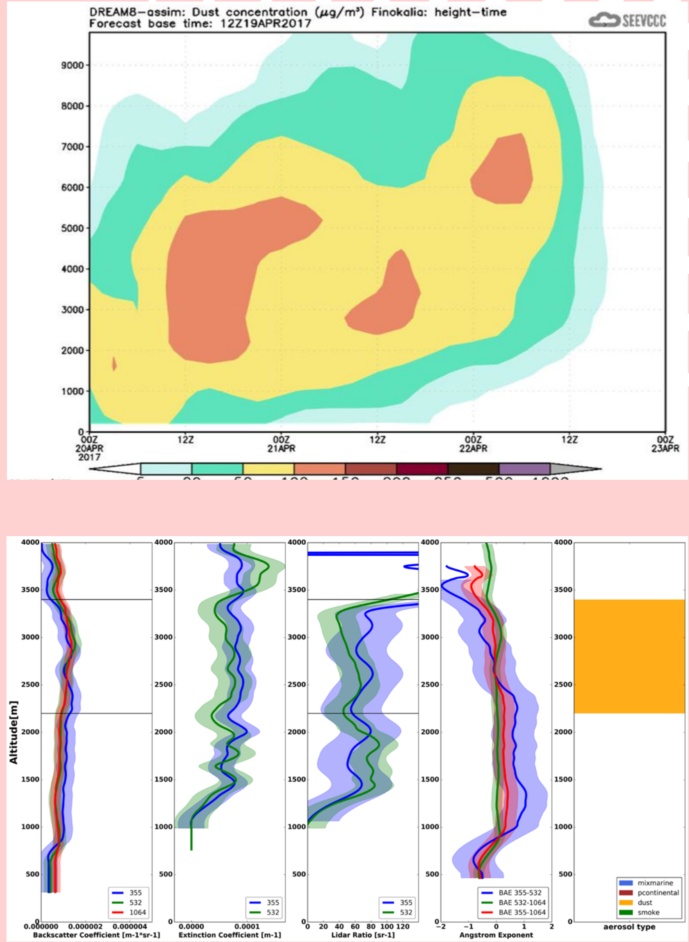

Figure 6. DREAM dust concentration simulations above Finokalia station on 20 to 23 April 2017 (Upper) and FLEXPART source supportion for the air masses arriving at Finokalia at 2.7 km on 20 April 2017 at 17:00 UTC (Lower).

information on the aerosol size distribution (Figure 6). For the demonstration case, a pristine coarse mode is present above the station.

Ancillary data are used for the characterization of the air masses observed, i.e. dust, sea salt and smoke transport model forecasts and analytical back-trajectories and source-receptor analysis for air-mass identification (see also http://pre-tect.space.noa.gr/data/). Figure 5 shows the DREAM dust concentration simulations above Finokalia station on 20 to 23 April 2017 (top) and the

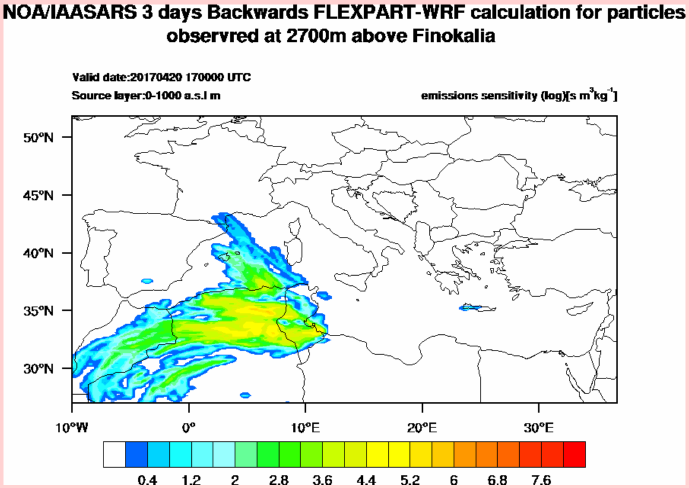

Figure 7: Optical products and aerosol typing from the AUTH classification algorithm on 20 April 2017 at 17:00 – 18:00 UTC.

FLEXPART (FLEXible PARTicle dispersion model) source supportion for the air masses traveling below 3 km before reaching Finokalia station at 2.7 km on 20 April 2017 at 17:00 UTC (bottom). The model output is given in terms of the decimal logarithm of the integrated residence time in seconds in a grid box. The dust-prone area of northern Africa (Morocco and northern Algeria) are most likely the sources of the aerosol layer.

For the aerosol characterization we are using the synergy of the sunphotometer and the lidar retrievals. The retrieved profiles of the particle backscatter and extinction coefficient, lidar ratios, and Ångström exponents are shown in Figure 7. The boundaries of the detected layer are marked with lines.

The observations show one particle thick layer, between 2.2 and 3.3 km. The lidar ratio values for the layer are found 65 ± 8 sr for 355 nm and 51 ± 8 sr for 532 nm. The mean AE 355/532 is 0.73 ± 0.4. The mean BAE 355/532, mean BAE 532/1064 and mean BAE 355/1064 are 0.11 ± 0.46, 0.06 ± 0.15 and 0.73 ± 0.4, respectively. The stability of the lidar ratio and Ångström exponent values is indicator of homogeneity and small variability of the aerosol type within the layer. The retrieved values indicate the presence of coarse particles, similar to the one reported in literature for dust particles. The atmospheric column is dominated by dust, as further confirmed by the coarse-mode-dominated AERONET distribution (Figure 6). Moreover, the combined information of the backward trajectory analysis and the intensive property values indicate the presence of dust particles over Finokalia.

Several aerosol typing schemes have been developed within EARLINET for the multi-wavelength Raman measurements [5, 6, 7] making use of the available aerosol-type-sensitive intensive properties and provides the main aerosol components as a function of height. Figure 7 shows the aerosol classification of the demonstrated case using the AUTH classification scheme.

The algorithm has correctly detected dust as the main component of this layer.

The aforementioned classification algorithms can be evaluated with in-situ observations from airborne platforms.

Although the algorithms succeed in correctly classifying a lot of cases, their classification fail in humidify aerosol layers which are erroneously categorize as marine dominated [7].

3.2. Water vapor in dust

An important parameter to be considered when studying dust is the water vapor mixing ratio and the relative humidity conditions within the dust layer. During PRE-TECT these profiles are derived following the methodology of [3] using the observations of the PollyXT-NOA lidar and of the INOE microwave radiometer. Figure 8 shows the water vapor mixing ratio (left) and the relative humidity (right) for the demonstrated dust case. We see that the relative humidity inside the dust layer is increasing with altitude from 40% at around 2.2km to almost 80% at 2.7km. Once the relative humidity is higher than 80% the optical lidar products are effected significantly and additional algorithms are needed to derive their microphysics [8].

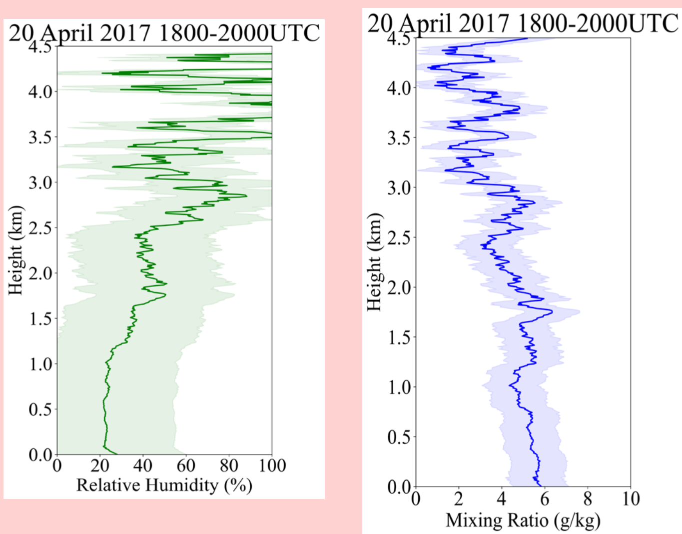

Figure 8: Water vapor mixing ratio (left) and relative humidity (right) from the PollyXT lidar on 20 April 2017 at 87:00 – 20:00 UTC.

4. Conclusions

All the aforementioned observations and advanced retrievals can be used for aerosol classification and characterization. The EARLINET advanced aerosol typing schemes can be applied to reveal the presence of desert dust in polarization lidar measurements as well as the mixing conditions with other aerosol types. Further evaluation with airborne retrievals is going to be applied. Additionally, further analysis of these advanced products with other measurements from synergistic instruments (eg. cloud radar, pyranometers) will pave the way for better aerosol-radiation-cloud interaction studies.

Acknowledgements

The authors would like to acknowledge EARLINET (https://www.earlinet.org/) and ACTRIS (https://www.actris.eu) for the data collection, calibration, processing and dissemination. This research was supported by: (a) D-TECT (Grant Agreement 725698) funded by the European Research Council (ERC) under the European Union's Horizon 2020 research and innovation program. (b) the ECARS under grant agreement No 602014 from the European Union's Horizon 2020 Research and Innovation program. (c) the European Union's Horizon 2020 research and innovation program under grant agreement No 654109 (ACTRIS).

References

[1] Baars, H., et al.: An overview of the first decade of PollyNET: an emerging network of automated Raman-polarization lidars for continuous aerosol profiling, Atmos. Chem. Phys., 16, 5111–5137, https://doi.org/10.5194/acp-16-5111-2016, 2016.

[2] Engelmann, R., et al.: The automated multiwavelength Raman polarization and water-vapor lidar PollyXT: the neXT generation, Atmos. Meas. Tech., 9, 1767–1784, https://doi.org/10.5194/amt-9-1767-2016, 2016.

[3] Freudenthaler et al.: Depolarization ratio profiling at several wavelengths in pure Saharan dust during SAMUM 2006. Tellus B, 61: 165-179. doi:10.1111/j.1600-0889.2008.00396.x, 2009.

[4] Dai, G., et al.: Calibration of Raman lidar water vapor profiles by means of AERONET photometer observations and GDAS meteorological data, Atmos. Meas. Tech., 11, 2735–2748, https://doi.org/10.5194/amt-11-2735-2018, 2018.

[5] Nicolae, D., et al.: A neural network aerosol-typing algorithm based on lidar data, Atmos. Chem. Phys., 18, 14511–14537, https://doi.org/10.5194/acp-18-14511-2018, 2018.

[6] Papagiannopoulos, N., et al.: An automatic observation-based aerosol typing method for EARLINET, Atmos. Chem. Phys., 18, 15879 – 15901, https://doi.org/10.5194/acp-18-15879-2018, 2018.

[7] Voudouri et al.: Aerosol Typing in the Eastern Mediterranean during Pre-TECT Campaign over Finokalia, Crete, European Lidar Conference (ELC) 2020.

[8] Tsekeri, A., et al.: Profiling aerosol optical, microphysical and hygroscopic properties in ambient conditions by combining in situ and remote sensing, Atmos. Meas. Tech., 10, 83–107, https://doi.org/10.5194/amt-10-83-2017, 2017.

*Corresponding author: vamoir@noa.gr

Aerosol Remote Sensing research in ACTRIS

L. MONA[a], D. NICOLAE[b]
Consiglio Nazionale Delle Ricerche, Istituto di Metodologie per l'Analisi Ambientale, Potenza, Italy
National Institute of R&D for Optoelectronics, Magurele, Romania

Abstract: *The Aerosol, Clouds and Trace Gases Research Infrastructure (ACTRIS) is an ESFRI type initiative for producing high-quality observations of short-lived atmospheric constituents at European scale and beyond. ACTRIS is already partially operational, building on existing networks such as EARLINET (European Aerosol Research Lidar Network), AERONET (Aerosol Robotic NETwork), CLOUDNET, EUSAAR/CREATE (European Supersites for Atmospheric Aerosol Research, NDACC (Network for the Detection of Atmospheric Composition Change) and EUROCHAMP (EUROpean simulation CHAMbers). This paper presents the current activities and results of the aerosol remote sensing components in ACTRIS.*

Keywords: aerosol, remote sensing, research infrastructure.

1. Introduction

The ability to predict the future behaviour of the atmosphere over all time scales (hours to decades) brings great benefits to society and the economy. Examples include short-term hazardous weather and health warnings as well as long-term evaluation of air quality, climate change and policy effectiveness. Atmospheric predictions of all kinds use complex models that are underpinned by observations. Without high quality observation data to constrain predictive models any forecasts of the atmosphere are highly unreliable. The Aerosol, Clouds and Trace Gases Research Infrastructure (ACTRIS) is a pan-European initiative consolidating actions amongst European partners producing high-quality observations of short-lived atmospheric constituents. ACTRIS integrates, harmonizes and deliver different observations and services provided by a vast set of first-class national observatories and facilities located in 23 European countries. ACTRIS provides access to its facilities, open-access data, measurement support, instrument calibration and development, and training to various user groups. By providing data and access ACTRIS enhances science, but it also generates and disseminates knowledge, boosts technological development, and creates human capital and jobs for the benefit of the society.

ACTRIS data are harmonized through standardized quality controls, which guarantee that all ACTRIS data are comparable across Europe and outside, properly processed, archived and accessible to all users for a long term. Similarly, physical and

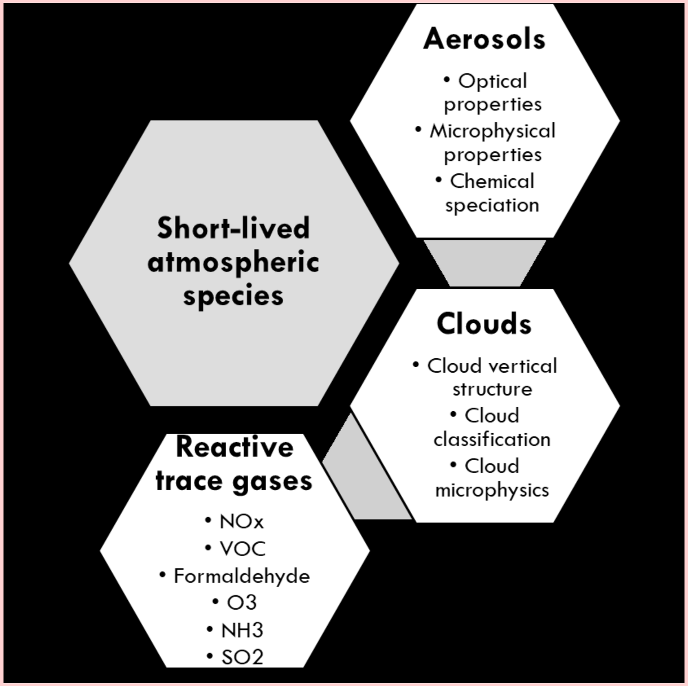

Fig. 1 Schematics of the ACTRIS scientific focus

remote access to ACTRIS services are processed and managed in a coordinated and harmonised manner.
ACTRIS focuses on producing high-quality observations of short-lived atmospheric constituent to improve air quality, to monitor climate trends, and to warn of atmospheric hazards and knowledge about processes driving their atmospheric lifetime. Short-lived atmospheric constituents have a residence time in the atmosphere from hours to few weeks, which make their concentrations highly variable in time and space.

An additional level of complexity to natural variability of climate is linked to the issue of man-induced climate–processes and interactions. Emissions of pollutants change the atmospheric composition contributing to climate change through the climate components, and, vice-versa, climate change influences atmospheric composition through a series of feedback process including changes in temperature, dynamics, hydrological cycle, atmospheric stability, emission intensity of biogenic compounds, temperature-dependent transformation processes in the troposphere, effects on health and ecosystems, etc. The level of scientific understanding of the climate drivers, interactions and impacts is very low.
ACTRIS results from more than 15 years of consistent development funded from national sources and the European Commission Research Infrastructure programme. ACTRIS was initiated as an Integrated Initiative in 2011 building on three historical European research collaborations: EARLINET (European Aerosol Research Lidar Network, EU-FP5 and FP6 projects), EUSAAR/CREATE (European Supersites for Atmospheric Aerosol Research, EU-FP6 project, Construction, use and delivery of an European aerosol database, EU-FP5 project) and Cloudnet (started as an EU-FP5 project for observing cloud profiles). New integration of long-term trace-gas observatories was then added in 2011 (ACTRIS-I3 EU-FP7 project, see Figure 1). The current operations are pursued as part of ACTRIS-2, funded as an IA programme by the European Commission in H2020. ACTRIS

National facilities include also atmospheric simulation chambers which have been operating for years within the EUROCHAMP (European Simulation Chambers for Investigating Atmospheric Processes) projects, currently EUROCHAMP-2020.

In 2016 ESFRI selected ACTRIS as a new RI on its roadmap encouraging ACTRIS implementation within a 10-year time frame. The ACTRIS Preparatory Phase Project (PPP) (EU-H2020 project) supports the RI development at the organizational level and, hence, enables the transition from a project-based network of research facilities to a centrally coordinated integrated pan-European RI. ACTRIS PPP will set a solid basis for ACTRIS as a research infrastructure in terms of legal, financial and technical maturity to continue towards the implementation of the RI and later on towards operation expected in 2025.

2. Experimental

2.1. Methodology

2.1.1. The scientific perimeter of ACTRIS

The atmosphere is a highly complex system where occurrence of different chemical, physical, and optical reactions can take place which involves different dynamics and energetic processes. ACTRIS contributes with its expertise and provision of information related to short-lived atmospheric constituents. ACTRIS provides the needed information to address the complex interactions between aerosols, clouds, and trace gases, which requires both measurements of the four dimensions with a proper quality assurance needed to create climate and air pollution data and capacity to understand interactions amongst the constituent performing experiments in controlled environments. As a consequence, ACTRIS needs to address a large variety of measurements and variables, documenting the atmosphere from ground to stratosphere, with time scales ranging from seconds to days. Essentially, ACTRIS knowledge focus on: a) the chemical, optical and physical properties of aerosols near the surface, their extinction and backscattering profiles throughout the troposphere and the lower stratosphere and their integrated columnar properties; b) the concentration of specific reactive trace gases near the surface and throughout the troposphere and lower stratosphere; c) the chemical and physical properties of cloud droplets and ice crystals and their dynamical evolution in natural clouds, leading to the formation of precipitation; d) the processes by which aerosols, clouds and trace gases interact to lead to the observed atmospheric composition, variability and trends in the atmosphere.

2.1.2. ACTRIS structure

ACTRIS is organized around the National Facilities and Central Facilities.

The major task of the **National Facilities** (NF) is the acquisition and delivery of quality-controlled long-term and process related data on aerosols, clouds and reactive trace gases. The

Fig. 2 Schematics of the ACTRIS structure

data are provided to the users by the ACTRIS Data Centre (DC) following the ACTRIS Data Policy. The operation of the NFs is supported by the Topical Centres (TCs) to assure the application of ACTRIS standards and the quality of the data.

Central Facilities (CF) are constituted by six Topical Centres(TCs), the Data Centre (DC) and the Head Office (HO). Each CF is jointly operated as a consortium with 2 or more Units around Europe.

ACTRIS Data Centre (DC) provides the management of ACTRIS data and value-added products including long-term archiving and access to data, tools for data production, visualization, evaluation, and analysis. ACTRIS data means data from observational NFs and exploratory NFs complying with the procedures established within ACTRIS. The DC is responsible for the data curation, which is the activity that stores, manages and ensures access to all data sets produced within the infrastructure.

Topical Centres (TCs) support the operation of NFs and are responsible for a) defining procedures and tools for quality assurance and quality control of ACTRIS measurements and data, b) performing quality assurance and quality control of ACTRIS measurements and data, c) ensuring training and transfer of knowledge to ACTRIS operators and users, and d) improvements of measurement methodologies for aerosols, clouds, and reactive trace gases. Six TCs are required to respond to the scientific and technical needs of ACTRIS, each with a particular focus on either remote sensing (from the ground) or in situ (near surface) measurement techniques: a) Centre for Aerosol Remote Sensing; b) Centre for Aerosol In-Situ Measurements; c) Centre for Cloud Remote Sensing; d) Centre for Cloud In-Situ Measurements; e) Centre for Reactive Trace Gases Remote Sensing; f) Centre for Reactive Trace Gases In-Situ Measurements.

2.1.3. Aerosol Remote Sensing structures

Aerosol remote sensing measurements involves both aerosols column and aerosol profiling and their synergetic uses, primarily at ground-based level. Measurements collected at the National Facilities go through the specific quality assurance program organized by the topical Centre for Aerosol Remote Sensing (CARS) and the Aerosol Remote Sensing unit (ARES) at the ACTRIS Data Centre.

The role of CARS is to offer operational support to ACTRIS National Facilities operating the following instrumentation:

a) high-power aerosol lidar – elastic-Raman-polarization lidar (generally at several wavelengths), not eye-safe, generally with supervised and not continuous operation; b) automatic low-power aerosol lidar - elastic backscatter lidars, eye-safe, operated continuously and unattended, commercially available; c) automatic sun/sky/polarized/lunar photometer - sun/sky (and moon) photometer with direct sun/moon and sky measurements in nine spectral bands.

Aerosol profile observations are covered in ACTRIS by automatic low-power lidars and high-power lidars. Due to the differences at the hardware level (e.g. laser power and sounding wavelengths), the data products which can be retrieved from these measurement techniques are essentially different.

Automatic low-power lidars and ceilometers (ALC) are currently used to provide aerosol layering and attenuated backscatter at one wavelength, information which is used in combination with cloud radars and microwave radiometers to complete the cloud classification at the ACTRIS Cloud Remote Sensing National Facilities. In addition, these parameters could be used to study fog formation that is of great importance for visibility studies. The temporal coverage and low overlap of low power lidar instruments is a valuable add-on used to study the diurnal variation of aerosol layers and to trigger advanced measurements performed using high-power lidar instruments. Even single wavelength low-power lidars are able to detect high resolution dynamics of aerosol layers.

Aerosol high-power aerosol lidars (AHL) are aerosol lidar which thanks to the higher power can provide besides the same quantities reported for the ALC, more quantitative information about the aerosol optical properties. In particular, AHL used to provide profile aerosol optical properties (aerosol backscatter coefficient, aerosol extinction coefficient and aerosol linear depolarization ratio) at one or more wavelengths, allowing subsequent calculation of several spectral parameters (Angstrom exponents, lidar ratios) of the lofted aerosol layers, and therefore aerosol typing.

It is estimated that, with the progress of the technology (especially lasers and detectors), these two measurement techniques will evolve in the future to a low-cost, low-maintenance, automatic multiwavelength aerosol profiler. For the moment, however, the procedures for QA/QC, as well as the algorithms for data processing are instrument-specific and should be treated separately by CARS.

Aerosol column observations are covered in ACTRIS by **automatic sun/sky/lunar photometers** (ASP). The state-of-the-art photometric measurement techniques and associated retrieval techniques provide aerosol properties both directly (e.g. daytime and night time spectral extinction AOD and daytime downward sky angular, spectral and polarized radiance) and indirectly (size distribution, refractive indexes, single scattering albedo, spherical fraction, scattering properties.

These measurement techniques are related to the following ACTRIS variables obtained and managed by ARES: a) high-power aerosol lidar: aerosol backscatter profile, aerosol extinction profile, linear particle depolarization ratio (several wavelengths), water vapor mixing ratio profile, aerosol lidar ratio(s), aerosol Angstrom coefficients (if multiwavelength);

b) automatic low-power aerosol lidar: attenuated backscatter profile, aerosol layer height, cloud base; c) automatic sun/sky/polarized/lunar photometer: columnar spectral aerosol optical depth, spectral angular radiance and polarization, size distribution, absorption, spherical/non-spherical fraction, refractive index, and other derived radiative properties. Synergies between aerosol profile and column observations are being greatly developed within ACTRIS-1/2 to provide higher-level aerosol variables such as daytime extinction, backscatter, absorption and mass concentration (total, fine, coarse) and columnar aerosols optical and microphysical properties.

Fig. 3 ACTRIS aerosol remote sensing stations, May 2020

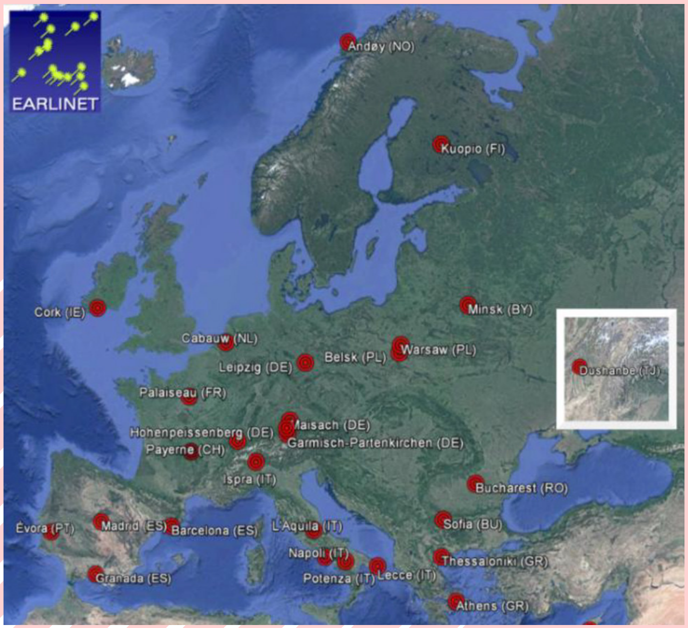

Currently, there are 28 aerosol remote sensing sites operating in ACTRIS, distributed as shown above. Each of the sites operate co-located aerosol high-power lidars and sub/sky/lunar photometers.
The data products workflow from the aerosol remote sensing NFs to the ACTRIS Data Portal is shown below.

2.2. Results

2.2.1 Dynamics of the aerosol structures

A simple product from the lidar measurements is the temporal variation of the vertical aerosol structures, so-called “lidar quicklooks” [2]. This is obtained either as not calibrated Range Corrected Signal (RCS), or as calibrated attenuated backscatter, and reflects how the intensity of the backscattered light changes with altitude and time.

Fig. 4 Workflow of the aerosol remote sensing data and data products

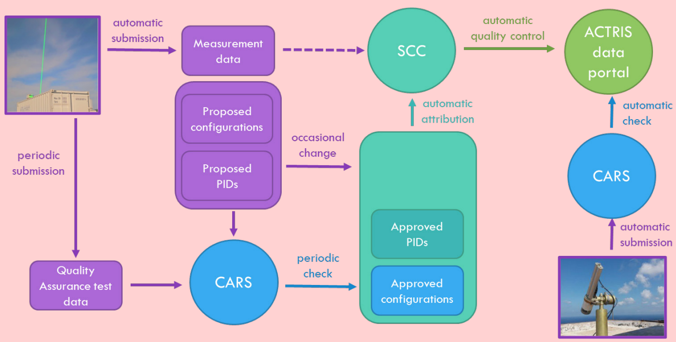

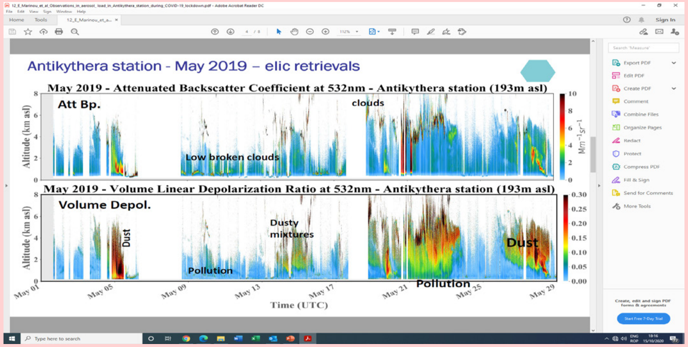

Fig. 5 Aerosol features identification from the time variation of the attenuated backscatter (upper panel) and volume depolarization profiles (bottom panel) at Antikythera aerosol remote sensing station. Courtesy of Eleni Marinou et al., NOA

By analyzing these plots, we have a first indication for the presence of lofted aerosol layers and clouds, aerosol injection into the Planetary Boundary Layer (PBL) and particle shape. Also, these plots can point out on instrument problems (energy drop, misalignments, instability, etc.).

2.2.2 Profile of the aerosol optical properties

More quantitative information is obtained by processing the lidar measurements with the Single Calculus Chain operated by ARES [1]. With the current setup of most of the ACTRIS lidars, the following data products are calculated by the SCC:

- aerosol backscatter coefficient at 1064nm (b1064)
- aerosol backscatter coefficient at 532nm (b532)
- aerosol backscatter coefficient at 355nm (b355)
- linear particle depolarization ratio at 532nm (d532)
- linear particle depolarization ratio at 355nm (d355)
- aerosol extinction coefficient at 532nm (a532)
- aerosol extinction coefficient at 355nm (a355)

Depending on the design of the lidar, Raman channels can be operated during daytime (if the lidar system is equipped with optics/detectors optimized for the reduction of the sky background), or only during nighttime. As such, the related data products in general differ from day to night, in terms of evaluation approach. In general, the aerosol extinction coefficient is still limited to the night time operation because of the low signal to noise ratio during daytime. The aerosol backscatter coefficient is a measure of the aerosol load. The linear particle depolarization is a measure of the aerosol non-sphericity.

2.2.3 Aerosol microphysical properties

Further analysis can be made based on the full set of data products above, for example to separate the contribution of spherical and non-spherical particles out of the total aerosol load in the vertical or retrieve the fine and coarse volume concentrations. Several methods can be

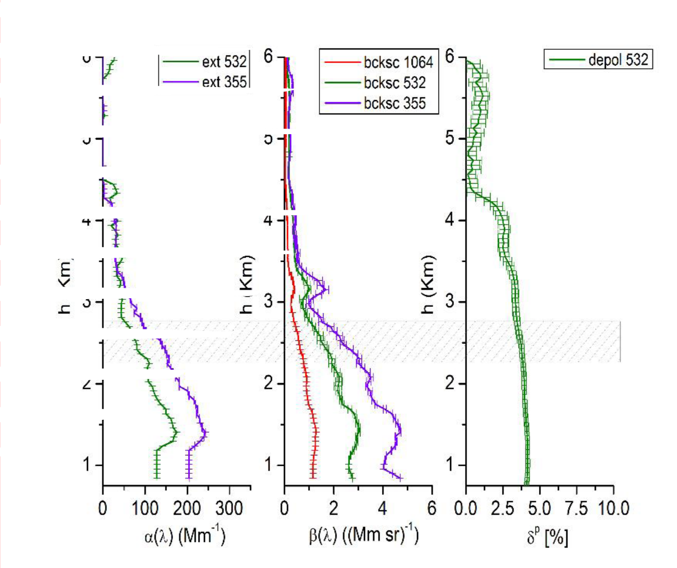

Fig. 6 Aerosol optical products retrieved with the Single Calculus Chain for the Bucharest aerosol remote sensing station: a) aerosol extinction coefficient at 255 and 532 nm; b) aerosol backscatter coefficient at 355, 532 and 1064 nm; c) linear particle depolarization ratio at 532 nm.

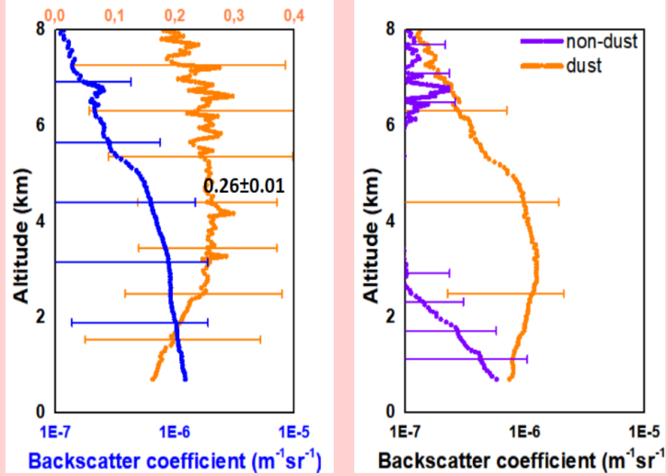

Fig. 7 Separation of the aerosol backscatter coefficient from spherical and non-spherical particles at Antikythera aerosol remote sensing station. Courtesy of Eleni Marinou et al., NOA

employed, starting from the simple POLIPHON method [3], to the more complex GRASP retrieval [4] which combines information from the time coincident lidar and the photometer measurements.

2.3. Conclusions

Significant progress has been made in ACTRIS to harmonize and standardize the procedures for data collection and data processing. The aerosol remote sensing component inherits from the previous project-based collaboration in EARLINET and AERONET, however new data products are now possible, and a more complex quality assurance and quality control program is in place.

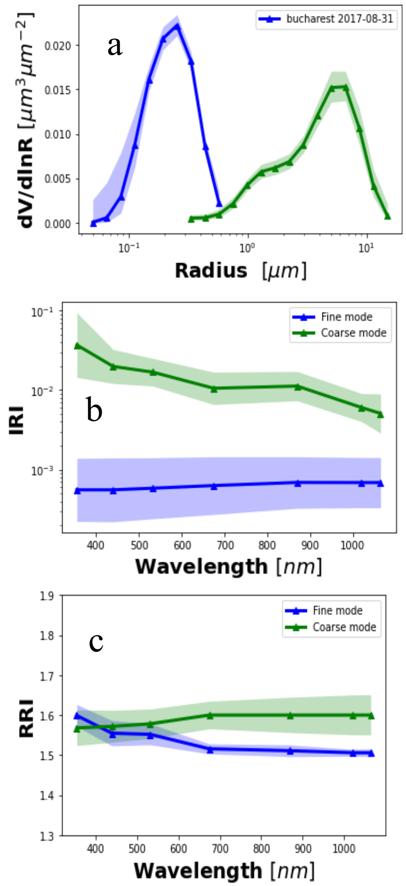

Fig. 8 GRASP retrieval for the Bucharest aerosol remote sensing station:
a) column-averaged size distribution;
b) column-averaged aerosol refractive index (real part);
c) column-averaged aerosol refractive index (imaginary part);

Acknowledgements

This research was partially supported by the ACTRIS-IMP project financed by the European Commission under the H2020 program; by the Romanian Ministry of Research and Innovation through Program Development of the national research development system, Subprogram 1.2—Institutional Performance—Projects of Excellence Financing in RDI, Contract No.19 PFE/17.10.2018, by the Romanian National Core Program Contract No.18N/2019; by the European Regional Development Fund through the Competitiveness Operational Programme 2014–2020, POC-A.1-A.1.1.1-F—2015, project Research Centre for Environment and Earth Observation CEO-Terra, SMIS code 108109, contract No. 152/2016; and by PREPARE project, code MY SMIS 107874, financed by European Regional Development Fund through Competitiveness Operational Programme 2014-20020.

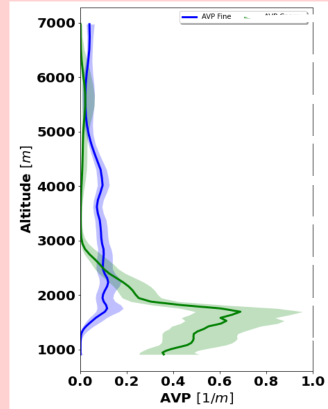

Fig. 9 Fine and coarse modes volume concentration profiles retrieved with GRASP for the Bucharest aerosol remote sensing station

References

[1] G. D'Amico, A. Amodeo, H. Baars, I. Binietoglou, V. Freudenthaler, I. Mattis, U. Wandinger, G. Pappalardo, Atmos. Meas. Tech., **8**, 4891 (2015).
[2] G. D'Amico, A. Amodeo, I. Mattis, V. Freudenthaler, G. Pappalardo, Atmos. Meas. Tech., **9**, 491 (2016).
[3] Ansmann, P. Seifert, M. Tesche, U. Wandinger, Atmos. Chem. Phys., **12**, 9399 (2012).
[4] O. Dubovik, M. Herman, A. Holdak, T. Lapyonok, D. Tanré, J.L. Deuzé, F. Ducos, A. Sinyuk, A. Lopatin, Atmos. Meas. Tech., **4**, 975 (2011).

*Corresponding author: D. NICOLAE
nnicol@inoe.ro

ACTRIS-EARLINET campaign during COVID-19 lockdown

I. STACHLEWSKA[a], D. NICOLAE[b]
University of Warsaw, Faculty of Physics, Warsaw, Poland National Institute of R&D for Optoelectronics, Magurele, Romania

Abstract: *In April 2020 ACTRIS (Aerosol, Clouds and Trace gases Research Infrastructure) mobilized its structures to study the possible impact of the COVID-19 related restrictions on the atmospheric composition. An intensive lidar measurement campaign was organized in May 2020, in order to clarify if, and how much the aerosol has changed compared to climatological values. This paper describes the preliminary findings at the 21 participating lidar stations.*

Keywords: aerosol, remote sensing, COVID-19 lockdown.

1. Introduction

In recent times air pollution has arisen as an environmental issue of major concern worldwide, particularly for developing countries, and may extend from local to global scale (Fang et al., 2009). Emissions of primary pollutants comprising particulate matter (aerosols) and gases (nitrogen dioxide / NO2 and carbon monoxide / CO) play a vital role on environment and human health. Earth-atmospheric radiation budget is greatly affected by the aerosols through scattering and absorption of incoming solar radiation, which further influences the formation of clouds and precipitation.
Following the outbreak of the novel corona virus (COVID-19) and its declaration by the World Health Organization (WHO) to be a public health emergency of international concern, several countries across the globe imposed national lockdowns to contain the pandemic. Despite the dramatic health and socioeconomic consequences of COVID-19 lockdowns, their environmental impact might be beneficial. Bans on mass gatherings, mandatory school closures, and home confinement during lockdowns have all resulted in lower traffic-related pollutant emissions and improved air quality in Asia, Europe and America [1],[2]. The restrictions also present an opportunity to evaluate the cascading responses from the interaction of humans, ecosystems, and climate with the global economy.
The European Aerosol Research Lidar Network, EARLINET, was established in 2000 as a research project with the goal of creating a quantitative, comprehensive, and statistically significant database for the horizontal, vertical, and temporal distribution of aerosols on a continental scale. Since then EARLINET has continued to provide the most extensive collection of ground-based data for the aerosol vertical distribution over Europe, using high-power lidars. EARLINET is now part of ACTRIS (Aerosol, Clouds and Trace gases Research Infrastructure), a pan-European initiative consolidating actions amongst European partners producing high-quality

observations of aerosols, clouds and trace gases.
In April 2020 ACTRIS mobilized its structures to study the possible impact of the COVID-19 related restrictions on the atmospheric composition. Despite the limited access to the laboratories, EARLINET/ACTRIS observation sites organized an intensive measurement campaign in May. The scope of the campaign was twofold: a) to monitor the atmosphere's structure during the lockdown and early relaxation period in Europe; b) to identify possible changes due to decreased emissions, by comparison to the aerosol climatology in Europe.

2. Experimental

2.1. Methodology

2.1.1. Campaign organization

During the intensive lidar campaign in May 2020, the near-real-time (NRT) capability of the EARLINET-ACTRIS was to be facilitated and demonstrated. EARLINET currently comprises 31 active stations. Out of these, 21 participated in this campaign, covering different regions over Europe. These stations operate either automatic and/or remotely controlled instruments, or they are located in regions where a complete lock-down was/is not effective.

Table 1 List of participating lidar stations and coordinates.
In red: continuous operating stations

Location	Coordinates
Athens	37.9600 N, 23.7800 E, 212 m
Barcelona	41.3930 N, 2.1200 E, 115 m
Belsk	51.8300 N, 20.7800 E, 180 m
Bucharest	44.3480 N, 26.0290 E, 93 m
Cabauw	51.9700 N, 4.9300 E, 0 m
Clermont-Ferrand	45.7610 N, 3.1110 E, 420 m
Evora	38.5678 N, -7.9115 E, 293 m
Granada	37.1640 N, -3.6050 E, 680 m
Kuopio	62.7333 N, 27.5500 E, 190 m
Lecce	40.3330 N, 18.1000 E, 30 m
Leipzig	51.3527 N, 12.4339 E, 125 m
Lille	50.6117 N, 3.1417 E, 60 m
Limassol	34.6700 N, 33.0400 E, 10 m
Hohenpeissenberg	47.8019 N, 11.0119 E, 974 m
Palaiseau	48.7130 N, 2.2080 E, 156 m
Potenza	40.6000 N, 15.7200 E, 760 m
Roma-Tor Vergata	41.8330 N, 12.6500 E, 110 m
Thessaloniki	40.6300 N, 22.9500 E, 50 m
Warsaw	52.2100 N, 20.9800 E, 112 m
Antikythera	35.8600 N, 23.3100 E, 193 m
Belgrade	44.8557 N, 20.3913 E, 89 m

The lidars measured in an intensified schedule, at least twice per day (minimum two hours at noon, and minimum two hours after sunset). For data evaluation the SCC was used. The SCC is a tool for the automatic analysis of aerosol lidar measurements developed within EARLINET network [3]. The main aim of SCC is to provide a data processing chain that allows all EARLINET stations to retrieve, in a fully automatic way, the aerosol backscatter and extinction profiles, starting from the raw lidar data collected by the lidar systems they operate [4]. All input parameters needed to perform the lidar analysis are stored in a database to keep track of all changes which may occur for any EARLINET lidar system over the time, assuring the traceability of the data.

The data products calculated by the Single Calculus Chain / individual algorithms depend on the configuration of the lidar system (i.e. the available channels) [5]:

- b1064 – the aerosol backscatter coefficient at 1064nm, calculated from the elastic channel (1064nm) with the Fernald-Klett algorithm; assumption of the lidar ratio at 1064nm is required
- b532 – the aerosol backscatter coefficient at 532nm, calculated from the elastic channel (532nm) with the Fernald-Klett algorithm; assumption of the lidar ratio at 532nm is required
- b355 – the aerosol backscatter coefficient at 355nm, calculated from the elastic channel (355nm) with the Fernald-Klett algorithm; assumption of the lidar ratio at 355nm is required
- d532 – the linear particle depolarization ratio at 532nm, calculated from the combination of polarization channels at 532nm
- d355 – the linear particle depolarization ratio at 355nm, calculated from the combination of polarization channels at 355nm
- a532 – the aerosol extinction coefficient at 532nm, calculated from the Raman signals at 607nm with the Raman algorithm
- a355 – the aerosol extinction coefficient at 355nm, calculated from the Raman signals at 387nm with the Raman algorithm
- b(a)532 – the aerosol backscatter coefficient at 532nm, calculated from the combination of elastic (532nm) and Raman (607nm) channels
- b(a)355 – the aerosol backscatter coefficient at 355nm, calculated from the combination of elastic (355nm) and Raman (387nm) channels

Out of all the retrieved data products, this study focuses on b532 and d532 only, as being commonly available from many stations, both during daytime and nighttime. However, further analysis will include also other optical products (aerosol extinction coefficients, Angstrom exponents, lidar ratios), as well as synergy products (fine and coarse mode volume concentrations).

The aerosol backscatter coefficient is a measure of the aerosol load. The linear particle depolarization is a measure of the aerosol non-sphericity. These physical quantities were averaged within two different altitude ranges to investigate the aerosol variability related to the boundary layer and the

free troposphere. The low troposphere is defined up to 3 km altitude, where local influences are still possible. The high troposphere is defined from 3 km up to 7 km, where typically long-range transport of aerosols occurs and local influences are no longer present. The average over the daytime and the nighttime is provided separately per each altitude range.
The average values are provided at 532 nm, as this is a wavelength at which the majority of the lidars operate. This wavelength is also preferable for a first analysis because many available satellites, models and passive sensors provide information in the visible range. For those sites for which only backscatter at 355 nm was available, the values were scaled to 532 nm considering a backscatter Angstrom exponent of 1. No wavelength dependence has been regarded for the particle depolarization ratio.
The number of profiles used for calculation of the mean values is reported in white, for the others no full information necessary for calculations of the mean values was available. Being an intensive parameter, the linear particle depolarization ratio values are considered significant only when the aerosol load is high enough to allow the depolarization characterization. Specifically, the values that are satisfying simultaneously the following three criteria, are used for the averaging procedures: backscatter > 5x10-7 m-1sr-1 and error_backscatter/abs(backscatter) < 50% and error_depolarization/abs(depolarization) < 50%. The average values are reported only for those parameters that were measured at least 3 times within the considered slot of measurement (e.g. daytime low troposphere).

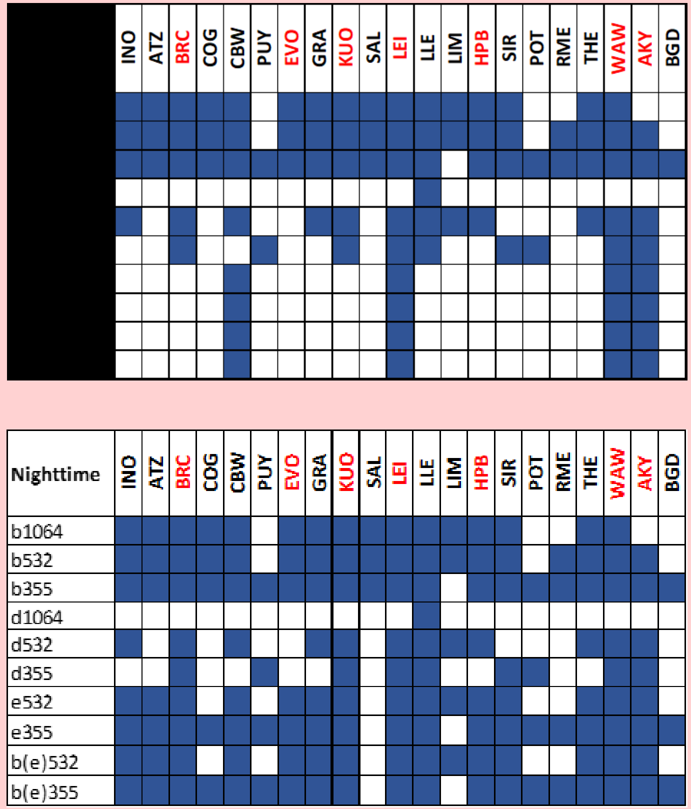

Fig. 1 Data products calculated for each station during: daytime (upper panel) and night-time (lower panel); in red, stations providing quasi-continuous measurements.

This first analysis is based on the data processed by the SCC and directly public on the THREDDS server in NRT. These datasets are not fully quality controlled because the 2 quality

control steps (manual checks at station level and automatic centralized quality control procedure at data center level) currently running on the EARLINET "standard" datasets are here not applied for the aim of a NRT data provision.
For the purposes of the campaign, the measurements were submitted and processed in the near-real time in maximum 12h after the end of the mandatory noon and nighttime observation. Each station performed some visual inspection for selecting the most suitable profile for the fast analysis of aerosol, situation and highlighting the presence of clouds not correctly captured by the SCC Cloud masking module. However, this is still preliminary data until the full set of the quality assurance / quality control (QA/QC) procedures is applied and the re-analysis is performed and finalized.
Depending on the configuration and on the power of the lidar system, the various stations can provide all, or some of the data products, as shown below.
All 21 stations performed measurements. In general, there were very few technical problems, except the Potenza station (from 16 May no observations due to laser failure).
Many of the stations experienced days with unfavorable weather conditions for observations (rain or very low clouds saturating the lidar signal).
Out of the 1302 scheduled observations, 693 were performed, representing 53%. Although many stations have performed additional measurements, for the reason of ensuring equal sampling, only 2 datasets per day per station were selected for the analysis. The rest of the datasets are remaining available for detailed studies. In 27% of the cases, measurements could not be performed due to weather conditions (rain or very low clouds). Access to the laboratory and lack of personnel made the measurements impossible in 12% of the cases (especially in the first week), while only 8% of the measurements could not be performed due to technical problems, or instrument setting and check-ups.

2.1.2. Meteorological context

After the exceptionally dry and sunny April 2020, May 2020 was accompanied by many vicissitudes of weather. During the first days of the month, cold arctic air masses were present in North Europe, combined with the frontal occlusions over Scandinavia. Atmospheric circulation above Europe

Fig. 2 MSG-RGB Dust Satellite Image and Geopotential height at 500hPa for 18 May 2020 06UTC (source:http://eumetrain.org/ePort_MapViewer/).

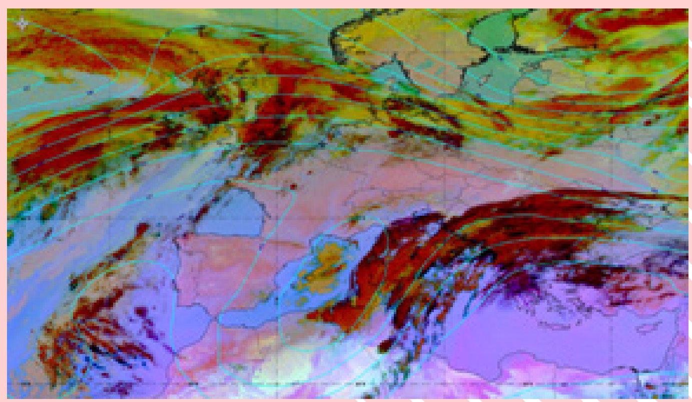

was described by zonal flow, with no large horizontal temperature or pressure gradients. During the second week (8-15 May), the circulation can be described by upper high-pressure fields above Balkans and deep trough/low over western Iberian Peninsula, along with cold arctic air-masses aloft over North Europe. During the third week (14-21 May), the large-scale dynamics provoked a heat-wave, very rare for mid-May, which expanded across the southern Mediterranean from North Africa, spread into south Italy, southern Balkans, and Turkey. During the last week (24-31 May), a frontal activity in combination with a classic dipole pattern was underway across European continent. A cold front over eastern and northern Europe at the beginning of the week, and another one over Northern Europe at the end, resulted in cloudy and rainy weather.
During the campaign period, the European region was affected with five dust outbreaks.
More specifically, during 2-5 of May, a surface low pressure system over the Atlantic Ocean that was enhanced by a well-structured trough in the upper troposphere, resulted in the strong South winds that loaded dust mass above the Western Mediterranean. Dust mass was spread to the area of Portugal and, gradually, extended towards the East, thus affecting Spain. During 6-8 of May, the formation of a low-pressure system over Egypt loaded dust mass from Morocco to the Western Mediterranean. At the same time, a deeper low-pressure system above Morocco with high winds, gradually spread dust in parts of central and Eastern Europe and the Eastern Mediterranean until 13 of May. The most intense dust outbreak of the month was initiated on 12 of May, by a surface low pressure system over the dust sources of North Sahara, enhanced by a deep trough in the upper troposphere. This was associated with thick cloud cover.

2.2. Results

2.2.1 Mean values of the optical products in Europe

We present a brief analysis for the entire time period of the NRT campaign (01-31 May 2020) of the average values for two optical parameters commonly measured at the observation sites: aerosol backscatter coefficient and particle linear depolarization ratio.
Aerosol backscatter coefficient is a measure of the aerosol load. Linear particle depolarization is a measure of the aerosol non-sphericity. Low troposphere is here defined up to 3 km altitude, where local influences are still possible. High troposphere is defined from 3 km up to 7 km, where typically long-range transport of aerosols occurs and no local influences are present. For sites for which only backscatter at 355 nm was available, the values were scaled to 532 nm considering a backscatter Angstrom exponent of 1. No wavelength dependence has been considered for the particle depolarization ratio. The number of profiles used for the mean calculation is reported in white.
Being an intensive parameter, the particle depolarization

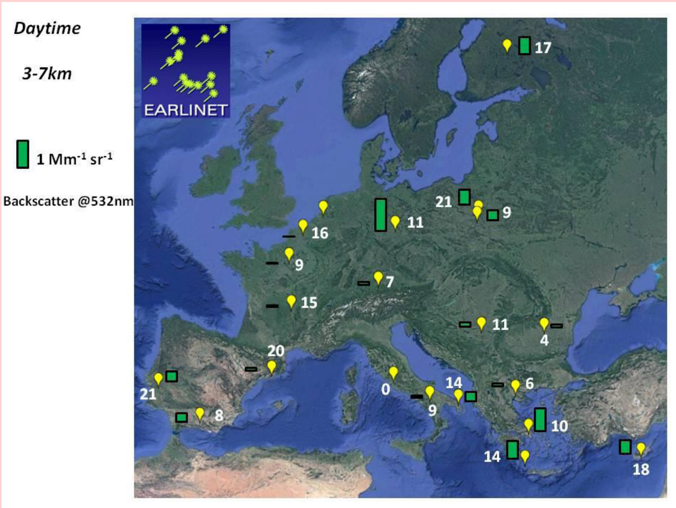

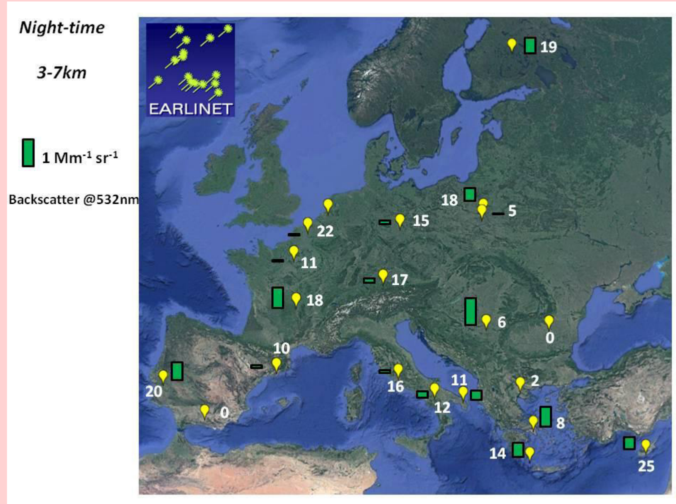

Fig. 3 Monthly mean values of the aerosol backscatter coefficient (532 nm) for low troposphere (bottom panel) and high troposphere (upper panel) during daytime. The number of averaged profiles is reported in white.

Fig. 4 Monthly mean values of the aerosol backscatter coefficient (532 nm) for low troposphere (bottom panel) and high troposphere (upper panel) during nighttime. The number of averaged profiles is reported in white.

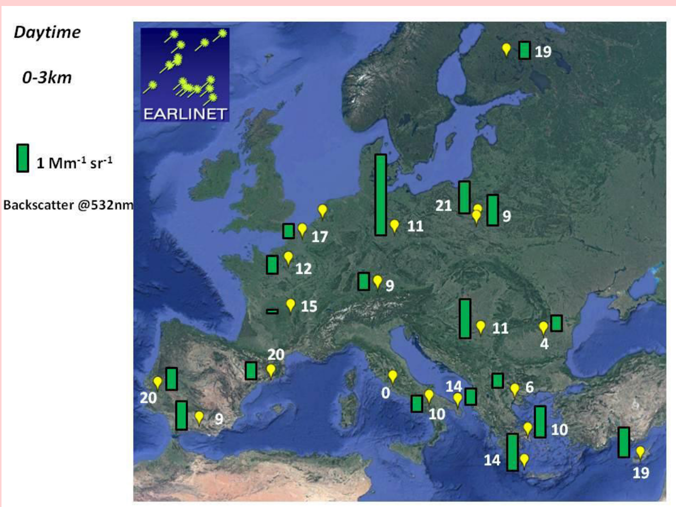

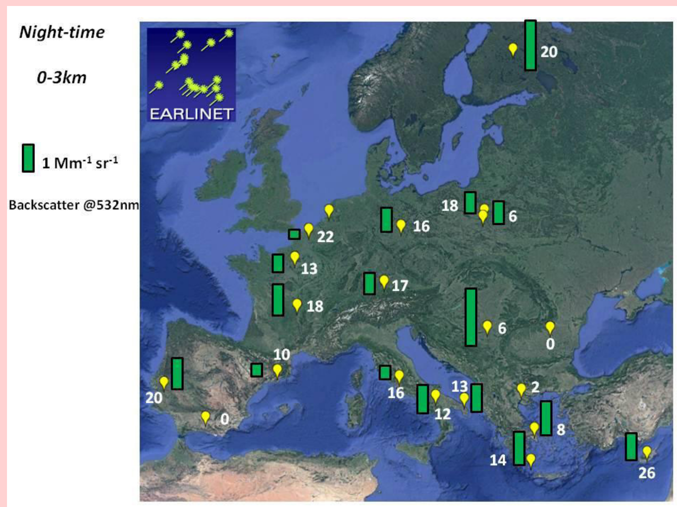

values are considered significant only when the aerosol load is high enough to allow the depolarization characterization. Specifically, the depolarization values satisfying the following criteria, satisfied simultaneously, are considered for the averaging procedures: backscatter > 5x10-7 m-1sr-1 and error_backscatter/abs(backscatter) < 50% and error_depolarization/abs(depolarization) < 50%. Weekly means are reported only for parameters measured at least 3 times for the considered slot of measurement.

Monthly mean values of the aerosol backscatter coefficient (532 nm) for low troposphere (bottom panel) and high troposphere (upper panel) during daytime. The number of averaged profiles is reported in white.

Monthly mean values of the aerosol backscatter coefficient (532 nm) for low troposphere (bottom panel) and high troposphere (upper panel) during nighttime. The number of averaged profiles is reported in white.

Aerosol backscatter at 532nm is typically higher in the Southern Europe respect to the Central and Northern Europe, because of the dust intrusion described in the meteorological context reported above. The almost equal mean values reported for daytime and nighttime observation both in the lowest troposphere and high troposphere is another signature of the relevance of the dust intrusion over Eastern Mediterranean stations (Italy, Greece, Cyprus). This is reflected also in the depolarization ratio values reported below, with values around 20% on average over the month both in low and free troposphere. Especially in Antikythera and in Limassol the depolarization ratio remains relatively constant during daytime and nighttime, within both tropospheric layers, in agreement with the vertical distribution and the time evolution of the dust plume transported over this region. On the contrary the big difference in daytime and nighttime backscatter mean value in the 0-3 km altitude range for Evora highlights the absence of dust and is the result of the marked PBL diurnal cycle.

Northern Europe is characterized by very low depolarization values and typically low values in the aerosol backscatter values both in low and high troposphere.

2.2.2 Optical products at regional scale

The graphs below show changes of the aerosol backscatter coefficient in the low and high troposphere during the

Fig. 5 Time evolution of the mean aerosol backscatter coefficient in the low troposphere (< 3 km altitude) and in the high troposphere (> 3 km altitude) at European scale in May 2020

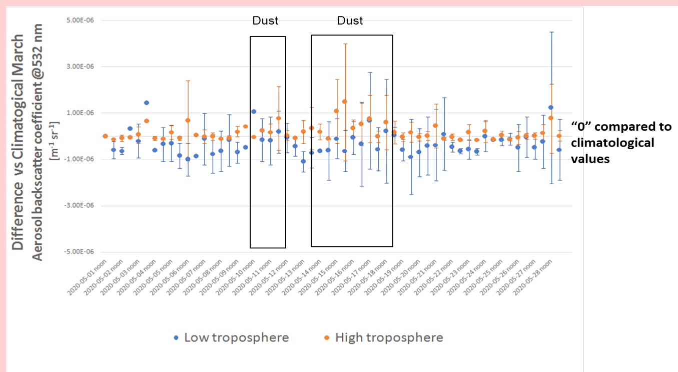

week of interest. They are calculated as a difference to the climatological values for May between 2000 – 2015 [6]. Positive values indicate higher aerosol load than the climatological mean.

As a preliminary result, we noticed that no significant decrease of the aerosol backscatter coefficient was measured in the high troposphere, which is affected only by natural variability during the Spring season. In the low troposphere, a small decrease of the aerosol backscatter coefficient is measured, fluctuating however during dust and biomass burning outbreaks, or pollen rise-up. The small decrease visible at European level seems to cancel out towards the end of May, when most of the countries have relaxed the restrictions.

2.3. Conclusions

The preliminary analysis made on aerosol lidar data shows that by simply comparing the observed values with the climatological values from 2000-2015 is not sufficient to extract a clear conclusion on how much the COVID-19 lock-down has impacted the aerosols in the atmosphere. The changing meteorological conditions, the persistent periods with very low clouds and rain which made the lidar measurements difficult (therefore decreasing the number of measurements), as well as the presence of dust transported from North Africa to the Southern stations have reduced the statistical relevance.

Although it is clear from the analysis that the lock-down did not affected the high troposphere, for the low troposphere a certain effect can be seen, however within the climatological variability. Interestingly, when looking at the continental scale, decreased values of the aerosol backscatter coefficient in the low troposphere are mostly measured during May, while values for March and April are closer to the climatological values. This is, however, an effect of averaging over all stations. It is known that the restrictive measures were imposed at different times in Europe, therefore the effect of the lock-down (if any) has manifested at different times in the different regions. For example, in Eastern Mediterranean lower values of the aerosol backscatter coefficient were observed starting February, while in Central and Eastern Europe such decrease started in March. The amplitude is also different in various regions, being related to the intensity of the economic activity that was affected by the lock-down. April and the beginning of May seems to be uniformly characterized by lower values in the low troposphere; this is the time when restrictive measures were present in most of the regions.

The aerosol backscatter coefficient analyzed in this study is a proxy for the aerosol concentration, however a more quantitative analysis must be made to consolidate the conclusions. The values reported for the linear particle depolarization ratio show that pollen, as well as dust transported from North Africa sometime overlapped with the local aerosol.

Acknowledgements

This research was partially supported by the ACTRIS-IMP project financed by the European Commission under the H2020 program; by the Romanian Ministry of Research and Innovation through Program Development of the national research development system, Subprogram 1.2—Institutional Performance—Projects of Excellence Financing in RDI, Contract No.19 PFE/17.10.2018, by the Romanian National Core Program Contract No.18N/2019; by the European Regional Development Fund through the Competitiveness Operational Programme 2014–2020, POC-A.1-A.1.1.1-F—2015, project Research Centre for Environment and Earth Observation CEO-Terra, SMIS code 108109, contract No. 152/2016; and by PREPARE project, code MY SMIS 107874, financed by European Regional Development Fund through Competitiveness Operational Programme 2014-20020.

References

[1] P. Sicard, A. De Marco, E. Agathokleous, Z. Feng, X. Xu, E. Paoletti, J.J.D. Rodriguez, V. Calatayud, Sci. Total Environ., **735** (2020).
[2] G. He, Y. Pan, T. Tanaka, Nat. Sustain., **24**, (2020).
[3] G. Pappalardo, A. Amodeo, A. Apituley, A. Comeron, V. Freudenthaler, H. Linné, A. Ansmann, J. Bösenberg, G. D'Amico, I. Mattis, L. Mona, U. Wandinger, V. Amiridis, L. Alados-Arboledas, D. Nicolae, M. Wiegner, Atmos. Meas. Tech., **7**, 2389 (2014).
[4] G. D'Amico, A. Amodeo, H. Baars, I. Binietoglou, V. Freudenthaler, I. Mattis, U. Wandinger, G. Pappalardo, Atmos. Meas. Tech., **8**, 4891 (2015).
[5] I. Mattis, G. D'Amico, H. Baars, A. Amodeo, F. Madonna, M. Iarlori, Atmos. Meas. Tech., **9**, 3009 (2016).
[6] EARLINET All 2000-2015. World Data Center for Climate (WDCC) at DKRZ. https://doi.org/10.1594/WDCC/EARLINET_All_2000-2015, 2018.

*Corresponding author: D. NICOLAE
nnicol@inoe.ro

Assessment of waste burning in Romania

L. MARMUREANU[a*], C. MARIN[a], J. VASILESCU[a], L. LEVEI[b], E. LEVEI [b] M. BOLDEANU[a], B. ANTONESCU[a], S. ANDREI[a], R. PIRLOAGA[a], D. ENE[a], A. DANDOCSI[a], C. RADU[a],

[a]*National Institute of Research and Development for Optoelectronics INOE 2000, Remote Sensing Department, 409 Atomistilor Street, Magurele, 077125 Ilfov, Romania*

[b]*National Institute of Research and Development for Optoelectronics INOE 2000, Research Institute for Analytical Instrumentation Subsidiary, 67 Donath Street, 400293 Cluj-Napoca, Romania*

Abstract: *It is a common practice in some countries to burn vegetation to clean the land, all over the year or to burn waste especially in cold season as a source of heating especially in villages or peri urban area where energetic poverty is present. In Romania, the vegetation ignition especially during spring and summer it is a common practice. During the 2015-2018 more than 5000 fires were detected by satellite in the agricultural areas. Using fixed and mobile measurements different sources of burning processes have been identified in four urban and peri urban area in Romania.*

Keywords: agricultural waste, municipal waste, burning process

1. Introduction

Recent studies [1] have identified that the principal source for particles matter pollution is solid fuels combustion. In Europe [2,3] residential wood combustion represents the main source for fine particles. Depending on weather conditions, agricultural and biomass burning have a considerable (30−50%) contribution to the total air pollution in urban areas. Agricultural waste burning causes significant pollution of local and regional air, land and water as well. Usually, waste burning is used in less developed regions to diminish agricultural residues. To overcome this situation, all over the world, efforts were made to reduce and even eliminate the agriculture waste burning, including crop, vegetation after harvest, due to their extended harmful potential for surrounding areas. Several studies indicate that smoke plumes from agricultural waste burning in Eastern Europe are the source of essential pollution episodes in Northern-Western Europe [4]. In the case of Ukraine, the agricultural practices related burning represented 91% of active fires during 2002−2008 [5]. There are only few studies regarding agricultural waste burning are done for Hungary and Romania using satellite imagery [6]. Resources as MODIS Normalized Difference Vegetation Index are necessary to map the use of cropland, as is done in Estel et al. 2016 [6] for entire Europe. Field crops, leaves or wood are principal organic refuse burned, their contributions to the total emissions being dependent on the moisture content. Emission factors of 10 and 5 g/kg for PM (particulate matter) and PM10 have been noticed for a different type of

agricultural waste burning [7].
Beside the agricultural waste burning, the combustion of municipal waste represents an issue in developing countries, especially in the areas where the energetic poverty is present. Although Romania made essential steps to enhance the environment quality, waste management remains a crucial challenge, as the recycling and composting percentage are lower than the EU target levels [8]. The National Waste Management Strategy for 2014–2020 (2017) [9] was recently legislated (HG942/2017), allowing a better image on the present situation and future measures regarding waste management. According to Eurostat data [10], in 2016, Romania produced 177,557,063 tons of wastes, of which 5,218,255 tons represent household wastes. The report for 2017 [12] shows that in 2016, 5,260,000 tons of municipal wastes were collected by the municipalities, of which 70% represents household wastes. For 2009, the waste generated by the population without access to waste collection services has been calculated using a standard daily rate of 0.9 kg/capita/day for the urban areas and 0.4 kg/capita/day in rural areas [13]. Both the amount of collected municipal wastes and household waste had an increasing trend in the last years [10]. The deficiency present in a waste management system can determine the quantities of wastes burned especially in the villages.
The purpose of this study was to assess the presence of different type of waste burned in Romania, using satellite data, fixed and mobile measurements of different gaseous or particles pollutant.

2. Methodology

2.1. Agricultural waste burning

The analysis conducted here for agricultural waste burning assessment is based on data on fire locations provided by the Moderate Resolution Imaging Spectroradiometer (MODIS) carried on a polar orbit by the Terra and Aqua satellites [14]. The near-real-time thermal anomalies and fire locations from MODIS are processed by NASA Land, Atmosphere Near real-time Capability for EOS (LANCE) Fire Information for Resource Management System (FIRMS, https://earthdata.nasa.gov/earth-observation-data/near-real-time, accessed on 1 February 2019) using swath products (MOD14/MYD14). Both the thermal anomalies and the fire locations are represented on a grid with 1 km spatial resolution using the algorithm developed by Giglio et al. (2003) [15]. Thus, each 1 km pixel can contain one or more thermal anomalies and active fires. For the current analysis, we used data from MODIS (MODIS Collection 6) [16] for Romania and Hungary, covering the interval 1 January 2015–30 November 2018.
To identify the agricultural areas burned, the CORINE Land Cover (CLC) inventory (land cover/land use changed between 2012–2018, European Environmental Agency 2018) was adopted for the present analysis.

2.2. Municipal waste burning

2.2.1 Locations

To identify the area where municipal waste burning can occur, four different locations (cities and the peri urban regions) where choosen (Deva, Cluj, Focsani, Magurele). Two intensive sampling campaigns in winter (2018-2019; 2019-2020) and one in summer (2019) were performed. Here we present just campaign from winter 2019.

Fig. 1 Locations chosen for identification of residential waste burning

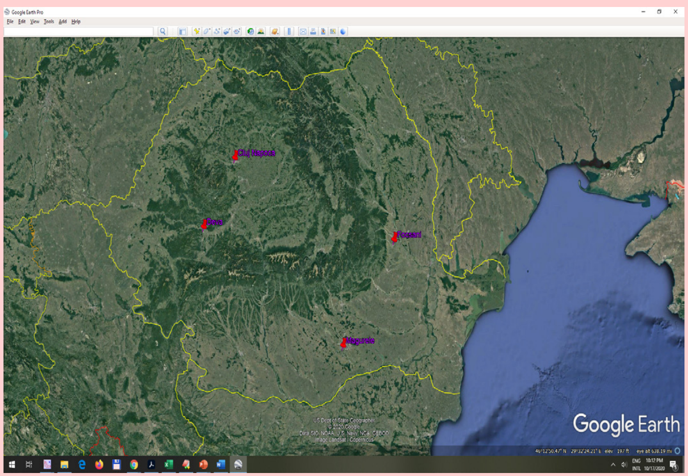

2.2.2 Fixed campaign

For the fixed campaign, all four stations were equipped with Digitel DHA-80 high volume sampler with sequential changer using Advantec QR-100 quartz fiber without binder. The concentrations are reported in µg m^{-3} for ambient conditions. The time resolution is always 24 hours (0–24).
For Cluj-Napoca, Deva and Focsani the data reported by Environment Protection Agency for CO, SO_2, O_3, NO, NO_2, NO_x and Meteo were used (www.calitateaer.ro and ECMWF-ERA5 for parts of meteorological parameters).

2.2.3 Mobile campaign

The mobile measurements took place in the same cities and the same time were the fixed measurements were performed. We take into account the main type of land cover in the region: residential area, low and high-density houses, industrial zone, intense traffic districts.
The mass concentration of the particles (PM1, PM2.5 and PM10) as well optical size distribution was measured with a Grimm EDM180. For mobile measurements, the highest time resolution of the instrument (6 seconds) was used. Multiple Nafion dryers (with additional pumps) were used in order to reduce the humidity influence on particles, especially in the hilly areas where the fog is present during the cold season.
In all settlements, the mobile measurements were performed by following pre-defined routes. Two types

of routes (short and long) were planned for all locations (Magurele, Focsani, Deva, Cluj). The length of the short routes varied around ~20 km, whereas that of the long routes was around 30−40 km. The short route was made in three periods of the day (morning, noon and evening) and was repeated 2−3 times. The paths might slightly be different from each other. For the visualization of the data, a number of procedures had to be implemented. The data from all the different instruments were synchronized at the time resolution of the GPS tracker (1-second resolution). The data were filtered using the speed recorded by the GPS tracker. A threshold of 10 km h^{-1} was selected to remove points that had very high values due to the traffic (being stuck at traffic lights, the influence of the van that carried the instruments). The values range for PM2.5 and PM10 is between 0−100 µg m^{-3}. This was used to show the spatial variation of the data. All values higher than 100 µg m^{-3} are represented in red, and the size of the circle indicates the value.

3. Results

3.1. Agricultural waste burning

To identify agricultural waste burning, we choose data from MODIS products with a confidence level equal to or greater than 70% (Tab.1) In total, regardless of the confidence level, 15,418 fires were detected over Romania. The number of fires over Romania is reduced at 5,996 when a threshold of 70% is applied to the confidence level (Tab. 1).

Total number of fires detected	Fires with confidence level≥70%	Fires with confidence level 100%
15,840	5,996	365

Table 1 Number of fires detected depending on the confidence level

To understand the spatial and temporal evolution of agricultural burning in Romania, first, the agricultural land was identified and classified according to with CORINE Land Cover (CLC) inventory. The inventory containing 44 classes of land cover with a minimum mapping unit of 25 hectares was acquired from the Copernicus land monitoring service (https://land.copernicus.eu/pan-european/corine-land-cover/lcc-2012-2018, accessed on 1 February 2019). Second, to select only the fires that occurred on agricultural land the locations of the fires were overlaid with the CLC using QGIS, QGIS, an open-source desktop geospatial software package (QGIS Development Team 2016) [1716]. Thus, the fires were considered agricultural fires if they occurred over these CLC categories 1) complex cultivation patterns, 2) fruit trees and berry plantations, 3) land principally occupied by agriculture with significant areas of natural vegetation, 4) non-irrigated arable land, 5) pastures, 6) permanently irrigated land, 7) rice fields and 8) vineyards.

Agricultural category	Number of fires (percent)
Complex cultivation patterns	81 (1.51%)
Fruit trees and berry plantations	47 (0.88%)
Land principally occupied by agriculture with significant areas of natural vegetation	112 (2.09%)
Non-irrigated arable land	4670 (87.16%)
Pastures	352 (6.57%)
Permanently irrigated land	2 (0.04%)
Rice fields	9 (0.16%)
Vineyards	85 (1.59%)
Total	5358

Table 2 Number of fires identified in different agricultural category

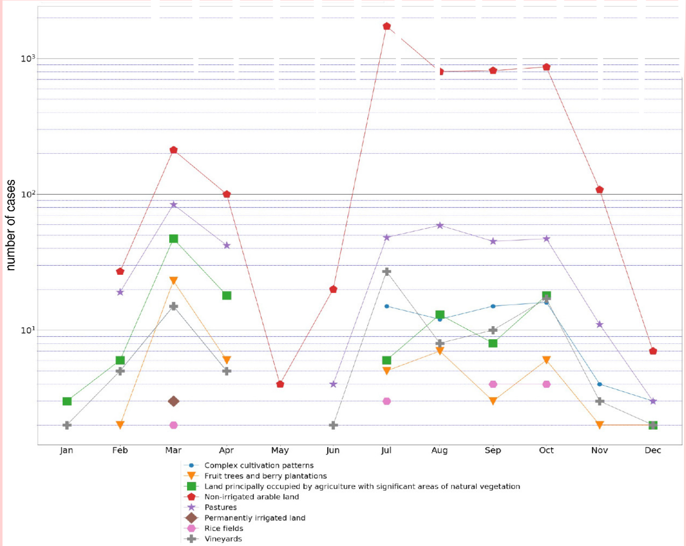

Fig. 2. The monthly distribution of agricultural fires

Over Romania, agricultural burning accounted for 33% of all fires. The majority of agricultural fires occurred over non-irrigated arable land (87.16%), followed by fires over pastures (6.57%) (Table 2).

The annual number of agricultural fires has increased in Romania between 2015 (1,133 fires) and 2016 (1,671), followed by a decrease since 2016.During the year, fires detected over non-irrigated arable land and those over vineyards have the main maximum in July and a secondary max in March (Fig. 2). Fires noticed over pastures, land principally occupied by agriculture with significant areas of natural vegetation and fruit trees and berry plantations reach a maximum in March and then remain almost constant between July–October. Is interesting to note that, except fires over non-irrigated arable land, no agricultural fires have been detected in May.

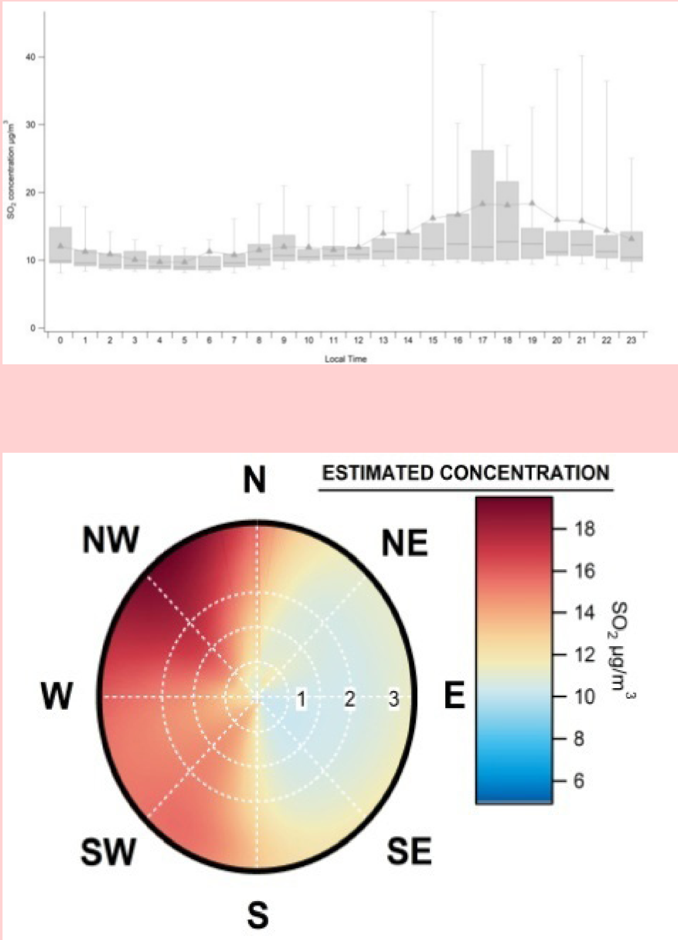

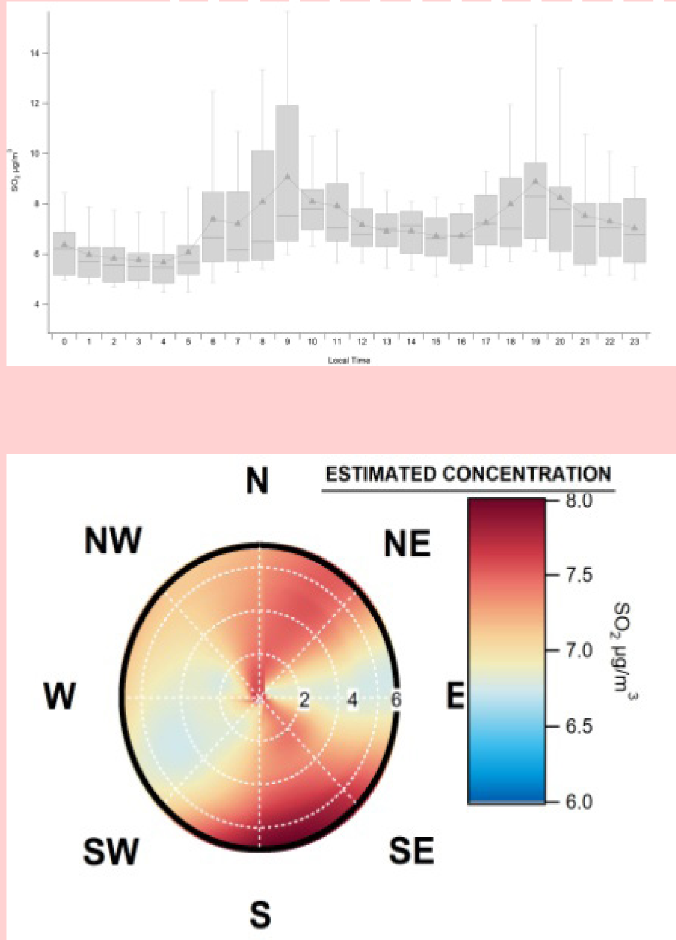

Fig. 3 SO_2 diurnal trends (a) and source estimation plot (b) in Deva

Fig. 4 SO_2 diurnal trends (a) and source estimation plot (b) in Cluj (b)

3.2.2 *Cluj-Napoca* (a)

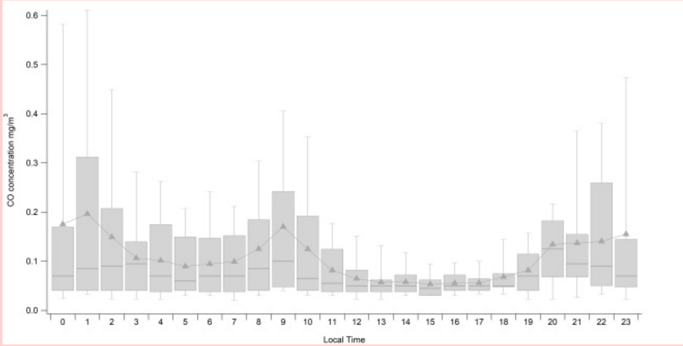

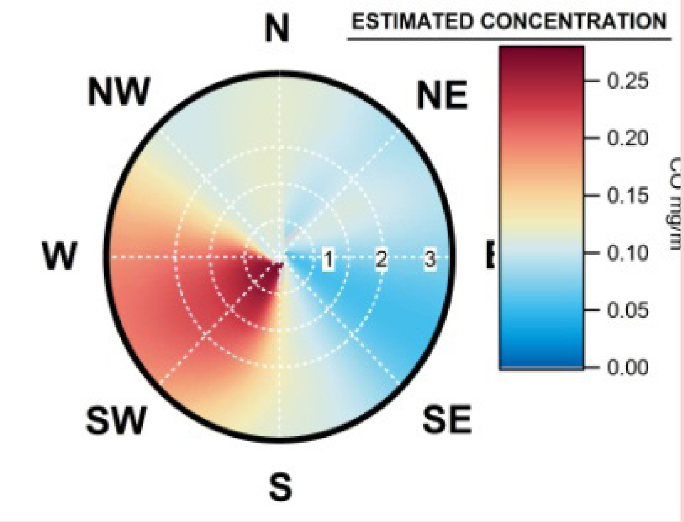

Fig. 5 CO diurnal trends (a) and source estimation plot (b) in Focsani

3.2. Municipal waste burning

The municipal waste burning was investigating, based on diurnal pattern of gases emitted usually in combustion processes, and also based on rose plot of pollutants after methodology described previously [18].

3.2.1 *Deva*

In Deva city the different number of sources can be seen in the SO_2 diurnal distribution where three peaks are visible. One small peak is visible in the morning at 9:00 AM and two in the evening between 17:00–19:00 and at 21:00. The highest peak from the afternoon is related to district heating and thermal power plant activity from Electrocentrale Deva no. 2. The small peak from the morning (9:00 AM) and from the afternoon (21:00) can be related to household heating (Fig.3 (a)). From the source estimation plot, the highest SO_2 concentration comes from NW where the thermal power plant location (NW 10 km from Deva) is. The high concentrations of SO_2 are coming from SW and are supposedly related to residential heating from that area (Fig.3 (b))
To distinguish between sources in Cluj-Napoca was very difficult based on fixed measurements, since the area is influenced by both traffic and household emissions. The primary pollution sources are located in the S part as well in

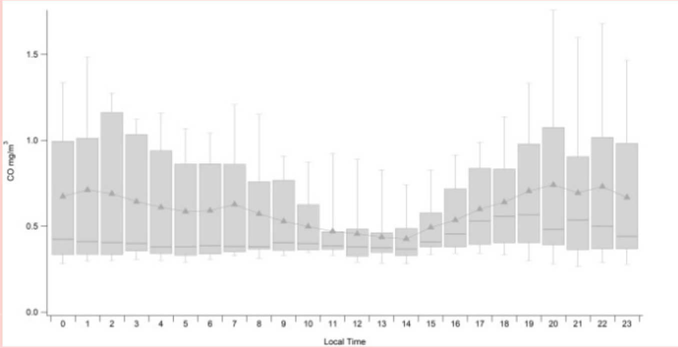

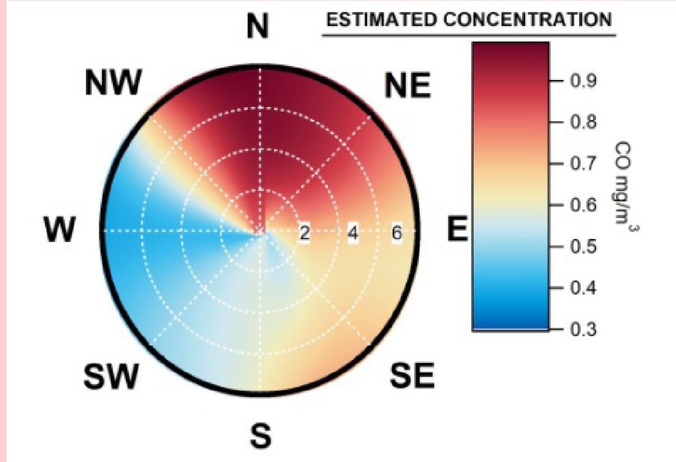

the N part (Fig.4b). The influence of the Somesul Mic river can be seen in the source estimation plot for SO_2 pollutant, lower concentrations being estimated on the E-W direction that corresponds to the riverbed.

3.2.3 *Focsani*

Besides traffic origin, CO is related to residential heating processes, but no separation is possible based on gaseous measurements. Usually, during the cold season household heating is started two times per day, early morning and late evening. The studied period was not characterized by low temperature, but CO diurnal trends present extended high concentrations during the night opposite to the temperature and the planetary boundary layer height.

Fig. 6 CO diurnal trends (a), source estimation plot (b) and mobile PM2.5 concentration(c) in Magurele

3.2.4 Magurele

The CO measured had an average concentration of 0.6 mg m^{-3}, with a maximum value of 2.35 mg m^{-3} and time series showed two periods (28–30 January and 02–04 February) with high concentrations. Three peaks out of four from CO diurnal trend correspond to the morning (7–9 AM) and evening (18–20) ones being related to traffic sources. Smaller peak around 01 AM is present in CO and PM_{10} diurnal trends (not shown), may be due to accumulation processes. One more substantial peak on CO diurnal trend at 22:00 and CO wind rose which estimate an additional source in the Eastern part of the site than could be attributed to residential heating
It can be noted that residential area with high concentration of $PM_{2.5}$ in the western part of the city (Fig. 6(c)) that was persistent all over the day according to our mobile measurements was not detected with the stationary measurements. Also, the main roads in the city seem that does not to affect the measurements sites that much as compared to Bucharest city and its ring road.

4. Conclusions

Agricultural waste burning is a common practice in Romania with high incidence during spring and summer.
Important sources were recorded in Deva residential area, being associated with a local power plant and residential heating. In Focsani, the main sources identified are associated with traffic activities.
For Magurele mobile measurements, similar hotspots were identified in 2019 and 2020. The hotspots are related to traffic, near the Bucharest ring road and residential heating in the west and east part of the route.
The concentrations measured by mobile measurements are instant values and can help in the identification of local hotspot. The high-resolution data (at one second) offer valuable information about the spatial and temporal distribution of different local sources. At the fixed locations, the measured concentrations are diluted, and not all punctual sources can be identified. Also, the hourly or daily average concentrations give us indications about exposure time but not about sources. Due to this, discrepancies between fixed and mobile measurements can occur.

Acknowledgements

This work was funded by the "Analyzing the effect of residential solid waste burning on ambient air quality in Central and Eastern Europe and potential mitigation measures" (No 310 07.027737/2018/788206/SER/ENV.C.3)
This research was partially supported by the Romanian Ministry of Research and Innovation through Program I—Development of the national research development system, Subprogram 1.2—Institutional Performance—Projects of Excellence Financing in RDI, Contract No.19 PFE/17.10.2018, by the Romanian National Core Program Contract No.18N/2019; by the European Regional Development Fund through the Competitiveness Operational Programme

2014–2020, POC-A.1-A.1.1.1-F—2015, project Research Centre for Environment and Earth Observation CEO-Terra, SMIS code 108109, contract No. 152/2016; and by PREPARE project, code MY SMIS 107874, financed by European Regional Development Fund through Competitiveness Operational Programme 2014-20020.

References

1. S.C. Anenberg, K. Balakrishnan, J. Jetter, O, Masera, S. Mehta, J. Moss, V. Ramanathan, Environ. Sci. Technol., **47**, 3944–3952, 315 https://doi.org/10.1021/es304942e, (2013).

2. L. Mărmureanu, J. Vasilescu, J. Slowik, A.S.H. Prévôt, C.A. Marin, B. Antonescu, A. Vlachou, A. Nemuc, A. Dandocsi, S. Szidat, Atmosphere, **11**, 385, https://doi.org/10.3390/atmos11040385, (2020).

3. C. Gonçalves, C. Alves, C. Pio, Atmos. Environ., **50**, 297–306, https:/doi.org/10.1016/j.atmosenv.2011.12.013, (2012).

4. A. Stohl, T. Berg, J. F. Burkhart, A. M. Fjǽraa, C. Forster, A. Herber, Ø. Hov, C. Lunder, W. McMillan, S. Oltmans, M. Shiobara, D. Simpson, S. Solberg, K. Stebel, J. Ström, K. Tørseth, R. Treffeisen, K.Virkkunen, K. E. Yttri, Atmos. Chem. Phys., **7**, 511-534, https://doi.org/10.5194/acp-7-511-2007, (2007).

5. W.M. Hao, S.P. Urbanski, B. Nordgren, A. Petkov, Daily Fire Occurrence in Ukraine from 2002 to 2008. In: Kogan F., Powell A., Fedorov O. (eds) in NATO Science for Peace and Security Series C: Environmental Security. Springer, Dordrecht, (2011).

6. S. Estel, T. Kuemmerle, C. Levers, M. Baumann, P. Hostert, Environ. Res. Lett. **11** 024015, https://doi.org/10.1088/1748-9326/11/2/024015, 2016

7. B. Sivertsen, Waste Management and the Environment, WIT Transactions on Ecology and the Environment, **92**, doi:10.2495/WM060471, (2006).

8. The Environmental Implementation Review available at http://ec.europa.eu/environment/eir/pdf/factsheet_ro_en.pdf (2019).

9. National Waste Management Strategy for 2014-2020 available at http://www.mmediu.ro/app/webroot/uploads/files/PNGD_vers5.pdf, (2017).

10. Eurostat available at http://appsso.eurostat.ec.europa.eu/nui/show.do?dataset=env_wasgen&lang=en, (2019)
ANPM available at http://www.anpm.ro/raport-de-mediu, (2017a).

11. ANPM available at http://www.anpm.ro/documents/12220/2209838/Raport+stare+mediu+anul+2017.pdf/12fc7560-32e3-4540-8c36-2432fe7674ae, (2017b).

12. Almasi available at https://www.eea.europa.eu/publications/managing-municipal-solid-waste/romania-municipal-waste-management, (2013).

13. J.L. McCarty, C.O. Justice, and S. Korontzi, Remote Sensing of Environment, **108**, 151–162. 2007.

14. L. Giglio, J. Descloitres, C.O. Justice, and Y.J. Kaufman, Remote Sensing of the Environment, **87**, 273–282, (2003).

15. MODIS Collection 6: MODIS Collection 6 NRT Hotspot/Active Fire Detections MCD14DL. Available on-line at http://earthdata.nasa.gov/firms (accessed on 1 February 2019).

16. QGIS Development Team, 2016: QGIS: A free and open source Geographic Information System. Open Source Geospatial Foundation Project. [Available online at http://www.qgis.org/.]

17. J.E. Petit, O. Favez, A. Albinet, F.A. Canonaco, Environ. Model. Softw., **88C**, 183–187, (2017).

Using Lidar Together with Cloud Radar and Wind Profiler Data to Investigate an Optically Thick Layer of Aerosol over Great Britain and Ireland

H. M. A. RICKETTS[a], C. WALDEN[b], C. WESTBROOK[c], J. JEFFERY[b], E. O'CONNOR[d], J. PREISSLER[e], E. NORTON[a]

[a]National Centre for Atmospheric Science, University of Manchester, United Kingdom, h.ricketts@manchester.ac.uk [b]STFC Chilbolton Observatory, United Kingdom, [c]University of Reading, United Kingdom [d]Finnish Meteorological Institute, Helsinki, Finland - University of Reading, UK, [d]Leosphere, France.

Abstract: On 16th October 2017 a layer of optically thick aerosol was advected over the British Isles. This layer made it possible to view the sun with the naked eye in the middle of the day and gave the sun a red colour. Initially, the layer was reported in the media as being Saharan dust which had been well forecast. But the previous day, forest fires had broken out in Portugal. This paper sets out to analyse the aerosol layer in more detail using ground-based remote sensing techniques.

Keywords: lidar, cloud radar, wind profiler, aerosol, layer.

1. Introduction

To detect aerosol layers in the atmosphere, lidar is the best choice as light is strongly scattered by aerosol. Using a network of lidars on Great Britain and Ireland it was possible to track the strongly absorbing layer. Figure 1 shows an example of the layer as captured by the HALO Doppler lidar (in blue) based at the Chilbolton Atmospheric Observatory (CAO) in the United Kingdom (UK). It shows a sloping and in places deep layer of aerosol. The bottom part of this layer rises as the layer passes overhead. This is reflected in measurements at other sites in the UK.

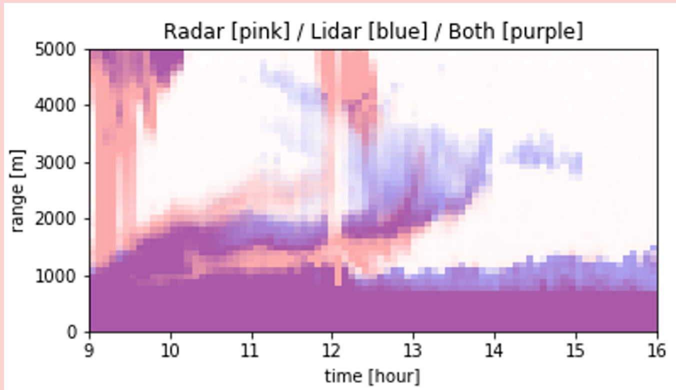

Fig. 1. Radar reflectivity (pink) and lidar backscatter (blue) for 16th October 2017. The values are scaled to provide a comparison between the two datasets. Areas where both datasets overlap is shown in purple.

2. Results

Interestingly, the layer of aerosol also shows up in the Copernicus Cloud Radar at CAO. Figure 1 shows the return power of the radar (in pink). The aerosol layer can be seen clearly. As the radar is designed to detect cloud, its wavelength is chosen to scatter most efficiently off cloud droplets and ice crystals. Cloud droplets have a typical diameter of 10–40 µm. So initially this suggests that the aerosol particles being detected by the radar are of that size order. Similar behaviour was seen in the ash plume from the Eyjafjallajökull eruption in Iceland in 2010 [1].

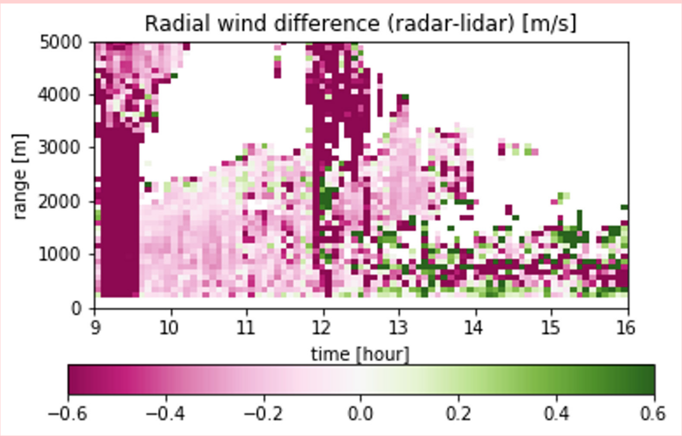

Fig. 1. Radar reflectivity (pink) and lidar backscatter (blue) for 16th October 2017. The values are scaled to provide a comparison between the two datasets. Areas where both datasets overlap is shown in purple.

The Doppler velocities of the aerosol layer as measured by the radar and lidar differ by about 0.4 m/s (Figure 2), indicating that they are seeing different aerosol populations. Using the boundary layer wind profiler at CAO it will be possible to retrieve particle fall velocities of the particles detected by the lidar and the radar. A Leosphere Doppler lidar and Metek cloud radar also collected data on the aerosol event at the Mace Head Atmospheric Research Station in Ireland, providing information on the evolution of the aerosol layer.

Details of the passage of the aerosol layer across the British Isles will be presented as well as an in-depth analysis using the lidar and radar data from both Chilbolton and Mace Head.

References

[1] F. Madonna, A. Amodeo, G. D'Amico and G. Pappalardo, J. Geophys. Res. Atmos., **118**:10,056– 10,071 (2013).

*Corresponding author: H. M. A. Ricketts

h.ricketts@manchester.ac.uk

Root exudation modulates soil microbiota: consequences on soil functions

E.D. KOVACS[a,b*], C. ROMAN[a], M.H. KOVACS[a], L.W. SZAJDAK[c]

[a.)] *Research Institute for Analytical Instrumentation, INCDO INOE 2000, 400293, Cluj Napoca, Romania*

[b.)] *Chemistry and Chemical Engineering Faculty, Babes-Bolyai University, 400014, Cluj Napoca, Romania*

[c.)] *Institute for Agricultural and Forest Environment, Polish Academy of Sciences, 60809 Poznan, Poland*

Abstract: Rhizodeposition is a major input pathway of organic matter to subsoils, but little knowledge exists on carbon dynamics and its influence on soil microbiota structure abundance. The aim of this study was to investigate the influence of root exudates on carbon allocation and microbiota structure abundance in rhizosphere and bulk soil of farmlands with multiple cultivars management. Mass spectrometric analysis revealed that root exudates vary with cultivars species and management. Bacterial community was more influenced by root exudates type and amount than fungal community. Root exudates – soil microbiota interaction could relate to positive influence on carbon and phosphorous cycle but potential negative effect on nitrogen cycle was observed also.

Keywords: root exudates, microbiota, agriculture.

1. Introduction

Microorganisms in the rhizosphere and bulk soil promote numerous functions of soil, contributing to provision of soil ecosystem services. Plant roots through exudates release their fixed carbon into soils. Through root exudates type and amount, plant community could modulate soil microbiota structure and abundance. Although indirectly they could influence nutrient cycling in soil by either promoting an increased microbial activity in soil or by shifting their abundance and structure, the effects that they induce on soil microbiota are not yet fully understood.

From several decades ago it is considered that bacterial community benefit from labile carbon released by plant roots [1, 2]. Recent study performed by Zhang [3] and Shahbaz [4] evidenced that higher trophic levels of the soil food web as fungi could exploit labile carbon faster than bacteria. This could have major implications for the whole soil community structure and abundance.

Considering that current agricultural farmers are under pressures of increased feed production for a global growing population but in a sustainable manned, microorganism-based management strategies started to be exploited as alternative potential technologies [5]. This technology could enhance nutrient uptake by cultivars, promote crop growth and not in the last to protect plats form harmful pests or diseases [6].

However, a detailed knowledge is lacking on what microbial species are particularly promoted or suppressed through their artificial manipulation. In this work, we conducted comprehensive and systematic comparisons on the soil microbial community structure and its putative functions among monoculture crops, rotated crops and mixed crop cultivars focusing on (1) root exudates differentiation within cultivars; (2) root exudates influence of soil microbiota structure and abundance; and (3) potential consequence on representative soil functions as nutrient cycling.

2. Experimental

2.1. Samples collection

The study was conducted on three agricultural farmlands with the following cultivars type and management:

(1) monocrops of soybean (Glycine max), wheat (Triticum aestivum) and maize (Zea mays);
(2) crop rotation between soybean (Glycine max) – maize (Zea mays); maize (Zea mays) – wheat (Triticum aestivum);
(3) mixed crop cultivars of root vegetables and leafy vegetables

Studied agricultural farmlands were in Turda, Transylvanian. Farmlands soil was characterized as vertic phaeoziom with a clay-loamy texture. This region is characterized by continental climate with 11.4 °C average temperature and 345 – 495 mm average precipitation.
50 g of cultivars rhizosphere and bulk soil were collected from studied cultivars and management for root exudates and soil microbiota phenotypic structure and abundance analysis.

2.2. Root exudates analysis

Root exudates gas chromatographic analysis targeted the following classes: carbohydrates, amino acids, and organic acids.
Carbohydrates as d-(-)-arabinose, d-(-)-fructose, d-(+)-galactose, d-(+)-glucose, α-lactose monohydrate, d-(+)-maltose monohydrate, d-(+)-mannose, d-(-)-ribose, sucrose, and d-(+)-xylose. Carbohydrates extraction was performed on 10 g of soil samples according with method presented by [7]. 10 mL of dichloromethane was used to recover derivatized solution of carbohydrates. Of this solution, 1 µL was injected in a gas chromatograph with flame ionization detector (GC-FID 7890, Agilent Technologies) under the following condition: splitless injection with inlet and detector temperatures of 225 and 300 °C, respectively. The temperature program started at 180 °C with a hold for 3 min followed by an increase by 3 $°C \times min^{-1}$ up to 250 °C. This final temperature was maintained for 20 min [8].
Soil amino acids content including free physiological amino acids and protein hydrolysates were analyzed on gas chromatograph with flame ionization detector (GC-FID 7890, Agilent Technologies). Sample preparation for the amino acid

analysis was performed according with method presented by [9] on 5 g of soil. The resulting derivatized extract was analyzed with the following gas chromatographic conditions: splitless injection mode with inlet and detector temperatures of 250 and 320 °C, respectively. The temperature program started at 110 °C with a hold for 2 min followed by an increase by 32 °C×min^{-1} up to 320 °C. This final temperature was maintained for 1 min [8].

Organic acids content analysis referred at acetic acid, adipic acid, L-ascorbic acid, benzoic acid, butyric acid, citric acid, isobutyric acid, formic acid, fumaric acid, L-(+)-lactic acid, DL-isocitric and trisodium salt hydrate, maleic acid, malonic acid, D-(+)-malic acid, oxalic acid, phytic acid, propionic acid, (-)-quinic acid, succinic acid, shikimic acid, and D-(-)-tartaric acid. Organic acids extraction was performed on 10 g of soil sample with acetone:1.5 mM borate buffer (50:50) and analyzed by gas chromatography with flame ionization detector. The conditions were as follows: splitless injection with inlet and detector temperatures of 200 and 300 °C, respectively. The oven temperature program started at 70 °C with a hold for 3 min followed by an increase by 5 °C×min-1 up to 250 °C. This final temperature was maintained for 5 min.

2.3. Rhizosphere and bulk soil microbiota analysis

Phospholipid derived fatty acids (PLFA) were extracted from soil according with method described by [10] and [11]. Extraction were performed on two gram of soil using Bligh-Dyer reagents. The organic phase of extract was used to fractionate neutral lipids and phospholipids using a silicic acid column. Eluted lipids were subjected to mild alkaline methanolysis after that the resulting fatty acid methyl esters were analyses on an Agilent 7890 A gas chromatograph equipped with a flame ionisation detection system (FID). Identification and quantification of fatty acid methyl esters was done with Sherlock MIDI (Microbial ID, Inc., Newark, DE). Briefly iso and anteiso branched fatty acids were use as biomarker for gram negative bacteria, monounsaturated fatty acids, and cyclopropyl 17:0 and 19:0 fatty acids were used as biomarkers for gram negative bacteria, 10 methyl 16:0 and 10 methyl 18:0 fatty acids were used as biomarkers for actinomycetes, fungi were identified with 18:2 w6 cis fatty acid and arbuscular mycorrhizae using 16:1 w5 cis fatty acid. Fatty acids were named according to the ω-designation described as follows: fatty acids are expressed as total number of carbon atoms with number of double bonds followed by the position of the double bond from the methyl end (w) of the molecule. With “a” and “i” are expressed anteiso and isobranching fatty acids respectively, while cy refers to cyclopropane fatty acids. 10Me represent a methyl group on the 10th carbon atom from the carboxyl end of the molecule [11].

3. Results and discussions

3.1. Root exudates differentiation within studied cultivars

Chromatographic analysis revealed differentiation within root exudates types and amount within studied cultivars. Analyzing Figure 1 it was observed that amino acids content was higher in leafy vegetable root rhizosphere, carbohydrates was detected in significant amount in wheat rhizosphere soil, while organic acids were prevalent soybean root rhizosphere. Organic acids average amount within cultivars root rhizosphere varied as follows: soybean (934.4 nmol×g^{-1} d.w.) > maize (789 nmol×g^{-1} d.w.) > leafy vegetables (590.6 nmol×g^{-1} d.w.) > wheat (567.5 nmol×g^{-1} d.w.) > root vegetables (346.3 nmol×g^{-1} d.w.).

Differentiation within organic acids were observed between studied cultivars. In soybean root rhizosphere prevalent organic acids were adipic acid (201.8 nmol×g^{-1} d.w.), malic acid (195.5 nmol×g^{-1} d.w.), maleic acid (135.2 nmol×g^{-1} d.w.) and malonic acid (112.4 nmol×g^{-1} d.w.). Prevalence of fumaric acid (178.2 nmol×g^{-1} d.w.), malic acid (113.5 nmol×g^{-1} d.w.) and oxalic acid (114.5 nmol×g^{-1} d.w.) was determined in maize root rhizosphere. Propionic acid was detected in higher content among studied

Fig. 1. Root exudates variation within cultivars rhizosphere soils

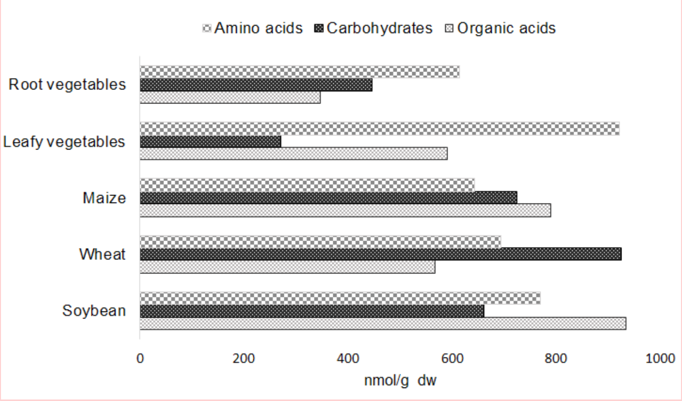

Fig. 2. Principal component analysis of cultivars rhizosphere exudated carbohydrates within studied cultivated species

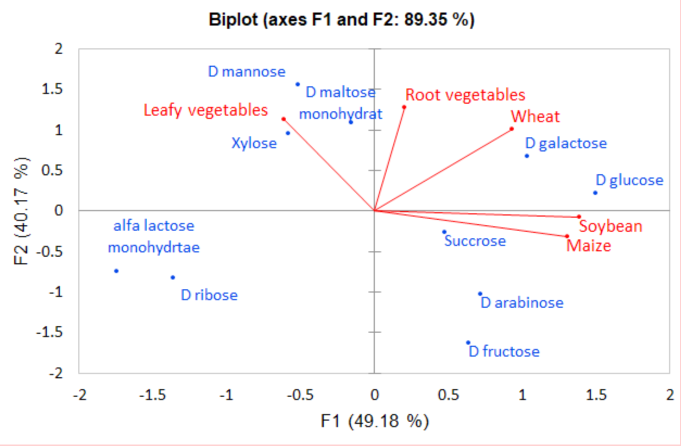

	F1	F2	F3	F4	F5
d-arabinose	0.358	**0.592**	0.024	0.011	0.015
d-fructose	0.155	**0.822**	0.000	0.020	0.003
d-galactose	**0.613**	0.212	0.005	0.170	0.001
d-glucose	**0.857**	0.014	0.128	0.000	0.001
α-lactose	**0.782**	0.114	0.103	0.000	0.001
d-maltose	0.024	**0.916**	0.032	0.023	0.005
d-mannose	0.114	**0.851**	0.009	0.006	0.020
d-ribose	**0.706**	0.213	0.032	0.049	0.000
sucrose	**0.496**	0.129	0.253	0.008	0.113
xylose	0.220	**0.485**	0.240	0.033	0.022

Table 1. Loading for PC1 and PC2 of the PCA

organic acids in wheat (152.7 nmol×g^{-1} d.w.), leafy vegetables (80.2 nmol×g^{-1} d.w.) and root vegetables (46.5 nmol×g^{-1} d.w.) rhizosphere.

Carbohydrates content were positively correlated with soybean and maize cultivars. A summary of the total variation of the composition or carbohydrates in cultivars root rhizosphere is presented by their factors loading for the first two factors of PCA (Figure 2). The first two dimensions of PCA model were found to be significant and explained 89.35 % of variance. All variables appeared to be related to the first principal component F1 and F2 as their squared cosines obtained by PCA analysis were remarkably high, ranging from 0.496 – 0.857 and 0.485 – 0.916, respectively (Table 1). The squared cosines of the other variables were low (Table 1). Values in bold correspond for each observation to the factor for which the squared cosine is the largest.

Amino acids presented also differentiated pattern in studied cultivars rhizosphere. The highest amount of amino acids was determined in leafy vegetables rhizosphere (919.8 nmol×g-1) and soybean rhizosphere soil (769.6 nmol×g-1). Redundancy analysis

According with Figure 3, among identified amino acids in studied cultivars rhizosphere soils, glutamic acid was detected in highest amount in soybean (211.2 nmol×g-1), maize (187.2 nmol×g-1) and root vegetables (62.8 nmol×g-1) rhizosphere. Aspartic acid was also determined in high amount in soybean (157.7 nmol×g-1), root vegetables (88.9 nmol×g-1) and wheat (80.2 nmol×g-1)

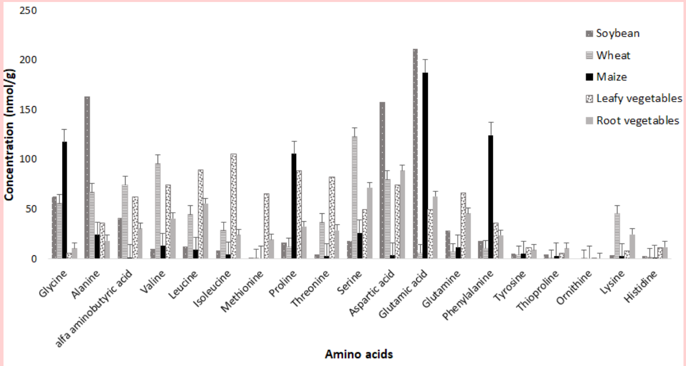

Fig. 3. Amino acids differentiation within studied cultivated species rhizosphere

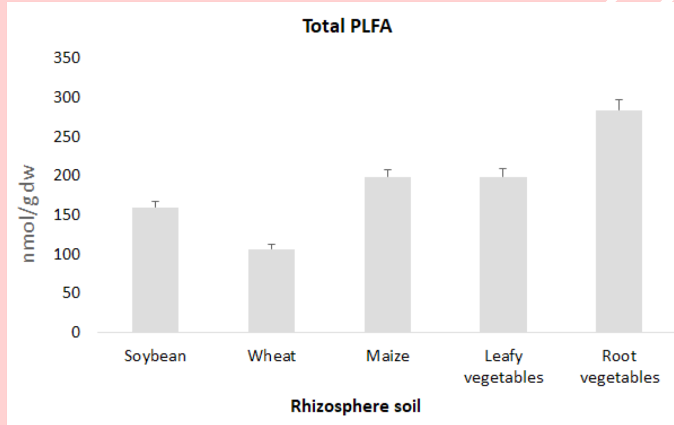

Fig. 4. Microbiota abundance in studied cultivars rhizosphere

rhizosphere. Serine was also determined in significant amount in wheat (123.2 nmol×g-1) and root vegetables (71.5 nmol×g-1) rhizosphere. Amino acids as alanine (163.2 nmol×g-1), valine (95.6 nmol×g-1) and isoleucine (105.6 nmol×g-1) were determined also in significant amount in soybean, wheat, and leafy vegetables rhizosphere soil, respectively (see Figure 3).

3.2. Rhizosphere microbiota differentiation within cultivars

Rhizosphere soil microbiota abundance was different within cultivars (Figure 4). Abundance varied within 106.9 – 283.6 nmol×g-1 with highest abundance identified in root vegetables rhizosphere.
Bacterial dominance was observed in all studied rhizosphere soils compared with fungal abundance. Fungal biomass abundance was highest in root vegetables rhizosphere. The total fungi abundance varied as follow: root vegetables rhizosphere (51.8 nmol×g-1) > soybean rhizosphere (26.5 nmol×g-1) > maize rhizosphere (21.8 nmol×g-1) > wheat rhizosphere (19.5 nmol×g-1) > leafy vegetables rhizosphere (12.6 nmol×g-1). Within fungi, Saprotrophic and ectomycorrhizal fungi abundance was significant in root vegetables rhizosphere with an abundance of 18.2 nmol×g-1 and 17.8 nmol×g-1, respectively. Arbuscular mycorrhiza fungi were also determined in high abundance especially in case of maize (10.2 nmol×g-1).and wheat (8.1 nmol×g-1) rhizosphere. Among bacteria, gram-negative bacteria dominated rhizosphere bacteria instead of gram-positive bacteria

Rhizosphere	Phenotype group	PLS coef.	C	AA	OA
Root vegetables	Bacteria	Stand. Coef.	**+2.85**	**+0.95**	**+0.78**
		R^2	0.714	0.514	0.488
	Fungi	Stand. Coef.	**+0.72**	-0.31	-0.27
		R^2	0.315	0.288	0.402
Leafy vegetables	Bacteria	Stand. Coef.	**+4.11**	-0.61	**+1.38**
		R^2	0.447	0.614	0.503
	Fungi	Stand. Coef.	**+0.88**	-0.27	-0.38
		R^2	0.411	0.278	0.387
Maize	Bacteria	Stand. Coef.	**+2.88**	**+1.27**	**+4.16**
		R^2	0.401	0.565	0.517
	Fungi	Stand. Coef.	-0.28	-0.19	**+1.25**
		R^2	0.389	0.427	0.389
Wheat	Bacteria	Stand. Coef	**+0.86**	-2.17	-3.05
		R^2	0.345	0.517	0.623
	Fungi	Stand. Coef	**+5.15**	-0.88	-1.86
		R^2	0.289	0.114	0.273
Soybean	Bacteria	Stand. Coef	**+4.12**	-2.89	**+3.25**
		R^2	0.285	0.319	0.188
	Fungi	Stand. Coef	-0.25	**+0.15**	**+1.28**
		R^2	0.455	0.287	0.107

Table 2. Summary of potential influence of root exudates on soil microbiota major phenotypic structure based on data obtained after PLS regression analysis

with an average value of 80.7 nmol×g-1. High dominance of aerobe bacteria was identified in root vegetables rhizosphere (Aerobe: Anaerobe bacteria – 8.4) followed by soybean (Aerobe: Anaerobe bacteria – 4.2) rhizosphere and wheat rhizosphere (Aerobe: Anaerobe bacteria – 4.1).

3.3. Root exudates influence on soil microbiota abundance and phenotypic structure

Partial least - squares (PLS) regression analysis was used to compare root exudates with soil microbiota major phenotypic structures abundance. This method analysis was based on functions of multiple linear regression, canonical correlation, and principal component analysis. It integrates these methods data analyses generated predicted data with those measured.

C – carbohydrates, AA – amino acids, OA – organic acids, Stand. Coef. – PLS standardized coefficient, R^2 – correlation coefficient

Therefore, through PLS regression, amount of root exudates was used as x - matrix (dependent variables), and microbiota major phenotypic groups abundance were used as y - matrix (independent variables). Their statistical relationships were established based on equation (1) and equation (2), where p is the number of independent variables and q is the number of dependent variables. Linear combinations from X and Y were extracted.

$$X = [x_1, x_2, \ldots, x_p]_{nxp} \quad (1)$$
$$Y = [y_1, y_2, \ldots, y_q]_{nxq} \quad (2)$$

As result of PLS regression, the score plot separated the root exudates that could influence positively or negatively major phenotypic groups (Table 2). PLS regression also generated loading values of abundance for each major phenotypic group. Based on measured and predicted data, models that rank each root exudates influence amplitude on soil microbiota representative phenotypic groups were established (Table 2). Positive influence of carbohydrates exudates was evidenced after PLS regression analysis almost on all phenotypic groups of rhizosphere microbiota, expecting only fungal community from maize and soybean rhizosphere (Table 2). Considering amino acids exudates content influence on soil bacterial and fungal community, positive correlation was observed only in case of bacterial community of root vegetables, maize, and soybean rhizosphere. Lower influence of organic acids content was observed also in case of organic acids exudates.

3.4. Potential consequence on soil functions mediated by microbiota

Mantel tests were performed to determine the relationship between soil microbiota x root exudates vs. extracellular enzymatic activity connected with carbon, nitrogen, and phosphorous cycle (Table 3). Correlation between microbiota abundance x root exudates and enzymatic activities variables were determined by Pearson correlation and then adjusted by false rate discovery rate method.

C cycle – carbon cycle, N cycle – nitrogen cycle, P cycle – phosphor cycle, EEA – extracellular enzymatic activity, PLFA – microbiota abundance expressed using phospholipids derived fatty acid content.

Table 3. Mantel test loadings

Nutrient cycle	EEA	PLFA x C	PLFA x AA	PLFA x OA
C cycle	Phenol oxidase	0.265	**0.558**	**0.639**
	b-glucosidase	0.468	**0.548**	**0.788**
	Amylase	**0.668**	**0.678**	**0.805**
	Invertase	**0.578**	0.324	**0.817**
N cycle	Urease	-0.125	-0.223	-0.815
	Catalase	-0.232	0.188	-0.119
P cycle	Phosphatase (ac.)	**0.769**	**0.559**	**0.506**
	Phosphatase (alc.)	**0.825**	0.432	0.344

Potential influences were observed on nutrients cycles as N, P, C of studied rhizosphere microbiota. Although the global nutrients cycles are largely driven by soil microorganisms, plant root exudates as carbohydrates, amino acids, and organic acids can profoundly modify soil microbiota structure and abundance and therefore influence microorganism involvement in nutrients cycling processes. Considering studied rhizosphere soil root exudates x rhizobiota abundance potential positive correlation was obtained for carbon cycle and phosphorus cycle.

4. Conclusions

Through this study it was observed that root exudates amount differed through cultivars. Higher amount of root exudates was determined in case of soybean rhizosphere followed by wheat and maize rhizosphere. Considering each groups or studied root exudates, in this study it was observed that amino acids content was higher in leafy vegetable root rhizosphere, carbohydrates was detected in significant amount in wheat rhizosphere soil, while organic acids were prevalent soybean root rhizosphere.

Differentiated abundance of rhizosphere microbiota was determined also. However, through this study bacterial community dominance was observed in all cases. According with performed PLS regression analysis positive influence of carbohydrates exudates was evidenced almost on all phenotypic groups of rhizosphere microbiota. Considering amino acids exudates content influence on soil microbiota, positive correlation was observed only in case of bacterial community of root vegetables, maize, and soybean rhizosphere. According with our data organic acids exerted a lower influence on rhizosphere microbiota communities. Potential influences were observed on nutrients cycles as N, P, C of studied rhizosphere microbiota. However, more studies and data are requested could understand the way how root exudates shape soil microbiota structure and abundance and consequently how they could change their role in soil functions and provided ecosystem services

Acknowledgements.

This work was supported by the 18N/08.02.2019 Contract, Project code PN19-18.01.01, Nucleu Program (08.02.2019-31.12.2022) and Contract no. 19PFE/17.10.2018 PROINSTITUTION project

References

[1] B. Wawrik, L. Kerkhof, J. Kukor, G. Zylstra, Appl. Environ. Microbiol, **71**, 6776 (2005).

[2] Q. Wang, J. Xiao, J. Ding, T. Zou, Z. Zhang, Q. L., H. Yin, Plant Soil, 2019

[3] G. Zhang, J. Bai, Q. Zhao, J. Jia, X. Wang, W. Wang, X. Wang, Catena, 196, 104831 (2021).

[4] M. Shahbaz, T. Katterer, B. Thornton, G. Borjesson, Biol. Fertil. Soils, 56, 759 (2020).

[5] C. Gougoulias, J.M. Clark, L.J. Shaw, J. Sci. Food Agric, **94**, 12 (2014).

[6] H. Yue, M. Wang, S. Wang, J.A. Gilbert, X. Sun, L. Wu, Q. Lin, Y. Hu, X. Li, Z. He, J. Zhou, The ISME Journal, 9, 1 (2015).

[7] C. Rumpel, M.F. Dignac, Soil Biol. Biochem, **38**, 1478 (2006).

[8] E.D. Kovacs, L. Silaghi-Dumitrescu, M.H. Kovacs, C. Roman, Anal. Lett, (2020).

[9] T. Mohabbat, B. Drew, J. Cromatogr. B, **862**, 86 (2008).

[10] A. Frostegard, A. Tunlid, E. Baath, Appl. Environ. Microbiol, **59**, 3605 (1993).

[11] J.S. Buyer, M. Sasser, Appl. Soil. Ecol, **61**, 127 (2012).

*Corresponding author: Kovacs Emoke Dalma, *Research Institute for Analytical Instrumentation, INCDO INOE 2000, 400293, Cluj Napoca, Romania,* dalma.kovacs@icia.ro

CHAPTER II

PVD technologies for optoelectronics, optical, decorative, plasmonic and medical applications

Biocompatible coatings used in the field of medicine

A. VLADESCU [a], M. SURMENEVA [b], C.M. COTRUT [c], R. SURMENEV [b], E. UNGUREANU [a], L.R. CONSTANTIN [a], M. DINU [a], V. BRAIC [a]

[a] *Department for Advanced Surface Processing and Analysis by Vacuum Technologies, National Institute of Research and Development for Optoelectronics – INOE 2000, 409 Atomistilor St., 077125 Magurele, Romania*

[b] *Physical Materials Science and Composite Materials Centre, Research School of Chemistry & Applied Biomedical Sciences, Tomsk Polytechnic University, Lenin's Avenue, 30, Tomsk, Russia*

[c] *Faculty of Materials and Science Engineering, University Politehnica of Bucharest, Splaiul Independenţei 313, Bucharest, Romania*

Abstract. Biomaterials play a vital role in medicine, being useful in many applications such as bone implants, repair/healing of different tissues, molecular probes, biosensors. Biomaterials have now been effectively developed and their success is governed by the selection of a material. Nevertheless, biomaterials induce reactions which should be moderated or controlled to avoid implant failure. Despite significant efforts, there is no ideal biomaterial and thus the challenge is to find the proper one for a particular biomedical application.

Keywords: hydroxyapatite, carbide, nitride and carbonitride coatings, oxynitride.

1. Introduction

Biomaterials are classified in four groups: metallic, polymeric, composite and ceramics [1]. Biomaterials can be used as artificial hip joint, kidney dialysis machine, sutures, bone plates, screws, cardiac pacemaker, intraocular lens, muscle stimulator, probes and catheters, etc. The first bone plates were presented around 1900s for fixation of long bone fractures [1]. Most of these plates fail due to improper design - too thin and too stressed. In the 1950s, the heart valve replacements were taken, while in the 1960s, the cemented joint replacements were performed [2–6].

Metallic materials were used as biomaterials for many years, but their weakness, low osseointegration and bioactivity limited their use [3–6]. During the years, it was a challenge to eliminate disadvantages of metallic implants by coating their surface with various types of biocompatible coatings using different techniques [1-6]. The results are very promising, because there are developed many coatings, but none of them have all the inquirer properties necessary in medical applications. Thus, discussion on the development of novel biomaterials should be envisaged the final application and specific properties of an implant should be taken into account. The importance of coating is given by its properties cannot be obtained by other techniques such as casting, melting, forging or heat treatment. The goal of the present paper is to review and summarize different biocompatible coatings developed for biomedical applications.

2. Biocompatible coatings-based calcium phosphates

Calcium phosphates (CaPs) are the most used types of biocompatible coatings for improving the bond between the metallic implants and bone [4]. The research about the CaP as a biomaterial has been started in the 1970s, being proposed for a large variety of orthopedic and dental applications [7]. The properties of sputtered CaP coatings were strictly dependent on the deposition parameters (Fig.1). For example, the deposition temperature is critical for the crystalline structure of CaP coatings: amorphous structure was obtained at the temperature ranged from 80°C to 400°C, while from 500°C to 800°C, the crystallinity increased [8]. Moreover, the CaP coatings deposited at 700°C and 800°C exhibited high electrochemical behaviour and promoted cell growth after 7 days of incubation with MG63 osteoblast-like cells [8].

It is well known that the mechanical properties and tribological performance of CaP are insufficient. Thus, it is proposed to improve these characteristics by adding different elements into the CaP structure such as Ti, Mg, Si etc. [9–12]. Moreover, for improving the antibacterial properties of CaP, the addition of small amount of Ag is proposed, in such a way to preserve other properties [13,14].

Fig. 1. Evolution of cell viability after 7 days, corrosion current density (i_{corr}) and hardness (H) of sputtered hydroxyapatite coatings (HAP) deposited at different temperature ranged from 400°C to 800°C

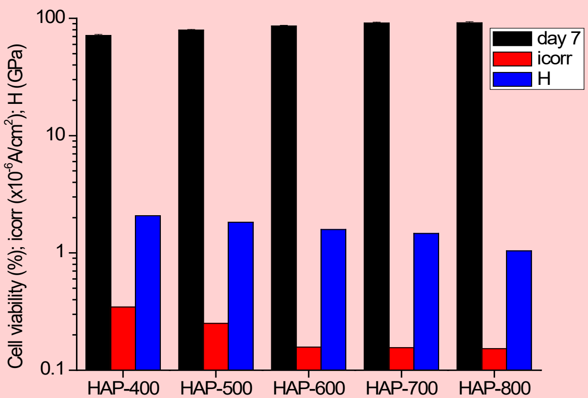

The properties of the CaP coatings are also influenced by the applied substrate bias. It is reported that the CaP coatings prepared without the substrate bias have the best corrosion resistance in SBF at 37 °C, due to a smoother and less porous surface [15].

One of the most important disadvantage of sputtered CaP coating is adhesion to the substrate [16–18]. Vladescu et al. proposed the introduction of an intermediate layers such as TiC, NbC and ZrC between Ti6Al4V substrate and CaP coatings [19]. All three proposed layers enhanced the adhesion between CaP and Ti alloy substrate, but the best adhesion was found for the coatings with NbC interlayer, which conducted to superior protective efficiency to the corrosive attack in SBF solution, while best gene expression was observed in the presence of TiC layer [19].

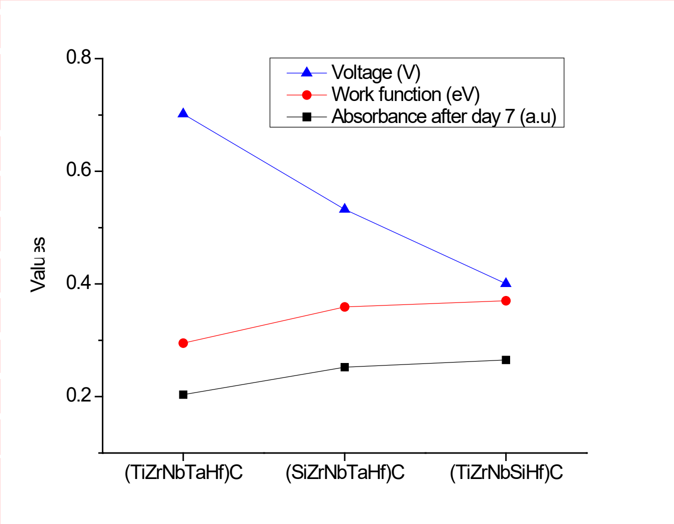

Fig. 2. Evolution of cell viability after 7 days, work function and electrical potential of multi-principal element (MPE) coatings deposited on 316L stainless steel

In the last few years, new types of coatings namely multi-principal element (MPE) coatings were developed for biomedical purposes. Vladescu et al. investigated (TiNbZrTaHf)C coatings as well as the possibility for improving its biocompatibility by replacement of either Ti or Ta by Si [21]. This replacement conducted to a superior surface electrical charge, and to the superior biocompatible properties, with best results for the (TiZrNbSiHf)C coating (Fig. 2) [21].

Braic et al. studied multiple NbC coatings with different carbon concentration, obtained by DC magnetron sputtering [22]. It was showed that superior corrosion behavior in Ringer solution and the highest cell viability was exhibit by NbC coating with the highest carbon content, being a suitable surface for osteosarcoma cell colonization.

3. Biocompatible coatings-based carbides

In the paper of Pana et al. it was shown that TiC, ZrC, and TiNbC coatings prepared by cathodic arc evaporation method improved the mechanical, corrosive, and tribocorrosive characteristics of 316L stainless steel substrates [20]. TiNbC exhibited the lowest friction coefficient (μ=1.6) and lowest wear rate ($k=0.99 \times 10^{-5}$ $mm^3 \cdot N^{-1} \cdot m^{-1}$), signifying the best tribocorrosive performance in 0.9% NaCl at 37 ± 0.5 °C, being proper for biomedical applications where a low friction process along with a high corrosion resistance are required [20].

4. Biocompatible coatings-based nitrides

Dinu et al. [23] proposed the improvement of TiCN coatings by addition of small amount of Si in order to be used as coatings for load bearing implants due to superior mechanical, corrosion and wear resistance. TiSiCN coating exhibited the most electropositive corrosion potential (-14 mV) and the smallest corrosion current density (49.6 nA cm^2), having the best protection after immersion in 90% DMEM + 10% FBS [23]. The hardness of the coatings significantly increased when small amounts of Si were added (Fig. 3) and the best capacitive character was ascribed by TiSiCN coating. High tribologic-resistant ZrN coating deposited on CoCrMo alloy reduced Staphylococcus Epidermidis biofilm formation, when compared with smooth and rough orthopaedic implant surfaces [24]. In another study, the wear and metal ion release was investigated for a ZrN coated knee implant, in order to overcome metal ion hypersensitivity in patients [25]. In comparison with the uncoated implants, ZrN proved no sign of scratches or delamination/million cycles. In order to improve the biocompatibility and extend the life time of stainless steel dental implants, Nb-based nitride obtained by reactive unbalanced magnetron sputtering was investigated by Ramírez et al. [26]. Adhesion, proliferation and viability tested in vitro using human bone-like cells showed an improvement of cellular growth on the surfaces of the coatings in comparison to SS.

According to Kazemi et al. [27] the use of TiN coating along with hydroxyapatite improved the corrosion current density, polarization resistance and corrosion potential of Ti-6Al-4V alloy used for dental and orthopedic implants. This result can be ascribed to their finer, non-cracking structure, as indicated by FE-SEM results, with beneficial effects also on the adhesion strength of the coating to the substrate. Aiming at improving the wear resistance of implant medical devices, graded nano-TiN coating was deposited on Ti alloy by DC reactive magnetron sputtering [28]. Due to a gradual change in N composition, microstructure and mechanical properties, the adhesion to the substrate is

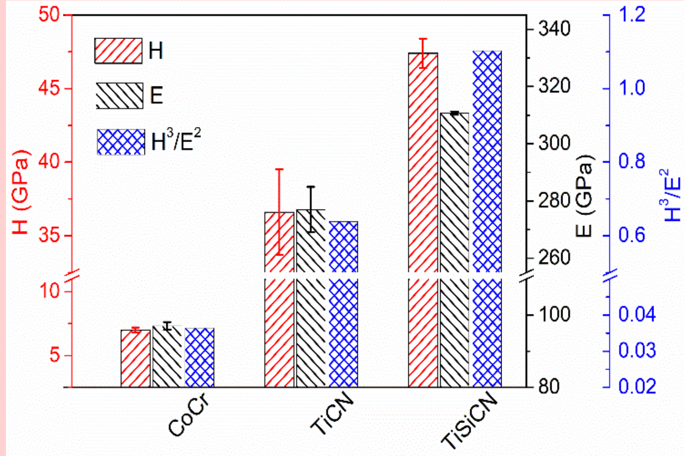

Fig. 3. Averaged hardness and reduced Young's modulus values for CoCr substrate, TiCN and TiSiCN coatings

increased. Low friction and high wear resistance were exhibited by the proposed coating in physiological environment. This founding was attributed to its hardness, toughness and surface roughness.

5. Biocompatible coatings-based carbonitrides

During the years, TiCN was proposed as biocompatible coating due to its good mechanical properties (Fig.3) and good corrosion resistance, and an acceptable wear resistance along with good cell viability [29–32]. Dinu et al. showed that the wear and friction, as well as the corrosion resistance (in 90% DMEM + 10% FBS, at 37 ± 0.5 °C) of TiCN can be improved by adding small amount of Si in its structure [23].

6. Biocompatible coatings-based oxynitrides

Pana et al. successfully prepared both mono (TiNO) and bilayer coatings (TiN/TiNO and TiNO/TiN) coatings by reactive cathodic arc deposition technique on 304 stainless steel substrates (SS) in order to be used as coatings in an aggressive saline environment [33]. By adding oxygen into TiN matrix, the grain size decreased, a higher density of nucleation sites for the passive film is found, leading in an enhanced formation of a passive layer and thus a superior corrosion resistance. Zr and Cr based silico-oxynitrides were deposited on CoCr dental alloys by cathodic arc evaporation method by Dinu et al. [34]. They reported that higher substrate bias enhanced the protective properties of the coatings in artificial saliva, ascribed to the intensified ion bombardment. Moreover, comparing with Cr-based coatings, ZrSiON showed lower porosity and higher protective efficiency in time, the formation of a passive Zr based oxide having a beneficial effect on the protective properties.
Cotrut et al. also analyzed TiSiON coatings as possible candidates for biomedical applications, especially for improving the adhesion between the dental ceramic and metallic substrate in dental restoration [35]. They reported that the characteristics of TiSiON are depended on the bias voltage: a maximum hardness (32 GPa) was determined for the coatings prepared at bias voltages between −100 and −150 V, the highest adhesion strength for a bias of −100 V, and the best corrosion resistance in artificial saliva (pH=5) for bias voltages of −100 and −150 V, and the best cell proliferation for the coatings deposited at −200V (Fig. 4). Furthermore, TiSiON coatings

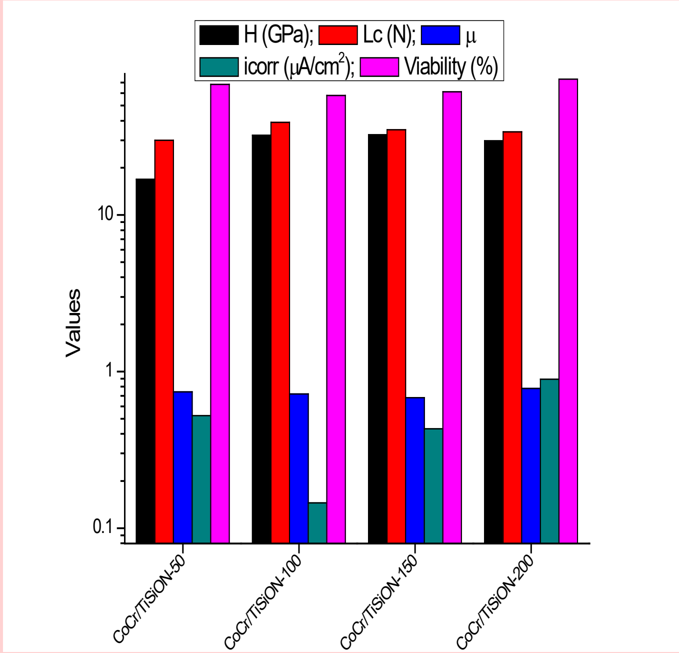

Fig. 4. Evolution of hardness (H), adhesion (Lc), friction coefficient (μ), corrosion current density (icorr), viability of the TiSiON coatings deposited on CoCr alloy at different bias voltage (-50, -100,-150 and -200V)

deposited by reactive cathodic arc evaporation at −200V on CoCr alloy exhibited superior tribological performance in NaCl solution [36].

7. Bioactive glasses

By comparing with other coatings, bioactive glasses are highly biocompatible to be well integrated with human tissue, making them the best solution to improve the biocompatibility and bioactivity of metallic implants. This conclusion is based on the apatite formation at the interface between the metallic implants and the host tissue. Bioactive glasses have the following advantages: ability to replace damaged bone tissue, promote tissue regeneration, and degrade at a similar rate of tissue regeneration [37]. Moreover, the bioactive glasses are resistant to corrosive attack of all solutions found in human body. In the literature, there are published papers which describe well the evolution of this field, e.g. Sola et al. reported that the bioactive glasses can be effectively used as films to coat metallic substrates, that one may merge mechanical strength with superior bioactivity [37]. The group of Bellucci and Sola reviewed more than 70 bioactive glasses to state the relation between their composition and coefficient of thermal expansion [38]. They found that by adding small oxides (such as K_2O and MgO), the coefficient of thermal expansion is reduced, the adhesion to metallic surfaces is promoted and the bioactivity is not altered [38]. In 2017, a review was published which is related to the development of bioactive glass and composite coatings on scaffolds and implants, and a description of characterization methods to compare the performance of these coatings [39]. Muzio et al. added an Ag nanocluster/SiO_2 glass composite coating on a polypropylene prosthesis comprising a porous mesh in contact with the parietal side and a 70-µm thick smooth layer that prevented adhesion with intestine and viscera [40]. In vitro experiments showed that the coating promoted the growth of human mesothelial cells, and revealed a superior resistance to Staphylococcus aureus due to the release of Ag^+ ions [40]. The superior ability to bond to bone tissue was first observed for glasses belonging to the $Na_2O–CaO–SiO_2–P_2O_5$ system [41,42]. Esfahani et al. developed a composite layer consisted of nanosized 58S particles (50-60 nm) and TiO_2 by sol-gel, and they found that by this addition the hardness is enhanced and in vitro bioactivity of nitinol alloy is significantly improved due to formation of hydroxyapatite agglomerates on the surface [43].

8. Conclusions and open challenges

In the present review paper, we presented the most recent achievements obtained by ReCAST group and their collaborators in terms of biocompatible coatings based on calcium phosphates, carbides, nitrides, carbonitrides, oxynitrides, TiO_2 nanotubes and bioglasses. There are still important challenges for the development of advanced coatings to be used in diverse fields of biomedical applications, but the main challenge is to obtain degradation-controllable and multifunctional biocompatible coatings with the proper interfaces with the substrates. The "ideal" coating for clinic applications should be resistant to corrosion, self-degradable, and biocompatible as well as wear resistant in some applications, and allows drug-loading and subsequent tailored release. But it's practically impossible to produce coatings with all properties mentioned above at this time point. Thus, the research in this field is still a challenge for the research community.

Acknowledgements

The authors are thankful for the financial assistance of the Romanian Ministry of Research and Innovation through the project no. COFUND-ERANET-RUS-PLUS-CoatDegraBac no.68/2018 and no. PN-III-P1-1.2-PCCDI-2017-0239/60PCCDI 2018, within PNCDI III. The EDS, SEM and XRD investigations were obtained using the systems purchased by the infrastructure project INOVA-OPTIMA SMIS code 49164, contract No. 658/2014 and modernized by the PROINSTITUTIO Project–contract No. 19PFE/17.10.2018.

References

[1] P. Parida, A. Behera, S. Chandra Mishra, Int. J. Adv. Appl. Sci. 1 (2012).
[2] C. Kenesi, in: Biomater. Orthop. Surg., 2009, pp. 1–11.
[3] Y. Su, C. Luo, Z. Zhang, H. Hermawan, D. Zhu, J. Huang, Y. Liang, G. Li, L. Ren, J. Mech. Behav. Biomed. Mater. 77 (2018) 90–105.
[4] Y. Su, I. Cockerill, Y. Zheng, L. Tang, Y.X. Qin, D. Zhu, Bioact. Mater. 4 (2019) 196–206.
[5] R.I.M. Asri, W.S.W. Harun, M. Samykano, N.A.C. Lah, S.A.C. Ghani, F. Tarlochan, M.R. Raza, Mater. Sci. Eng. C 77 (2017) 1261–1274.
[6] W.S.W. Harun, R.I.M. Asri, J. Alias, F.H. Zulkifli, K. Kadirgama, S.A.C. Ghani, J.H.M. Shariffuddin, Ceram. Int. 44 (2018) 1250–1268.
[7] W. Habraken, P. Habibovic, M. Epple, M. Bohner, Mater. Today 19 (2016) 69–87.
[8] A. Vladescu, M. Braic, F.A. Azem, I. Titorencu, V. Braic, V. Pruna, A. Kiss, A.C. Parau, I. Birlik, in: Appl. Surf. Sci., 2015, pp. 373–379.
[9]D.M. Vranceanu, C.M. Cotrut, M. Bramowicz, I. Titorencu, S. Kulesza, A. Kiss, A. Berbecaru, V. Pruna, M. Branzei, A. Vladescu, Ceram. Int. 42 (2016) 10085–10093.
[10] A. Vladescu, S.C. Padmanabhan, F. Ak Azem, M. Braic, I. Titorencu, I. Birlik, M.A. Morris, V. Braic, J. Mech. Behav. Biomed. Mater. 63 (2016) 314–325.
[11] M.A. Surmeneva, A. Vladescu, R.A. Surmenev, C.M. Pantilimon, M. Braic, C.M. Cotrut, RSC Adv. 6 (2016) 87665–87674.
[12] M. Dinu, A.A. Ivanova, M.A. Surmeneva, M. Braic, A.I. Tyurin, V. Braic, R.A. Surmenev, A. Vladescu, Ceram. Int. 43 (2017) 6858–6867.
[13] M. Badea, M. Braic, A. Kiss, M. Moga, E. Pozna, I. Pana, A. Vladescu, Ceram. Int. 42 (2016) 1801–1811.
[14] S. Ciuca, M. Badea, E. Pozna, I. Pana, A. Kiss, L. Floroian, A. Semenescu, C.M. Cotrut, M. Moga, A. Vladescu, J. Microbiol. Methods 125 (2016).

[15] S. Dudin, C.M. Cotrut, M. Dinu, A. Zykova, A.C. Parau, S. Yakovin, A. Vladescu, Ceram. Int. 43 (2017) 14968–14975.
[16] B.D. Ratner, S.J. Bryant, Annu. Rev. Biomed. Eng. 6 (2004) 41–75.
[17] R.A. Surmenev, Surf. Coatings Technol. 206 â (2012) 2035–2056.
[18] R.A. Surmenev, M.A. Surmeneva, A.A. Ivanova, Acta Biomater. 10 (2014) 557–79.
[19] A. Vladescu, V. Pruna, S. Kulesza, V. Braic, I. Titorencu, M. Bramowicz, A. Gozdziejewska, A. Parau, C.M. Cotrut, I. Pana, M. Dinu, M. Braic, Ceram. Int. (2019).
[20] I. Pana, A. Vladescu, L.R. Constantin, I.G. Sandu, M. Dinu, C.M. Cotrut, Coatings 10 (2020) 654.
[21] A. Vladescu, I. Titorencu, Y. Dekhtyar, V. Jinga, V. Pruna, M. Balaceanu, M. Dinu, I. Pana, V. Vendina, M. Braic, PLoS One 11 (2016) 1–18.
[22] M. Braic, V. Braic, M. Balaceanu, A. Vladescu, C.N. Zoita, I. Titorencu, V. Jinga, F. Miculescu, Thin Solid Films 519 (2011) 4064–4068.
[23] M. Dinu, I. Pana, P. Scripca, I.G. Sandu, C. Vitelaru, A. Vladescu, Coatings 10 (2020) 495.
[24] M. Pilz, K. Staats, S. Tobudic, O. Assadian, E. Presterl, R. Windhager, J. Holinka, Clin. Orthop. Relat. Res. 477 (2019) 461–466.
[25] A.L. Puente Reyna, B. Fritz, J. Schwiesau, C. Schilling, B. Summer, P. Thomas, T.M. Grupp, J. Biomech. 79 (2018) 88–96.
[26] G. Ramírez, S.E. Rodil, H. Arzate, S. Muhl, J.J. Olaya, Appl. Surf. Sci. 257 (2011) 2555–2559.
[27] M. Kazemi, S. Ahangarani, M. Esmailian, A. Shanaghi, Surf. Coatings Technol. 397 (2020) 126044.
[28] W. Cui, G. Qin, J. Duan, H. Wang, Mater. Sci. Eng. C 71 (2017) 520–528.
[29] L. Karlsson, L. Hultman, M.P. Johansson, J.-E. Sundgren, H. Ljungcrantz, Surf. Coatings Technol. 126 (2000) 1–14.
[30] T. Liskiewicz, R. Rybiak, S. Fouvry, B. Wendler, Proc. Inst. Mech. Eng. Part J J. Eng. Tribol. 220 (2006) 125–134.
[31] M. Lotfi, H. Ashrafi, S. Amini, A. Akhavan Farid, M. Jahanbakhsh, Proc. Inst. Mech. Eng. Part J J. Eng. Tribol. 231 (2017) 734–744.
[32] D. V. Shtansky, N.A. Gloushankova, A.N. Sheveiko, P. Kiryukhantsev-Korneev, I.A. Bashkova, B.N. Mavrin, S.G. Ignatov, S. Filippovich, C. Rojas, Surf. Coatings Technol. 205 (2010) 728–739.
[33] I. Pana, V. Braic, M. Dinu, E.S.M. Mouele, A.C. Parau, L.F. Petrik, M. Braic, Coatings 10 (2020) 710.
[34] M. Dinu, T. Hauffman, C. Cordioli, A. Vladescu, M. Braic, A. Hubin, C.M. Cotrut, Corros. Sci. 115 (2017) 118–128.
[35] C.M. Cotrut, C. Vitelaru, M. Dinu, T. Petreus, A. Vladescu, Sci. Adv. Mater. 7 (2015) 1351–1360.
[36] M. Dinu, M. Cojocaru, V. Braic, M. Tarcolea, M. Braic, F. Miculescu, A. Vladescu, C.M. Cotrut, Appl. Surf. Sci. 332 (2015).
[37] A. Sola, D. Bellucci, V. Cannillo, A. Cattini, Surf. Eng. 27 (2011) 560–572.
[38] D. Bellucci, V. Cannillo, A. Sola, Ceram. Int. 37 (2011) 2963–2972.
[39] F. Baino, E. Verné, Biomed. Glas. 3 (2017) 1–17.
[40] G. Muzio, S. Perero, M. Miola, M. Oraldi, S. Ferraris, E. Vernè, F. Festa, R.A. Canuto, V. Festa, M. Ferraris, J. Biomed.

Mater. Res. Part B Appl. Biomater. 105 (2017) 1586–1593.
[41] L.L. Hench, J. Mater. Sci. Mater. Med. 17 (2006) 967–978.
[42] L.L. Hench, H.A. Paschall, J. Biomed. Mater. Res. 7 (1973) 25–42.
[43] M. Nasr-Esfahani, R. Ebrahimi-Kahrizsangi, M. Saleh Dadash, S. Karbasi, Curr. Nanosci. 7 (2011) 568–575.

*Corresponding author: Alina Vladescu,
email: alinava@inoe.ro; Tel./Fax: +4021.457.57.59

Electrochemical impedance spectroscopy used for carbonitrides and oxynitrides investigation

M. DINU [1*], C.M. COTRUT [2], T. HAUFFMAN [3], A. LÓPEZ-ORTEGA[4], X. ALMANDOZ [4], A. VLADESCU [1], M. BRAIC [1]

[1] National Institute of Research and Development for Optoelectronics INOE2000, 409 Atomistilor, Magurele, Romania
[2] University Politehnica of Bucharest, Faculty of Materials Science and Engineering, 313 Sp. Independentei, Bucharest, Romania
[3] Vrije Universiteit Brussel, Department of Materials and Chemistry, Research Group Electrochemical and Surface Engineering, Pleinlaan 2, Brussels, Belgium
[4] Tekniker, Tribology Unit, Iñaki Goenaga 5, Eibar, Spain

Abstract: The present study focuses on the corrosion behavior of various coatings obtained by PVD methods in different media: Dulbecco's Modified Eagle's Medium with Fetal Bovine Serum (DMEM+FBS), saline solution (NaCl) and artificial saliva. Carbonitrides and oxynitrides, applied in medical and tribological field, were investigated by electrochemical impedance spectroscopy (EIS). In the case of Ti-based carbonitrides, it was showed that Si addition led to a decrease of both roughness and crystallite size, having a beneficial effect for corrosion behaviour. Also, the increase in carbon in the case of MPE coatings increased the corrosion performance. For TiSiON, CrSiON and ZrSiON, the effect of substrate bias had also a beneficial effect after 72 h immersion in corrosive solution.

Keywords: EIS, cathodic arc, coatings, carbonitride, oxynitride

1. Introduction

Electrochemical impedance spectroscopy (EIS) is an useful corrosion technique applied to characterize the material-electrolyte interfaces in terms of the on-site electrochemical process. When it comes to the applied signal, a sinusoidal potential of 10 mV root mean square (RMS) vs. open circuit potential (E_{OC}) (over a range of frequencies) is usually used [1]. To assess the time-dependent reactions that may happened in real life, more advanced EIS characterization techniques imply the use of a multisine signal [2, 3]. Therefore, additional information can be obtained in this case such as: information related to experimental noise; non-linear distortions and non-stationarity behavior; statistical evaluation based on the noise level; complex residual as an indication of the goodness-of-fit [4]. Eighter the type of the applied sinusoidal signal, the corresponding current is measured and the current amplitude and phase are used to obtain information about the impedance data [1]. All electrochemical interfaces, formed when a material is immersed in an electrolyte, can be represented as resistive and capacitive elements of an electrical equivalent circuit (EEC). By choosing optimal measurement conditions in order to obtain quality experimental data, evaluation of the fitting procedure and fitting using the appropriate EEC, the electrochemical parameters which characterize the on-going process are obtained.

Cassar et al. investigated a carburised CoCrMo over 24 h of immersion in Ringer's solution (pH= 7.4, 37ºC ±1ºC) [5]. The results showed that carburising led to an improvement of the metal's inherent protection. Another study takes into consideration 316 stainless steel, CoCrMo and Ti6Al4V alloys in Ringer Lactate solution (37˚C) [6]. Among them, Ti6Al4V proved to be the best material for implant applications. However, data in the literature include the corrosion evaluation using EIS not only for metallic, ceramic [7, 8] and polymeric materials [9], but also for coatings [10, 11].

The present study focuses on investigation of corrosion behavior by EIS in the case of carbonitride and oxynitride coatings obtained by PVD methods: cathodic arc evaporation and magnetron sputtering methods (direct current magnetron sputtering (DCMS)/ radio frequency magnetron sputtering (RFMS)/ high power impulse magnetron sputtering (HiPIMS) hybrid technique) for biological and tribological applications.

2. Experimental

TiCN and TiSiCN were deposited on CoCr alloy by cathodic arc deposition process in order to be used in medical applications. The coatings were investigated by EIS after 1h immersion in DMEM+FBS [12]. The thickness of the obtained coatings was around 2.5 µm. The deposition conditions are described in [12].

Multi-principal elements (MPE) carbonitride coatings TiCrCoNiV were deposited on C45 steel by a hybrid technique consisting in magnetron co-sputtering of high purity elemental targets in inert and reactive atmospheres of Ar and Ar+CH_4+N_2. A confocal magnetron sputtering system was used, equipped with five unbalanced magnetrons fed by HiPIMS (Cr target), DC (Ti and V targets) and RF (Co and Ni targets) sources. The thickness of the obtained coatings was around 2-3 µm. Atomic force microscopy (AFM) was used to investigate the surface morphology (AFM, INNOVA, Bruker, USA) operated in tapping mode. 2D images over an area of 1 × 1 μm^2 are presented.

Electrochemical behavior was investigated using a potentiostat/galvanostat VersaSTAT 3 (Princeton Applied Research, USA) and the data were recorded using a Versa Studio software. NaCl 0.9% at room temperature (22 ± 1˚C) was used as test medium for EIS studies. A three standard electrode cell was used with platinum as the counter electrode (CE), Ag/AgCl (KCl sat. (0.197 V)) as the reference electrode (RE) and the investigated specimens as the working electrode (WE) (mounted in a Teflon holder with 1 cm^2 exposed area). After immersion, the specimens were monitored for 12 h while the open circuit potential (Eoc) in time was recorded. Impedance measurements were performed with perturbing a.c. signal amplitude of 10 mV RMS vs. Eoc within 0.1 mHz to 10^3 Hz frequency range. Equivalent circuit fitting of the spectra was performed using

Zview software. The equivalent circuit for impedance data fitting took into consideration Rs (solution resistance), Q_{coat} (coating capacitance), R_{pore} (resistance associated to the current flow through the pores), Q_{dl} (double layer capacitance) and R_{ct} (charge transfer resistance). A CPE was used for a better-quality fit, correlated with α parameter, used also to characterize the solution-coating interface (α_{coat}) and the solution-substrate interface (α_{dl}).

TiSiON, CrSiON and ZrSiON were deposited on CoCr samples by the cathodic arc evaporation technique. The mentioned coatings were deposited at different substrate bias: V_b= -50 V and V_b= -200 V, having a thickness of about 3 µm. The deposition conditions for Cr and Zr based silico-oxynitrides

Fig. 1. Bode 3D graph corresponding to TiSiON, CrSiON, ZrSiON coatings (NS-noise due to non-stationary behavior, NL- noise due to nonlinear behavior) according to the applied amplitude, deposited on CoCr alloy at Vb= -50 V and Vb=-200V

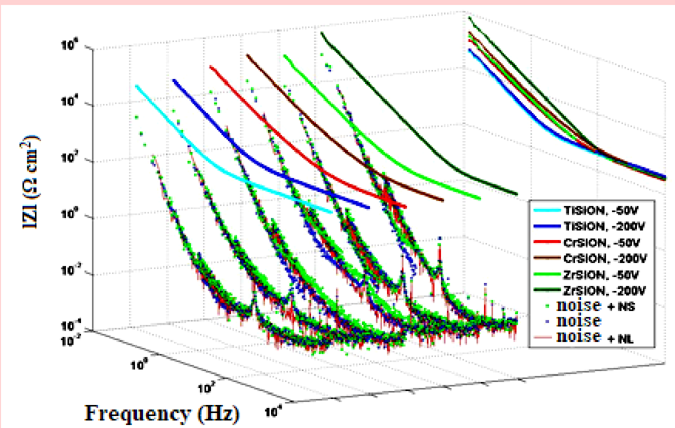

are described in [4, 13]. In this case, the coatings were analyzed by odd random phase multisine electrochemical impedance spectroscopy (ORP-EIS), therefore different amplitude values relative to the open circuit potential (EOC) were used. Whereas for TiSiON coatings, 5 mV amplitude was applied, for CrSiON and ZrSiON different values of amplitude were used according to their deposition condition (voltage bias used) and lower and higher frequency range of each analyzed system (Fig. 1) [4].

3. Results

TiCN and TiSiCN were deposited to improve the CoCr performance in load bearing applications [12]. For this purpose, *in vitro* corrosion investigations, including EIS studies, were performed in 90% DMEM + 10% FBS, (37 ± 0.5 ◦C). The addition of Si into TiCN matrix led to the best capacitive character in the case of TiSiCN, indicated by the coating's associated parameters: low value of Q_{layer} and the highest R_{pore} among the investigated specimens. This result was ascribed to the decrease in Ra roughness and crystallite size when Si was introduced, hindering the electrolyte ingress towards the substrate.

Another study took into consideration the use of MPE coatings in tribological applications. To have an insight on corrosion protective performance of $(TiCrCoNiV)C_{0.18}N_{0.10}$ and $(TiCrCoNiV)C_{0.32}N_{0.15}$ an EIS investigation over 12 h immersion was conducted. Fig. 2 shows the impedance data obtained for the investigated coatings. An electrical equivalent circuit was used to determine the electrochemical parameters described in Ref. [12] and the results are presented in Table 1.

As it can be observed, there is a drop in impedance for both investigated coatings after 12 h, as compared with 1h immersion in NaCl 0.9% at room temperature (22 ± 1˚C). Analyzing the coating corresponding parameters (Q_{coat}, α_{coat} and R_{pore}), when carbon content was higher, a decrease in capacitive character of the $(TiCrCoNiV)C_{0.32}N_{0.15}$ coating was observed after 1h of immersion, along with an increase of the resistance associated to the current flow through the pores generated by the coating defects. This can be ascribed to a more densified morphology, as shown by AFM results

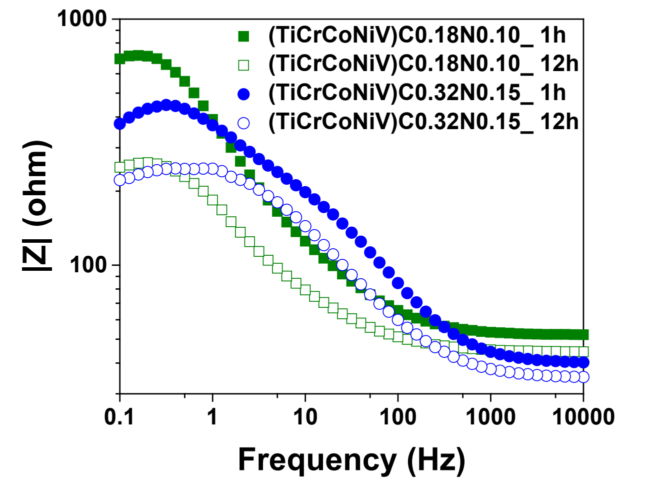

Fig. 2. a) Nyquist and b) Bode magnitude diagram of $(TiCrCoNiV)C_{0.18}N_{0.10}$ and $(TiCrCoNiV)C_{0.32}N_{0.15}$ coatings deposited on C45 steel

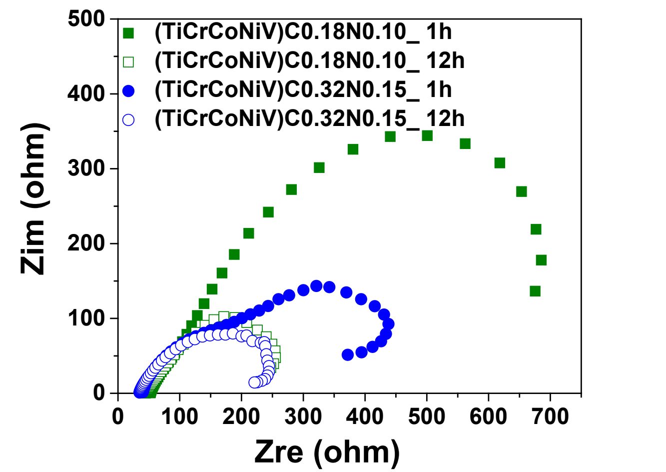

in Fig. 3. Moreover, α_{coat} parameter exhibited also a higher value correlated with a decrease in surface roughness from RMS= 5.22 nm for $(TiCrCoNiV)C_{0.18}N_{0.10}$ to RMS=3.06 nm for $(TiCrCoNiV)C_{0.32}N_{0.15}$. Similar behaviour was seen after 12 h of immersion, therefore a decrease of Q_{coat} and an increase of R_{pore} with increasing carbon content was observed.

Table 1. Electrochemical parameters for (TiCrCoNiV)$C_{0.18}N_{0.10}$ and (TiCrCoNiV)$C_{0.32}N_{0.15}$ coatings deposited on C45 steel, after 1h and 12h immersion in NaCl 0.9%

Coating	(TiCrCoNiV)$C_{0.18}N_{0.10}$		(TiCrCoNiV)$C_{0.32}N_{0.15}$	
	1h	12h	1h	12 h
R_s (Ω cm^2)	52	44	39	34
Q_{coat} (μF $s^{(\alpha-1)}$ cm^{-2})	342.49	1153.50	106.12	371.76
α_{coat}	0.75	0.67	0.77	0.67
R_{pore} (Ω cm^2)	151	141	189	256
Q_{dl} (μF $s^{(\alpha-1)}$ cm^{-2})	304.09	488.28	809.10	10834.00
α_{dl}	0.82	0.98	0.71	0.99
R_{ct} (Ω cm^2)	975	192	353	-

Fig. 3. AFM results of a) (TiCrCoNiV)$C_{0.18}N_{0.10}$ and b) (TiCrCoNiV)$C_{0.32}N_{0.15}$ coatings deposited on Si

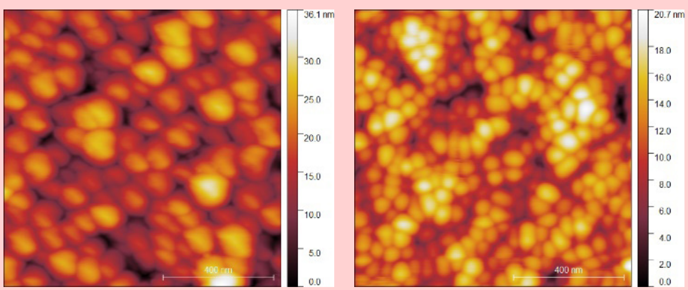

Other results involve the study of Ti, Cr, Zr- based oxynitrides used for dental application. Among them, ZrSiON showed better protective properties due to formation of a passive Zr based oxide on top of the surface [4]. When compared the coatings obtained at higher substrate bias, it was observed that the protective properties of the coatings increased in the case of both Cr and Zr-based coatings. These results were ascribed to an intensified ion bombardment that led to a defect-free structure and to the growth of metal oxide crystallites [4]. In Fig. 4 the impedance results for the investigated coatings deposited both at -50 V and -200 V bias are presented. As it can be observed, the same behavior was presented by TiSiON coating when immersed in artificial saliva: higher impedance values are depicted when -200 V substrate bias was used. The TiSiON associated electrochemical parameters obtained by fitting the impedance values are presented in Table 2.

As it can be observed, the capacitive response of Q_{coat} (characteristic to the coating/electrolyte interface) showed lower values in the case of TiSiON deposited at higher substrate bias. Cotrut et al. showed an increase of oxygen content with the substrate bias for the same coatings, which can have an influence on corrosion resistance [13]. However, the resistance associated with the current flow through the pores was higher in the case of TiSiON obtained at -50V (R_{pore}=0.43 kΩ cm^2). The charge transfer resistance at the substrate/electrolyte interface showed values of about 4 times higher for Ti-based silico oxynitride at Vb= -200 V, demonstrating in this case a smaller tendency of corrosion occurrence at the substrate. The values of α_{coat} were similar, the small difference among the investigated coatings being ascribed to the surface roughness which was higher in the case of TiSiON obtained at Vb= -200 V ($Ra_{TiSiON\ -50V}$= 1.4 µm, $Ra_{TiSiON\ -200V}$= 2.5 µm) [13]. α_{dl} showed lower values due to the measured surface roughness even higher for CoCr alloy than in the case of mentioned coatings (Ra_{CoCr}= 3.2 µm) [13].

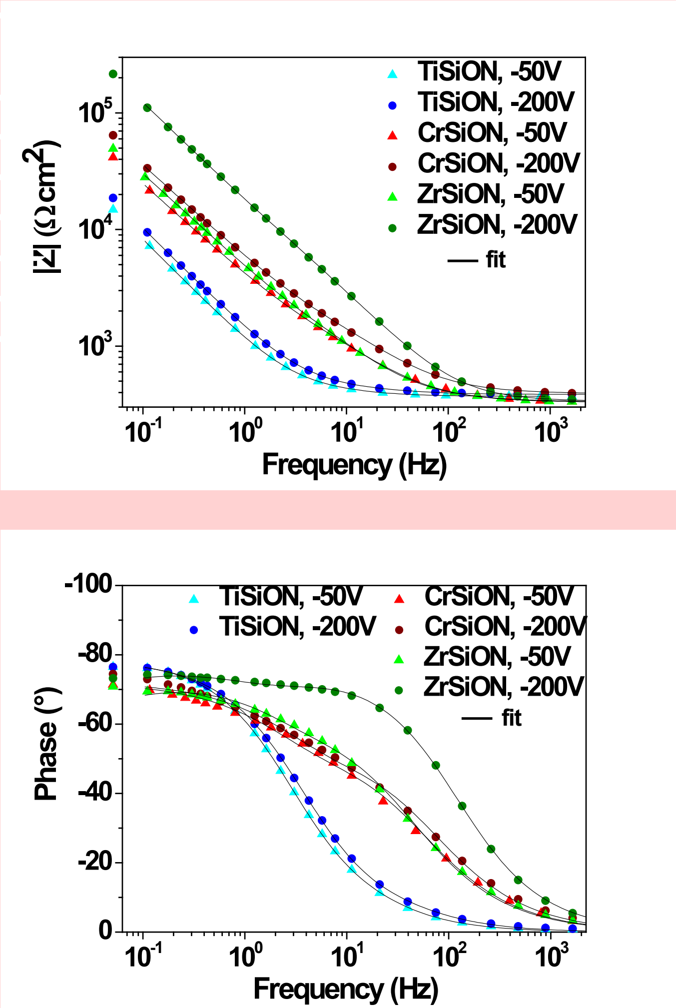

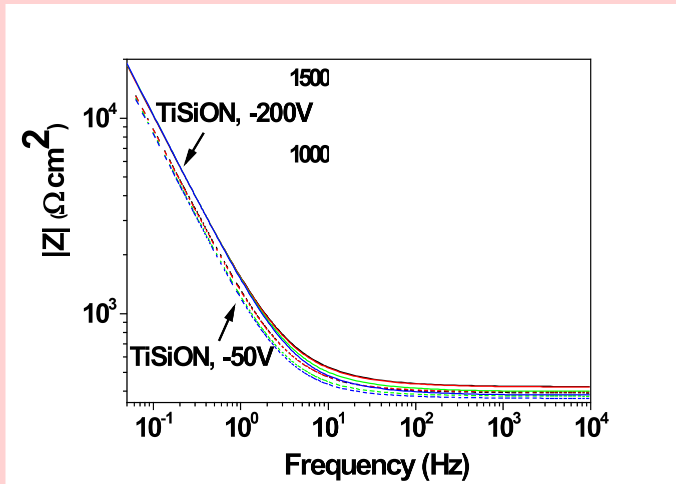

Fig. 4. Bode diagram of a) impedance and b) phase of TiSiON, CrSiON and ZrSiON coatings deposited on CoCr alloy at Vb= -50 V and Vb=-200V (continuous-fit line) after 72h immersion in artificial saliva

Fig. 5. Bode amplitude plots of TiSiON coating deposited on CoCr alloy at Vb= -50 V (dashed line) and Vb=-200 V (solid line) over 72h immersion in artificial saliva

Coating	TiSiON, -50V	TiSiON, -200V
Rs (Ωcm^2)	370.7	385.6
Q_{coat} ($\mu F\ s^{(\alpha-1)}\ cm^{-2}$)	136.76	87.86
α_{coat}	0.90	0.89
R_{pore} ($k\Omega\ cm^2$)	0.43	0.22
Q_{dl} ($\mu F\ s^{(\alpha-1)}\ cm^{-2}$)	47.37	59.08
α_{dl}	0.87	0.85
R_{ct} ($k\Omega\ cm^2$)	552	2237

Table 2. Electrochemical parameters obtained from fitting the experimental data with the equivalent electrical circuit for Ti-based coatings deposited on CoCr alloy at Vb= -50 V and Vb= -200V after 72h immersion in artificial saliva

The impedance behavior of TiSiON coating over 72h of immersion in artificial saliva is presented in Fig. 5. It can be observed that the investigated experimental samples showed only a slight decrease in impedance at the end of the test, demonstrating the stability and efficiency of the deposited layers in terms of protection of the CoCr alloy substrate. The results showed a decrease in impedance of maximum 10% for TiSiON deposited at Vb = -50 V and only 9% for the layer deposited at Vb = -200 V. The improvement of the corrosion resistance with the increase of the polarization voltage has been observed previously also for other types of coatings (CrAlN, TiN or NbAlN) [14-16].

4. Conclusions

Electrochemical impedance spectroscopy was used to evaluate the corrosion performance of various carbonitrides and oxynitrides. The coatings were obtained by cathodic arc evaporation and magnetron sputtering methods in order to be used in medical and tribological applications.

TiCN and TiSiCN coatings immersed 1h in DMEM+FBS showed an improvement with Si addition into TiCN matrix that led to low value of Q_{layer} and high R_{pore}.

$(TiCrCoNiV)C_{0.18}N_{0.10}$ and $(TiCrCoNiV)C_{0.32}N_{0.15}$ MPE coatings were evaluated after 1h and 12h in NaCl 0.9%. It was proved that higher carbon content was beneficial for their morphology and their grain size, therefore for corrosion protection.

Me-based silico-oxynitrides (where Me= Ti, Cr and Zr) used for dental applications were investigated in artificial saliva over 72 h. It was showed a better corrosion behavior when the depositions were made at higher substrate bias. Among all analyzed coatings, ZrSiON proved to be the best solution for CoCr alloy.

Acknowledgements

The authors acknowledge the support of the Romanian Ministry of Research and Innovation through PROINSTITUTIO project-contract no. 19PFE/17.10.2018, the Core Program project no. 18N/2019 and Medical Met

Mat project no. PN-III-P1-1.2-PCCDI-2017-0239/60 PCCDI 2018, within PNCDI III. The studies were also supported by Partnerships in priority areas program - PN II, developed with support from ANCS, CNDI - UEFISCDI, Coat4Dent project no. 175/2012 and M.ERANET-6059-TriboHEA project funded by The Ministry of Education and Scientific Research, Romania, UEFISCDI Programme 3, grant no. 113/2019 and by The Ministry for Economic Development and Infrastructures, Basque Country, Spain, Hazitek Programme, grant no. ZL-2019/00622.

References

[1] J.L.Gilbert, Electrochemical behavior of metals in the biological milieu, Materials Science and Materials Engineering, Comprehensive Biomaterials II **1**, 19 (2017).

[2] T. Breugelmans, E. Tourwé, Y. Van Ingelgem, J. Wielant, T. Hauffman, R. Hausbrand, R. Pintelon, A. Hubin, Odd random phase multisine EIS as a detection method for the onset of corrosion of coated steel, Electrochem. Commun. **12** (1), 2 (2010).

[3] T. Breugelmans, J. Lataire, T. Muselle, E. Tourwé, R. Pintelon, A. Hubin, Odd random phase multisine electrochemical impedance spectroscopy to quantify a non-stationary behaviour: Theory and validation by calculating an instantaneous impedance value, Electrochimica Acta **76**, 375 (2012).

[4] M. Dinu, T. Hauffman, C. Cordioli, A. Vladescu, M. Braic, A. Hubin, C.M. Cotrut, Protective performance of Zr and Cr based silico-oxynitrides used for dental applications by means of potentiodynamic polarization and odd random phase multisine electrochemical impedance spectroscopy, Corros. Sci. **115**, 118 (2017).

[5] J. Cassar, B. Mallia, A. Karl, J. Buhagiar, EIS of carburised CoCrMo: Evolution of parameters characterising the metal-electrolyte interface, Surf. Coat. Technol. **292**, 90 (2016).

[6] M. Songür, H. Çelikkan, F. Gökmeşe, S.A. Şimşek, N.Ş. Altun, M.L. Aksu, Electrochemical corrosion properties of metal alloys used in orthopaedic implants, Appl. Electrochem. **39**(8), 1259 (2009).

[7] Z. He, K.B. Andersen, F.B. Nygaard, K.K. Hansen, A combined SEM, CV and EIS study of multi-layered porous ceramic reactors for flue gas purification, Ceram. Int. **39**(1), 847 (2013).

[8] V. Yousefi, D. Mohebbi-Kalhori, A. Samimi, Equivalent electrical circuit modeling of ceramic-based microbial fuel cells using the Electrochemical Impedance Spectroscopy (EIS) analysis, J. Renew. Energy Environ. **6**(1), 21 (2019).

[9] M. Ates, Review study of electrochemical impedance spectroscopy and equivalent electrical circuits of conducting polymers on carbon surfaces, Prog. Org. Coat. **71**(1), 1 (2011).

[10] A. López-Ortega, R. Bayón, J.L. Arana, Evaluation of protective coatings for offshore applications. Corrosion and tribocorrosion behavior in synthetic seawater, Surf. Coat. Technol. **349**, 1083 (2018).

[11] A. López-Ortega, J. L. Arana, E. Rodríguez, R. Bayón, Corrosion, wear and tribocorrosion performance of a thermally sprayed aluminum coating modified by plasma electrolytic oxidation technique for offshore submerged

components protection, Corros. Sci. **142**, 258 (2018).
[12] M. Dinu, I. Pana, P. Scripca, I.G. Sandu, C. Vitelaru, A. Vladescu, Improvement of CoCr alloy characteristics by Ti-based carbonitride coatings used in orthopedic applications, Coatings, **10**(5), 495 (2020).
[13] C.M. Cotrut, C. Vitelaru, M. Dinu, T. Petreus, A. Vladescu, Synthesis and characterization of TiSiON biocompatible thin films used in biomedical applications, Science of Advanced Materials, **7**(7), 1351 (2015)
[14] Y. Lv, L. Ji, X. Liu, H. Li, H. Zhou, Influence of substrate bias voltage on structure and properties of the CrAlN films deposited by unbalanced magnetron sputtering, Appl. Surf. Sci. **258**(8), 3864 (2012).
[15] N.D. Nam, J.G. Kim, W.-S. Hwang, Effect of bias voltage on the electrochemical properties of TiN coating for polymer electrolyte membrane fuel cell, Thin Solid Films **517**(17), 4772 (2009).
[16] H.C. Barshilia, B. Deepthi, K.S. Rajam, K.P. Bhatti, S. Chaudhary, Structure and properties of reactive direct current magnetron sputtered niobium aluminum nitride coatings, J. Mater. Res. **23**(5), 1258 (2008).

*Corresponding author: mihaela.dinu@inoe.ro

A systematic experimental approach for design, deposition and characterization of PVD optical coatings

I. PANA[*], C. VITELARU, A.E. KISS,
N.C. ZOITA, M. BRAIC, V. BRAIC
National Institute of Research and Development for Optoelectronics – INOE 2000, Department for Advanced Surface Processing and Analysis by Vacuum Technologies, 409 Atomistilor St., 077125 Magurele, Romania

Abstract: In this contribution we present the results of a systematic experimental approach, starting from the deposition by magnetron sputtering technique and optical characterization of single oxides, nitrides and metallic layers. The measured monolayer characteristics were then used as input parameters in the design phase, targeting for specific spectral characteristics of multilayers. Three different kinds of applications were considered: AR (Vis reflectance < 4 %), low-e (Vis transmittance of 85 % combined with high IR reflectance ~ 80 %) and colored optical filters (Vis reflectance ~ 45 %, solar transmittance ~ 80 %).

Keywords: optical coatings, magnetron sputtering, multilayer thin films, design optimization, PVD processes

1. Introduction

Nowadays, the optical interference coatings are playing a key role in optical instruments, laser systems, fiber communication links, display systems, architectural glass, photoelectric converters, etc [1]. The advanced optical instrumentation has enjoyed a steady growth, being therefore necessary to improve the optical performances of a wide range of optical components by covering their surfaces with interference coatings [2]. A few common optical characteristics of interference coatings are shown in Fig. 1. The versatility of multilayers is demonstrated by the possibility to target a reduction of reflection at an interface, an enhanced absorption, a high-quality reflector in a laser cavity, a narrow spectral filter, a scalable beam splitter or a circular polarizer [3].
Moreover, the optical properties of a multilayer optical coating are strongly influenced by many factors, including the used coating technology (deposition parameters, vacuum conditions or substrate types). It is well known that the thin film deposition by Physical Vapor Deposition (PVD) techniques has many advantages such as the coating's improved durability and mechanical properties, tunability of optical characteristics or the possibility to cover large area substrates. The optical properties of PVD oxides and nitrides coatings received an increased attention in the last years. These multilayered coatings are widely used for different optical applications, such as colored optical filters, Bragg mirrors, high power optical, antireflective (AR) or low emissivity

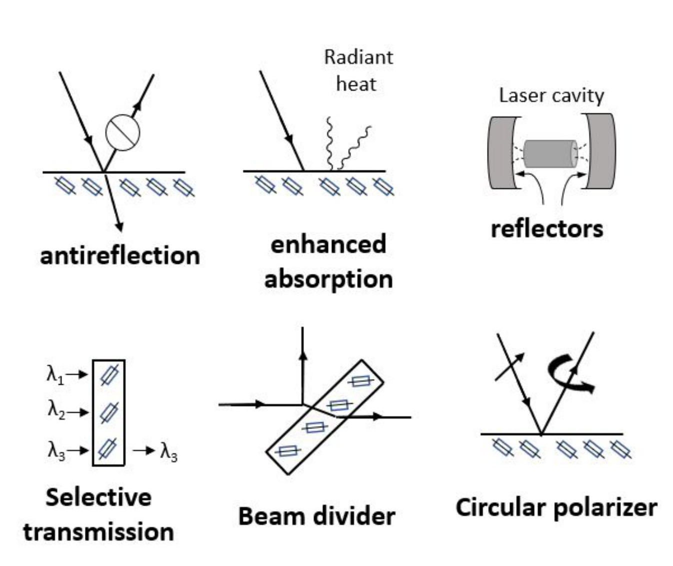

Fig. 1. Common optical characteristics of interference coatings

(low-e) coatings. The development of such applications [4] requires i) the control and reproducibility of the complex refractive index of the coatings; ii) synthesis of monolayers with amorphous and isotropic structure and no birefringence; iii) their good adhesion to the substrate, high scratch and abrasion resistance, iv) superior thickness uniformity (< 3 %) and low surface roughness of the coatings. The magnetron sputtering process is widely used on large industrial scale for production of coatings, fulfilling all the above-mentioned requirements [5].

Magnetron sputtering has a number of advantages, namely the possibility to obtain adherent coatings by using high deposition rates. Dense or porous optical coatings can be deposited homogeneously and reproducibly onto large optical components by using this deposition technique.
In this paper, the measured monolayer characteristics were used as input parameters in the design of different multilayer types, by combining the multilayer modelling and reverse engineering analysis, targeting specific spectral characteristics of multilayers. Three different kinds of applications were targeted: colored optical filters, low emissivity and antireflective coatings. The optical modelling process was performed considering a compromise between the coating's cost-effectiveness and overall performance, specific to each type of application.

2. Experimental

The magnetron sputtering systems used for mono- and multilayer deposition are equipped with three (Φ = 2.54 cm) and five cathodes (Φ = 5.08 cm), respectively, both in a confocal geometry (Fig. 2).
For both antireflective coatings and colored optical filters, the AJA-Minor deposition unit was equipped with two cathodes with SiO_2 and TiO_2 targets (99.99% purity, Kurt Lesker) fed by RF generators (13.56 MHz) (Table 1). In order to obtain low emissivity coatings, two cathodes of AJA-ATC-ORION unit

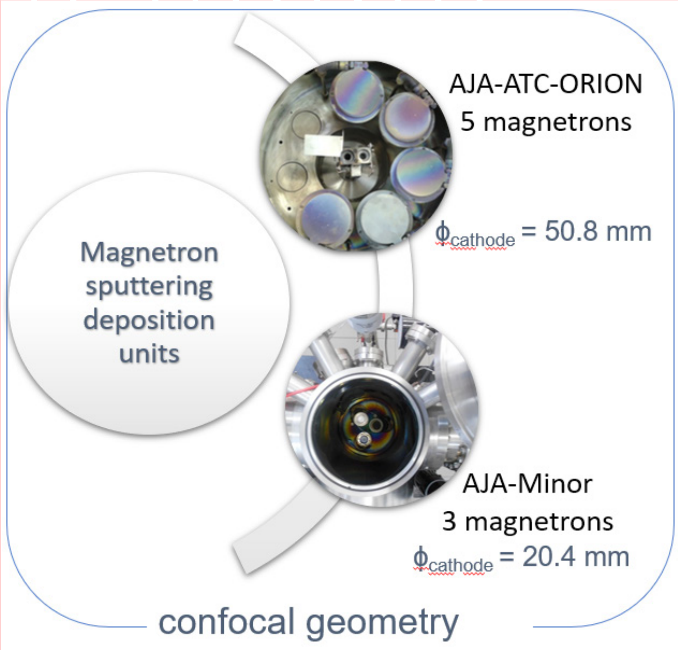

Fig. 2. An overview of magnetron sputtering deposition units used for obtaining the mono- and multilayers

were equipped with Si and Ag targets. The distance between the magnetron targets and the substrates holder was kept constant at 12 cm (AJA-Minor) and 17 cm (AJA-ATC-ORION). The uniformity of all films (± 2 %) was assured by using a continuous rotation of the substrate holder during the entire deposition process. All films were obtained at room temperature on 1 mm thick (10 × 15 mm^2) glass (Heinz-Herenz, Hamburg, Germany) and 0.525 mm thick Si (100) substrates. Before each deposition process, all substrates were ultrasonically cleaned in isopropyl alcohol and sputter cleaned for 15 min., in pure argon atmosphere at 0.67 Pa, applying 50 W RF power on the substrate holder. All the transmission and reflectivity spectra were measured on glass substrates at normal and 5° incidence angle by using a Jasco V670 spectrophotometer equipped with an integrating sphere (Φ=60 mm).

Table 1. Deposition conditions for TiO_2, SiO_2, TiO_x, SiO_x, SiN_x and Ag monolayers

	AR		Colored optical filter		Low-e	
Monolayer	TiO_x	SiO_x	TiO_x	SiO_x	SiN_x	Ag
Q_{Ar} (sccm)	10	10	21/0.21	21/0.21	8.5/1.5	10/-
$t_{substrate}$	RT	RT	RT	RT	RT	RT
d_{t-s} (cm)	12	12	12	12	17	17
Working pressure (Pa)	0.67	0.67	0.67	0.67	0.67	0.67
$P_{RF\ subst.}$ (V)	-60	-60	-60	-60	0	0
$P_{cathode}$ (W)	50 (RF)	50 (RF)	50 (RF)	50 (RF)	90 (RF)	42 (DC)
U_{bias} (V)	490	310	350	340	191	350
R_{dep} (nm/h)	80	138	80	138	1.3	9.8

Nanoindentation and nanoscratch measurements were carried out by using a Hysitron TI Premier nanoindenter equipped with a 100 nm radius Berkovich diamond tip. For both measurements, the progressive applied force was ranging from 1 to 10 mN. The hardness and reduced Young modulus values were derived by using the Oliver-Phar formalism.

3. Results and discussion

3.1. Optical characterization of substrates and coatings

The optical properties of individual monolayers, obtained by radio-frequency magnetron sputtering, are used as input parameters for the optical modelling. Consequently, the obtained multilayer structures contain already the experimentally measured optical properties of available monolayers.
The differences between the theoretical (S (n,k,d,λ)) and experimental (Ŝ (n,k,d,λ)) spectral characteristics of monolayers can be evaluated by using a merit function, DF: where “n” and “k” denote the refractive index and extinction coefficient, while “d” is representing the coating thickness. One can note that the second derivatives of

$$\mathrm{DF} = \sum_{j=1}^{L}\left[\frac{S(n(\lambda_j),k(\lambda_j),\delta,\lambda_j) - \hat{S}(\lambda_j)}{\Delta S_j}\right]^2 + \alpha_1\sum_{j=1}^{L}[n''(\lambda_j)]^2 + \alpha_2\sum_{j=1}^{L}[k''(\lambda_j)]^2.$$

"n" and "k" are used to obtain an accurate dispersion relation of its optical constants. Hence, the obtained optical properties of monolayers were as follows: TiO_x (arbitrary "n" and "k" dispersion between 2.2 - 2.4 and 0.1-0.2, respectively in the visible range), SiOx, SiO_2 (n ~ 1.47, k=0 in the visible range), TiO_2 (n ~ 2.35, k< 0.001 in the visible range), Ag (n ~ 0.2, k = 0.1 ÷ 15 in the 200 - 2000 nm spectral range), SiN_x (n ~ 1.8, k < 0.01 in 400-2000 nm spectral range).

3.2. Antireflective coatings

The first class of optical coatings that will be approached is represented by the antireflective (AR) coatings. AR coatings are frequently used in the medical field (e.g. eyeglass lenses), telecommunications (e.g. screens for mobile phones, monitors, tablets or laptops) or energy conversion (e.g. solar panels). Moreover, the glass panels covered with thin layers having AR properties are usually used in the optical applications field to improve the transparency of glass in the UV-Vis-NIR spectral interval. There are also used in order to avoid the appearance of undesirable optical phenomena such as the double object image behind the glass panels or multiple reflections of beams generated by different light sources [6]. Usually, glass panels have a reflectivity of ~ 8,7 % in the UV-Vis-NIR spectral range, this value representing the sum of the light reflections on each side of the glass. Therefore, a major inconvenience of glass panels is represented by their natural high reflectivity, being therefore necessary to lower it below 5 % by using a one-sided AR layer covering.

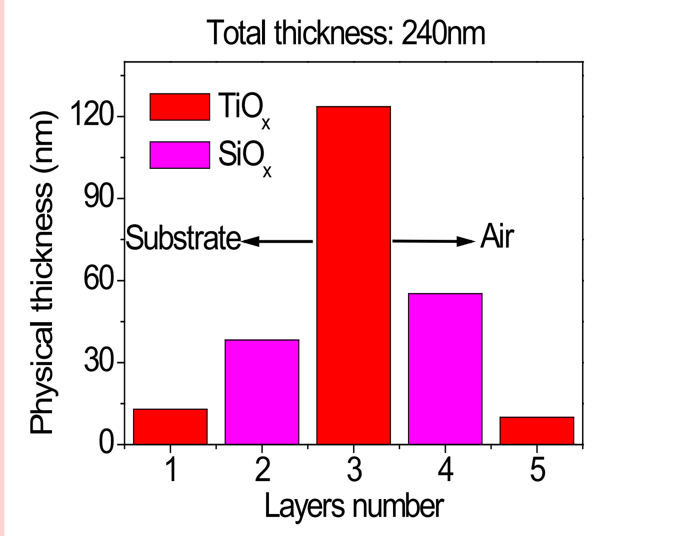

Fig. 3. AR design: thicknesses of alternating TiOx-SiOx layers

The individual layer thicknesses from the AR multilayer design are shown schematically in Fig. 3. The multilayer design is consisting of two SiO_z layers that are interspersed between three TiO_x layers. It should be noted that the thicknesses of the layers are ranging between 123 nm (TiO_x, layer no. 3) and 10 nm (SiO_2, outer layer), respectively. The optimization process of the AR multilayer aimed to simultaneously obtain a limited total thickness and as few layers as possible. The main imposed criterion was related to the minimum thickness of each monolayer which has to be greater than 10 nm in order to be able to obtain continuous thin layers by using the magnetron sputtering technique [7]. After the modeling

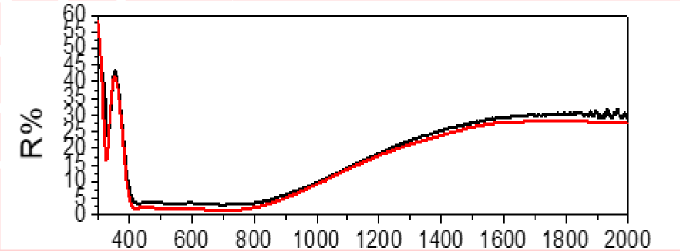

Fig. 4. Design (red curve) and experimental (black curve) spectrophotometric curves of AR multilayer

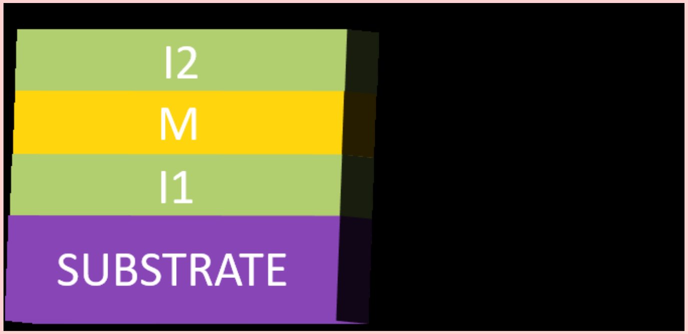

Fig. 5. The proposed dielectric-metal-dielectric structure of a low-e coating

process, a multilayer structure with a total thickness of 240 nm was selected to be experimentally produced. An important feature of this AR structure is the reflection average value smaller than 4 % in the entire visible spectral range (Fig. 4.).

3.3. Low emissivity coatings

In the last few years there has been a growing interest in the development of the global glazing industry in order to obtain energy-efficient windows [1]. The main requirements for modern windows are a higher transparency and a reduced heat loss, these being fulfilled by optimizing the solar transmission in the visible spectral range and increasing the reflectivity in the near-infrared spectral range (Table 2.).

One classical approach, introduced for the first time in the 80s, is to adjust the thicknesses and optical constants of individual layers within an insulator/metal/insulator (IMI) multilayer structure (Fig.5).

Even though the performance of solar control glazing's has been improved in recent years, most improvements were made by using different types of transparent oxides in an IMI multilayer structure such as TiO_2, AZO, ITO, SnO_2, SiO_2, VO_2, ZnO, etc. In this case, several studies indicated that the optical properties of the metallic layers (M=Al, Cu, Au, Ag) are altered by thermal oxidation and corrosion processes during the exposure to the atmospheric conditions.

Transmission and reflectivity	Spectral range	Specific values
T%	380-780 nm	70 ÷ 85 %
R%	>780 nm	75 ÷ 90 %

Table 2. Spectral characteristics of a typical low emissivity coating

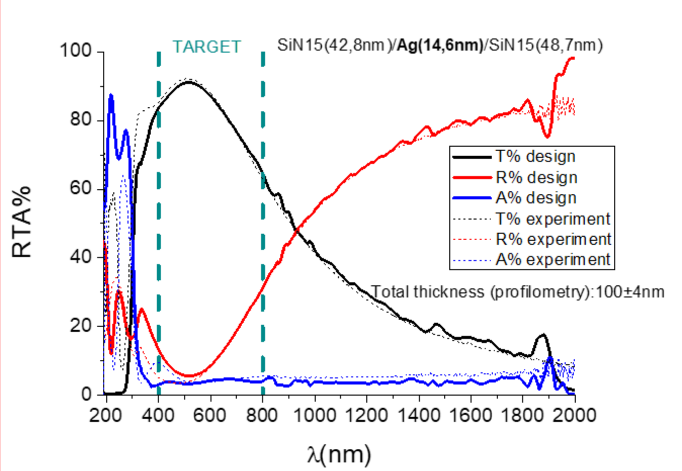

Fig. 6. Comparison between designed and experimental RTA curves of the low emissivity coating

Until now, part of the research studies has focused on the possibility of using nitrides layers in IMI structures instead of using oxides as antireflective layers. The aim of this study is to investigate the optical properties of a low emissivity SiN_x/Ag/SiN_x multilayer structure obtained by magnetron sputtering technique. The optical parameters of the amorphous SiN_x (1,11≤x≤1,66) and Ag thin films were evaluated by using spectrophotometric data. Also, a comparative study between the theoretical design and experimental spectral photometric curves of SiN_x/Ag/SiN_x with Ag layer thickness of 14,8 nm demonstrated a good concordance between the theoreticaly designed and experimentaly obtained curves (Fig. 5.).

3.4. Colored optical filters

Nowadays, the optical coatings consisting of dielectric alternating layers have attracted much attention for their large-scale applications. So far, many research studies have pointed out the advantages of using the SiO_2 and TiO_2 materials in different applications, because of their attractive optical and electronic properties. For this reason, the SiO_2 and TiO_2 single thin layers prepared at room temperature by physical vapor deposition processes are suitable candidates to be used in the fabrication of optical filters. The aim was to develop and optimize specific theoretical designs by using dedicated software (Optilayer Ltd.) [8], in order to produce

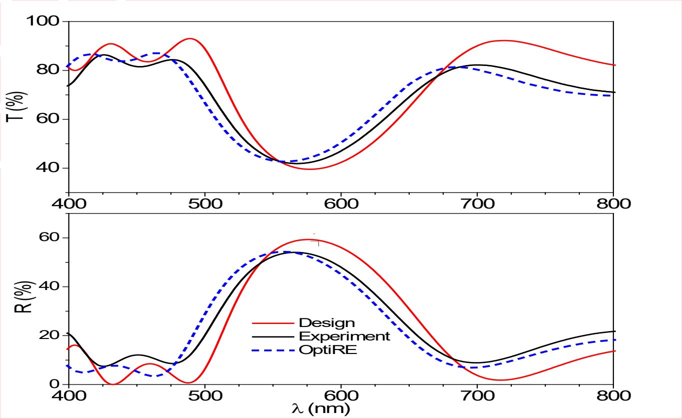

Fig. 6. Visible transmission and reflection spectra of the colored optical filter

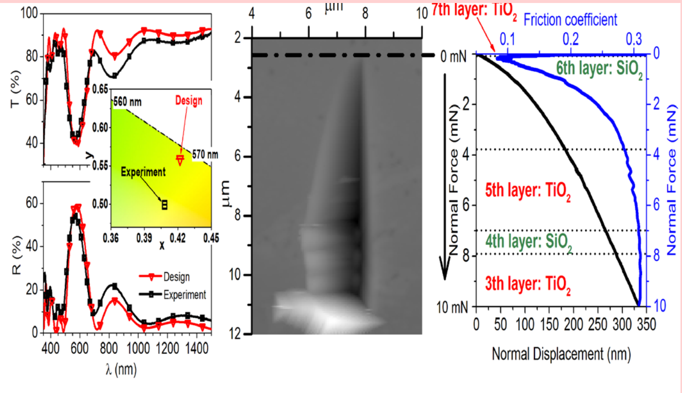

Fig. 7. Mechanical properties of the TiO_2-SiO_2 7- layered coating

TiO_2-SiO_2 multilayer structures. The experimental reflectivity curve in the spectral interval of 400 - 800 nm revealed an important maximum (~ 54 %) at 574 nm (green-yellow colour) which corresponds to a reflectivity factor in the visible range of ~ 45.39 % and a solar radiation transmission of ~ 80 % (Fig. 6). The mechanical properties of the multilayer were investigated by nanoindentation and nano-scratch measurements, resulting in a hardness (H) and reduced Young modulus (E_r) of 7.18 and 88.31 GPa respectively, as well as satisfactory scratch resistance for applied forces up to 10 mN. An average H/E_r ratio of 0.081 confirms the achievement of superior mechanical properties (friction coefficient µ ~ 0.3) of the multilayer as compared to those of the bare glass substrate (Fig. 7).

The thermal stability of the multilayer structure in the ambient air at temperatures up to 200 C for 1 h was evaluated. Also, the stability over time by air exposure at room temperature (35 days post-deposition) was evaluated. The spectrophotometry measurements revealed minor changes on recorded transmission and reflection curves. The proposed design can be considered to be an alternative solution for further integration into solar thermal collectors which are typically used for architectural purposes. Among the most important features of the design are the yellow-green color, and the thermal and mechanical properties which are satisfying the basic requirements for this type of coatings [9].

4. Conclusions

The investigation of the optical properties of the individual monolayers (SiN_x, Ag, SiO_x and TiO_x) in terms of refractive index and extinction coefficient was carried out by spectrophotometric measurements, combined with multilayer modelling and reverse engineering. The optical multilayer modelling process was performed considering a compromise between the coating's cost-effectiveness and overall performance, specific to each type of application.
The comparison between the designed and measured spectral photometric curves of three different multilayers, one for each of the above-mentioned applications, were presented, demonstrating a good concordance between the design and experiment. All experimental spectral photometric curves are in a good agreement with the optical simulations, with typical discrepancies less than a few percent.

Acknowledgements

The present work was supported by Romanian National Core Program No. 18N/18.02.2019 and PROINSTITUTIO Project No. 19PFE/17.10.2018. The SEM, XRD and nanomechanical results were acquired using the systems purchased by the infrastructure project INOVA-OPTIMA SMIS code 49164, contract No. 658/2014.

References

[1] A. Thelen, Design of optical interference coatings. **232**, (1989).
[2] O. Stenzel, Optical Coatings, **54** 2014; Vol.; ISBN 978-3-642-54062-2.
[3] P. W. Baumeister, Optical Coating Technology; (2010).
[4] L. Martinu, D. Poitras, Plasma deposition of optical films and coatings: A review. J. Vac. Sci. Technol. A Vacuum, Surfaces, Film. **18** (2000).
[5] J.A. Dobrowolski, J. R. Pekelsky, R. Pelletier, M. Ranger, B. T. Sullivan, A. J. Waldorf, Appl. Opt., **31** (1992).
[6] C. Battaglin, F.Caccavale, A. Menelle, M. Montecchi, E. Nichelatti, F. Nicoletti, **351** (1999).
[7] I. Pana, C. Vitelaru, N. C. Zoita, M.Braic, Tunable. Plasma Process. Polym. **13** (2016).
[8] A. V. Tikhonravov, M. K. Trubetskov, M. A. Kokarev, T. V. Amotchkina, A. Duparre, E. Quesnel, D. Ristau, , **2555** (2002).
[9] I. Pana, C. Vitelaru, A. Kiss, N.C. Zoita, M. Dinu, M. Braic, M.. Mater. Des. **130** (2017).

*Corresponding author: iulian.pana@inoe.ro

Optical emission spectroscopy techniques for controlling the reactive magnetron plasma processes and tuning the properties of thin films

C. Vitelaru, I. Pana, A.E. Kiss, A.C. Parau,
L.R. Constantin, N.C. Zoita, M. Braic

National Institute of Research and Development for Optoelectronics – INOE 2000, Department for Advanced Surface Processing and Analysis by Vacuum Technologies, 409 Atomistilor St., 077125 Magurele, Romania

Abstract: Optical emission spectroscopy is a valuable tool for plasma diagnostics, giving non-invasive direct access to the excited species in the plasma volume. The use of this technique is illustrated for describing the reactive sputtering process in three different configurations: nitrogen reactive gas with lack of hysteresis, oxygen reactive gas with marked hysteresis behavior, two reactive gas configuration with variable gas mixing. The process windows are identified and the tunability of the process is directly related with tunable properties of thin films, such as SiN_x, CuO_x and TaO_xN_y respectively.

Keywords: optical emission spectroscopy, reactive plasma, oxides, nitrides

1. Introduction

The technologies that use plasmas as a tool for surface processing and thin film deposition are of great interest, their inherent ecological characteristic being a great asset in the competition with chemical deposition methods [1]. Among the technologies used for thin film deposition the magnetron sputtering and reactive magnetron sputtering in particular are intensively used both in research and industry [2,3]. The use of a metal target and a gas mixture that contains reactive species, such as oxygen, nitrogen and hydrocarbon gases enables the creation of a large variety of compounds, including oxides, nitrides, carbides, oxynitrides, carbonitrides, etc. Due to the presence of the reactive gas in the plasma volume, complex and interdependent phenomena of compound formation and destruction occur on all surfaces and in the volume. One of the main characteristics of the reactive sputtering process is the presence of Hysterezis phenomena [4,5]. This can be seen by varying one control parameter, such a reactive gas flow, target current or power, and following the variation of another parameter, such as partial or total pressure, voltage, power, emission lines intensity etc. The increase followed by a decrease of the controlled parameter produces a variation of the measured parameter that follows a different path, creating a so-called hysteresis loop. This can lead to process instability, this region being hard to control, and to a dependence on the history of the system. In the same time, this is also a potential advantage, precisely this process window being that one that can be used to tune the properties of the thin films. Optical emission spectroscopy is a tool that can be successfully used for the characterization of such reactive process [6,7,8]. The knowledge of process intervals gives insight on the elementary processes occurring both on the surfaces and in the volume. By carefully choosing the process parameters, the tunability of thin films properties can be achieved. In this contribution an illustration is given for three distinct configurations, presented as case studies for tunability of reactive sputtering processes.

2. Experimental

2.1. Experimental Setup

The experimental setup consists of a vacuum chamber of 50 cm diameter, with a 2” planar magnetron target placed at the bottom, and a rotatable substrate holder placed in front of the target at a distance of 9 cm (Fig. 1). The light emitted in the dense plasma region in front of the target is collected by a collimator and guided towards a portable HR2000 spectrometer through an optical fiber. The emission spectra are registered on a computer and subsequently analyzed.

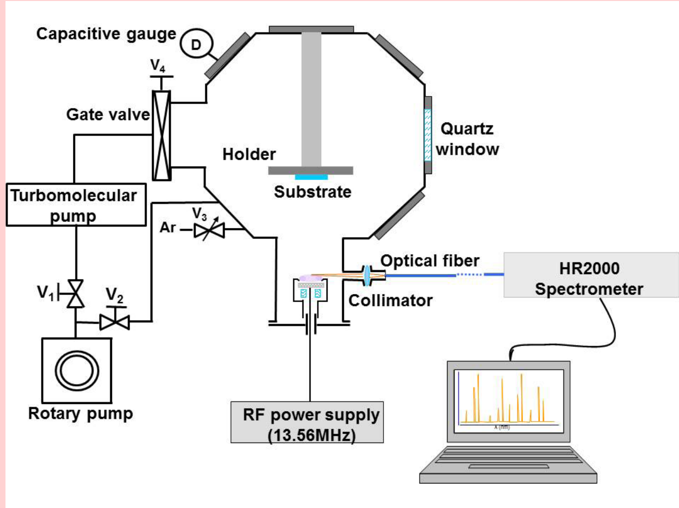

Fig. 1. Experimental setup of deposition chamber and optical emission spectroscopy assembly

For this study, three types of targets were used, namely Si, Cu and Ta, sputtered in gas mixtures containing Ar and one or two reactive gases (oxygen and nitrogen). The specific process conditions from each case are given in each section, each one being specific to the type of target and case study

2.1.1 Case study for SiNx, tuning the hysteresis free process

The first sputtering configuration to be described refers to the sputtering of Si in a Ar/N_2 environment, for the deposition of SiN_x [6] The sputtering under Ar/N_2 gas mixture is potentially

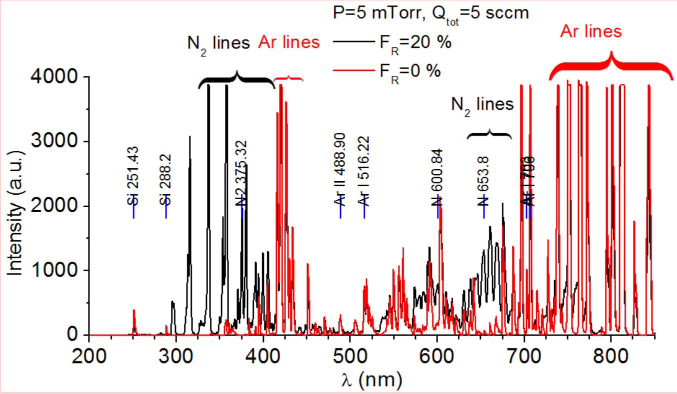

Fig. 2. Typical emission spectrum of Si sputtering plasma in Ar and Ar/N_2 gas mixtures respectively

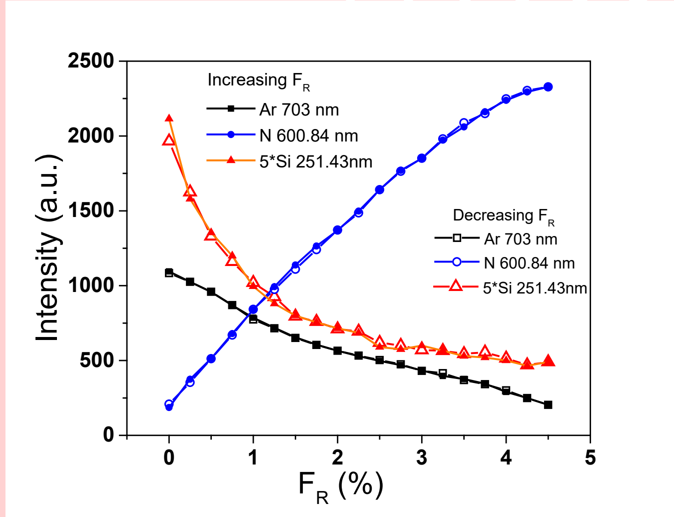

Fig. 3. Relative variation of emission line intensities as a function of reactive gas flow ratio.

easier to control, due to the lower reactivity of nitrogen. The specific experimental conditions for this study are the following: P_{RF}= 100 W, applied to the Si target, pumping section fixed so that the Ar pressure to be 0.67 Pa at 5 sccm Ar gas flow, total gas flow maintained constant at 5 sccm by decreasing the Ar flow as the N_2 flow was increased. The reactive gas flow ratio, F_R=FN_2/(FAr+FN_2), represents the ratio between the reactive gas flow and total gas flow.

The typical emission spectrum of Si sputtering plasma in pure argon, F_R = 0 % and Ar/N_2 gas mixture with 20 % nitrogen in total gas flow, F_R = 20 %, are represented in Fig. 2. Some of the representative emission lines of the species present in the plasma volume are identified and marked correspondingly. From the emission spectrum of the sputtering plasma, some specific lines were chosen to be followed, describing the reactive process. Their corresponding intensity evolution as a function of gas flow ratio is represented in Fig. 3. These evolutions are quite typical for a reactive process, with a marked decrease of the line intensity corresponding to the target material atoms, when increasing the reactive gas flow. Correspondingly, the emission line intensity of Nitrogen, both atomic and molecular, is increasing, while the emission line intensity of Argon is decreasing, due to the replacement of Ar

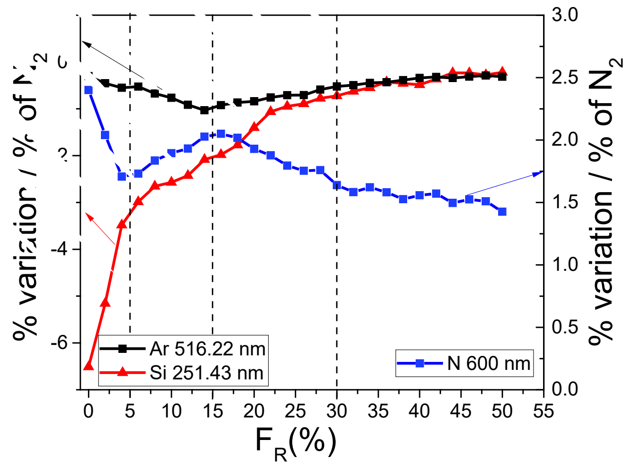

Fig. 4. Line intensity variation rate as a function of F_R, for selected emission lines corresponding to: Si, Ar, and N. Total gas pressure = 0.67 Pa, total gas flow = 5 sccm, constant pumping speed, P_{RF}=100 W

with nitrogen in the process gas mixture.

However, the lack of hysteresis behavior is observed for all the investigated emission lines. This indicates a relative stability of the process and the fact that the compound formation/ sputtering is a reversible process. This is a good indicator that the process can be easily controlled, around the specified working parameters, so that the properties of the obtained thin films are tunable in a certain range. The problem that remains is to identify the specific interval of reactive gas flow variation that is most appropriate for tuning the properties of the obtained thin films.

By analyzing the variation of the emission lines as a function of F_R, one can see that there are subtle changes in the slopes of the curves. These changes can be better exploited and visualized by using the derivatives of those curves, as it was initially proposed in [6]. Indeed, by registering a larger number of data points on a specific interval, F_R 0 to 50%, the derivatives of the line intensity variation curves were computed and are represented in Fig. 4. The curves were normalized, so that the values represent the percentage of line intensity variation corresponding to 1 % variation of the control parameter F_R. By using this type of representation certain features can be identified as follows: constant value over an interval represents stable process with low reactivity, the variation of F_R only leads to linear variation of line intensity; increasing absolute value of the derivatives represents transition towards a more dynamic state with higher reactivity, whereas decreasing absolute value signifies transition towards lower reactivity; the extreme values, either positive or negative, indicate that at that specific F_R the process is very sensitive to small changes and potentially unstable.

Using the above-mentioned features that define the reactivity of the process, 4 intervals were identified in the process window corresponding to F_R between 0 and 50 %, as follows:

- 0 to 5 %, mainly surface related processes, with pronounced variation of Si emission and N emission lines. The reactive gas is mainly consumed to form compound on all surfaces.

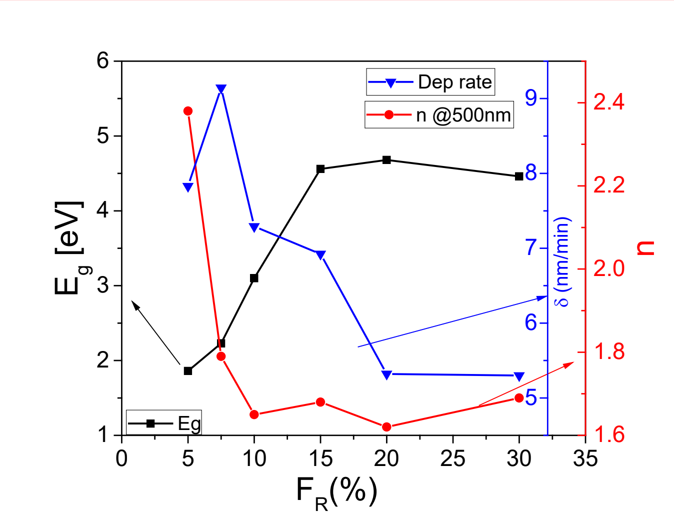

Fig. 5. Variation of deposition rate, band gap and refractive index of the samples deposited in the F_R interval from 5 to 30%

- 5 to 15 % decrease of Si emission line variation slope, coupled with increase in the variation rate of nitrogen lines. The volume related process become more important, variations of the F_R affecting mainly the gas composition. At F_R = 15 % the variation rate of emission lines corresponding to gas species, Ar and N, are at their maximum absolute value, suggesting that their concentration is very sensitive to small changes of F_R.
- 15 to 30 %, all the variation rates decrease, in absolute values, indicating a transition towards an equilibrium state.
- > 30 %, all variation rates become quasi-constant, indicating that an equilibrium state was established. Further increasing the reactive gas flow only influences linearly the gas composition, directly through the replacement of Ar with N_2 in the gas flow.

In order to test the validity of the identified process intervals, thin film deposition was performed for F_R values comprised between 5 an 30%. The parameters evolution related to film properties, such as deposition rate, band gap and refractive index are shown in Fig. 5. Those evolution showed indeed that the interval from 5 to 15 is the one that is characterized by the widest variations of the investigated parameters. Also, the deposition rate decreases in this interval and continues to decrease only up to 20 % F_R, becoming stable in the interval from 20 to 30 %. The obtained thin film band gap is increasing from 1.86 eV to 4.68 eV in the variation interval from 5 to 20 %, with a more pronounced variation between 5 and 15 %. For higher nitrogen flow ratios of 30 %, the measured band gap reach up a maximum around ~ 4.5 eV, approaching the values of bulk silicon nitride of 5.3 eV [9]. The variation of refractive index is also more pronounced in the interval from 5 to 15%, remaining almost constant for F_R values between 10 and 30 %.

2.1.2 Case study for CuOx, tuning the oxidation state

The second case study is related with the sputtering of Cu in Ar and Ar/O_2 gas mixture. The specific experimental conditions for this study are the following: I_{DC} = 150 mA, pumping section fixed so that the Ar pressure to be 0.67 Pa at 5 sccm Ar gas

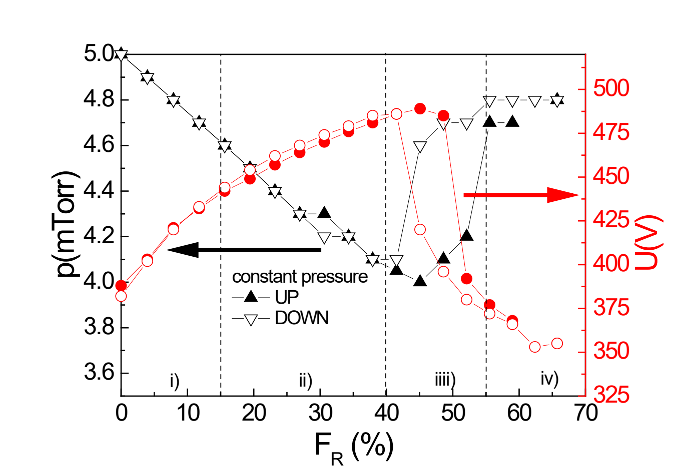

Fig. 6. Hysteresis behaviour of target cathode voltage and total pressure, I_{DC}=150 mA, P_{total}=5 mTorr for "plasma off" conditions

flow, total gas flow adjusted so that the total pressure remains constant at 0.67 Pa when the plasma is off [7]. Reactive gas flow ratio is varied in the interval of 0 to 70 %, starting from metallic mode and successively increasing then decreasing it. The hysteresis behavior was observed in this case by first increasing and then decreasing the reactive gas flow. The overall effect on the averaged parameters, such as total pressure and target voltage can be seen in Fig. 6. The typical emission spectrum of Cu sputtering plasma in pure argon, F_R = 0 % and Ar/O_2 gas mixture with 40 % oxigen in total gas flow, F_R = 40 %, were analyzed, identifying some of the representative emission lines. Their evolution only confirms the trends observed in Fig. 6, and is discussed in detail in [7]. For this particular case, with very pronounced hysteresis effect, the process intervals can be deduced using only the averaged parameters.

Indeed, from this representation it is clear that a hysteresis interval is identifiable in the interval between 40 and 55 % of reactive gas flow. Moreover, at least 4 process intervals were identified, by coupling the evolutions of all the registered parameters, as follows:

- F_R from 0 to 15 %, quasi metallic mode with pronounced decrease of total gas pressure and increase of voltage. Most of the reactive gas introduced in the process chamber is consumed by oxide formation due to the fresh layer of copper deposited on all surfaces.
- F_R from 15 to 40 %, the tendencies continue, with a slight change of slope. The compound formation gradually occurs also on the target surface.
- F_R from 40 to 55 %, represents the interval where Hysteresis occurs. Abrupt changes in all parameter's evolutions occur, indicating the changing to a fully oxidized target surface. Upon decreasing the reactive gas flow, the total pressure is significantly higher, due to the decreased reactive gas consumptions on the already oxygen saturated surfaces.
- For F_R > 55 %, a fully poisoned regime occurs when all the surfaces exposed to sputtering plasma are being covered with an oxide layer.

Following the identification of these process intervals, thin film deposition was performed for a selected number of process conditions. The Oxygen flow rate was varied in the interval from 0.6 to 3 sccm, yielding

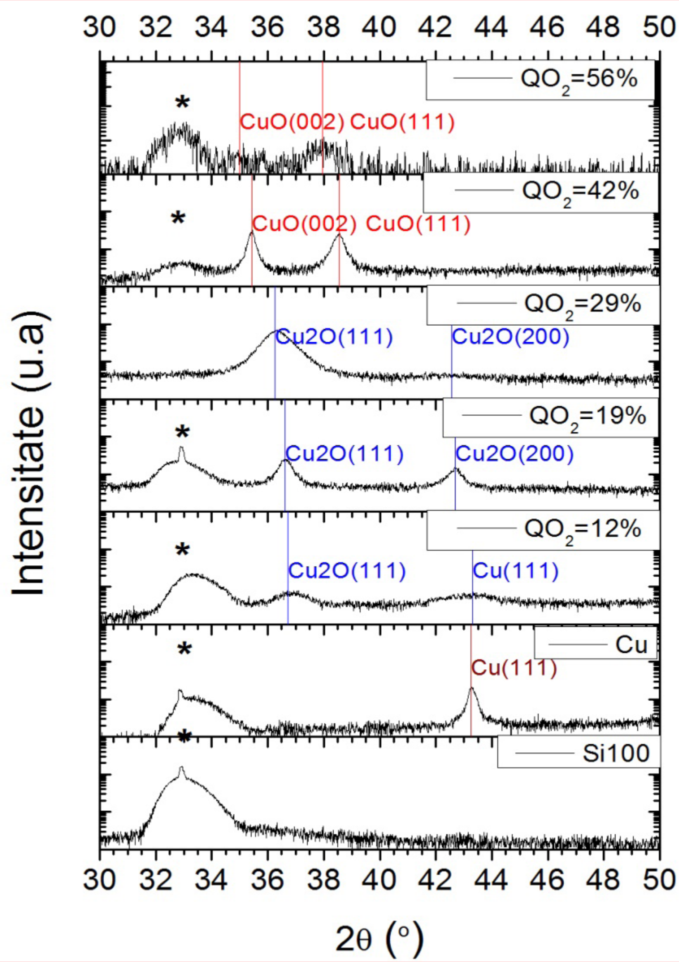

Fig. 7. XRD diffractograms of samples obtained at different oxygen flow rate. The discharge current was kept constant at 15 mA, the Ar flow was adjusted so that the total pressure (without plasma) remains constant at 0.67 Pa

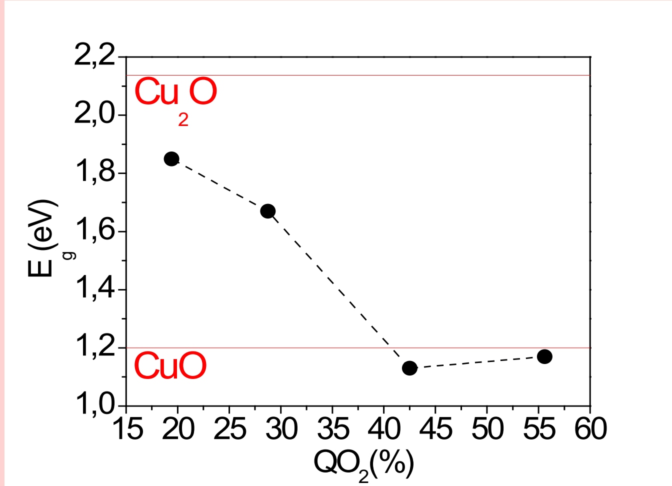

Fig. 8. Band gap variation of CuOx sample obtained at different oxygen flow rates

the following values of F_R: 12, 19, 29, 42 and 56 respectively.

The coatings deposited on Si (100) substrates were investigated by XRD, identifying the peaks using the following standards: CuO (ICDD no.04-015-5869), Cu_2O (ICDD no.04-003-6433) and Cu (ICDD no.04-0836). The main features identified by analysing the XRD patterns, were represented in Fig. 7 and indicate that at low oxygen flow rate F_R = 12 % a mixture of Cu and Cu_2O is formed, due to insufficient oxygen content. By increasing the Oxygen flow ratio to 19 and then 29 %, the Cu peak vanishes, gradually being replaced by Cu_2O phases. These values correspond to the second process interval ii), identified in Fig. 6. Further increasing the Oxygen flow ratio, and approaching the limit of the hysteresis interval at F_R = 42 %, leads to a significant change in the structure of the coatings, with the formation of CuO phase. This transition is in good agreement with the process intervals presented in Fig. 6. The optical and band gap properties were also evaluated for the same samples. Using the absorption coefficient of the CuO_x coatings on glass substrates and employing the Tauc algorithm [10], the band gap values were extracted and represented in Fig. 8. The sample obtained at F_R = 12 % could not be analyzed due to the high Cu content and its corresponding reduced transparency. For the other samples, a good correlation with the XRD results could be observed. The band gap values for samples obtained at F_R = 42 % and 56 % respectively are very close to the one of CuO. As for the Cu_2O samples, the values are slightly smaller than the theoretical ones, probably due to incomplete oxidation and presence of some phase mixing for these samples.

2.1.3 Case study for TaO_xN_y, tuning 2 reactive gases process

The last case study refers to the processes involving two reactive gases, namely oxygen and nitrogen, for the deposition of oxynitride thin films. Such a process is more complex than the previously described, since each of the reactive gas contributes with different reactivity to the overall process. The process that will be described in the following section implies the sputtering of Ta target in an $Ar/N_2/O_2$ gas mixture, for the deposition of TaO_xN_y thin fims with tunable composition and properties. The specific parameters for this process were: constant DC power applied to the target P_{DC} = 150 W, constant pumping speed ensuring 5 mTorr of Ar pressure at a gas flow of 5 sccm, constant Ar gas flow at 5 sccm.

As for the other cases, emission spectra of Ar, Ar/N_2 and Ar/O_2 gas mixture plasmas were recorded, and the specific emission

Fig. 9. Evolution of various process parameters when increasing and the decreasing the reactive gas flows. P_{DC}= 150 W, Q_{Ar}= 5 sccm, Q_{O2}/Q_{N2} = 2.5

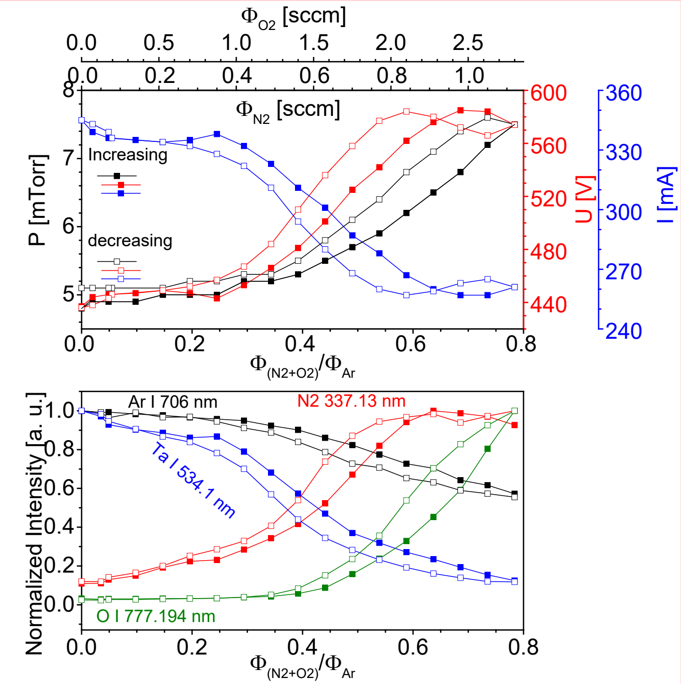

lines were identified. The chosen emission lines to be followed for describing the process are: l = 337.13 nm N_2 line, l = 534.1 Ta line, l = 706 nm Ar line and l = 777.19 O line. The hysteresis behavior was investigated individually for each of the reactive gas, in a similar way as described in the previous sections. The Nitrogen process revealed to be less reactive, with no visible hysteresis effect. In order to identify the most reactive conditions the derivative of the intensity variation vs gas flow was used, as described in section 2.1.1. The flow of 1 sccm of N_2 and 4 sccm of Ar correspond to the most reactive conditions. For the Ar/O_2 gas mixture a hysteresis interval was observed in the interval from 1.8 to 3 sccm of O_2. The most reactive process conditions were identified for an oxygen flow of 2.5 sccm. Starting from the features identified for the single reactive gas processes, one can proceed with the characterization of the process that involves the simultaneous use of two gases (O_2 and N_2). The content of oxygen and nitrogen in the thin films would be controllable by the independent variation of the flow of each reactive gas. This approach can lead to a complex experimental situation, where two independent parameters can be coupled by the phenomena occurring on the surfaces and in the plasma volume. In order to simplify the experimental procedure, we propose the use of one control parameter, namely the sum of the reactive gas flows. Supplementary, in order to account for the different reactivities of the two gasses, the ratio between the reactive gas flow is kept constant at 2.5, i.e. the ratio between the flows identified in the single

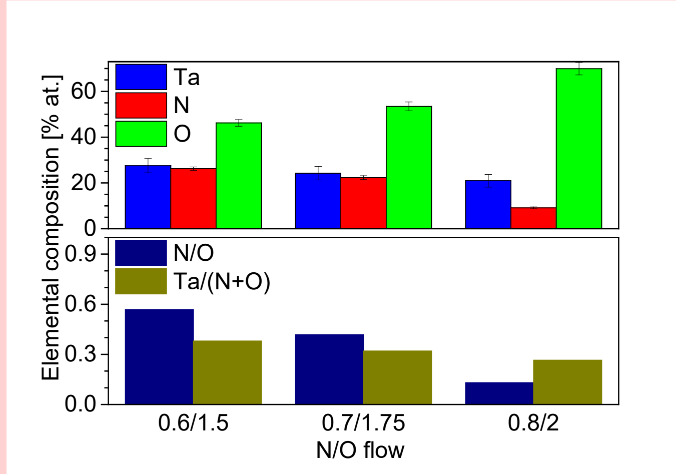

Fig. 10. Variation of elemental composition of TaO_xN_Y thin films and N/O and Ta/(N+O) ratios as a function of reactive gas flows

reactive gas processes as the most reactive conditions. The evolution of process parameters, pressure voltage current and emission line intensities is represented in Fig. 9, corresponding to an increase followed by a decrease of reactive gasses total flow. The hysteresis interval, seen on all the investigated parameters, is placed between 30 and 60 % proportion of reactive gas flow. The individual flows of each gas are much smaller than the ones identified for single gas processes, due the addition of surface contamination from both reactive gasses. The hysteresis interval is well defined, having all the main characteristics described for the single gas processes: current intensity decrease/ voltage increase, decrease of Ta emission line and increase of O an N emission lines.

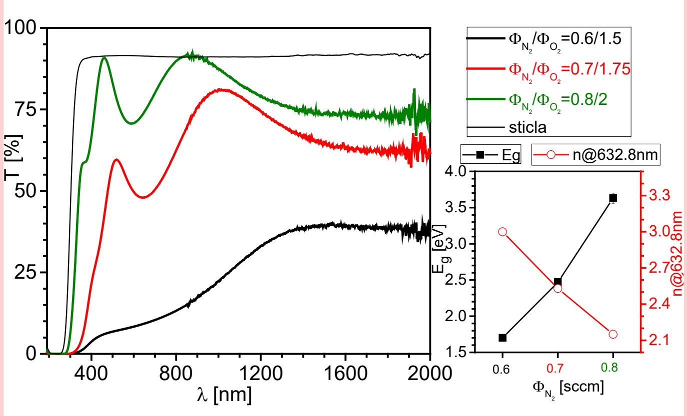

Fig. 11. Evolution of optical properties as a function of reactive gas flow. PDC=150W, QAr= 5 sccm

By applying the experimental procedure previously described it is possible to identify the process interval that would yield tunable properties for TaO_xN_y thin films. The films were deposited on glass and Si (100) substrates at three experimental conditions inside the hysteresis interval, corresponding to the nitrogen flows of 0.6, 0.7 and 0.8 sccm and oxygen flows of 1.5, 1.75 and 2 sccm.
The variation of thin film composition and the ratios of N/O and Ta/(N+O), evaluated by EDX, is represented in Fig. 10. The proportion of Ta is decreasing as the reactive gas flow is increasing, being replaced with the atoms of O and N respectively. The N to O ratio in the film composition decreases by a factor of 50 %, indicating a preferential addition of oxygen in the films. Although the gas flow ratio remains constant, the content of each element in the thin film is different, due to different reactivities of the two gases. The changes in the film composition leads to changes of their optical properties as well. The optical transmission curves, represented in Fig. 11, indicate a pronounced change in the absorption edge as a function of composition. The optical band gap variation, evaluated using the Tauc procedure, is represented in the inset of Fig. 11, together with the refractive index at 632.8 nm. The evolution of both parameters indicates a large interval of variation, between 1.7 and 3.2 eV for the bandgap (a factor of 2) and between 2.1 an 3 for the refractive index. This type of quasi linear variation was obtained by changing only the gas composition, following the experimental procedure previously described.

Acknowledgements

Funding by: the Romanian National Authority for Scientific Research, UEFISCDI, through project PN09-270203; Romanian Ministry of Research and Innovation, projects PN 16.40.01.01, PN 16.40.01.02, PN 18N/2019 and PROINSTITUTIO Project – contract no. 19PFE/17.10.2018.

References

[1] J. Rentsch, J. Jaus, K. Roth and R. Preu, Conference Record of the Thirty-first IEEE Photovoltaic Specialists Conference, 2005., Lake Buena Vista, FL, USA, 2005, pp. 931-934, doi:0.1109/PVSC.2005.1488284.

[2] J. Musil, P. Baroch, J. Vlček, K.H. Nam, J.G. Han, Thin Solid Films, **475** 1-2 (2005)
[3] I. Safi, Surface and Coatings Technology **127**, 2–3, (2000)
[4] S. Berg, H.-O. Blom, M. Moradi, and C. Nender, Journal of Vacuum Science & Technology A **7**, 1225 (1989)
[5] K. Strijckmans, R. Schelfhout, and D. Depla, Journal of Applied Physics **124**, 241101 (2018)
[6] I. Pana, C. Vitelaru, N.C. Zoita, M. Braic, Plasma Processes and Polymers, **13** (2016)
[7] C. Vitelaru, I. Pana, A.E. Kiss, N.C. Zoita, A. Vladescu, M. Braic, Journal of Optoelectronics and Advanced Materials, **21** (2019)
[8] G.Zambrano, H.Riascos, P.Prieto, E.Restrepo, A.Devia, C.Rincón, Surface and Coatings Technology, **172**, 2–3, (2003)
[9] G. Sasaki, M. Kondo, S. Fujita, A. Sasaki, Jpn. J. Appl. Phys. **21**, 1394, (1982)
[10] J. Tauc, Amorphous and liquid semiconductors, Plenum Publishing Corporation, **159**, 1974.

*Corresponding author: catalin.vitelaru@inoe.ro

CHAPTER III

Optoelectronics and optospintronics- emergent phenomena, materials and applications

Plasmonics, spintronics and label-free spectroscopies - lessons to be learned for interspecies discrimination

C. RIZEA[a], A-M. IORDACHE[b], S. M. IORDACHE[b], A. SOBETKII[c], C.N. ZOITA[b], C. R. STEFAN[b], C. GIUGLEA[d], A. MAZLUM[a], V. BARNA[e], L. TORTET[f], A. TONETTO[g], R. NOTONIER[f], M. MILITARU[h], C.E.A. GRIGORESCU[b]

[a]ROXY VETERINARY S.R.L. Magurele, Romania
[b]National Institute of R&D for Optoelectronics, INOE 2000, 409 Atomistilor Str., 077125, Magurele, Jud. Ilfov, Romania
[c]SC MGM STAR CONSTRUCT SRL, 7 Pancota Str., Building.13, Ap.19, Bucharest, 022773, Romania
[d]University of Medicine and Pharmacy Carol Davila, Bucharest, Romania
[e]University of Bucharest, Faculty of Physics, 405 Atomistilor, P.O. Box MG-38, 077125, Magurele, Romania
[f]Aix-Marseille Universitè, MADIREL & [g]Centrale Marseille, CNRS, Federation Sciences Chimiques Marseille – PRATIM, France
[h]Faculty of Veterinary Medicine-University of Agronomic Sciences and Veterinary Medicine, Bucharest, Romania, Splaiul Independentei, no. 105, sector 5, Bucharest, Romania.

Abstract. Discrimination of meat species is an important on-going research aimed at developing a simple and non-destructive method for evaluating basic food products and establishing their composition. Mislabeling and substitution of various meats, common fraudulent practices in the food industry have induced consumer demands for reliable and safe meat products. In this paper we present a short overview of the optical means (UV-Vis spectroscopy, FT-IR spectroscopy and Raman spectroscopy) for sample investigation to assess interspecies discrimination.

Keywords: plasmonic, spintronic, label-free spectroscopy, interspecies discrimination.

1. Introduction

When analyzing biological specimens it is important to use non-invasive and non-destructive means of investigation. Most optical measurements techniques provide a wide and gentle way of interaction with biomolecules while offering the potential for fast and reliable procedures for *in vivo* diagnostics [1]. Label-free molecular detection is the most important landmark in biochemical sciences. Researchers focus on exploiting localized surface plasmon resonances in metallic nanostructures, which are expected to have enormous impact on single-molecule detection. Metallic nanostructures are easily synthesized and due to their nanoscopic volume and high sensitivity to the local environment are perfect for label-free single-molecule detection [2,3].

Discrimination of meat species is an important on-going research aimed at developing a simple and non-destructive method for evaluating basic food products and establishing their composition. Mislabeling and substitution of various meats, common fraudulent practices in the food industry have induced consumer demands for reliable and safe meat products [4]. Romania was at the heart of an international food security issue in 2013 when Findus food retailer and Spanghero food producer accused two Romanian meat suppliers of substituting beef meat with horse meat [5]. Current technologies for meat speciation are expensive, time consuming and labor-intensive. In this paper we present a short overview of the optical means (UV-Vis spectroscopy, FT-IR spectroscopy and Raman spectroscopy) for sample investigation to assess interspecies discrimination.

2. Experimental

2.1. Fe_3O_4/Au core@shell synthesis

Fe_3O_4/AuNPs core@shell were prepared using reverse micelle synthesis. The Fe_3O_4 particles were dispersed in deionized water and the solution was mixed with polysorbat (Tween 20). The reverse micelle were formed by adding AuNPs dispersed into lavender oil. The obtained solutions were vigurously mixed in an ultrasonic bath. Ethanol (97%) and a magnet were used to separate the magnetic particles from the solution. The Fe_3O_4/AuNPs core@shell particles were dispersed into deionized water and fluorescein 5% was added.

2.2. Delivery of Fe_3O_4/Au core@shell in the *ex vivo* samples

Different types of samples (all layers of skin, fat, muscle and tumor tissue) were obtained from pet patients and were directly injected with 100 μL of Fe_3O_4/AuNPs core@shell particles. A detailed table of all the samples is presented in Table 1.

3. Results

The samples were investigated using UV-Vis spectroscopy and FT-IR spectroscopy. Fig.1. shows the traces of blood vessels

Fig. 1. Section through the skin showing the tracing of the blood vessels

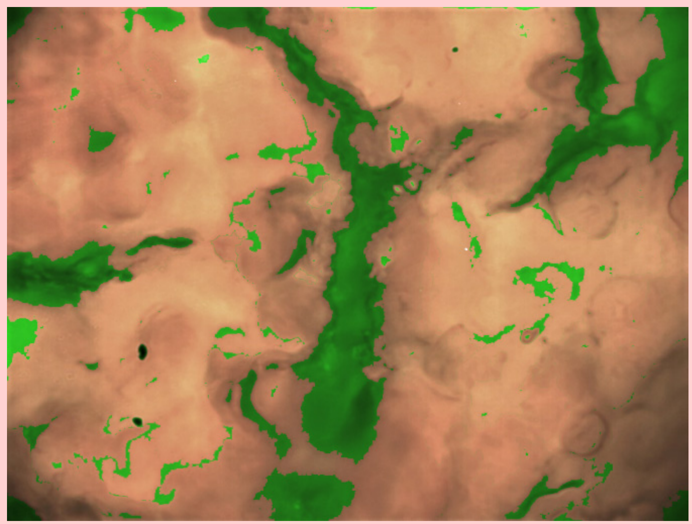

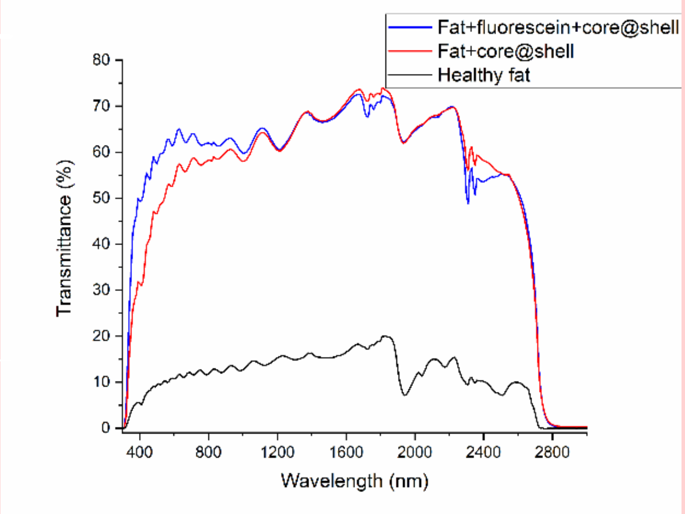

Fig. 2. Optical transmittance of the fat layer with and without fluorescein and Fe_3O_4/AuNPs core@shell

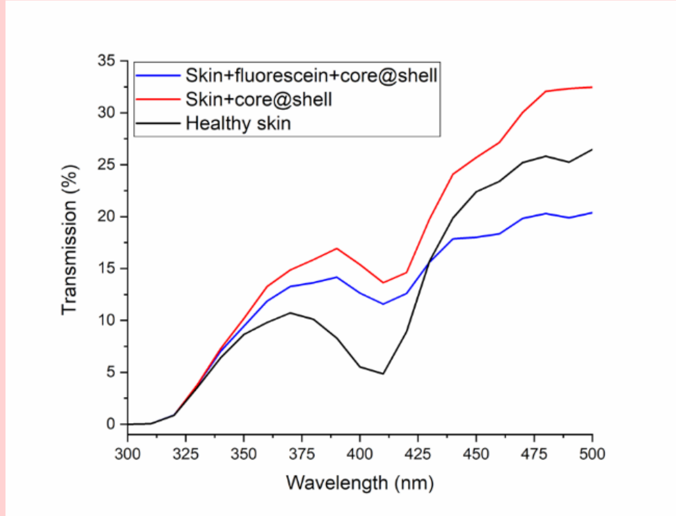

Fig.3. Optical transmittance of the skin layer with and without fluorescein and Fe_3O_4/AuNPs core@shell

when irradiated with UV light at 325 nm. Using fluorescein allows the visualization of blood vessels by sending photons through the vessel wall. UV-Vis spectroscopy revealed the optical optical transmittance of the fat layers with and without the Fe_3O_4/AuNPs core@shell particles.

The optical characteristics of the skin with and without the nanoparticles have been investigated using UV-Vis spectroscopy and FT-IR. Fig.2 and Fig.3 support our hypothesis that the use of these nanoparticles enhance the transmission of light (at specific wavelengths) through the upper level of the skin. This results has a direct impact for example in bariatric surgery, where the surgeon can easily see the blood vessels under the skin.

In the table below (Table 1) we present all the samples that were investigated. We define the absorption coefficient as the percentage of absorption per µm and calculate it for Λ=410 nm using the formula:

Abs coefficient=abs$_{(\Lambda 410\ nm)}$*100/sample thickness (1)

It is important to see that the highest absorption for 410 nm is observed for healthy epidermis (also the absorption coefficient is the highest among all the samples) and for healthy epidermis+dermis+sub-cutaneous connective tissue while the lowest is observed for the tumor tissue and lymph node with fluorescein and core@shell.

Table 1. List of all the samples under investigation and the main characteristics resulted from UV-Vis spectroscopy

Sample name	Sample thickness (µm)	Abs la $\lambda_{410\ nm}$ (a.u.)	Absorption coefficient (%/µm)
S1-lymph+F&CS	160	0.01149	0.00718125
S2-lymph+CS	120	0.03055	0.025458333
S3-tumor+F&CS	110	0.00996	0.009054545
S4-tumor+CS	140	0.01487	0.010621429
S5-fat+F&CS	140	0.02315	0.016535714
S6-fat+CS	190	0.05711	0.030057895
S7-skin+F&CS	250	0.12785	0.05114
S8-skin+CS	220	0.15538	0.070627273
S9-breast+F&CS	1220	0.04247	0.003481148
S10-breast+CS	230	0.11438	0.049730435
S11-epidermis	260	0.49729	0.191265385
S12-epi+dermis	290	0.06497	0.022403448
S13-epi+der+con	330	0.25908	0.078509091
S14-con	500	0.04346	0.008692
S15-fat	490	0.08248	0.016832653

Surface enhanced Raman scattering (SERS) occurs when surface plasmons of metal micro or nanostructures are resonantly excited by incident monochromatic light [6,7,8] and the biological material deposited onto such substrates provide high intensity Raman signals. Other benefits include higher spectral resolution and shortening of collection times. Cu, Ag and Au are the best known substrates for SERS, but practically any rough metal surface could serve as a SERS substrate. Copper is not a good material to be used in surgery since it can be easily oxidized. Noble metals are an appropriate choice for SERS substrates, but they are expensive-few could afford a blade made out of gold. We choose the surfaces of the stainless steel blades used in surgery, which are not optically flat and can be used as primary SERS substrate. Forensic science needs precise identification of traces through non-destructive analysis. Food safety as well needs precise identification of components in food products to limit counterfeit products and to protect consumers' health. Commonly, there are several techniques that are employed to discriminate between various traces, each one of them involving specific chemical tests for specific samples (genomic DNA for meat and meat bone [9], protein markers [4] and lectin panels [10]). However, Raman spectroscopy appears as an ideal technique for both food safety and forensics. Some important advances have been reported especially in body fluid recognition and meat quality assessment using tissue analysis [11]. As we can see in oncologic surgery issues, extending the spectral ranges provides more detailed information for meat analysis and fluid and tissue recognition, such as the presence of fat of either human or animal origin. Fat molecules are present everywhere: in the skin, fingerprints, blood stains, tissues. In our previous work, we investigated the effect of the spin-plasmonic through label free SERS measurements on *ex vivo* fragments of animal tissue slices of mammary tumours and mastocytoma [1]. The samples were procured as slices of about 500 micrometres thick, which were immobilized onto stainless steel surgical blades acting as substrates and investigated by normal Raman spectroscopy. Previously, the substrates have been modified with Au-magnetite and Ag-magnetite. Since our previous works [1,2] showed that peaks in the region of OH^- stretching could be considered "tumour marker" our aim was to enhance those peaks. Consequently, careful processing of the ~3311 cm^{-1} peak shows a 3 fold increase for the sample with Au coated magnetite compared with the samples with single magnetite and Ag coated magnetite [1]. The explanation we propose for this enhancement could be the incoherent spin pumping induced by the laser irradiation at the magnetite-gold interface. A thermal non-equilibrium state at the interface of ferromagnetic/paramagnetic materials can diverge the magnons in magnetite (our ferromagnet) and the electrons in gold from their equilibrium state and induce a spin current at the interface. Moreover, since the intensity of the Raman spectrum depends proportionally on the number of scattering centres, we can use it to quantitatively assess the cross-section of our sample. The reasoning behind using fluorescein together with magnetite and magnetite/gold core shell is to reveal the underlying blood vessels. As it is presented in fig.3, the upper layer of the skin shows few modifications due to the absorption of metallic nanoparticles, whereas the lower levels which have blood vessels are revealed in the Fig.1.

4. Conclusion

Our work has concluded that SERS is an important tool for nearly "real time" diagnostic in veterinary oncologic surgery as well as in food science and forensics research. Extending the spectral range up to 4000 cm^{-1} provides information about the type of fats and OH^- vibrations, both useful information for a negative surgical margins diagnostic and inter-species discrimination. Using nanostructured surfaces based on noble metals as SERS substrates removes/eliminates the auto-fluorescence shown if the samples were laid on glass substrates. There were no chemical interaction between the samples and the Ag and Au nanostructered substrates; this leads us to believe that in our experiments the scattering enhancement is of electromagnetic origin only.

We are currently working on the identification of different types of tissues in some sausage samples (raw, smoked and double smoked variation of sausages). In Fig.4 it is shown the confocal images of some of the types of tissues we find in these type of food products (muscle, fat and probably some skin). It is an ongoing research where we are trying to assess the species that provided the meat for these sausages.

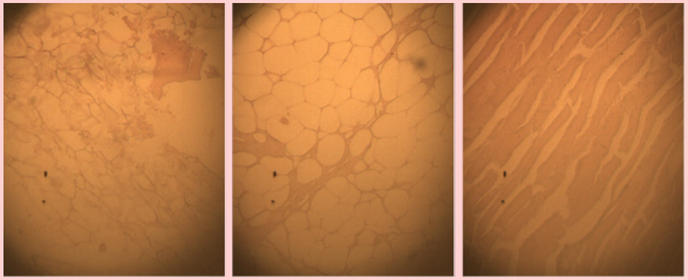

Fig.4. Different types of tissues in a sausage sample (skin, fat and muscle)

Acknowledgements

This work was supported by a grant of the Romanian Ministry of Education and Research, CNCS - UEFISCDI, project number PN-III-P1-1.1-PD-2019-1134, within PNCDI III, CORE Programme, Ctr. 18/N/2019 and Contract nr.19PFE/17.10.2018 financed by Ministry of Research and Innovation.

References

[1]. C. E. A. Grigorescu, A-M. Iordache, M. I. Rusu, C. R. Stefan (Iordanescu), S. M. Iordache, C. Rizea, T. Soare, M. Militaru, A. Diaconescu, L. Tortet, A. Tonetto, and R. Notonier, Spin Plasmonics and Surface Enhanced Raman Spectroscopy in Label Free Biomolecular Sensing , IEEE Xplorer ICTON, 181714 (2019).

[2]. C. Micsa, C. Rizea, M. I. Rusu, N. D. Becherescu-Barbu, R. Munteanu, M. V. Udrea, B. Chiricuta, A. Parau, A. Tonetto, R. Notonier, I. A. Birtoiu, C. E. A. Grigorescu, Surface Enhanced Raman Scattering in Surgery and Forensics, ICTON (2016).

[3]. A-M. Iordache, C. Rizea, C. Giuglea, C.N. Zoita, I. Stamatin, S. M. Iordache, C. R. Stefan (Iordanescu), M. I. Rusu, L. Tortet, A. Tonetto, R. Notonier, C. E. A. Grigorescu, Preparation and study of core shell Fe3O4/Au nanoparticles for traceability of blood vessels and biosensing by surface enhanced Raman spectroscopy, ICTON (2020).

[4]. G.D. Kim, J.K. Seo, H.W. Yum, J.Y. Jeong, H.S. Yang, Protein markers for discrimination of meat species in raw beef, pork and poultry and their mixtures, Food Chemistry 217, 163–170, (2017).

[5]. https://www.zf.ro/eveniment/procesatorii-romani-acuzati-au-transformat-hartie-carne-cal-carne-vita-diferenta-pret-intre-cele-doua-1-5-euro-kilogram-romania-exporta-carne-cal-13-mil-euro-an-mult-vita-10553932, accessed on 30 October 2020.

[6]. H. E. Toma, V. M. Zamarion, S. H. Toma, K. Araki, The Coordination Chemistry at Gold Nanoparticles, J. Braz. Chem. Soc., Vol. 21, No. 7, 1158-1176, (2010).

[7] S. Moraes Silva et al.: Gold coated magnetic nanoparticles: from preparation to surface modification for analytical and biomedical applications, Chem. Commun., 52, 7528 (2016).

[8]. Birtoiu IA, Rizea C, Togoe D, Munteanu RM, Micsa C, Rusu MI, Tautan M, Braic L, Scoicaru LO, Parau A, Becherescu-Barbu ND, Udrea MV, Tonetto A, Notonier

R, Grigorescu CEA, Diagnosing clean margins through Raman spectroscopy in human and animal mammary tumour surgery: a short review, Interface Focus: 6, 20160067 (2016).
[9].Y. Han, X. Wang, Y. Liu, L. Han, Z. Yang, X. Liu, A novel FTIR discrimination based on genomic DNA for species-specific analysis of meat and bone meal, Food Chemistry 294, 526–532 (2019).
[10].J. Carlsson, F. Winquist, B. Danielsson, I. Lundstrom, Biosensor discrimination of meat juice from various animals using a lectin panel and ellipsometry, Analytica Chimica Acta 547, 229–236 (2005).
[11].Jean-Louis Damez and Sylvie Clerjon, Meat quality assessment using biophysical methods related to meat structure, Meat Science 80, 132–149 (2008).

*Corresponding author: ana.iordache@inoe.ro

Synthesis and complex characterization of a zinc phosphate-tellurite glass as Faraday rotators

M. ELISA[1*], S. M. IORDACHE[1], A-M. IORDACHE[1], I. C. VASILIU[1], B. A. SAVA[2], L. BOROICA[2], M. C. DINCA[2], A. V. FILIP[2], A. C. GALCA[3], C. BARTHA[3], V. KUNCSER[3] AND M. EFTIMIE[4]

[1]National Institute of R & D for Optoelectronics, INOE 2000, 409 Atomistilor Str., 077125, Magurele, Jud. Ilfov, Romania
[2]National Institute for Laser, Plasma and Radiation Physics, 409 Atomistilor Str., 077125, Magurele, Jud. Ilfov, Romania
[3]National Institute of Materials Physics, 405 A Atomistilor Str., 077125, Magurele, Jud. Ilfov, Romania
[4]University Politehnica of Bucharest, 313 Spl. Independentei, Bucharest, Romania.

Abstract. This work explores the structural, thermal, optical, magnetic and magneto-optical properties of a novel zinc phosphate-tellurite glass belonging to the $40ZnO$-$10Al_2O_3$-$40P_2O_5$-$10TeO_2$ system. The glass was synthesized by a wet method of processing the reagents followed by melting–quenching–annealing. Properties such as thermal expansion coefficient, characteristic temperatures, optical transmission, optical band gap, refractive index, magnetization and magneto-optical Faraday effect have been presented. Magnetic and magneto-optical measurements reveal the diamagnetic character of the TeO_2-doped glass associated with the decreasing of the positive Faraday rotation angle with wavelength. The final product is a mixture of a non-crystalline vitreous phase and Te-based nanoclusters.

Keywords: phosphate glass, tellurite glass, optical absorption, diamagnetic material, magneto-optical effect

1. Introduction

The tellurite glasses can be arranged into high-TeO_2 content compositions (50 mol. %) having application in lasers, optical fibers, amplifiers [1-6], and into low-TeO_2 content compositions where this oxide is added as dopant [7-10].
The tellurite glasses doped by rare-earth elements are characterized by low energy phonons [1, 11-16] and the un-doped tellurite glasses show luminescence properties as well [2].
These vitreous materials of various compositions (zinc oxide, phosphate, vanadate, borate, etc.) show a NIR broadband emission and a lifetime of tens of microseconds, being successful materials for producing broadband amplifiers, optical fibers, windows, lenses or tunable lasers in visible (Vis) [3-6,17-19] or in infrared (IR) domain [17,20].
Due to the high polarizability, high refractive indices and good transparency from the visible to the middle infrared domain, TeO_2-containing optical fibers and glasses have the characteristics essential for the development of performant magneto-optical (MO) components. [21-24]. The magneto-optical components

are the Faraday rotators applied in optoelectronics to prevent the reflection of the laser beam, which can disrupt the optical emission systems from the laser cavity.

2. Experimental

2.1. Methods and equipment

The X-ray diffraction (XRD) measurement was performed at room temperature (RT), in the 10–80° range, with a 0.05° step and 3 s integration time, using a Bruker D8 Advance device (CuKα, λ = 1.54056 Å), Billerica, Massachusetts, USA.

Fourier transform infrared (FTIR) spectroscopic measurements were carried out at RRTT, in the range 500–1500 cm^{-1}, using a Perkin Elmer Spectrophotometer-Spectrum 100 provided with Universal Attenuated Total Reflectance (UATR) accessory Llantrisant, UK, in transmission and universal attenuated total reflection (ATR, ZnSe/Germanium window) modes.

Raman spectra were collected at RT with a LABRAM-HR 800 Horiba Jobin Yvon spectrometer, (Montpellier, France), in the 200–1500 cm^{-1} range, by using Ar^+ laser excitation (λ = 514.5 nm).

The thermal expansion coefficient was determined by the dilatometry using a horizontal Netzsch DIL 400 PC device, NETZSCH Holding, Selb, Germany. The temperature was increased at 3 °C/min. The characteristic temperatures as well as the thermal expansion coefficient of the glass were estimated by processing the results from the thermal analysis.

The optical and magneto-optical measurements (conventional spectroscopy and transmission ellipsometry) were carried out with a Woollam Variable Angle Spectroscopic Ellipsometer, VASE (J.A. Woollam Co., Lincoln, NE, United States), equipped with a high-pressure Xenon discharge lamp (Hamamatsu Photonics K.K., Japan), incorporated in an HS-190 monochromator (J.A. Woollam Co., Lincoln, NE, United States).

The magnetic field-assisted Faraday rotation measurements were performed with the aid of a toroidal permanent magnet, and the field applied parallel to the wave-vector.

Photoluminescence emission of the zinc phosphate-tellurite glass was collected with a Horiba Jobin-Yvon Fluorolog 3 spectrofluorometer in the range 350-650 nm, at RT, by 270 nm wavelength excitation.

The magnetic behavior of the sample was investigated over a large range of applied magnetic fields by using a superconducting quantum interference device (SQUID) magnetometer (MPMS 7T from Quantum Design, USA).

2.2. Synthesis of zinc phosphate-tellurite glass

A novel zinc phosphate-tellurite glass has been prepared and investigated with regard to optical, structural, magnetic and magneto-optical properties, with application for Faraday rotators.

The vitreous material belonging to the oxide system $40ZnO-10Al_2O_3-40P_2O_5-10TeO_2$ was prepared by a non-conventional wet method of raw materials processing, followed by melting quenching-annealing of the final product [1, 2, 3].

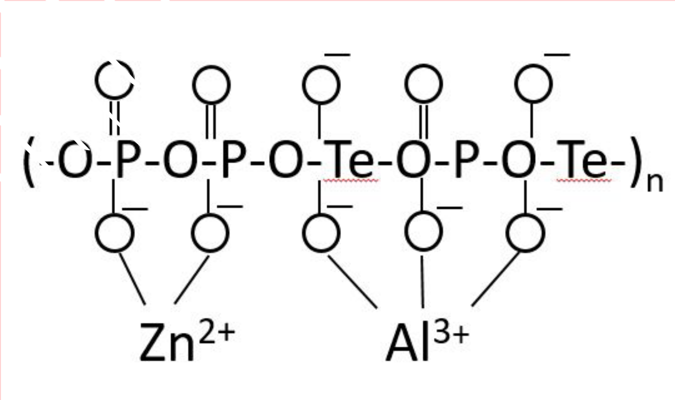

Fig.1. Structure of the zinc phosphate-tellurite glass

The starting reagents were high purity powders (99.95%): ZnO, Al_2O_3 and TeO_2 together with H_3PO_4 solution (85 wt. %). All the chemical were purchased from Sigma Aldrich Company. Mechanical stirring of the initial batch and final glass melt was applied to improve the optical and chemical homogeneity. ZnO and Al_2O_3 are vitreous network modifiers. Zinc oxide increases the glass forming tendency and Al_2O_3 improves the chemical and thermal stability of the final glass. Phosphorous pentoxide and tellurium dioxide and TeO_2 are vitreous network formers.

2.3. Structure of the zinc phosphate-tellurite glass

The structure of the zinc phosphate-tellurite glass is presented in Fig.1. The composition of the synthesized glasses was designed in order to favor the formation of the metaphosphate structure that exhibits a high chemical and thermal stability. The structure is composed of metaphosphate chains in which phosphorous atoms are replaced by tellurium atoms, forming a mixt vitreous network. The chains are formed by PO_4 tetrahedra linked by bridging oxygen atoms. The non-bridging oxygen atoms are linked by the network modifiers cations, Zn^{2+} and Al^{3+}.

2.3.1. X-Ray Diffraction analysis

In Fig.2, XRD pattern of the zinc phosphate-tellurite glass is presented. From Fig.2, it is proved an amorphous character of the explored glass.

Fig.2. XRD pattern of the zinc phosphate-tellurite glass

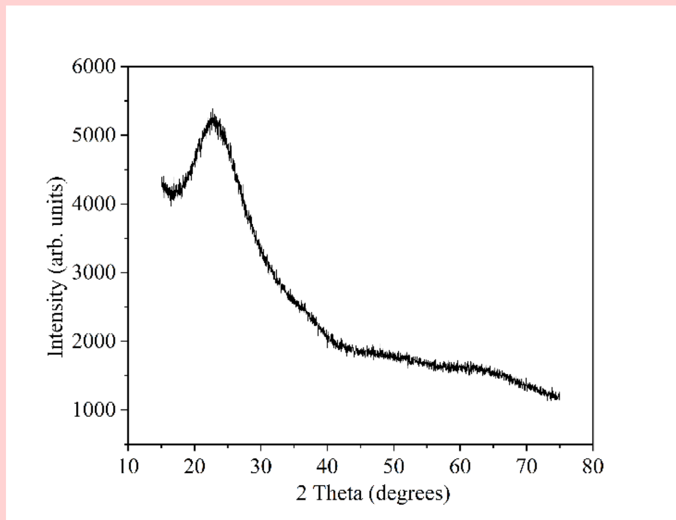

2.3.2. Fourier Transform Infrared (FTIR) Spectroscopy

FTIR analysis (Fig.3) reveals optical phonons specific to phosphate and, respectively, tellurite network. Bending (δ) and stretching (ν), symmetrical /asymmetrical vibration modes are revealed. In the range 500-750 cm^{-1} tellurite network vibration mode are prevalent whereas over 750 cm^{-1}, mainly phosphate network vibration modes are seen.Optical phonons certify the vitreous network forming role of TeO_2 and P_2O_5

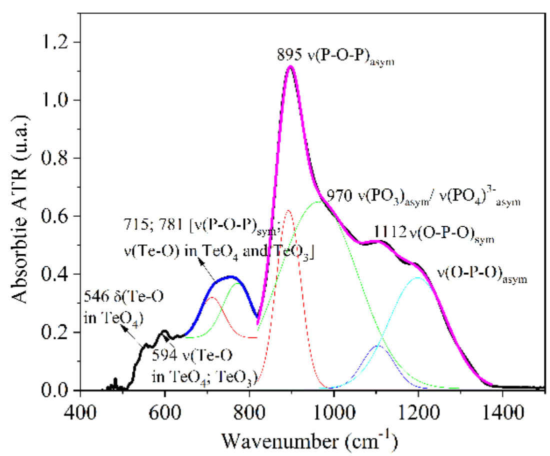

Fig.3. FTIR spectrum of the zinc phosphate-tellurite glass

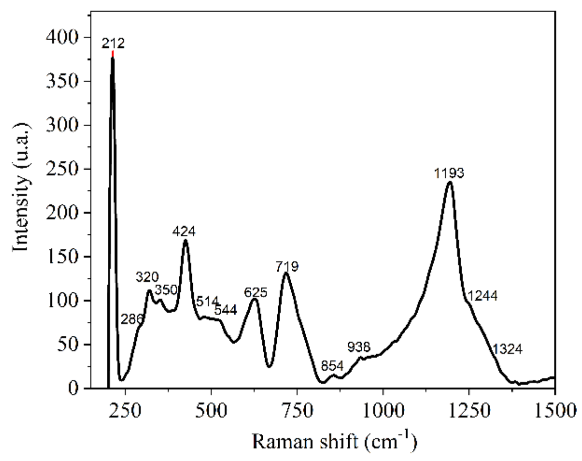

Fig.4. Raman spectrum of the zinc phosphate-tellurite glass

2.3.4. Raman spectroscopy

Raman spectrum of the zinc phosphate tellurite glass is shown in Fig.4. The attribution of Raman peaks is presented in Table 1.

Table 1. Assignment of Raman vibration modes of the zinc phosphate-tellurite glass network

Vibration modes (cm^{-1})	Assignment
212	Te_2 clusters
286; 320	δ(Te-O-Te) and ν(TeO_4, TeO_{3+1}, TeO_3)$_{sym}$ and δ(P_2O_7)$^{4-}$, δ(P-O-P), δ(O-P-O), δ(Zn-O) from ZnO_4
350; 424; 514; 544	δ(TeO_4)$_{sym}$; δ and ν(Te-O-Te) in TeO_4, TeO_{3+1}, TeO_3, Zn-O from ZnO_4, harmonics of δ(P-O-P and O-P-O)
625	δ(TeO_4 continuous network, TeO_{3+1}, TeO_3, P-O-P)
719	ν(P-O-P)$_{sym}$ in Q^2 and Q^1 units; ν(Te-O) in TeO_{3+1}, TeO_3
854; 938	ν(Te-O)
1193	ν (PO_3)$^{2-}_{sym}$ in Q^1, ν(O-P-O)$_{sym}$ in (PO_4)$^{3-}$ and in Q^2; ν(TeO_3)
1244	ν(PO_2) in Q^2
1324	ν(P=O) in long phosphate chains

From Table 1, bending and stretching vibration modes are revealed, specific to the mixt phosphate-tellurite glass.

2.4. Thermal expansion analysis

The thermal behavior of the zinc phosphate-tellurite glass was performed by dilatometry analysis. The thermal expansion behavior in the range 20-300°C is shown in Fig.5. From Fig.5, the characteristic temperatures of the investigated glass have been deduced, as follows: strain point (T_S = 429°C), transition temperature (T_g = 429°C), annealing point (T_A = 437°C) and dilatometry softening point (T_D = 453°C).

Fig.5. The dilatometry thermal expansion graph of the zinc phosphate-tellurite glass

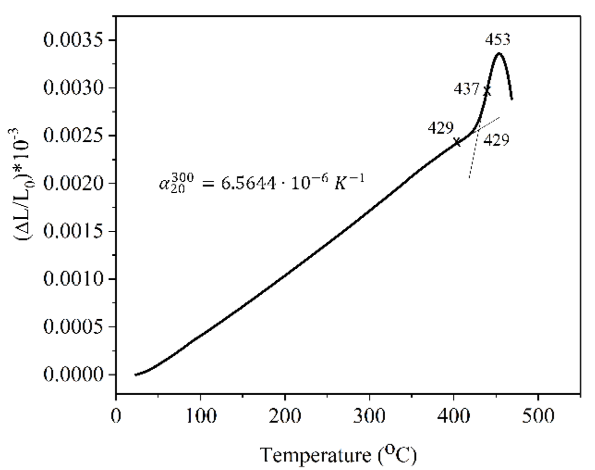

2.5. Optical properties

2.5.1. Optical absorption

Optical absorption of the investigated glass is presented in Fig.6. In Fig. 6, two absorption bands at 420 and 532 nm are noticed, specific to the electronic transitions of the Te_2 molecules that were formed as a result of TeO_2 decomposition at the melting temperature. Te_2 molecules are responsible for absorption characteristics in the visible domain. The absorption band from 432 nm is assigned to the $^3\Sigma_g \rightarrow {}^3\Sigma_u$ transition whereas the strong 532 nm absorption band is due to colloidal metallic Te [4, 7, 25–28].

The final product is a composite material comprising a non-crystalline vitreous phase and Te_2 nanoclusters, the latter giving the dark reddish color of the glass. Diatomic tellurium molecule-based nanoclusters exhibit a green absorption range, the complementary transmitted light is noticed in the red domain of the visible spectrum.

2.5.2. Optical band gap

The optical band gap of the zinc phosphate-tellurite glass was determined by a graphical method (see Fig.7), according to Mott and Davis/Tauc equation (1), as reported in [25, 29, 30].

$$\alpha h\nu = (h\nu - E_g)^n$$

Fig.6. Optical absorption of the zinc phosphate-tellurite glass

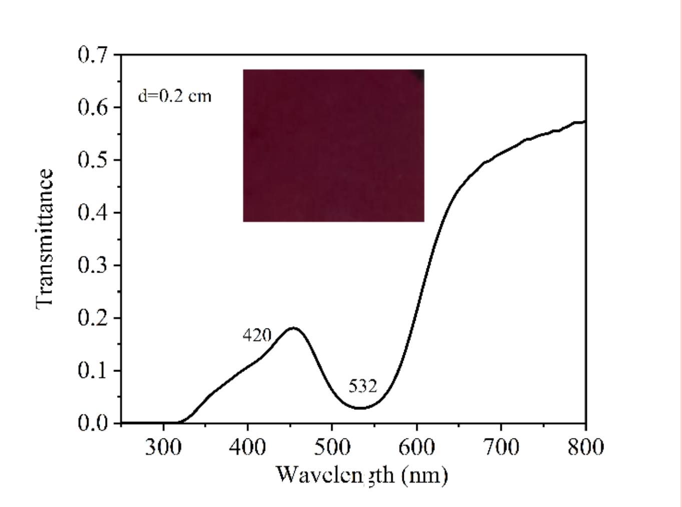

Fig.7. The graphical determination of the energy band gap, E_g.

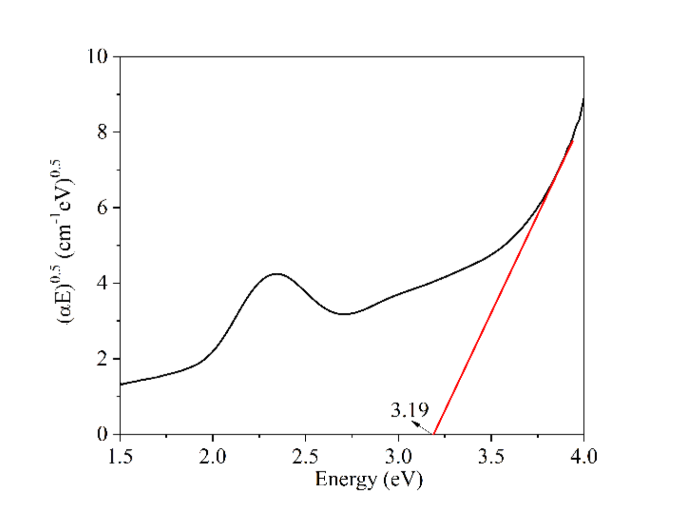

where, α is the absorption coefficient, h is the Planck constant, v is the light frequency, n is a coefficient equal to 2 for allowed indirect electron transitions from the valence to the conduction band, valid for amorphous materials From Fig.7, it was determined the value of the optical band gap, $E_g = 3.19$ eV.

2.5.3. Refractive index

In Fig.8, the dependence of the refractive index on wavelength (optical dispersion) is presented.
The refractive index of the glass is influenced by the interaction of the light with the electrons of the component atoms of the vitreous material.
The refractive index is related to the electronic polarization of the ions and the local field inside the glass. The non-bridging oxygen atoms exhibit a high polarizability, the amount of these oxygen anions determine the value of the refractive index.

2.5.4. Luminescence spectroscopy

In Fig.9, the luminescence in dependence on wavelength in the case of the zinc phosphate-tellurite glass is shown. There are noticed emission peaks in the blue domain of the visible spectrum due to Te^{4+} ions.

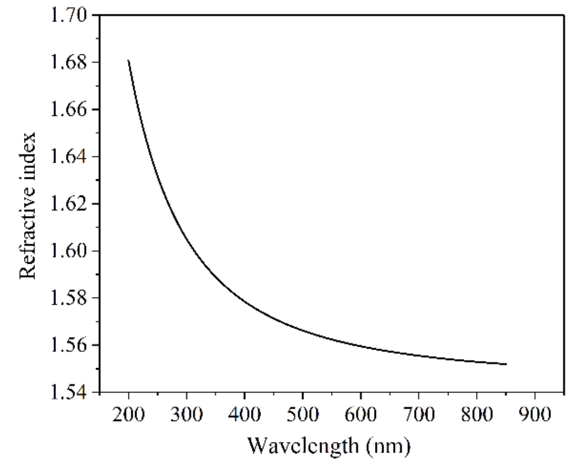

Fig.8. Refractive index in dependence on wavelength, in the visible domain, for the zinc phosphate-tellurite glass

2.6. Magnetic and magneto-optical properties

2.6.1. Magnetization

The magnetization in dependence on the applied magnetic field, collected at RT, in the case of the investigated glass, is shown in Fig.10. A typical increase of the negative values of the magnetization with the applied magnetic field is observed, the negative slope disclosing a diamagnetic behavior of the explored glass. The magnetic susceptibility, determined from the slope of the graph presented in Fig.7, is -60(1) □10^{-8} emu/

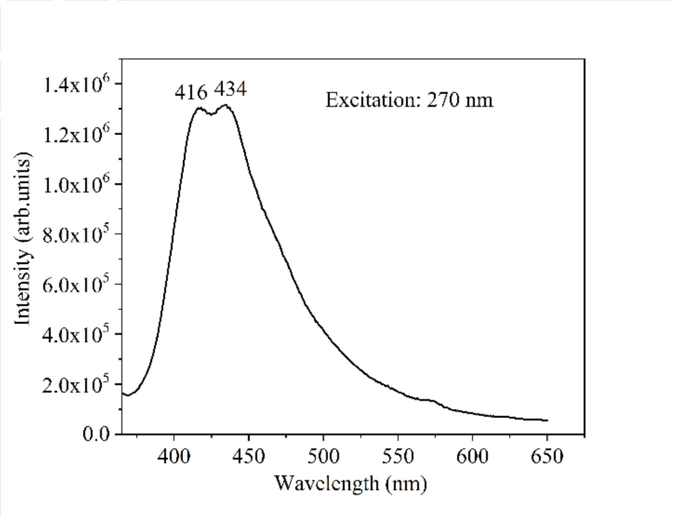

Fig.9. Luminescence of the zinc phosphate-tellurite glass

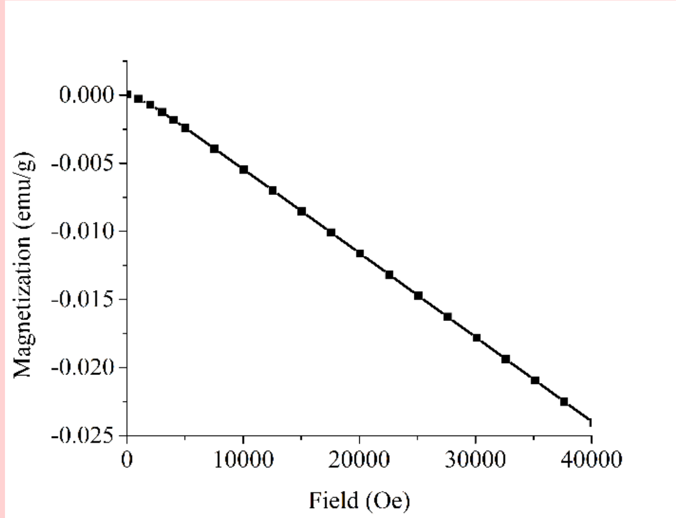

Fig.10. Magnetization in dependence on applied magnetic field, in the case of the zinc phosphate-tellurite glass

(g⍰Oe)= -75(1)⍰10^{-10} m^3/kg.

2.6.2. Magneto-optical effects

When a normal polarized light is passing through the glass, a rotation of the polarization plan of the transmitted light through the glass is noticed, when a magnetic field is applied. This phenomenon is the magneto-optical effect Faraday, the rotation angle, θ_F is explicated by equation (2):

$$\theta_F = VBd$$

where, V is the Verdet constant (characteristic for each material), B is the magnetic induction and d is the glass sample thickness.

Fig.11 presents the dependence of the rotation angle, θ_F in dependence on wavelength, in the visible domain, in the case of the zinc phosphate-tellurite glass at RT.

In Fig.8, ψ_{B+} is the ellipsometric angle measured with the applied magnetic field (+0.2 T) and $\psi_{B=0}$ is the ellipsometric angle without an applied magnetic field.

The wavelengths of 400 nm and 650 nm are considered references for comparison the Faraday rotation angle values of different materials. Thus, in the case of the examined glass, $\theta_F = 0.341^o$ at 400 nm and 0.125^o at 650 nm.

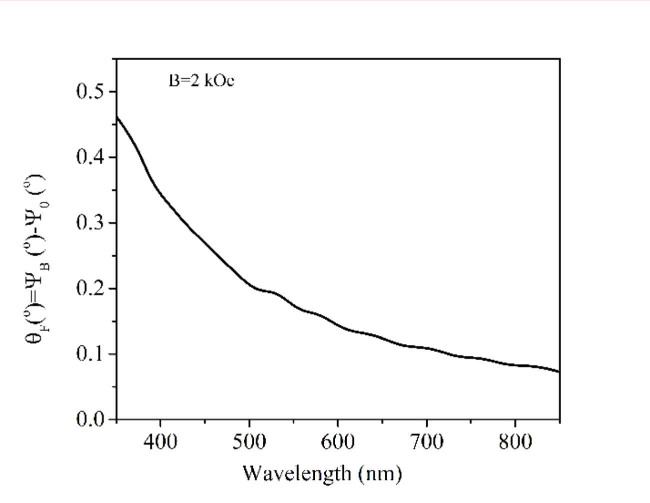

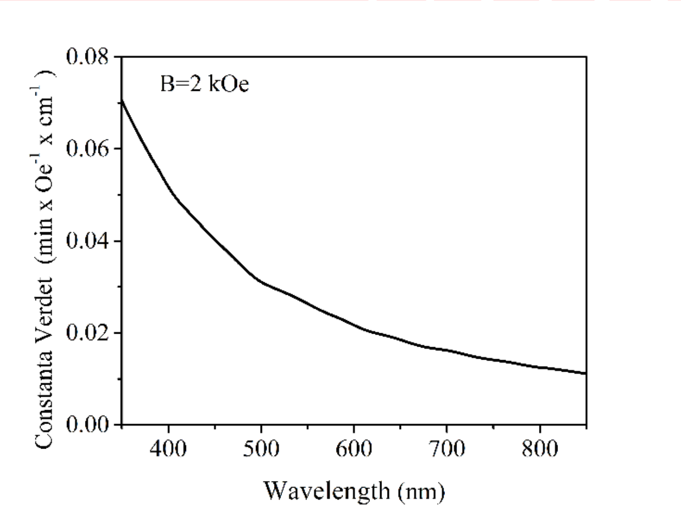

Fig.11. Faraday rotation angle in dependence on wavelength, in the visible domain, for the zinc phosphate-tellurite glass

Fig.12. Verdet constant in dependence of wavelength

It is noticed a decreasing of the Faraday rotation angle with wavelength, θ_F being 0.341° at 400 nm and 0.125° at 650 nm. The Verdet constant in dependence of wavelength is shown in Fig.12.

From Fig.12, the decreasing of the Verdet constant with wavelength is observed, V being 0.052 min/(Oe·cm) at 400 nm and 0.019 min/(Oe·cm) at 650 nm.

3. Conclusions

A new zinc phosphate-tellurite glass composition has been synthesized by a not conventional wet route of starting reagent mixture processing, followed by melting, quenching and annealing.

A complex, thermal, optical, magnetic and magneto-optical characterization of the synthesized glasses have been performed.

These vitreous materials are promising candidates for optoelectronic applications as Faraday rotators in laser cavities to prevent the undesired reflections of the laser beam, which can disrupt the emission optical system.

Acknowledgements

This work was supported by UEFISCDI (Executive Unity for Financing of Higher Education, Research and Innovation), Core Program, contracts no. 16N/2019, 18N/2019, and 21N/2019, project PN-III-P1-1.2-PCCDI-2017-0871/contract 47PCCDI/2018, project PN-III-P1-1.2-PCCDI-2017-0619/ contract 42PCCDI/2018, by the Ministry of Research and Innovation through Program I - Development of the National R & D System, Subprogram 1.2 - Institutional Performance - Projects for Excellence Financing in RDI, contract no.19PFE/2018.

References

[1] M. Elisa, R. Stefan et al, J. Non-Cryst. Solids, 521, 119545 (2019).

[2] M. Valeanu, M. Sofronie, M. Elisa, et al, J. Phys. D: Appl. Phys., 49(7), 075001 (2016).

[3] M. Sofronie, M. Elisa, B. A. Sava, L. Boroica, et al, Rev. Sci. Instr., 86(5), 053905-1 (2015).

[4] G. Lakshminarayana, M. Kawa, S. O. Kaky, A. Baki, L. Priyanka Nayar, I. V. Kityk, M. A. Mahdi, J. Alloys Comp., 690, 799-816 (2017).

[5] N. Elkhoshkhany, R. Abbas, R. El-Mallawany, A. J. Fraih, Ceram. Int., 40, 14477 (2014).

[6] Q. Chen, F. Zhang, Z. Chen, J. Qiu, J. Non-Cryst. Solids, 458, 76 (2017).

[7] K. M. Kaky, G. Lakshminarayana, S. O. Baki, I. V. Kityk, Y. H. Taufiq-Yap, M. A. Mahdi. Res. Phys., 7, 166 (2017).

[8] Q. Chen, H. Wang, Q. Wang, Q. Chen, Appl. Phys. A., 120, 1001 (2015).

[9] G. Kalampounias, G. Tsilomelekis, S. Boghosian, J. Chem. Phys., 142, 154503 (2015).

[10] J. L. Liu, W. C. Wang, Y. B. Xiao, S. J. Huang, L. Y. Mao, Q. Y. Zhang, J. Non-Cryst. Solids, 506, 32 (2019).

[11] S. Sripada, Int. J. Eng. Res. Appl., 4(1,3), 136 (2014).

[12] T. Naito, A. Matsuda, D. Shiojiri, et al, J Ceram. Soc. Japan., 121(5) 452 (2013).

[13] Q. Chen, F. Zhang, Z. Chen, J. Qiu, J. Non-Cryst. Solids, 458, 76 (2017).

[14] P. Mošner, K. Vosejpková, L. Koudelka, L. Beneš, J. Therm. Anal. Calorim., 107, 1129 (2012)

[15] K. Jha, M. Jayasimhadri, J. Amer. Ceram. Soc., 100(4), 1402 (2017).

[16] X. Y. Sun, Z. X. Wen, X. J. Liu, Q. L. Hu, Q. M. Yang, Z. Kang, J. Amer. Ceram. Soc., 102(3), 896, 2018

[17] C. Yu, Z. Yang, J. Qiu, Z. Song, Z. Dacheng, J. Amer. Cer. Soc., 101(2), 612 (2017).

[18] C. Yu, Z. Yang, J. Zhao, A. Huang, J. Qiu, Z. Song, D. Zhou, B. Liu, J. Amer. Ceram. Soc., 102(7), 4200(2019).

[19] E. Golis, M. Reben, B. Burtan-Gwizdala, J. Filipecki, J. Cisowski, P. Pawlik, RSC Advances, 5, 102530(2015).

[20] E. Golis, RSC Advances, 6, 22370 (2016).

[21] G. Gupta, S. Balaji, K. Biswas, A. Kalyandurg, J. Amer. Ceram. Soc., 101(9), 3900 (2018).

[22] X. Du, L. Zhang, G. Dong, et al, J. Amer. Ceram. Soc., 97(1), 185 (2013).

[23] H. Takebe, S. Pujino, K. Morinaga, J. Amer. Ceram. Soc., 77(9) 2455 (1994).
[24] Z. Zhang, J. Cao, Y. Xue, L. Tan, S. Xu, Z. Yang, M. Peng, J Amer. Ceram. Soc., 101(5), 1916 (2017).
[25] S. Elazoumi, S. Ab Aziz, Y. Rammah, R. El-Mallawany, H. M.Kamari, K. Matori, M. H. M. Zaid, Res. Phys., **8**, 16 (2018).
[26] N. Tagiara, D. Palles, E. Simandiras, V. Psycharis, A. Kyritsis, E. Kamitsos, J. Non-Cryst. Solids, **457**, 116 (2017).
[27] G.-G. Lindner, K. Witke, H. Schlaich, D. Reinen, Inorg. Chim. Acta, **252**, 39 (1996).
[28] S. Khonthon, S. Morimoto, Y. Arai, Y. Ohishi, J. Ceram. Soc. Jpn., **115**, 259 (2007).
[29] B. Sava, L. Boroica, M. Elisa, O. Shikimaka, D. Grabco, M. Popa, Z. Barbos, R. Iordanescu, A. Niculescu, V. Kuncser, et al, Ceram. Int. 44, 6016 (2018).
[30] M. Halimah, M. Faznny, M. Azlan, H. Sidek, Res. Phys., **7**, 581 (2017).

*Corresponding author: M. Elisa
Include e-mail address: astatin18@yahoo.com

Silicon-based tandem heterojunction solar cells incorporating copper oxide: performance optimization and defect analysis

L. FARA[1,2]*, Ø. NORDSETH[3], I. CHILIBON[4], R. KUMAR[5], I. C. VASILIU[4], D. SAVASTRU[4], L. BASCHIR[4], D. CRACIUNESCU[1], S. FARA[1], E. MONAKHOV[5]

[1]Department of Physics, Faculty of Applied Sciences, Polytechnic University of Bucharest (PUB), Romania
[2]Academy of Romanian Scientists, Bucharest, Romania
[3]Institute for Energy Technology (IFE), Kjeller, Norway
[4]National Institute of Research and Development for Optoelectronics (INOE-2000), Bucharest-Magurele, Romania
[5]Department of Physics/Center for Materials Science and Nanotechnology, University of Oslo (UiO), Norway

Abstract: A four-terminal Cu_2O/c-Si tandem heterojunction solar cell was investigated. The electrical and optical characteristics for aluminium doped ZnO (AZO) and un-doped Cu_2O thin film layers synthesized by magnetron sputtering were determined. Numerical modelling allowed to analyse the main electrical parameters of the two subcells, in order to maximize the performance of the solar device. A power conversion efficiency of 24.7 % for the four-terminal Cu_2O/c-Si heterojunction solar cell was obtained. The effect of interface defects on the electrical characteristics of the AZO/Cu2O heterojunction was evaluated. The analysis suggested that the incorporation of a buffer layer could enhance the performance of the heterojunction solar cell. ***Keywords:** four-terminal, Cu_2O/c-Si, tandem heterojunction solar cell, AZO, numerical modeling, interface defects*

1. Introduction

The photovoltaic (PV) market is dominated in present by crystalline silicon solar cells (more than 90%) [1]. Cost reduction of this technology could be obtained by promoting silicon –based tandem solar cells with low cost metal oxide materials. Cuprous oxide (Cu_2O) is considered an attractive material for PV applications since it is a p-type semiconductor with high optical absorption and a direct bandgap of about 2.1 eV. To construct a metal oxide p-n heterojunction, Cu_2O can be combined with various n-type oxide materials, such as ZnO, and the potential to reach 14% conversion efficiency, which accordingly, one can foresee a heterojunction solar cell fully based on low-cost metal oxides. However, the highest conversion efficiency currently achieved experimentally in this way is about 8% [2]-[3], with suggests that further investigation of Cu_2O-based solar cells is required in order to realize their full potential in PV applications (the theoretical maximum efficiency is 19-20%) [4]

2. Cu_2O/c-Si tandem solar cell concept

The tandem solar cell is constituted from two subcells: the top subcell based on the heterojunction ZnO/Cu_2O and the bottom one based on c-Si (Fig.1). This representation allowed the increasing the power efficiency beyond the limitation of conventional silicone solar cell. It is remarked that the low energy photons are transmitted through the top subcell, while the high energy photons are transmitted through the bottom subcell (Fig.2).
The current density of the top subcell is half that of the bottom subcell; this fact dictates a 4-terminal configuration of the tandem solar device.

Fig1. The diagram of the tandem heterojunction solar cell

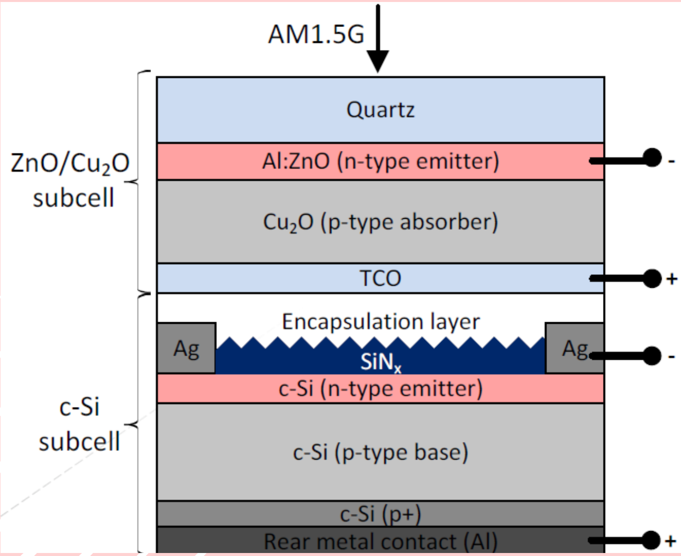

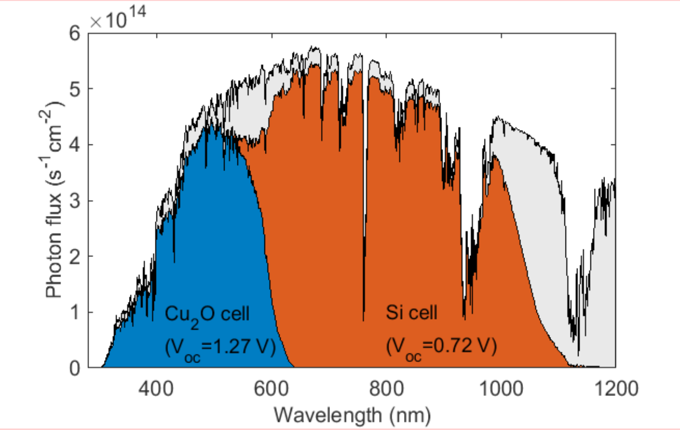

Fig 2. The spectral repartition of the photon flux between the two subcells (ZnO/Cu_2O and c-Si)

Cuprous oxide (Cu_2O) [4]-[5] layer is acting as photo-absorber. It is earth-abundant, non-toxic and low production cost material. Its main physical properties are: p-type semiconductor, bandgap E_g=2.1eV, high absorption coefficient, sharp absorption edge and high carrier mobility. Its theoretical conversion efficiency is 19% under 1 Sun, but the highest conversion efficiency obtained experimentally is 8.1%.
Other properties are: low electron affinity (3.2 eV), band offsets with n-type heterojunction partner, small heat formation (-171 kJ/mol), interface prone to oxidation and formation of an interface defects layer (IDL).

3. Experimental approach

3.1 Thin films deposition by a sputtering system

Cu_2O layer was deposited on quartz substrate by a magnetron sputtering system [6],[7],[8] and [9]. It was considered a Cu target in O_2/Ar with a substrate temperature of 400⁰C. The power density was fixed at 2.2W/cm^2 and the sample was rotated at a constant speed of 12 rpm during the sputtering process. The Cu_2O thin films of ~500 nm thickness were deposited with a deposition rate ~25nm/min; they were subsequently annealed at 900⁰C for 3 min at p ~0.1 Torr. Al-doped ZnO layer was deposited by co-sputtering of a 99.99% ZnO target and a 99.999% Al target in Ar; the substrate temperature was of 400˚C.

The structure of the heterojunction solar cell based on sputtering deposition of metal oxides is designed in *Fig.3.*

Fig.3 The heterojunction solar cell based on sputtering deposition of metal oxides

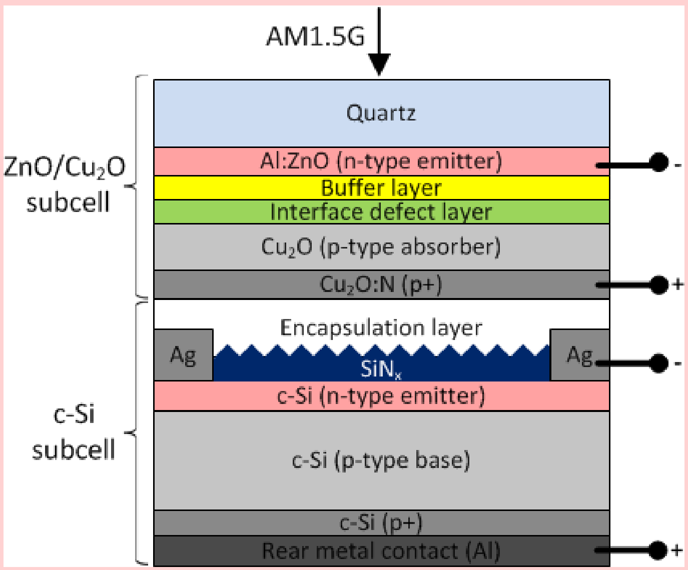

3.2 Morphological and optical characterization

The morphology of the Cu_2O thin films samples was investigated [10]-[11] using a QUANTA INSPECT F 50 scanning electron microscope (SEM) equipped with an electron field emission gun with a resolution of 1.2 nm. In addition, the samples were analyzed using a Veeco Innova atomic force microscope (AFM), with a RTESPA Si doped probe. The AFM images had a resolution of 512 × 512 pixels. SPM Lab Analysis v.7.0 software was utilized for the image analysis. An XRF material analyzer from Bruker type TRACER III-SD was used for carrying out X-ray fluorescence spectroscopy measurements [12]. The optical band gap of the Cu_2O films was determined from ultraviolet–visible spectrophotometer measurements (Shimadzu SolidSpe-3700 DUV) in the wavelength range from 290 to 1500 nm. The thin film thickness and complex refractive index were determined by spectroscopic ellipsometry [13]-[14] using an UVISEL ellipsometer from HORIBA Jobin Yvon in the wavelength range from 190 to 2100 nm. A model fit to the measured ellipsometry parameters was made using DeltaPsi ver. 2.6 software.

3.3 Physical parameters of Cu_2O thin films

Room temperature Hall effect measurements (LakeShore 7604) were carried out using the van-der Pauw configuration. The hole mobility, film resistivity and hole concentration for the 500 nm thick as-grown and annealed Cu_2O thin film deposited on quartz, derived from room temperature Hall effect measurements are presented in *Table 1.* The data suggest that the electrical properties for the Cu_2O thin films are enhanced after annealing, i.e., the majority carrier (hole) mobility increases from 10 to 50 $cm^2/V\cdot s$ and the resistivity decreases from 560 to 200 $\Omega\cdot cm$ after annealing. These values are comparable to those reported previously for sputter-deposited polycrystalline Cu_2O thin films on quartz [15],[16],[17], which recommends that the annealed Cu_2O thin films are well suited for photovoltaic applications. The increase in carrier mobility after annealing can be attributed to the increase in grain size and reduced grain-boundary scattering.

Table 1 Physical parameter values of $C_{u2}O$ (as-grown and annealed) for the 500 nm thickness deposited on quartz and AZO (4% Al) thin films

Physical parameter	**Cu_2O as-grown**	**Cu_2O annealed**	**AZO(4%Al)**
Carrier mobility ($cm^2/V\cdot s$)	10	50	20
Resistivity ($Ohm\cdot cm$)	560	200	5×10^{15}
Carrier concentration (cm^{-3})	3×10^{15}	1×10^{15}	3×10^{15}

3.4 I-V characteristics for metal oxide heterojunction tandem solar cell

I-V curve for the studied heterojunction tandem solar cell shows a rectifying behavior (Fig.4). However it has to be solved its stability and reproducibility in the future research.

4. Solar device modeling. Simulation results.

The modeling of solar device was based on two main simulation software packages: 1) Silvaco Atlas used for the top Cu_2O/Zn O subcell (*Fig 5*), and 2) PC1D/Quokka 2 for the bottom c- Si subcell (*Fig 6)* [3],[18],[19].

Fig.4 I-V characteristics for metal oxide Cu_2O/AZO heterojunction tandem solar cell

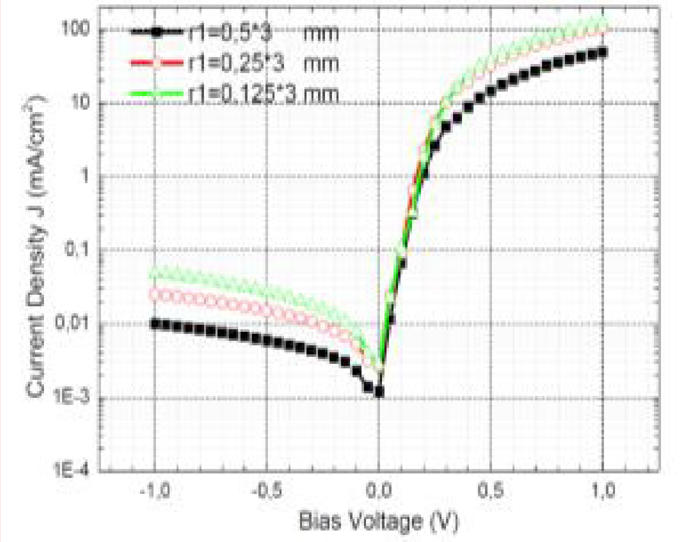

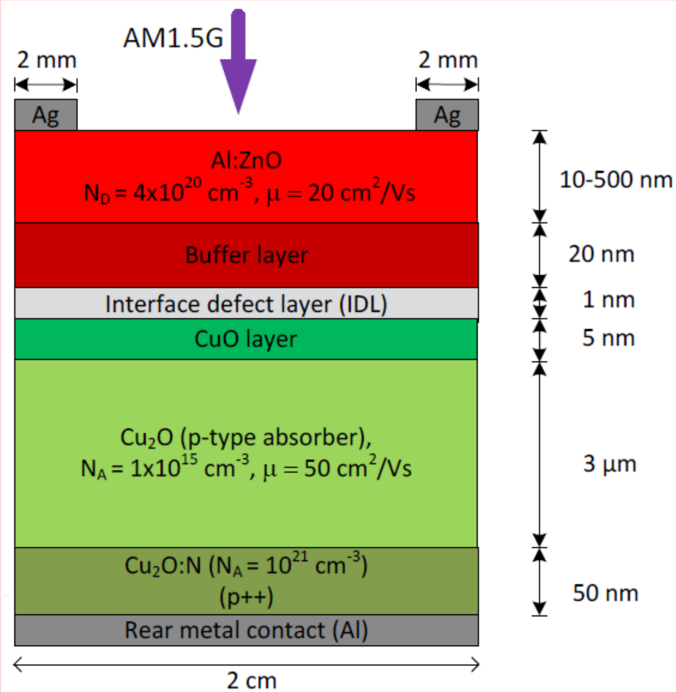

Fig.5 Silvaco Atlas (TCAD) software used for ZnO/Cu_2O heterojunction top subcell

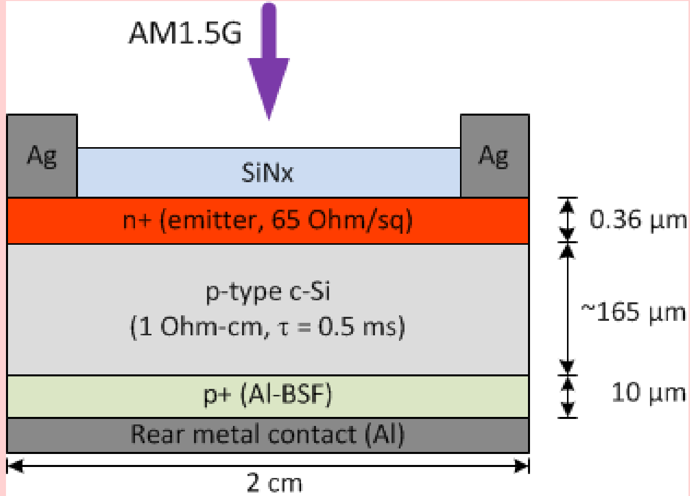

Fig.6 PC1D / Quokka 2 software used for c-Si bottom subcell

For the top subcell, the properties at the level of heterojunction are very important in order to obtain the highest conversion efficiency. Reducing the density of defects at the heterojunction interfaces is critical in avoiding recombination losses. In addition, ZnO causes a conduction band offset of approximately 0.9eV with Cu_2O, which produces a low open circuit voltage (V_{oc}). For this reason, various buffer layers inserted between the layers of ZnO and Cu_2O have been investigated, with the aim of improving the alignment of the energy bands. The main materials proposed for the buffer are: $Zn_{1-x}Ge_xO$, Ga_2O_3, TiO_2, ZnS and Zn(O,S) [20],[21],[22]. With respect to the metal oxide subcell, the model developed in Silvaco aimed at optimizing the subcell structure and the material parameters (*Table 2*) for its layers. The influence of the material characteristics of the buffer layer (electron mobility, buffer layer thickness and electron affinity) on the energy performance of the cell (η, FF, J_{sc}, V_{oc}) was analyzed.

Table 2 ZnO/Cu_2O subcell I-V parameters for different buffer layers.

Buffer layer materials	**J_{sc} (mA/cm²)**	**V_{oc} (V)**	**FF (%)**	**η (%)**
no buffer	9,7	1,00	28,3	2,7
ZnO (ideal)	9,8	1,16	74,0	8,3
ZnS	9,8	1,15	58,4	6,6
TiO_2	9,8	1,14	52,2	5,8
Ga_2O_3	9,7	1,14	51,7	5,8
Zn(O,S)	9,7	1,14	47,0	5,2

For the silicon bottom subcell, a model was developed in the Quokka 2 platform, which was then compared to the experimental data [22]-[23]. Therefore, a predictive model of the silicon subcell has been developed. Following the model improvement, a EQE modeled curve was obtained that simulates a real Si subcell behavior (*Fig. 7*). With regard to the J-V curve, the developed model is very close to the experimental curve (*Fig. 8*).

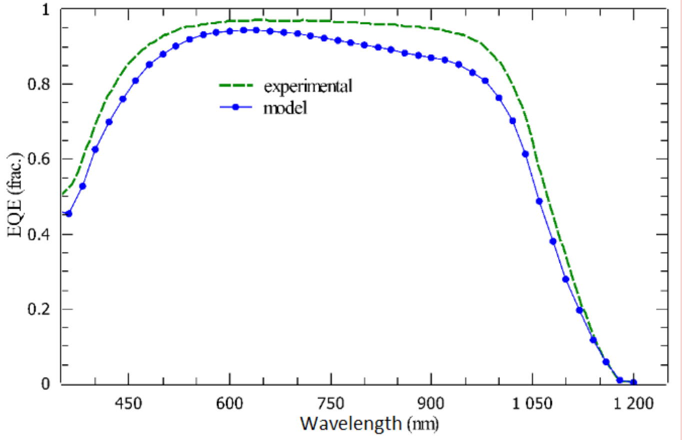

Fig.7 EQE experimental curve vs Quokka model for the c- Si subcell

Fig. 8 J-V experimental curve vs Quokka model for the c- Si subcell

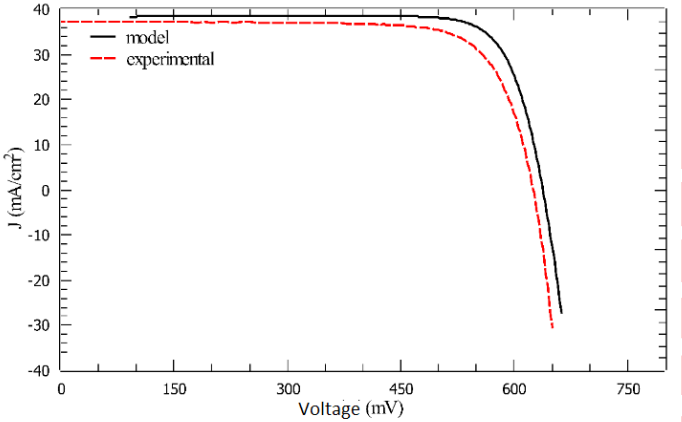

5. Analysis of the interface defects by modeling investigation

Solar cell performance is usually very different from theoretical predictions due to impurities, defects, and interface states. Defects, such as oxygen vacancies, cause Shockley-Read-Hall recombination, resulting in free-charge carriers. Natural metal oxide materials used in the production of solar cells are characterized by a very high density of defects and therefore have poor energy performance [24]. In addition, the interface states generated by the mismatch between two different heterostructure materials can also cause serious problems, such as recombination and tunneling effects. Since recombination losses can adversely affect the optical performance of the cell, the study of interface defects is essential for a realistic approach to the modeling of silicon metal oxide solar cell. To analyze the feasibility of heterojunction and metal oxides, the device should be simulated taking into account the influence of defects and interface states [24],[25],[26,[28],[29].
The electrical parameters of the solar cell have been determined according to the defect density of interface defect layer (IDL), for different thicknesses. The results are presented in *Figs 9 - 12*

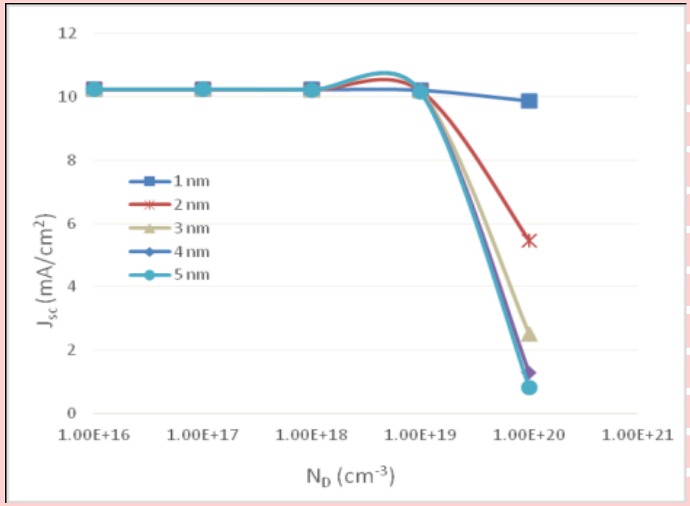

Fig. 9 Short-circuit current density as function of IDL defect density

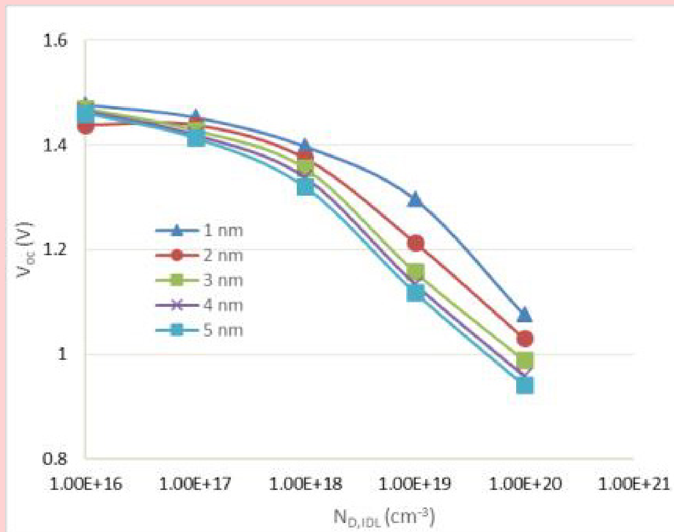

Fig.10 Open-circuit voltage as function of IDL defect density

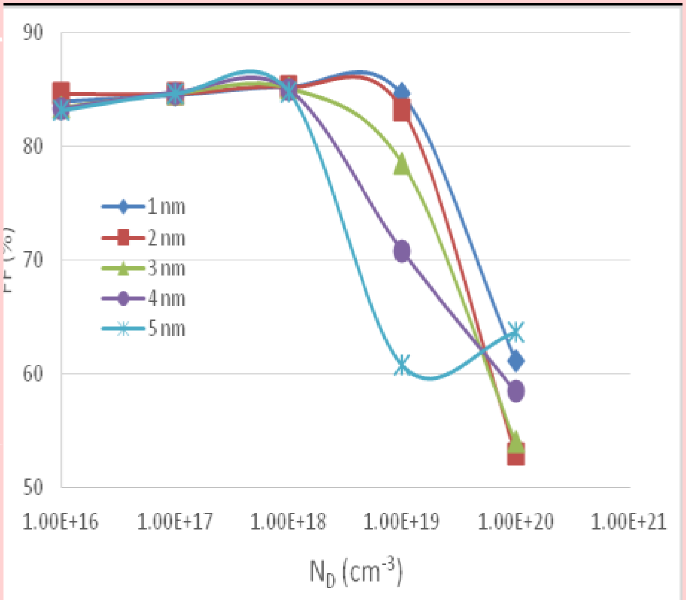

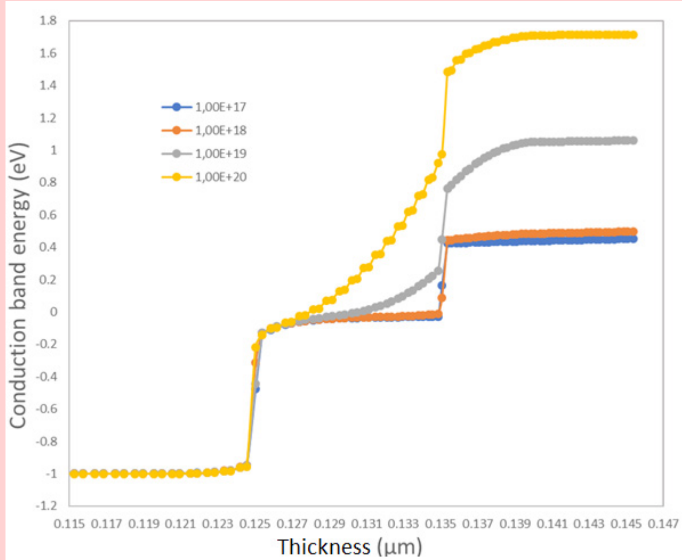

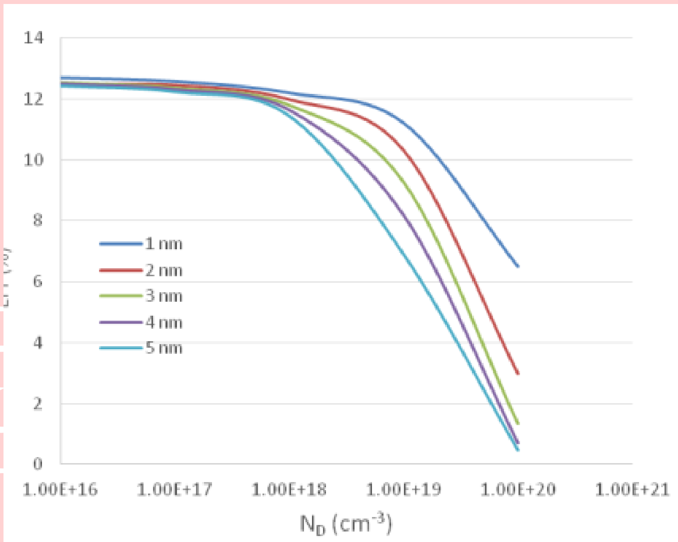

Fig. 11 Fill factor as function of IDL defect density.

Fig. 12 Cell conversion efficiency as function of IDL defect density

Fig. 13 Conduction band energy for different defect densities of IDL

The obtained results indicate a significant reduction in the energy performance of the tandem solar cell for a defect density in the IDL over 10^{19} cm^{-3}, the thickness of the IDL being irrelevant. For this reason, the thickness of the IDL was fixed at 5 nm and the defect density at 10^{18} cm^{-3}.
The behavior of the conduction band for different defect densities of IDL, with a fixed thickness of 5 nm (*Fig13*), was analyzed. A significant increase in the bandgap between the buffer layer and the IDL for a defect density above 10^{19} cm^{-3} can be observed, resulting in a decrease in solar cell performance.

6. Concluding remarks

The main innovative results obtained in this article are as follows:

- it was developed an improved structure of tandem solar cell based on a combined ZnO/Cu_2O heterojunction subcell with c-Si solar subcell:
- it was established a 4-terminal tandem configuration of metal oxide solar cell;
- specific simulation models were developed for design and optimization of the tandem solar cell using material parameters from experimental characterization;
- the experimental implementation of a metal oxide heterojunction tandem solar cell was put in evidence by the I-V characteristics;
- a theoretical conversion efficiency of the studied advanced solar cell greater than 30 % was considered;
- the defect analysis based on numerical modeling showed how the interface defects and band offsets of the considered Cu_2O heterojunction tandem solar cell reduce top cell performance .

Acknowledgments

This research activity was conducted under the research project *"High-performance tandem heterojunction solar cells for specific applications (SOLHET)",* for IFE, UiO, PUB and INOE funded by the Research Council of Norway (RCN), project no. 251789, and the Romanian Executive Agency for Higher Education, Research, Development and Innovation Funding (UEFISCDI), contracts no. 34/2016 and no. 35/2016, through the M-ERA.NET program.

References

[1]. L. Fara, I. Chilibon, Ø. Nordseth, D. Craciunescu, D. Savastru, C. Vasiliu, L. Baschir, S. Fara, R. Kumar, E. Monakhov and J. P. Connolly, Complex Investigation of High Efficiency and Reliable Heterojunction Solar Cell based on an Improved Cu_2O Absorber Layer, Energies, **13**, Issue 18, 4667; doi:10.3390/en13184667 (2020)

[2] Ø. Nordseth, R. Kumar, K. Bergum, L. Fara, S. E. Foss, H. Haug, F. Dragan, D. Craciunescu, P. Sterian, I. Chilibon, C. Vasiliu, L. Baschir, D. Savastru, E. Monakhov, B. G. Svensson. Optical Analysis of a ZnO/Cu_2O Subcell în a Silicon-Based Tandem Heterojunction Solar Cell, Green and Sustainable Chemistry (GSC), **7**, 57-69 (2017).

[3] Y. Takiguchi, S. Miyajima. Device simulation of cuprous oxide heterojunction solar cells, Jpn. J. Appl. Phys., **54,** 112303 (2015).
[4] T. K. S. Wong, S. Zhuk, S. Masudy-Panah, G. K. Dalapati, Current status and future prospects of copper oxide heterojunction solar cells, Materials, **9**(4), 271 (2016).
[5] B. G. Svensson, S. J. Pearton, C. Jagadish, Oxide Semiconductors, Semiconductors and Semimetals, Elsevier & Academic Press, Amsterdam, 88 (2013).
[6]. T. Minami, Y. Nishi and T. Miyata, Efficiency enhancement using a $Zn_{1-x}Ge_x$ -O thin film as an n-type window layer în Cu_2O-based heterojunction solar cells, Appl. Phys. Express**, 9,** 052301 (2016).
[7]. T. Minami, T. Miyata and Y. Nishi, Cu_2O-based heterojunction solar cells with an Al-doped ZnO/oxide semiconductor/thermally oxidized Cu_2O sheet structure, Solar Energy **105** ,206-217 (2014).
[8] J. Gan, V. Venkatachalapathy, B.G. Svensson, and E.V. Monakhov, Influence of Target Power on Properties of Cu_xO Thin Films Prepared by Reactive Radio Frequency Magnetron Sputtering, Thin Solid Films, **594,** 250-255 (2015).
[9] S. Ishizuka, T. Maruyama and K. Akimoto, Thin-film deposition of Cu_2O by reactive radiofrequency magnetron sputtering, Japanese Journal of Applied Physics, **39,** L786-L788 (2000).
[10] Ø. Nordseth, I. Chilibon, R. Kumar, K. Bergum, C. Vasiliu, R. Iordanescu, L. Baschir, D.Savastru, A. Kiss, A. Parau, L. Fara, R. Trusca, E. Monakhov, S. E. Foss, B. G. Svensson, Characterization of Cuprous Oxide Thin Films Prepared by Reactive Direct Current Magnetron Sputtering, Sensors & Transducers, **220**(2), 53-60 (2018).
[11] D.T. Read, Y.W. Cheng and R. Geiss, Morphology, microstructure, and mechanical properties of a copper electrodeposit, Microelectronic Engineering, **75**(1), 63-70 (2004).
[12] I. Chilibon, L. Fara, Ø. Nordseth, R. Kumar, B. G. Svensscen, C. Dumitru, F. Dragan, V. Muscurel, C. Vasiliu, R. Stefan, Characterization of Cuprous Oxide Thin Films used in solar cells by fluorescence and FTIR, AOSR Annals 11 (1), 61-69 (2018).
[13] I. Chilibon L. Fara, Ø. Nordseth, R. Kumar, B. G. Svensson, C. Dumitru, F. Dragan, V. Muscurel, C. Vasiliu, A. Parau, Structural and electrical analysis of Cu_2O layers for solar cell application, AOSR Annals 11 (1),53-60 (2018).
[14] Ø. Nordseth, S. E. Foss, B. G. Svensson, R. Kumar, I. Chilibon, C. Vasiliu, R. Iordanescu, L. Baschir, D. Savastru, A. Kiss, A. Parau, L. Fara, and L. R. Trusca, Cu_2O photosensitive thin films for solar cell application, Sensor devices Proc.2017, 47-52 (2017).
[15] K. Bergum, H. N. Riise, S. Gorantla, P. F. Lindberg, I. J. T. Jensen, A. E. Gunnæs, A. Galeckas, S. Diplas, B. G. Svensson and E. Monakhov, Improving carrier transport în Cu_2O thin films by rapid thermal annealing, J. Phys.: Condens. Matter **30,** 075702 (2018).
[16] H. Zhu, J. Zhang, C. Li, F. Pan, T. Wang and B. Huang, Cu_2O thin films deposited by reactive direct current magnetron sputtering, Thin Solid Films **517**, 5700–5704 (2009).
[17] S. Ishizuka, T. Maruyama, and K. Akimoto, Thin-Film Deposition of Cu_2O by Reactive Radio-Frequency Magnetron Sputtering. Japanese Journal of Applied Physics, **39**, L786-L788 (2000).

[18] Ø. Nordseth, R. Kumar, K. Bergum, L. Fara, I. Chilibon, S. E. Foss, E. Monakhov and B. G. Svensson, Silicon-based tandem solar cells Boosting the performance using non-toxic metal oxides, GIT Laboratory Journal, **7-8**, 25-27 (2017).
[19] Ø. Nordseth, R. Kumar, K. Bergum, L. Fara, C. Dumitru, D. Craciunescu, F. Dragan, I. Chilibon, E. Monakhov, S. E. Foss, B. G. Svensson,, Metal oxide thin-film heterojunctions for photovoltaic applications, Materials **11**(12),2593,doi: 10.3390/ma11122593 (2018).
[20] C. Malerba, F. Biccari, C.L.A. Ricardo, M. D'Incau, P. Scardi, and A. and Mittiga, Absorption Coefficient of Bulk and Thin Film Cu_2O, Solar Energy Materials and Solar Cells, **95,** 2848-2854 (2011).
[21]. Ø. Nordseth, L. Fara, R. Kumar, S. E. Foss, C. Dumitru, V. F. Muscurel, F. Drăgan, D. Crăciunescu, K. Bergum, H. Haug, P. Sterian, I. Chilibon, C. Vasiliu, L. Baschir, D. Savastru, E. Monakhov, B. G. Svensson - Electro-optical modeling of a ZnO/Cu_2O subcell în a silicon-based tandem heterojunction solar cell ,presented at EUPVSEC 2017, 25- 29 Sept. 2017, Amsterdam, Netherlands, published in EUPVSEC 2017 Proceedings.
[22]. C. Dumitru, L. Fara, Ø. Nordseth, I. Chilibon, R. Kumar, B. G. Svensson, F. Drăgan, V. Muscurel, D. Crăciunescu, P. Sterian - Electro optical analysis and numerical modeling of Cu_2O as absorber layer in advanced solar cells, presented at the International Conference on Photovoltaic Science and Technologies PVCON 2018, Ankara, Turkey, published in IEEE Xplore Proceedings of PVCON 2018.
[23]. C. Dumitru, V. Muscurel, Ø. Nordseth, L. Fara, P. Sterian - Optimization of electrio-optical performance and material parameters for a tandem metal oxide solar cell, the 18th International Conference on Computational Science and Its Applications, ICCSA Proceedings (2018).
[24] F. Baccara, Defects and doping in Cu_2O, PhD Thesis, Universita di Roma, (2009).
[25] R.E. Brandt, M. Young, H.H. Park, A. Dameron, D. Chua, Y.S. Lee, G. Teeter, R.G. Gordon and T. Buonassisi, Band Offsets of N-Type Electron-Selective Contacts on Cuprous Oxide (Cu_2O) for Photovoltaics, Applied Physics Letters, **105** (2014).
[26] Y. Wang, P. Miska, D. Pilloud, D. Horwat, F. Mücklich, and J.F. Pierson, Transmittance Enhancement and Optical Band Gap Widening of Cu_2O Thin Films after Air Annealing, Journal of Applied Physics **115**, 073505 (2014)
[27] S. Siol, J. C. Hellmann, S. D. Tilley, M. Graetzel, J. Morasch, J. Deuermeier, W. Jaegermann and A. Klein, Band alignment engineering at Cu_2O/ZnO heterointerfaces, ASC Appl. Mater. Interfaces **8**, 21824 (2014).
[28] T.P. White, N.N. Lal and K.R. Catchpole, Tandem Solar Cells Based on High Efficiency c-Si Bottom Cells: Top Cell Requirements for >30% Efficiency, IEEE Journal of Photovoltaics **4**, 208-214 (2014).
[29] S. Nandy, A. N. Banerjee, E. Fortunato and R. Martins, A Review on Cu_2O and CuI-Based p-Type Semiconducting Transparent Oxide Materials: Promising Candidates for New Generation Oxide Based Electronics, Reviews in Advanced Sciences and Engineering, **2**, 273–304 (www.aspbs.com/rase) (2013).
[30] L. Fara, M. Yamaguchi., Advanced Solar Cell Materials, Technology, Modeling, and Simulation, IGI Global Publishing

House, Hershey (2013).
[31] R. Mitroi, V. Ninulescu, L. Fara. Perfomance Optimization of Solar Cells based on Heterojunctions with Cu_2O: Numerical Analysis. Journal of Energy Engineering, **143**(4), 04017005 (2017).
[32] D. Zhang, W. Soppe and R.E. Schropp, Design of 4-Terminal Solar Modules Combining Thin-Film Wide-Bandgap Top Cells and c-Si Bottom Cells, Energy Procedia, **77**, 500-507 (2015).

*Corresponding author: lfara@renerg.pub.ro

Structural modification pattern of plasma deposited graphene nanowall layers induced by nitrogen doping

Alexandra M.I. TREFILOV [a,*], Bogdan I. BIŢĂ [a], Lavinia CARPEN [b], Ana-Maria IORDACHE [b], Sorin VIZIREANU [a], Bogdan A. SAVA [a], Gheorghe DINESCU [a]

[a] National Institute for Laser, Plasma and Radiation Physics, 409 Atomistilor Str., 077125, Magurele, Jud. Ilfov, Romania
[b] National Institute of R & D for Optoelectronics, INOE 2000, 409 Atomistilor Str., 077125, Magurele, Jud. Ilfov, Romania

Abstract. Vertically-oriented graphene nanowalls or carbon nanowalls (CNW), consisting of interconnected vertical few-layered graphene sheets, are considered nowadays one of the most promising candidates for energy applications due to their high surface area, elevated electrical conductivity as well as good chemical and physical stability. To further enhance their structural and electrical properties, incorporating nitrogen atoms in the graphene lattice is regarded as a key technique. In this respect, both pristine CNWs and nitrogen doped CNWs (N-CNWs) were produced by plasma-enhanced chemical vapor deposition, underlining the differences between direct and ulterior doping treatments. The principal aim of this work was to morphologically, structurally end electrically characterize the fabricated structures to determine the presence of key properties required for electrical components: high conductivity, mechanical stability, superhydrophobicity and chemical purity. In this sense, the CNWs and N-CNWs morphology, structure quality and electrical properties were investigated by Scanning electron microscopy, Photoelectron Spectroscopy and electrometry.

Keywords: graphene nanowalls, radio-frequency plasma deposition, nitrogen doping, SEM, Raman, XPS

1. Introduction

Starting with the discovery of graphene in 2004, carbon nanomaterials have been in the spotlight due to their ideal electronic, mechanical, and thermal properties [1,2.3]. Nowadays, graphene-based nano-structures and thin films play an important role in the development of “green” energy sources as they increase power densities and overall performance in batteries and fuel cells [4], enhance the power conversion efficiency in solar cells [5] and improve charge–discharge cycling performance and capacity in supercapacitors [6].

A recent advancement in the field, the acclaimed carbon nanowalls (CNWs) or vertical oriented graphene (GN), arises as another type of graphene structure composed of stacks of carbon nanoflakes with open boundary edges perpendicular to the substrate. CNWs are easily produced by low temperature plasma: radio-frequency (RF), direct-current (DC) and microwave discharges [7, 8, 9]. However, plasma-enhanced chemical vapor deposition (PECVD) is the most frequently used method due to its reproducibility, scalability, substrate compatibility, sample homogeneity and relatively low temperature working conditions [10, 11].

The two-dimensional vertically graphene sheets can be readily introduced as components in energy related applications due to their low fabrication costs, high conductivity, large surface area, tunable band gap, high mechanical robustness and other remarkable properties [12]. These properties are easily tailored for the required device components from the synthesis conditions by adjusting the temperature, pre-treatment of the support substrate and deposition plasma pressure and power [13].

In addition to the modifications related with the nucleation and growth of the CNWs, their surface properties can be modified by incorporating heterogeneous atoms. For example, the electrical characteristics can be enhanced by incorporating the nitrogen atoms in the CNWs structure [14]. In this regard, two methods are highlighted: in situ method where the N doping occurs during the growth of CNWs and a post-treatment method where the completed CNW are treated in a nitrogen-containing atmosphere [15,16].

Building on past examples of nitrogen doped CNW, we intend to point out the morphological, structural and electric properties modification sustained by N-CNWs produced by the up-mentioned methods, in comparison to the classical CNWs. We'll also pinpoint their individual efficiency in relation with energy related applications, specifically: high conductivity, mechanical stability, superhydrophobicity and chemical purity.

2. Experimental

2.1. Materials and methods

Graphene nanowalls (CNWs) were produced by plasma-enhanced chemical vapor deposition onto commercially available silicon oxide (SiO_2) and quartz substrates. Before deposition the substrates were thoroughly cleaned by isopropyl alcohol and deionized water and dried under nitrogen stream.

PECVD is performed in two steps: a) cleaning the substrate in a low-pressure mixed argon (Ar: 1400 SLM) and hydrogen (H_2: 25 sccm) plasma for 10 minutes, and b) growing CNW on the substrate by injecting acetylene (C_2H_2: 2 sccm) in the previous gas setup for 1 hour. The CNWs films are obtained on a heated substrate at 700 °C placed downstream the gas nozzle (Figure 1). During CNW growth the plasma source power amasses to 300 W and the pressure inside the chamber during deposition is 1 mBar. At the end of the process, the probe was left to cool down freely in nitrogen atmosphere.

In situ N doped CNWs (N-CNW-S) were produced by applying the same working conditions with the addition of a nitrogen stream (N_2: 10 sccm) during the growth process.

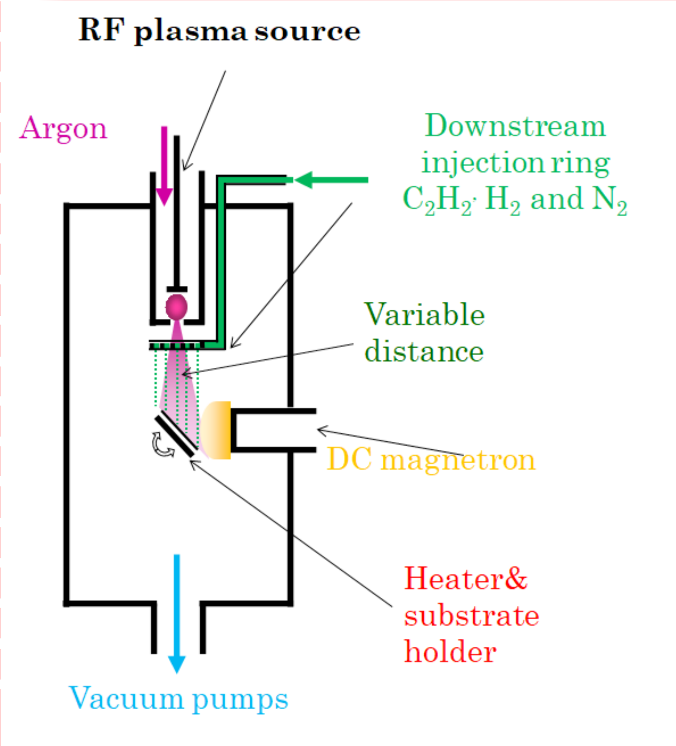

Fig. 1. Schematic representation of the experimental setup where the plasma-enhanced chemical vapor deposition takes place

The nitrogen doping of CNWs employing the post treatment method (N-CMW-P) include the production of the up mentioned pristine CNWs, followed by 10 min treatment in nitrogen (N_2: 10 sccm) and argon plasma immediately after completing the CNW growth.
All used reagents were commercially viable.

2.2. Instrumentation and characterization methods

The morphology and topography were acquired by scanning electron microscopy (SEM) employing an Apreo S ThermoFisher SEM, with a working voltage of 10 kV and a chamber pressure of 3×10^{-3} Pa. The structural modifications induced by the nitrogen doping were studied by Raman spectroscopy. All spectra were obtained with a research-grade micro-Raman spectrometer (NRS-3100, JASCO, Japan) using a 531.94 nm excitation source in 800-3800 cm^{-1} range. Photoelectron Spectroscopy (XPS) scans of the main elements were conducted on a Escalab Xi+ system, Thermo Scientific. The survey scans were obtained using an Al Ka gun with a spot size of 900 µm, pass energy of 100.0 eV and an energy step size 1.00 eV. The hydrophobicity was determined according to the sessile drop method by calculating the Static contact angles. Drops of 2,5 µL - 3 µL of deionized water were placed on the sample surface at room temperature. Temporal series of frameworks (10 to 40 images were captured with a time frame of 1 s) were captured by a CCD camera. The contact angle value was obtained using the Young/Laplace equation in the fitting calculation. All samples were tested after 4 days when the wettability of the samples becomes stable due to the aging phenomena. Four probe electrical measurements were performed using a Keithley 2400 source-meter and a Keithley 6517a electrometer, commanded by a computer, at room temperature.

3. Results and Discussions

3.1. Physical properties

Four-probe measurements returned electrical sheet resistance values of 0.323 Ω ·cm for CNW, 0.391 Ω ·cm for N-CNW-S. Considering the CNWs thickness measured by SEM investigations of 0.88 µm, the conductivity of the

Fig. 2. Several series of images of a water drop placed on a) CNWs, b) N-CNW-S, c) N-CNW-P – in the first 10 sec after dropping and d) N-CNW-P - 20 sec after dropping, presenting the high hydrophobicity of the CNWs and in situ doped CNWs and the hydrophilicity of the post treated nitrogen doped CNW

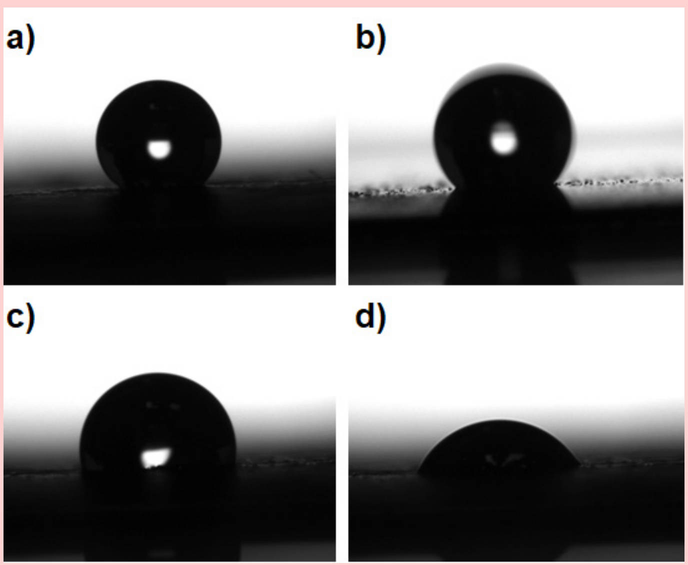

samples is calculated at 30.9 S·cm for CNW and 25.6 S·cm for N-CNW-S. *Contact angle* measurements indicate the general hydrophobic/hydrophilic profile of the materials, showing a superhydrophobic profile for both CNW and N-CNW-S samples with contact angles of 118.72° and, respectively, 136.04°. This behavior is directly related with their topography, as the hydrophobicity increases with the decrease of defects from the carbon networks [17].
In comparison, the N-CNW-P samples present a highly hydrophilic character due to the exfoliation process which occurs during the post treatment. Even though the images acquired in the first ten seconds present a contact angle of 93.06° as shown in Fig. 2. c), after 10 more seconds it decreases to 28.51° (Fig. 2. d).

3.2. Microscopic investigations

Top view SEM micrographs of the three samples offer insights on the effects of patterning on surface morphology. Fig. 3 shows pristine and nitrogen doped CNWs. The pristine CNWs (Fig 3. a and b) consist of randomly distributed two-dimensional nanowalls which form a slightly inter-connected network, oriented perpendicular to the substrate. The individual nanowall length is in the range of 500 nm - 2 µm, while the edge thickness is less than 50 nm.
The N-CNW-P surface (Fig 3. c) presents a pronounced morphology modification as the walls become more branched with dangling edges. This modification occurs

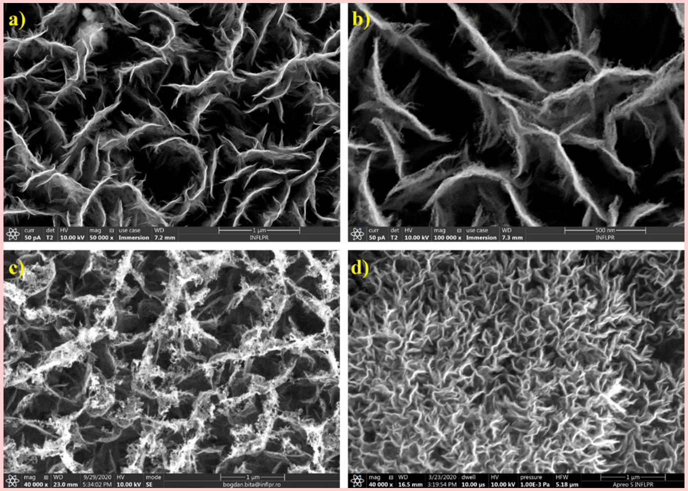

Fig. 3. SEM images of a) CNWs surface with distinct nanowall structure, b) CNWs network structure emphasizing the linked walls, c) N-CNW-P produced by the post-treatment method with exfoliated nanowall edges, and d) in situ produced N-CNW-S with smaller and narrower branches

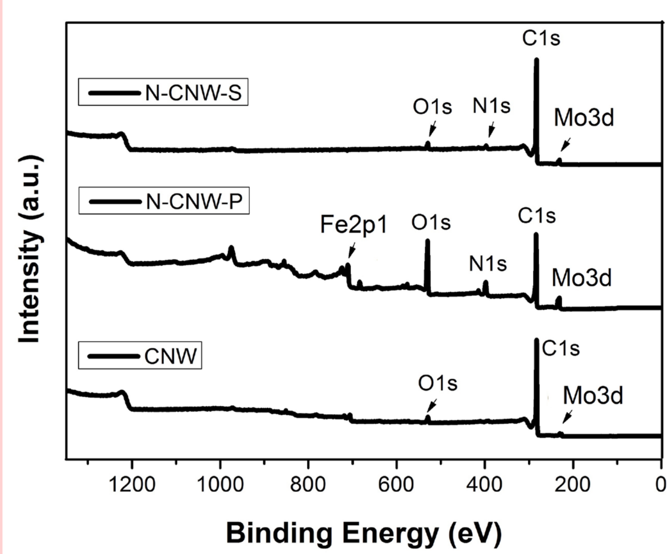

Fig. 4. d) XPS surveys for the as-prepared a) CNWs, b) N-CNW-P and c) N-CNW-S

due to the Ar/N_2 plasma which etches the thin edges [18]. The in situ doped CNWs (Fig 3. d) present the same branching characteristics as the pristine CNWs, but at a much smaller scale, with edge thickness smaller than 25 nm and lengths lower than 500 nm. This behavior can be explained due to a modification in the plasma discharge energy induced by the addition of N_2 stream which leads to a delay in acetylene decomposition and a much slower nanowall growth.

3.3. Spectroscopic investigations

XPS investigations (Fig. 4 d) show in all cases preeminent C1s peaks in the 283 - 284 eV range and O1s peaks of different intensities in the 528-530 eV range of binding energy. Different from the surveys for the pristine CNWs and in situ N-doped CNWs which present low percentage of atomic oxygen (6.17% and, respectively, 3.12 %), the N-CNW-P sample presents a higher percentage of 22.6%. The

high concentration of oxygen is considered to be partially responsible for the high hydrophilicity of the CNWs treated in the nitrogen-containing atmosphere.
Regarding the nitrogen composition, the N-CNW-S samples present a small percentage of atomic nitrogen at the material surface (2.76%) due to the fact that the nitrogen is bonded inside the graphene structure, while the N-CNW-P presents up to 10.3 % bonded mostly at the upper margins.
In addition, small traces of molybdenum appear due to the gas injection nozzle which is etched during plasma deposition.

Conclusions

Seeking to provide promising materials for energy applications, we produced pristine and two different architectures of nitrogen doped graphene nanowalls by plasma-enhanced chemical vapor deposition. We thoroughly investigated the material properties in terms of morphology, structure, hydrophobicity and electrical conductivity. Top view SEM investigations show pronounced morphology modification between these three materials in terms of scale, range and thickness depending on the type of plasma used during deposition. As a confirmation, the hydrophobic/hydrophilic character also depends on the sample structure. Electrical measurements revealed high conductivities, proving the viability of introducing the materials as electrical components.
The XPS spectra present the structural characteristics of the samples, emphasizing the elemental composition.
However, further studies are required in order to integrate pristine or nitrogen doped CNW structures with such physical features into complex electrical devices.

Acknowledgements

This work was financially supported by UEFISCDI Romania, in the frame of the projects: PN-III-P1-1.1-PD-2019-0684 contract 106PD/2020, PN-III-P1-1.1-PD-2019-0540 contract 103PD/2020, PN-IIIP1-1.2-PCCDI-2017-0387 contract 80PCCDI/2018, PN-IIIP1-1.2-PCCDI-2017-0619-contract 42PCCDI/2018, PN-IIIP1-1.2-PCCDI-2017-0871-contract 47PCCDI/2018.
The authors would like to thank Ms. Andreea Matei for her assistance concerning the XPS characterizations.

References

[1] K.S.Novoselov, A.K. Geim, S.V. Morozov, D. Jiang, Y. Zhang, S.V. Dubonos, I.V. Grigorieva, A.A. Firsov, Science, **306**, 5696 (2004) 666-669.
[2] E.P. Randviir, D.A.C. Brownson, C.E. Banks, Materials Today, **17**, 19 (2014) 426-432.
[3] F.T. Johra, J.W. Lee, W.G. Jung, J. Industrial and Engineering Chem., **20** (2014) 2883 - 2887.
[4] S. Hossain, A.M. Abdalla, S.B.H. Suhaili, I. Kamal, S.P.S.Shaikh, M.K. Dawood, A.K.Azad, J. Energy Storage, **29** (2020) 101386.
[5] T. Mahmoudi, Y. Wang, Y.B. Hahn, Nano Energy,

47 (2018) 51-65.
[6] Z. Yang, J. Tian, Z. Yin, C. Cui, W. Qian, F. Wei, Carbon, **141** (2019) 467-480.
[7] K. Davami, M. Shaygan, N. Kheirabi, J. Zhao, D.A.Kovalenko, M.H. Rümmeli, J. Opitz, G. Cuniberti, J.S. Lee, M. Meyyappan, Carbon, **72** (2014) 372-380.
[8] Y. Wu, P. Qiao, T. Chong, and Z. Shen, Advanced Materials, **14**, 1 (2002) 64–67.
[9] M. Hiramatsu, K. Shiji, H. Amano, and M. Hori, Applied Physics Letters, **84**, 23 (2004) 4708–4710.
[9] Y. Tzeng, W.L. Chen, C. Wu, J.Y.Lo, C.Y. Li, Carbon, **53** (2013) 120-129.
[10] B. Bita, S. Vizireanu, D. Stoica, V. Ion, S Yehia, A Radu, S. Iftimie, G. Dinescu, J. of Nanomaterials, ID 881459 (2020).
[11] J. Wang, M. Zhu, R.A. Outlaw, X. Zhao, D.M. Manos, B.C. Holloway, Carbon, **42** (2004) 2867-2872.
[12] C. Zhang, L. Fu, N. Liu, M. Liu, Y. Wang, Z. Liu, Adv. Mater., **23** (2011) 1020–1024.
[13]
[14] N.M. Santhosh, G. Filipič, E. Kovacevic, A. Jagodar, J. Berndt, T. Strunskus, H. Kondo, M. Hori, E. Tatarova, U. Cvelbar, Nano-Micro Lett., **53** (2020), https://rdcu.be/b9msV.
[15] W. Takeuchi, M. Ura, M. Hiramatsu, Y. Tokuda, H. Kano, M. Hori, Appl. Phys. Lett., **92** (2008) 213103.
[16] K. Teii, S. Shimada, M. Nakashima, A.T.H. Chuang, J. Appl. Phys., 106 (2009) 084303.
[17] S. Vizireanu, M.D. Ionita, R.E. Ionita, S.D. Stoica, C.M. Teodorescu, M.A. Husanu, N.G. Apostol, M. Baibarac, D. Panaitescu, G. Dinescu, Plasma Processes and polymers (2017) DOI: 10.1002/ppap.201700023.
[18] A. Achour, S. Solaymani, S. Vizireanu, A. Baraket, A. Vesel, N. Zine, A. Errachid, G. Dinescu, J.J. Pireaux, Mat. Chem. and Physics, **228** (2019) 110-117.

*Corresponding authors: *alexandratrefilov@gmail.com*; *bita.bogdani@gmail.com*

Collective phenomena of branching for overcritical currents in arrays of intrinsic Josephson junctions

MARINA CUZMINSCHI[1,2], ALEXEI ZUBAREV[3*], STEFAN-MARIAN IORDACHE[4], ANA-MARIA IORDACHE[4], CRISTIANA E.A. GRIGORESCU[4]

[1]"Horia Hulubei" National Institute for Physics and Nuclear Engineering, Magurele, Romania

[2]University of Bucharest, Faculty of Physics, 405 Atomistilor, P.O. Box MG-38, 077125, Magurele, Romania

[3]National Institute for Laser, Plasma and Radiation Physics, 409 Atomistilor Str., 077125, Magurele, Jud. Ilfov, Romania

[4,]National Institute of R & D for Optoelectronics, INOE 2000, 409 Atomistilor Str., 077125, Magurele, Jud. Ilfov, Romania

Abstract: Josephson junctions pave their way in modern electronic devices like qubits, traveling wave parametric amplifiers, quantum metrology. For many applications artificially assembled arrays of Josephson junctions can be replaced by high-temperature superconductor thin films oriented along c-axes direction. An important feature of Josephson junctions is presence of a hysteresis on their IV-characteristic. IV-characteristic of arrays of low-dissipative coupled Josephson junctions has a complex structure with multiple branches and the breakpoint region. In our work we described behavior of strongly coupled highly dissipative arrays of Josephson junctions. We put in evidence branching for overcritical currents and charge density traveling waves generation.

Keywords: Josephson junctions, branching, self-organization, overcritical currents, charge traveling waves.

1. Introduction

The Josephson effect was predicted theoretically in 1962 by Brian D. Josephson [1] meaning that superconducting current may flow through a weak link placed between superconductor without any resistance being met. This device (two superconductors connected by a weak link such as a normal metal, an insulating layer or even a ferromagnet) was named a Josephson junction. The effect was experimentally confirmed a year later after the prediction by Anderson and Rowel [2]. For the prediction of this effect in 1973 Josephson was the Nobel Prize in Physics.

The three main effects that Josephson predicted are:

- Tunneling of Cooper pairs through the weak link without any electromagnetic field leading to current flow though the junction. This effect is referred to as DC Josephson effect.
- In the presence of voltage applied across the junction, the current flows through the system, however its

value is not equal to the critical current, it has a sinusoidal form and oscillated with the amplitude of the critical current. This is the AC Josephson effect.

- The inverse AC Josephson effect refers to the appearance of Shapiro steps on the IV-characteristic due to application of the microwave electromagnetic radiation to the junction [3]. The height of the steps on the IV-characteristic will be proportional to the frequency of the microwave radiation.

Since then, Josephson junctions have found application in quantum information [4-6] as superconducting qubits [7] due to the fact that they have a hysteresis zone in the IV-characteristic know as McCumber-Stewart hysteresis [8], as coherent radiation emitters [9]. At this moment more interest present arrays of Josephson junctions, which can be used for spin-current control [10] and as charge density traveling wave amplifiers [11].

Previous studies of arrays of Josephson junctions were concentrated at the subcritical current region on the IV-characteristics. In the framework of CCJJ+DC model was first observed the breakpoint region [12], which appearance was experimentally confirmed [13] on the IV-characteristics. At the breakpoint region branching appears in the stack of Josephson junctions and it corresponds to transition of some junctions from resistive to superconducting state. In that region was also observed a resonance-related hysteresis [14], whose presence was connected to appearance of charge density waves in that region. It is also a collective phenomenon observed in other systems [15,16].

Experimental implementation of stacks of Josephson junctions is also quite easy, since Kleiner and Müller demonstrated that thin films of high-temperature superconductors can be viewed as stacks of intrinsic Josephson junctions [17]. This also means reduction in cost for maintenance of the stack, since most of the high-temperature superconductors operate at temperatures of the liquid nitrogen, while manufactured Josephson junctions require liquid helium conditions [18].

In our research [19] we have observed branching for overcritical current for stacks of intrinsic Josephson junctions. Moreover, this phenomenon was experimentally detected for nanowires and nanobridges of YBCO recently [20]. We link this phenomenon to appearance of charging on the superconducting layers, the same phenomenon that leads to appearance of resonance related hysteresis [14] for subcritical values of current. In section 2 we describe the capacitively coupled Josephson junctions with direct current (CCJJ+DC) model. In section 3 we present main results of our studies and after that the conclusions are drawn.

2. CCJJ+DC model

The two main equations for a single junction are:

$$I_s = I_c \sin\varphi,$$
$$V(t) = \frac{\hbar}{2e}\frac{d\varphi}{dt}.$$

where φ is the phase difference between the two superconductos and I_c is the critical current. While considering a stack of N Josephson junctions (a periodic structure [21-24]), consisting of N insulating and N+1 superconducting layers the total current can be written as the sum of superconducting, quasiparticle, and diffusion currents:

$$I = I_c^l \sin\varphi_l + C\frac{dV_l}{dt} + \frac{\hbar}{2eR_N}\frac{d\varphi_l}{dt}. \qquad (1)$$

CCJJ+DC model provides results which are in agreement with the experiment because it takes into account lack of entire charge screening in the superconducting layers which leads to the appearance of diffusion current [25,26]. In the above equation, V_l represents the voltage between superconducting layers number l and (l+1), normalized to

$$V_0 = \frac{\hbar\omega_p}{2e}, \quad \omega_p = \sqrt{\frac{2eI_c}{\hbar C}}$$

is the plasma frequency and C is the capacitance. R_N is the resistance of the junctions. The demeanor of the stack can be described by the equation:

$$\frac{\partial^2\varphi_l}{\partial t^2} = \sum_{l'} A_{ll'}\left(I - \sin\varphi_{l'} - \beta\frac{\partial\varphi_{l'}}{\partial t}\right) \qquad (2)$$

where I is the current injected in the system,

$$\beta = \sqrt{\hbar/(2eCR_N^2 I_c)}$$

is the dissipation parameter, and A is the matrix which varies for periodic and non-periodic boundary conditions. In case the thickness of the first and last superconducting layers are different in comparison with the thickness of the rest of the layers in the stack, we are dealing with the non-periodic boundary conditions. In this case, the matrix takes the form:

$$A = \begin{bmatrix} 1+\alpha G & -\alpha & 0\ldots & & & \\ -\alpha & 1+2\alpha & -\alpha & 0\ldots & & \\ 0 & -\alpha & 1+2\alpha & -\alpha & 0\ldots & \\ \cdots & \cdots & \cdots & \cdots & \cdots & \cdots \\ & & & \ldots & 0-\alpha & 1+\alpha G \end{bmatrix}$$

where $G = \gamma + 1$ and $\gamma = d_S/d_{S_0} = d_S/d_{S_N}$ where d_S is the thickness of intermediate superconducting layers in the stack, $d_{S_0} = d_{S_N}$ is the thickness of the first and last layers in the system. In case of periodic boundary conditions, the matrix takes the form:

$$A = \begin{bmatrix} 1+2\alpha & -\alpha & 0 & \ldots & & & -\alpha \\ -\alpha & 1+2\alpha & -\alpha & 0 & \ldots & & \\ 0 & -\alpha & 1+2\alpha & -\alpha & 0 & \ldots & \\ \cdots & \cdots & \cdots & \cdots & \cdots & \cdots & \cdots \\ -\alpha & & & \ldots & 0 & -\alpha & 1+2\alpha \end{bmatrix}$$

and the time in the system is measures in units of inverse plasma frequency. The coupling parameter is given by:

$$\alpha = \frac{\varepsilon r_D^2}{d_S d_I}, \qquad (3)$$

where ε represents electrical permittivity of the superconducting layers, r_D is the Debye screening length, and d_I represents the thickness of the insulating layer, taken equal for all intrinsic Josephson junctions.

The equation (2) is solved using the 4^{th}-order Runge-Kutta method. The simulation procedure is as follows: the current-voltage characteristic is obtained running the current from value I_{min} to I_{max} with step in current δI first increasing and then decreasing the value of current.

The voltages are obtained as:

$$\frac{\partial \varphi}{\partial t} = \sum_{l'} A_{ll'} V_{l'} \qquad (4)$$

and the voltage value corresponding to the current value is obtained as:

$$< V_l >= \frac{1}{T_{max} - T_{min}} \int_{T_{min}}^{T_{max}} V_l dt \qquad (5)$$

where T_{max} and T_{min} determine the time averaging interval which is covered with time step ΔT.

Using Maxwell's equation:

$$\nabla \cdot \vec{E} = Q/\varepsilon\varepsilon_0, \qquad (6)$$

where ε_0 is the electrical permittivity of vacuum and Q is charge density, we can determine the charging of the superconducting layers as function of voltage:

$$Q_l = Q_0 \alpha (V_{l+1} - V_l) \qquad (7)$$

with $Q_0 = \varepsilon\varepsilon_0 V_0 / r_D^2$. More detailed description of numerical procedure is given in Refs. [27-30]. Numerical stability of the obtained results was determined by doubling and dividing by two the time step, the step in current and the time interval

$T_{max} - T_{min}$.

Fig. 1. Existence of two branches in the IV-characteristic can be easily observed for overcritical currents (the outermost and traveling wave branches). The case of =0 corresponds to the case when N=1.

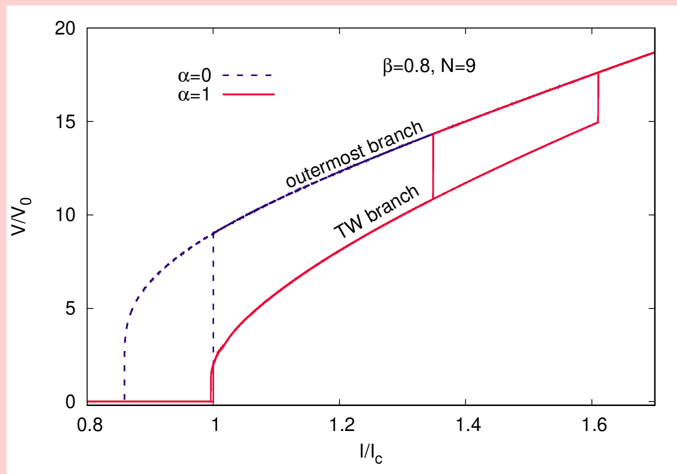

3. Main results

From Fig. 1 can easily be observed the difference between the two possible IV-characteristics the first one with low coupling parameter and the second one with high coupling parameter. We observe that the value of the return current is lower in the case of the low coupling parameter, so that the McCumber-Stewart hysteresis zone is large and there is no branching for overcritical currents. However, in the case of the large coupling parameter the value of the return current is pretty close to the critical current, such

Fig. 2. Charging for the increase (green) and for the decrease (blue) of current. With the solid lines are shown the IV-characteristics and with arrows is identified the direction of current. The parameters

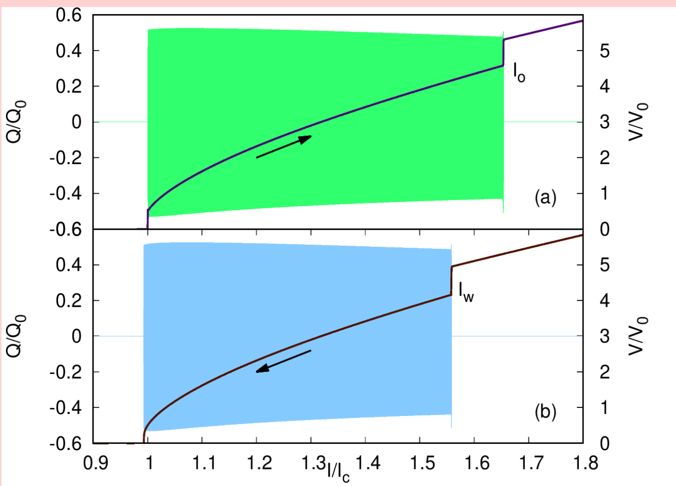

that McCumber-Stewart hysteresis zone becomes close to absent, but in the IV-characteristic for overcritical currents appears branching. The two branches that are present are the outermost branch with the high voltage values, and the second one is the traveling-wave branch with the voltage values that are significantly lower.

In Fig.2 is illustrated the dependence of charge density on current together with the corresponding current-voltage characteristic for the increase and the decrease of current. We mark that lower values of voltage correspond to presence of charging on the superconducting layers. When the generation of charge-density waves is absent in the stack, the values of voltage are much higher and the branch that the system follows is the outermost one. For the increase of current, the system first starts following the traveling wave branch and switches to the outermost branch at the current value I_o. For the decrease of current the system switches from outermost to traveling wave branch at current value I_w.

$\alpha = 1$, $\beta = 0.9$ and N=3. Current corresponding for switching to outermost branch (I_o) and to switching to the traveling wave branch (I_w).

Comparison between the IV-characteristics for the case of periodic (all of the superconducting layers have the same thickness) and non-periodic (first and last superconducting layers have thicknesses that are different from the rest of the superconducting layers) are presented in Fig. 3. While in case of periodic boundary conditions the IV-characteristic for all three junctions looks the same, in

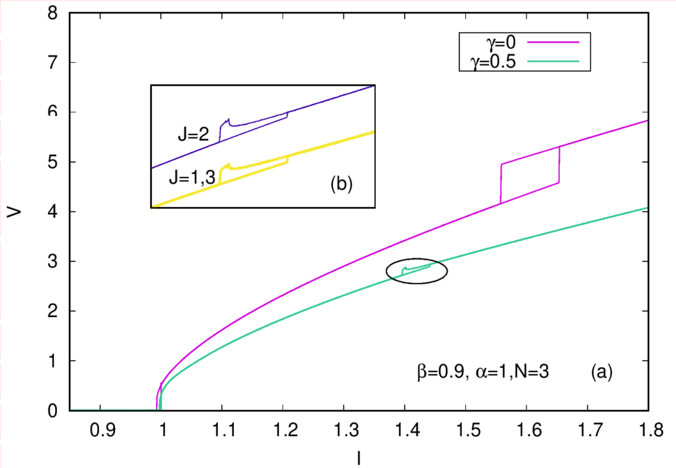

Fig. 3. In case we assume that the thickness of the first and last superconducting layers is different from the rest of the superconducting layers we also observe branching. In the inset is shown the IV-characteristic for all 3 junctions when $\gamma = 0.5$*. Current is measured in units of critical current and voltage in units of* V_0*.*

case of non-periodic boundary conditions for the first and the last junctions the IVs coincide, while for the middle junction it has a distinct form with larger values of voltage (see inset of Fig. 3). Just like in the case of periodic boundary conditions, the branching for overcritical currents can be observed in case of non-periodic boundary conditions. However, in the last situation the branching is not as prominent on the IV-characteristic.

Conclusions

In this study we have demonstrated the existence of branching in the IV-characteristics for overcritical currents in case of large coupling and large dissipation in the framework of CCJJ+DC model for high values of coupling and dissipation parameters. This branching is linked to generation of charge density plasma waves in the stacks of intrinsic Josephson junctions, which also can be viewed as thin films of high-temperature superconductors. The branching for overcritical currents is present for a large interval of currents, which paves the way for novel applications of intrinsic Josephson junctions. The branching is present even for large arrays of intrinsic Josephson junctions.

Acknowledgements

The authors thank Yu. M. Shukrinov, I. Rahmonov and K. Kulikov for useful discussions and research consolation. A. Zubarev acknowledges financial support from the projects 16N/08.02.2019 and EURATOM WPJET1_C. A.M. Iordache was supported by a grant of the Romanian Ministry of Education and Research, CNCS – UEFISCDI, project number PN-III-P1-1.1-PD-2019-1134, within PNCDI III.

References

[1] B. Josephson, Phys. Lett. 1, 251 (1962).

[2] P. W. Anderson, J.M. Rowel, Phys. Rev. Lett. 10.6, 230 (1963).

[3] S. Shapiro, Phys. Rev. Lett. 11.2, 80 (1963).

[4] A. Zubarev, M. Cuzminschi, A. Isar, Rom. J. Phys. 64, 108 (2019).

[5] M. Cuzminschi, A. Zubarev, A. Isar, Proc. Rom. Acad. A 20.3 251 (2019).

[6] M. Cuzminschi, A. Zubarev, A. Isar, Rom. J. Phys. 65, 117 (2020).

[7] H. Paik, et.al., Phys. Rev. Lett. 107, 240501 (2011).

[8] W.C. Stewart, App. Phys. Lett. 12, 277 (1968).

[9] U. Welp, K. Kadowaki, R. Kleiner, Nat. Phot. 7, 702 (2013).

[10] A. Kadigrobov, R. I. Shekhter, M. Jonson, Europhys. Lett. 54, 394 (2001).

[11] C. Macklin, et. al., Scien. 350, 307 (2015).

[12] Yu. M. Shukrinov, F. Mahfouzi, M. Suzuki, Phys. Rev. B 78, 134521 (2008).

[13] A. Irie, Yu. M. Shukrinov, G. Oya, App. Phys. Lett. 93, 152510 (2008).

[14] Yu. M. Shukrinov, M.A. Gaafar, Phys. Rev. B, 84, 094514 (2011).

[15] D. I. Palade, Phys. of Plasm. 23.7, 074504 (2016).

[16] D. I. Palade, Phys. Rev. B 98.24, 245401 (2018).

[17] R. Kleiner, P. Müller, Phys. Rev. B 49, 1327 (1994).

[18] H. Y. Zhai, W. K. Chu, App. Phys. Lett. 76.23 3469 (2000).

[19] M. Cuzminschi, A. Zubarev, Cryst. 9.7, 327 (2019).

[20] M. Lyatti, et. al., Phys. Rev. B 98, 054505 (2018).

[21] A. Zubarev, Int. Semicond. Conf. 2014 IEEE (2014).

[22] A. Zubarev, D. Dragoman, Appl. Phys. Lett. 104.18, 183110 (2014).

[23] A. Zubarev, D. Dragoman, J. Phys. D: App. Phys. 47.42, 425302 (2014).

[24] A. Zubarev, D. Dragoman, J. Phys. D: App. Phys. 46.24, 245301 (2013).

[25] Yu. M. Shukrinov, F. Mahfouzi, Phys. C 434.1, 6 (2006).

[26] Yu. M. Shukrinov, F. Mahfouzi, P. Seidel Phys. C 449.1, 62 (2006).

[27] H. Matsumoto, et al., Phys. Rev. B 60.5, 3666 (1999).

[28] A. E. Botha, Yu M. Shukrinov, M. R. Kolahchi, Chaos, Sol. & Fract. 48, 32 (2013).

[29] Yu. M. Shukrinov, I. R. Rahmonov, J. Exp. Theor. Phys. 115.2, 289 (2012).

[30] T. Koyama, M. Tachiki, Phys. Rev. B 54.22, 16183 (1996)

Corresponding author: alxzubarev@gmail.com*

Plasma Self-organization in High Intensity Laser Beam

A. ZUBAREV[a], M. CUZMINSCHI[b,c,*], A. M. IORDACHE[d], S. M. IORDACHE[d],C. A.E. GRIGORESCU[d]

[1]National Institute for Laser, Plasma and Radiation Physics, 409 Atomistilor Str., 077125, Magurele, Jud. Ilfov, Romania

[2]"Horia Hulubei" National Institute for Physics and Nuclear Engineering, Magurele, Romania

[3]University of Bucharest, Faculty of Physics, 405 Atomistilor, P.O. Box MG-38, 077125, Magurele, Romania

[4,]National Institute of R & D for Optoelectronics, INOE 2000, 409 Atomistilor Str., 077125, Magurele, Jud. Ilfov, Romania.

Abstract: Upon the influence of high intensity laser beam solid target almost instantly is transformed in overdence plasma. After that laser radiation influence leads to high energy particles emission, that makes this technology very attractive for compact laser driven accelerators. After the threshold values of the laser power and laser pulse duration was observed the phase transition in plasma caused by magnetic reconnection. After the phase transition energy distribution of the emitted particles changes and and a high energy component appears. As well in plasma current filaments are generated. During this processes entropy production decreases.

Keywords: plasma, laser, self-organization, filamentation, instabilities.

1.

1. Introduction

Plasma is a quasi-neutral fully or partially ionized environment in which long range interactions have significant contribution to particles behavior [1]. Plasma is considered a fluid [2], however in plasma can be observed generation of quasi-stable structures [3,4] and long-living instabilities [5,6]. Due to permanent ionization and recombination processes plasma can be stable only if a continuous energy flux exists [7]. In nature or technological devices in can be a current flux [6,8], laser radiation [9,10], intense heat flux [11], ionizing radiation [12] or high-energy particles beam [13]. As well some phenomena in condensed matter physics, like Josephson junctions phase dynamics [14] and behavior of electrons in atomic clusters [15,16] can be described considering electrons in the system as quantum plasma. Resent discoverers significantly pushed forward plasma based technologies and made possible its applications for signal processing [17], micro-wave radiation emission [18], electrons[19,20] and ion [9,21] acceleration, and sound sources for different environments [22]. As well plasma is intensively used for surface treatment [23], thin film deposition [24], fabrication of nanostructures [25] and electronic devices [26].

A powerful and easy manipulated source of energy for plasma production and control is laser radiation[9,19,21]. When a laser pulse interact with a solid target due to ionization over-dense plasma is generated[21]. For modern high-intensity laser the ionization process have place almost instantly

and only a few part of pulse energy use used for plasma generation[20,21].
In function of laser intensity and pulse duration in plasma supposed to laser radiation different precesses occur, with leads to changes in plasma spatial distribution, plasma heating, emission of microwave radiation and high-energy particle beams [21, 27, 28].
High-power laser facilities as ELI-NP [29], PHELIX PW [30], CETAL [31] and Vulkan PW [32] offers excellent conditions for fundamental research and elaboration of novel technological applications.
Principal directions of fundamental research on those facilities are simulations of astrophysical phenomena [21], high-energy atomic physics [33] and study of interaction of electromagnetic radiation with atomic nucleus [29].
The most important applications of high-intensity lasers are inertial confinement for nuclear fussion [34] and laser driven plasma based electrons [19,20] and ion [9,21] accelerators for high-energy physics[21], proton imaging, biological experiments[35]. Both precesses are strongly influenced by plasma instabilities, density spatial distribution and energy distribution of component particles[19,34].
The general patterns of phenomena which take place in plasma supposed to intense energy flux is increase of spatial scale of instabilities and segregation of a high energy density components. Such processes are strongly nonlinear and occurs in several stages [3,14].
At the fist stage the most effected plasma component is electrons, due to their low mass. Electrons are accelerated by intense electromagnetic fields specific for laser radiation and charge separation appears [35].
At the next stage in plasma are generated secondary field that can be much greater then laser field, and ionic component start to move. Due fluctuation and nonuniform intensity of laser radiation at this stage first low-scale instabilities appears [36].
At low scale dominant instability in laser driven plasma is Weibel instability [37]. Weibel instability is generated in plasma due to collision-less shocks in strong magnetic fields. Such conditions appears upon laser radiation influence and in astrophysical plasmas. Non-uniformity of laser beam significantly increase rate of Weibel instability growth and generation of plasma filaments. Laser radiation usually satisfies conditions of Gaussian beam [38,39,40] and its evolution can be described analytically except nonlinear environments.
Weibel instabilities consists the seeds for large scale that are generated in plasma after the magnetic reconnection. Magnetic reconnection is a fast change of magnetic lines topology, which decrease potential energy of magnetic field and increase kinetic energy of plasma [41]. During magnetic reconnection Taylor principle of minimum magnetic energy is satisfied [42].
From the thermodynamic point of view, the magnetic reconnection is a second order phase transition which changes the energy distribution of plasma components, plasma transport properties and make plasma inhomogeneous [42]. New plasma configuration is more

stable and is characterized by smaller values of entropy production and entropy per energy densities value [43].
At this large-scale instabilities has most important contribution in plasma behavior. Plasma becomes spatial separated in two phases with different temperatures, current densities, fluid velocities. Hot component form long-living current filaments [44]. Even after the energy flux from laser pulse stops, current filaments remain stable and absorb energy from surrounding plasma [44,45].
Experimental generation of long-living plasma filaments upon high-intensity laser radiation was confirmed in recent experiments at Vulkan PW and PHELIX PW lasers [44]. As well long-living plasma filaments were obtained during numerical simulations presented in references [44,45].
In our research we describe magnetic reconnection and generation of large scale instabilities from thermodynamic point ow view. As well we prove that generation of plasma filaments is a self-organization process and respectively plasma switches from less ordered in more ordered state.

2. Model description

2.1. Weibel Instability in laser driven plasma

Intense laser radiation generate high-intensity electric and magnetic fields in laser driven plasma. Due to low mass electrons are strongly influenced by ponderomotive force and obtain greater accelerations towards almost immobile heavy ions. Upon laser radiation in plasma appears a preferential anisotropic velocity distribution spontaneously appears transversal electronic waves.

Theoretical derivation of Weibel instability is given in Ref. [37]. E. Weibel considered Boltzmam transport equation for colisionless plasma and neglecting nonlinear terms of perturbations dynamics:

$$\frac{\partial f}{\partial t} + \vec{v} \cdot \frac{\partial f}{\partial \vec{r}} + \frac{e}{m}\left[\vec{v} \times \vec{B}_0\right] \cdot \frac{\partial f}{\partial \vec{v}} = -\frac{e}{m}\left[\vec{E} + \vec{v} \times \vec{B}\right] \cdot \frac{\partial f_0}{\partial \vec{v}}, \quad (1)$$

where the following notations ware used: f for perturbation term of distribution function, $\vec{B}_0$ for constant component of magnetic field, $\vec{E}$ and $\vec{B}$ for perturbation of the electric and magnetic fields respectively $f_0(\vec{v})$ is a nonisotropic distribution that is in our case stationary and.

The simplest form of particles phase distribution $f(\vec{v}, \vec{r}, t)$, electric $\vec{E}(\vec{r}, t)$, and magnetic $\vec{B}(\vec{r}, t)$ field perturbations is $\exp(i\omega t + i\vec{k} \cdot \vec{r})$ with main variables position $\vec{r}$ and time t. By using Maxwell equations we can eliminate magnetic field $\vec{B}$ from the Boltzmann equation and obtain:

$$i\left(\omega + \vec{k} \cdot \vec{v}\right) f - \frac{e\vec{B}_0}{m} \cdot \left[\vec{v} \times \frac{\partial f}{\partial \vec{v}}\right] = -\frac{e}{m\omega}\left\{\omega \vec{E} \cdot \frac{\partial f_0}{\partial \vec{v}} + \left[\vec{k} \times \vec{E}\right] \cdot \left[\vec{v} \times \frac{\partial f_0}{\partial \vec{v}}\right]\right\}. \quad (2).$$

This equation takes into account systems anisotropy by including the term $-e/(m\omega)[\vec{k} \times \vec{E}] \cdot [\vec{v} \times \partial f_0/\partial \vec{v}]$.. We can observe that the main source of instability is perturbation field components and the constant field component can be neglected.

The main direction of magnetic field $\vec{B}_0$ and wave

number $\vec{k}$ has place along the radiation propagation axe (z-axes) and electric field $\vec{E}$ is perpendicular to this axes.
As well we assume:
$f_0(\vec{v}) = F(v_0, v_z), \quad v_0^2 = v_x^2 + v_y^2,$
where:
where the distribution function is given by the expression:
Let us consider the distribution function given by:

$$f_0 = \frac{n}{u_0^2 u_3 (2\pi)^{3/2}} \exp\left[-\frac{v_0^2}{2u_0^2} - \frac{v_3^2}{2u_3^2}\right], \tag{5}$$

finally we obtain the following relation:

$$k^2 - \omega^2 = \omega_p^2 \left\{ A - \left(A\frac{\omega \pm \omega_c}{u_3 k} + \frac{\omega}{u_3 k} \right) \phi\left(\frac{\omega \pm \omega_c}{u_3 k} \right) \right\}, \tag{6}$$

where

$$\phi(z) = \exp\left(-\frac{1}{2}z^2\right) \int_{-i\infty}^{z} \exp\left(\frac{1}{2}\xi^2\right) d\xi, \tag{7}$$

with notations:

$$\omega_p^2 = ne^2/m, \quad \omega_c = eB_0/m, \quad A = (u_0/u_3) - 1. \tag{8}$$

As leads the growth rate of Weibel instability is:

$$\gamma_W(k) = k\left(\frac{T_{||0}}{m_e} \frac{P - c^2k^2/\omega_{pe}^2}{1 + -c^2k^2/\omega_{pe}^2} \right)^{1/2} \tag{9}$$

2.1. Magnetic reconnection and transition to large scale instabilities

Estimation of Weibel instability growth rate is important because it determine the time scale of all important processes in plasma as: critical time when the magnetic reconnection occurs, the growth rate of plasma filaments and their decay time. Magnetic reconnection occurs due to non-uniform distribution of magnetic field. It has place when the secondary magnetic field generated by inner plasma processes reaches a critical value, which makes change of magnetic field topology energetically and thermodynamically convenient.

To study the magnetic reconnection we make the following assumptions about plasma behavior: the plasma evolution take place in a quasi-collisionless regime, only long waves generated in plasma, for which , where is the Debye length are taken into account.

It allow as to study plasma in near reconnection conditions as a fluid and to assume that quasi-neutrality is preserved. As follows the continuity equation for ions charge density is:

$$\partial_t n = -\nabla \cdot \vec{v}_i n = -\nabla \cdot \vec{v}_e n. \tag{10}$$

At the next step we can derive the equations of motions for ionic plasma component:

$$m_i n(\partial_t \vec{v}_i + \vec{v}_i \cdot \nabla \vec{v}_i) =$$
$$-\nabla p_i + en(\vec{E} + \frac{v_i}{c} \times \vec{B}) - \nabla \cdot \pi_i - ne\eta\vec{j}, \tag{11}$$

and respectively for electrons:

$$m_e n(\partial_t \vec{v}_e + \vec{v}_e \cdot \nabla \vec{v}_e) =$$
$$-\nabla p_e + en(\vec{E} + \frac{v_e}{c} \times \vec{B}) - \nabla \cdot \pi_e - ne\eta\vec{j}, \tag{12}$$

where the following notations are assumed for ions and electrons: $p_{i,e}$ for scalar pressures, $\pi_{i,e}$ for the stress tensor and η for scalar resistivity.

The total current density is given by the formula:

$$\vec{j} = ne(\vec{v}_i - \vec{v}_e) \qquad (13)$$

And the stress tensor is given by:

$$\nabla \cdot \pi_{i,e} = n\mu_{i,e}\nabla^2\vec{v}_{i,e}, \qquad (14)$$

with scalar viscosities noted as $\mu_{i,e}$.

As well we can assume that during magnetic reconnection plasma evolve adiabatically:

$$\partial_t p_{i,e} + \vec{v}_{i,e} \cdot \nabla p_{i,e} = -\gamma p_{i,e} \nabla \cdot \vec{v}_{i,e}. \qquad (15)$$

The flow velocity becomes:

$$\vec{v} = (m_i\vec{v}_i + m_e\vec{v}_e)/(m_i + m_e) \simeq \vec{v}_i \qquad (16)$$

Finally after all approximaton MHD equations becom: incompressible resistive MHD equations become:

$$\partial_t\vec{\omega} - \nabla \times (\vec{v} \times \vec{B}) - \nabla \times (\vec{j} \times \vec{B}) = \mu_i \nabla^2 \vec{\omega}, \qquad (17)$$

$$\partial_t \vec{B} - \nabla \times (\vec{v} \times \vec{B}) = \eta \nabla^2 \vec{B}, \qquad (18)$$

$$\nabla \cdot \vec{v} = \nabla \cdot \vec{B} = 0, \quad \vec{\omega} = \nabla \times \vec{v}, \quad \vec{j} = \nabla \times \vec{B}$$

where $\vec{\omega}$ is the vorticity in the plasma.

During the plasma evolution is respected conservation of entropy $S = PB^{\gamma}$.

Let us to introduce effective temperature given by the formula:

And effective temperature of the plasma can be calculated using the formula:

$$\tilde{T}k_B = \int E\tilde{f}_0(E, a=0)dE = \int Ef_1(E, a=a_1)dE, \qquad (21)$$

This formula is used for energy per entroia ratio estimation.

3. Results and discussions

Experimental observation of laser was efectuated at VULKAN PW laser [43]. Was observed that during temporal evolution spatial profile of magnetic field changes significantly. In Fig. 1 is reproduced magnetic field evolution during this experiment.

We can observe that magnetic field fluctuations significantly increase in time. At the begin of laser pulse magnetic field maxims are placed chaotically, but after a threshold value of time became quasi-periodically. This moment is associated

Fig. 1. Magnetic field spatial profile at different times after start of plasma laser interaction. Experimental data from VULKAN PW laser. (Ref. 43)

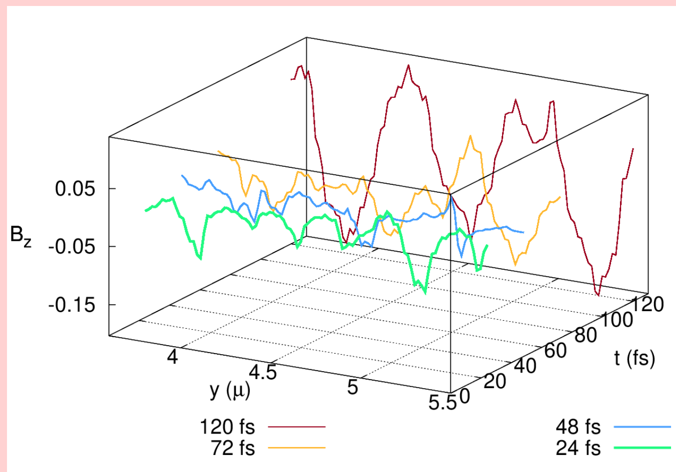

with magnetic reconnection.

In this work we estimated temporal evolution of mean magnetic field (Fig. 2 bottom) and calculated energy per entropy ratio for the system (Fig. 2 top). We observed that after the threshold time this ratio increase fast.

This fact suggests that at this moment (around 65 fs for this experiment) magnetic reconnection occurs and self-organization starts. After this pulse duration generation of plasma filaments can be observed.

The minimal pulse duration τ for corresponding laser intensity I and frequency ω is given by the formula.

Fig. 2. Temporal evolution of mean magnetic field (bottom) and total energy per entropy ratio (top).

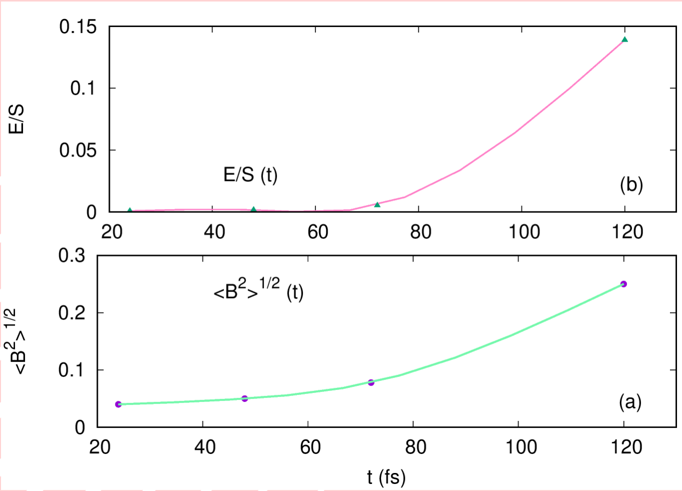

Conclusions

Self-organization processes in plasma plays an important role, and determine generation of long-living large scale instabilities. Transition from low to large scale instabilities occurs after the magnetic reconnection, which can be viewed as second order phase transition. For laser irradiated plasma large scale instabilities represent long-living current filaments. Current filaments are characterized by low entropy production, high energy density and low entropy per energy density values. They play important role in particle acceleration and plasma confinement.

Acknowledgements

The authors thanks Florin Spineanu, Madalina Vlad and Dragos-Iustin Palade for useful discussions and research consolation. A. Zubarev acknowledges financial support from the projects 16N/08.02.2019 and EURATOM WPJET1_C. A.M. Iordache was supported by a grant of the Romanian Ministry of Education and Research, CNCS – UEFISCDI, project number PN-III-P1-1.1-PD-2019-1134, within PNCDI III.

References

[1] R. F. Fernsler, S. P. Slinker, G. Joyce, Phys. Rev. E 71.2, 026401 (2005).

[2] P. Colella, R. D. Milo, D. W. Daniel, J. Comp.l Phys. 152.2, 550 (1999).

[3] C. B. Smiet, et al, Phys. Rev. Lett. 115.9, 095001 (2015).
[4] B. A. Klumov, G. E. Morfill, JETP Lett. 90.6 444 (2009).
[5] M. Ryutova, et al. Solar Physics 267.1, 75 (2010).
[6] S. K. H. Auluck, Atomkernenergie Kerntechnik 36.3,173 (1980).
[7] T. Gougousi, M. F. Golde, R. Johnsen, Chem. Phys. Lett. 265.3, 399 (1997).
[8] W. Kim, et al., IEEE Trans. Plasma Sci. 34.6 2545 (2006).
[9] H. Schwoerer, et al.,Nature 439.7075, 445 (2006).
[10] D. Devaux, et al., J. of Appl. Phys. 74.4, 2268 (1993).
[11] J. Heberlein, A. B. Murphy, " J. Phys. D 41.5, 053001 (2008).
[12] J. M. Shull, M. E. van Steenberg, Astrophys. J. 298, 268 (1985).
[13] P. M. Stier, C. F. Barnett, G. E. Evans, Phys. Rev. 96.4, 973 (1954).
[14] M. Cuzminschi, A. Zubarev, Cryst. 9.7, 327 (2019).
[15] D. I. Palade, Phys. Rev. B 98.24, 245401 (2018).
[16] D. I. Palade, Phys. of Plasm. 23.7, 074504 (2016).
[17] Ya. B. Fainberg, Plasma Phys. Rep. 26.4, 335 (2000).
[18] R. Kersting, et al., Phys. Rev. Lett. 79.16, 3038 (1997).
[19] P. Chen, et al., Phys. Rev. Lett. 54.7 693 (1985).
[20] T. Katsouleas, J. M. Dawson, Phys. Rev. Lett. 51.5, 392 (1983).
[21] H. Schwoerer, et al., Nature 439.7075, 445 (2006).
[22] S. Buogo, Act. Acust. 84.6, 1025 (1998).
[23] L. Y. Yuan, S. S. Shyu, J. Y. Lai, J. App. Pol. Sci. 42.9 2525 (1991).
[24] A. Lavoie, S Mandyam, U.S. Patent 9, 611, 544 (2017).
[25] L. Jiang, H. L. Tsai, App. Phys. Lett. 87.15, 151104 (2005).
[26] L. H. Kim, et al., ACS App. Mat. & Interf. 6.9, 6731 (2014).
[27] T. Baeva, S. Gordienko, A. Pukhov, Phys. Rev. E 74.4, 046404 (2006).
[28] S. J. Gitomer, et al., Phys. Fluids 29.8, 2679 (1986).
[29] F. Negoita, et al. " Rom. Rep. Phys. S 68, 37 (2016).
[30] P. Neumayer, et al., Las. Part. Beams 23.3, 385 (2005).
[31] O. Budriga, E. d'Humieres, Las. Part. Beams 35.3, 458 (2017).
[32] C. Hernandez-Gomez, et al., J. Phys.: Conf. Ser. 244, 3 (2010).
[33] A. Di Piazza, A., Rev. Mod. Phys. 84.3, 1177 2012).
[34] K. A. Brueckner, S. Jorna., Rev. Mod. Phys. 46.2, 325 (1974).
[35] R. J. Romani, Adv. Food Res. 15, 57 (1966).
[36] V. P. Krainov, J. Phys. B 36.15, 3187 (2003).
[37] A. Debayle, et al. Phys. Rev. E 82.3, 036405, (2010).
[38] A. Zubarev, M. Cuzminschi, A. Isar, Rom. J. Phys. 64, 108 (2019).
[39] M. Cuzminschi, A. Zubarev, A. Isar, Proc. Rom. Acad. A 20.3 251 (2019).
[40] M. Cuzminschi, A. Zubarev, A. Isar, Rom. J. Phys. 65, 117 (2020).
[41] M. Yamada, K. Russell, H. Ji., RevMod. Phys. 82.1, 603 (2010).
[42] R. Fitzpatrick, Phys. Plasm. 11.3, 937 (2004).
[43] R. Numata,Y. Zensho, Phys. Rev. Lett. 88.4, 045003 (2002).
[44] K. Quinn, et al., Phys. Rev. Lett. 108.13, 135001 (2012).
[45] M. S. Wei, et al., Ann. Rep. Cent. Las. Fac. Rutherford Appleton Laboratory 7 (2001).

*Corresponding author: marina.cuzminschi@gmail.com

Electrical and morphological characterization of carbon nanowall layers obtained by a low-pressure plasma jet

Bogdan I. Bita[1,3*], Alexandra M.I. Trefilov[1], Stefan-Marian Iordache[2], Sorina Iftimie[3,*], Sasa Yehia[1,3], Sorin Vizireanu[1], Gheorghe Dinescu[1,3]

[1]National Institute for Laser, Plasma and Radiation Physics, 409 Atomistilor, 077125, Magurele, Jud. Ilfov, Romania
[2]National Institute of R&D for Optoelectronics, INOE 2000, 409 Atomistilor, 077125, Magurele, Jud. Ilfov, Romania
[3]University of Bucharest, Faculty of Physics, 405 Atomistilor, 077125, Magurele, Romania

Abstract: Carbon nanowalls (CNWs), consisting of interconnected vertical carbon sheets built from small graphene domains with their *c*-axis parallel to the substrate, were fabricated by plasma-enhanced chemical vapor deposition by injecting hydrogen and acetylene in a radio-frequency argon plasma jet. The main goal of this study was to morphologically and electrically characterize the fabricated architectures. In this sense, we determined that despite their thickness, which was larger than 1 µm, their individual shapes were preserved, even after they were cover with a 300 nm gold layer. The current-voltage characteristics showed the typical behavior of semiconductors and the concentration of charge carriers evaluated by Hall measurements was 7.8×10^{19} cm^{-3}, at room temperature.

Keywords: carbon nanowalls, Hall effect, p-type semiconductor

1. Introduction

Starting with 2010, the year of winning the Nobel Prize in Physics for the graphene discovery, carbon materials have been a climax in the development of electronic devices. Generally, nowadays, carbon-based thin films and carbon-based nanostructures play a very important role in the development of electronic and optoelectronic devices [1]. A major interest in carbon-based thin films was due to their specific physical and chemical properties, such as tunable bandgap and chemical stability [2]. Moreover, because many of the carbon-based materials inherited some of the graphene features like working energy, which has a conventional value of 4.5 eV [3], they can be used with a large variety of metallic contacts; this value can be customized by thermal and chemical treatments or by the number of deposited layers [4].
From 0-dimensional structures as fullerenes, two-dimensional as carbon nanowalls (CNWs), and one-dimensional as carbon nanotubes structures were rapidly developed and its increases theirs use in complex devices [5].

Both, the morphological and electrical properties of carbon nanowalls structures became crucial for electronic applications, such as sensors [4], field emission devices [6, 7], and super-capacitors [8]. Due to some technological challenges, only recent, the electrical properties of CNWs structures were deeply analyzed and discussed but there are still a lot of factors influencing them; i.e. the degree of graphitization, the density of defects, the voids present in the nanosheets [8], and the doping percentage, and the obtained conclusions are just partial milestones to the final decision. On the other hand, due to the present innovative morphological techniques, the features of CNWs were intensely investigated and many results regarding their aspect ratio are already available in the literature.
By this study, we are pointing out both the morphological and electrical properties of fabricated CNWs structures by plasma-enhanced chemical vapor deposition.

2. Experimental

Since 2002, when carbon nanowalls (CNWs) were first synthesized [9], the use of such architectures for various applications continuously increased, and, nowadays, they play an important role in the semiconductor device industry [10, 11]. In this study, CNWs were fabricated by plasma-enhanced chemical

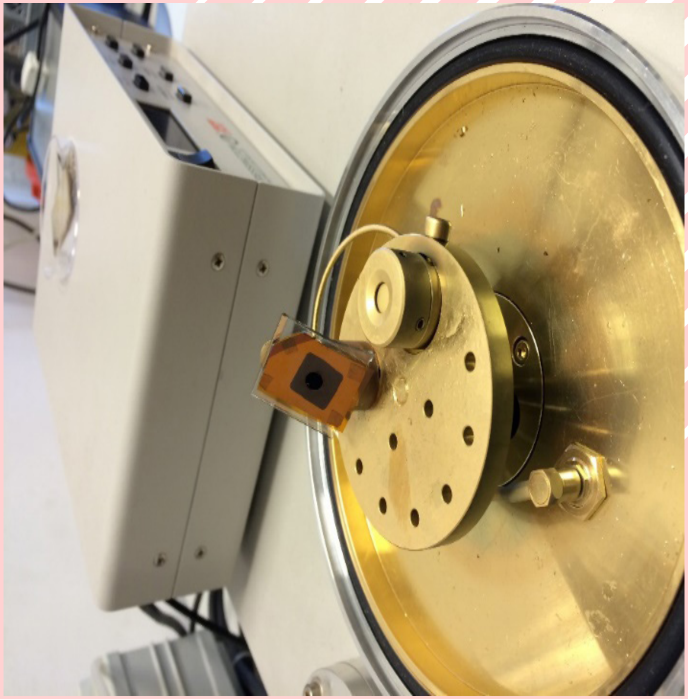

Figure 1. The magnetron samples' holder system (upper part) and the schematic representation of the obtained samples (bottom part).

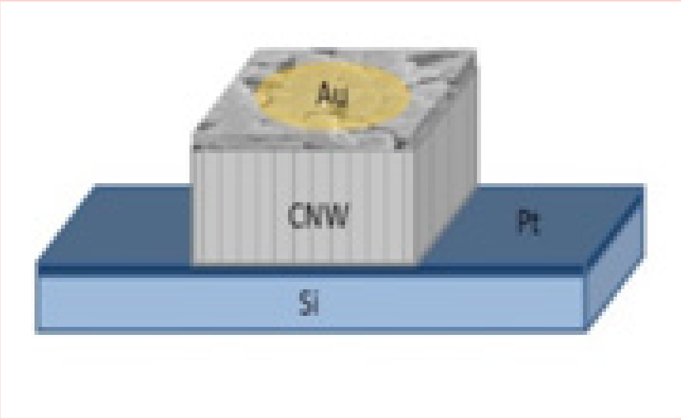

vapor deposition (PECVD) from precursors such as argon (Ar, 1400 sccm), hydrogen (H_2, 25 sccm), and acetylene (C_2H_2, 1 sccm) [8]. At the end of the deposition process, the probe was cool down at room temperature in an Ar atmosphere. The gold (Au) film was deposited by magnetron sputtering by using a 108auto/SE Cressington machine. First, the probe was covered with a Kapton mask with a 5 mm diameter aperture in the middle. Then, the probe was glued with a silver (Ag) paste on a holder and placed at a 30° degree angle from the magnetron source. The deposition was made in automatic mode, by setting a thickness of the film of 75 nm and working current of 40 mA. The magnetron samples' holder system and the schematic representation of the sample's structures are shown in Figure 1.

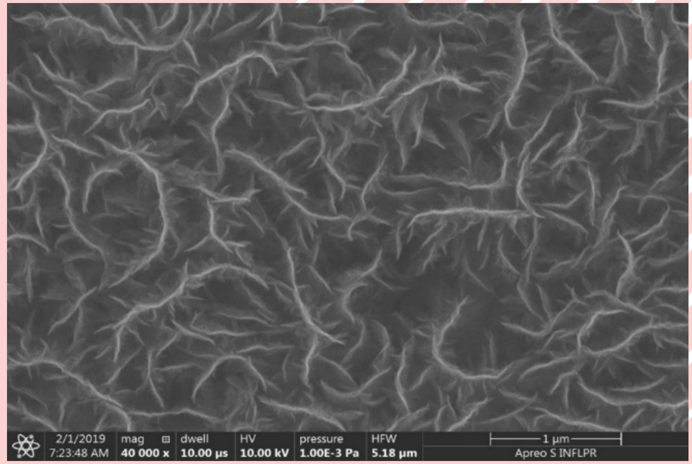

Figure 2. SEM top view micrograph of pristine CNWs

3. Results and discussions

3.1. Morphological investigations

The morphology features of fabricated samples were investigated by using an Apreo S ThermoFisher scanning electron microscope (SEM), with a maximum resolution of 0.7 nm. SEM micrographs were acquired at a working voltage of 10 kV and pressure of 3×10^{-3} Pa. Figure 2 shows the top view image of the pristine CNWs, while the Figure 3 presents the 45 degree view micrograph of CNWs after the on top deposition of a 300 nm gold layer. One can easily observe in Figure 1 that the length of the individual CNWs is about 1 – 1.5 µm, and the thickness is around 10 nm. Moreover, despite their substantial length, no clusters appeared and the individual characteristic was preserved during the growth process. This behavior is strongly correlated with the intrinsic properties of such structures usually denoted as highly oriented graphene sheets [12]. Due to this advantage, even after the deposition of the gold layer, the growth direction remains clearly visible. In Figure 4 we have a cross-section of CNWs on platinum.

3.2. Electrical behavior

Electrical measurements were performed by using a Keithley 2400 source-meter and a Keithley 6517a electrometer, commanded by a computer, at room temperature.

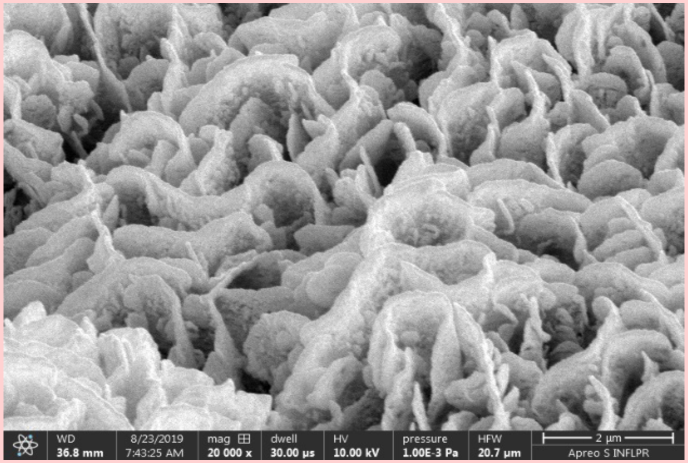

Figure 3. SEM 45 degree view micrograph of CNWs covered with a gold film

Figure 4. SEM cross-section of CNWs on platinum

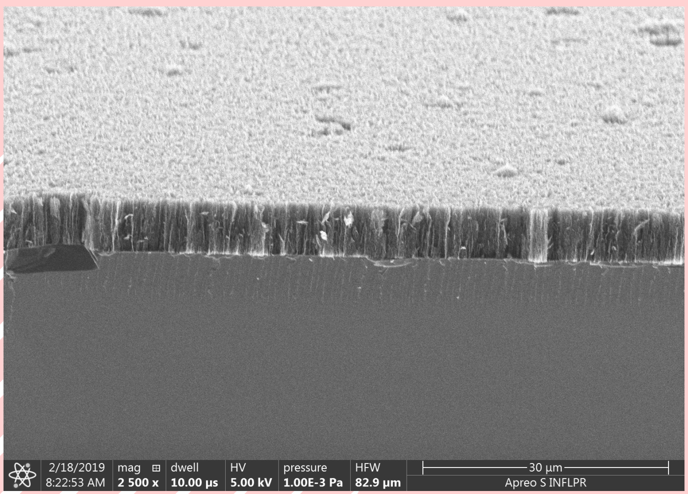

For the prepared samples, both forward and reverse current-voltage (I-V) characteristics were acquired in the ranges of -0.5 – 0.5 volts, and the obtained results are shown in Figure 5; one contact was considered the gold layer, while the second electrode was platinum (Pt) and was fabricated by magnetron sputtering following the same working routine as for Au film. The substrate used was silicon. For a complete electrical characterization, Hall Effect measurements (6 A current and 0.7 T magnetic field, room temperature) were performed, and the Hall coefficient and the concentration of charge carriers were evaluated. The Hall coefficient, R_H, was calculated to be 0.206 m^3/C, and the carrier concentration was 7.8×10^{19} cm^{-3}. The positive value of R_H indicated that the fabricated samples are *p*-type electrical conduction, at room temperature.

Conclusions

In this study, the morphological and electrical properties of CNWs structures obtained by plasma-enhanced chemical vapor deposition were investigated. Top view SEM micrographs showed that the length of the CNWs structures was in the ranges of 1 – 1.5 µm, while their edges were about 10 nm. The current-voltage characteristics proved the semiconductor behavior of such structures by their asymmetry between forward and reverse curves. Also, the positive value of the Hall coefficient indicates that samples are *p*-type electrical

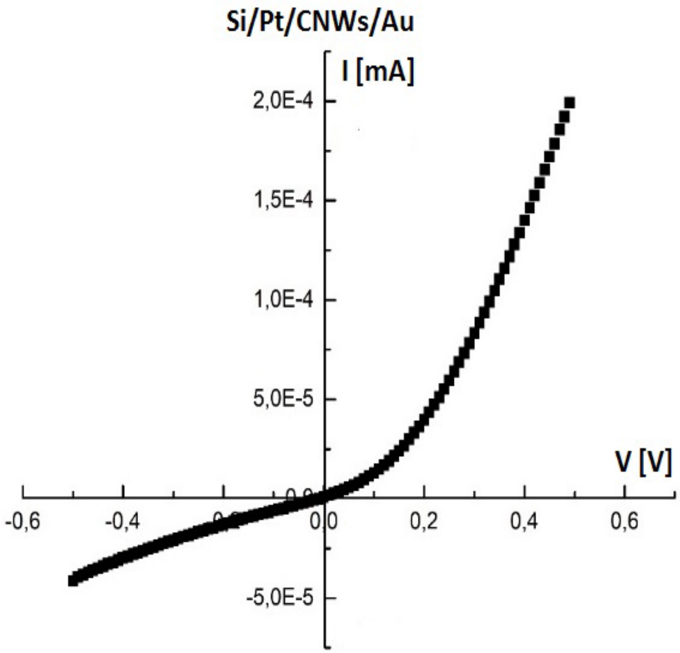

Figure 5. The I-V characteristics of Si/Pt/CNWs/Au structure, acquired at room temperature

conduction, at room temperature. In order to integrate CNWs structures with such physical features into complex devices, further studies are required.

Acknowledgements

Financial support from the Executive Unit for Financing Higher Education, Research, Development, and Innovation (UEFISCDI) through PN-III-P1-1.1-PD-2019-0540/103PD/2020, grant no. PN-III-P1-1.2-PCCDI-2017-0637/33PCCDI/2018, PN-III-P1-1.2-PCCDI-2017-0172/15PCCDI/2018, and grant no. 40PCCDI/2018 is acknowledged.

References

[1] J.B. Wu, H.A. Becerril, Z.N. Bao, Z.F. Liu, Y.S. Chen, P. Peumans, Appl. Phys. Lett. 92, 2008, 263302.

[2] K. Kobayashi, M. Tanimura, H. Nakai, A. Yoshimura, H. Yoshimura, K. Kojima, M. Tachibana, J. Appl. Phys. 101, 2007, 094306.

[3] Z. H. Ni, H. M. Fan, Y. P. Feng, Z. X. Shen, B. J. Yang, and Y. H. Wu, J. Chem. Phys. 124, 2006, 204703.

[4] A. Tiliakos, A.M.I. Trefilov, E. Tanasa, Adriana Balan, I. Stamatin, J. Power Sources 384, 2018, 145-155.

[5] N.M. Santhosh, G. Filipic, E. Tatarova, O. Baranov, H. Kondo, M. Sekine, M. Hori, K. Ostrikov, U. Cvelbar, Micromachines 9, 2018, 565.

[6] J. Wang, T. Ito, Diam. Relat. Mater. 16, 2007, 589-593.

[7] P. Hojati-Talemi, G.P. Simon, Carbon N.Y. 49, 2011, 2875-2877.

[8] M.A. Gentoiu, R. Betancourt-Riera, S. Vizireanu, I. Burducea, V. Marascu, S.D. Stoica, B.I. Bita, G. Dinescu, R. Riera, J. Nanomater. 2017, 2017, 1374973.

[9] Y. Wu, P. Qiao, T. Chong, Z. Shen, Adv. Mater. 14,

2002, 64-67.
[10] J. Wu, Y. Shao, B. Wang, K.K. Ostrikov, J. Feng, Q. Cheng, Plasma Process. Polym. 13, 2016, 1008-1014.
[11] K. Yu, Z. Bo, G. Lu, S. Mao, S. Cui, Y. Zhu, X. Chen, R.S. Ruoff, J. Chen, Nanoscale Res. Lett. 6, 2011, 202.
[12] A. Guerra, A. Archour, S. Vizireanu, G. Dinescu, S. Messaci, T. Hadjersi, R. Boukherroub, Y. Coffinier, J.J. Pireaux, Appl. Surf. Sci. 481, 2019, 926-932.

Include e-mail addresses: bogdan.bita@inflpr.ro

*Corresponding author: * Sorina Iftimie;
sorina.iftimie@fizica.unibuc.ro

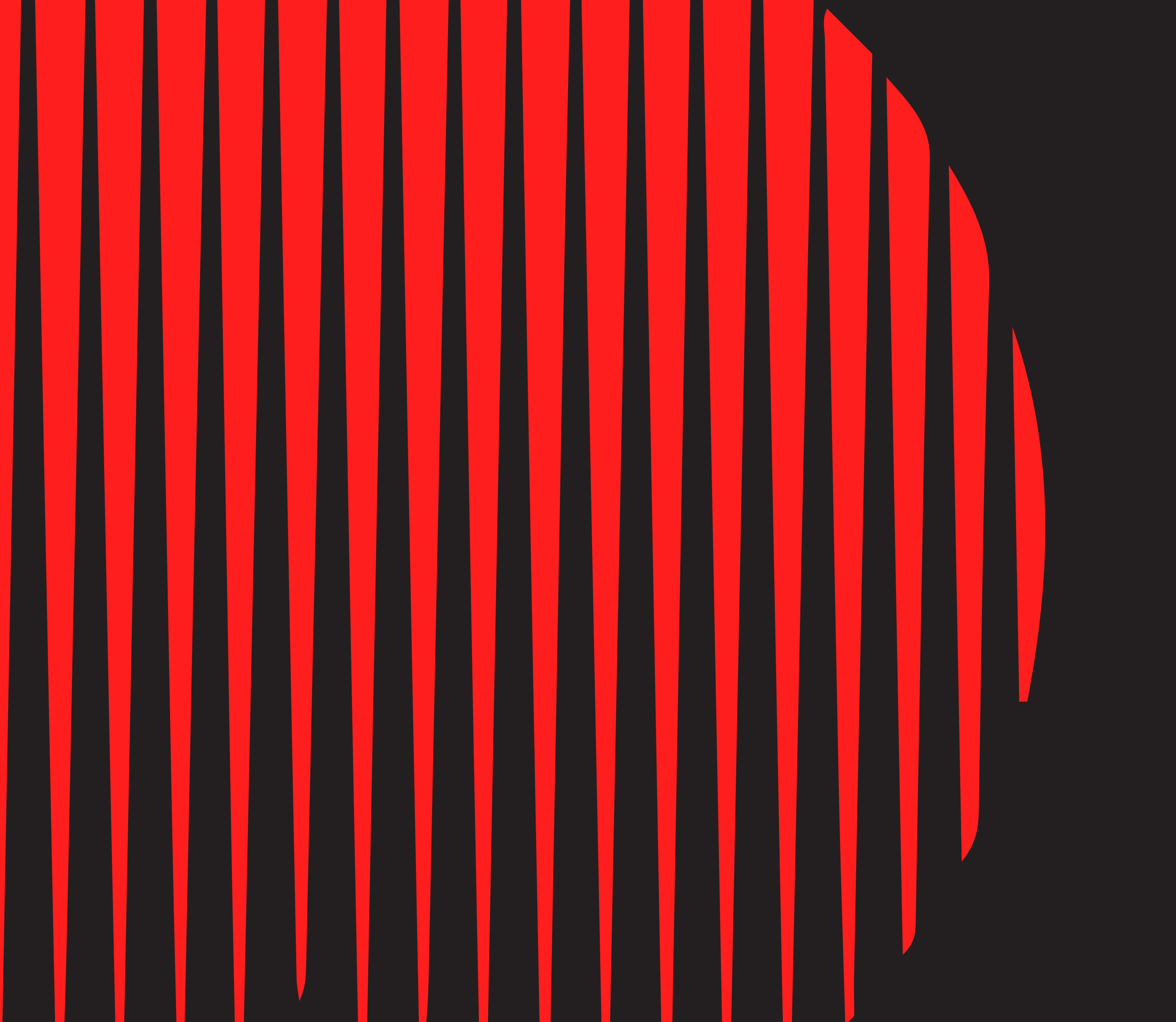

CHAPTER IV

Optoelectronics- materials, sensors and products

Surface water quality monitoring – a citizen science perspective

E.M. CARSTEA[*], C.L. POPA, S.I. DONTU
National Institute of R&D for Optoelectronics INOE2000, Atomistilor 409, Magurele, 077125, Ilfov

Abstract: Citizen science represents an untraditional approach to environmental research, where citizens supply site observations and water samples with a high time and cost efficiency. In this study, the types of data generated by citizens are reviewed, with potential application in Romania. Site observations and in situ measurements are suited to urban citizens, who may offer their leisure time for training and monitoring activities. The sample collection approach may be applied to both rural and urban areas, if the activities are supervised by a local coordinator. Social media mining may be complementary to the other approaches, but limited to touristic areas.

Keywords: *water quality, citizen science, public participation, social media.*

1. Introduction

Citizen science represents the involvement of non-professionals in scientific investigations, allowing them to ask questions, collect data or interpret results [1]. In the recent years, a growing interest has been given to citizen science projects in environmental research, in particular to water quality monitoring. Such programs reduce costs associated with monitoring, increase environmental databases, provide early warning of water pollution events, cover wide geographic areas, increase public awareness and education, strengthen social ties, explore various world views and investigate local pollution issues [2]–[4]. In addition, citizens science programs lead to the democratization of the environment and science [2].
The key elements of project success or the factors affecting the outcomes of citizen science actions have been widely discussed in literature. For example, Rambonnet et al. [4] have shown that factors such as a clear project goal, the involvement of policy makers in the activities or acknowledging the help of volunteers reduce the risks of project failure and ensure a long-term impact. In addition, the success of the project depends on the levels of citizen knowledge, their socio-economic background and level of commitment [5]. The long-term impact of a citizen science programs also depends on how much information and how many routes professional researchers use to extract data. They can extract data from measurements made by citizens

alone or together with scientists, or from social media [6]. Very few citizen science programs have been undertaken in Romania and it is unknown what routes of information collection can be explore here. In this study, the classes and sources of information generated by citizens are reviewed. In addition, we analyze the potential routes for collecting data from citizen science projects that can be implemented in Romania.

2. Citizen science data

Citizen science actions can be classified into five categories depending on the nature of the project, which also define the level of participant involvement: contractual, contributory, collaborative, co-created and collegial [1] (Table 1). The contributory model is the most common, where citizens supply the data, under the request of scientists [7]. Nevertheless, this model may also provide limited involvement of citizens in decision-making (Table 1). Other types of models offer more opportunities for involvement, but they require higher levels of commitment from authorities and scientists. Professional researchers can extract either structured or unstructured data. Structured data are generated by programs that employ specific monitoring and reporting tools on particular parameters, locations and times. Unstructured data are extracted from social media, supplied unwillingly by citizens [6].

Table 1. Levels of participation [1] *and the potential of involving citizens in decision-making.*

Level of participation	Data collection	Potential involvement in decision-making
Contractual	Structured	High
Contributory	Structured / Unstructured	Medium to low
Co-created	Structured	High
Collaboratory	Structured	High to medium
Collegial	Structured	Medium

2.1 Site observations

This type of data includes visual observations and in situ measurements. Usually, visual observations represent aquatic vegetation or surface litter, mostly of qualitative nature and subjected to errors. For example, in one study, citizens were requested to submit via smartphone applications, information about the presence of fish, plants or birds, without specifying the species [8]. In another study, volunteers were asked to conduct surveys of floating litter [9]. These observations are usually accompanied by photographs, which help in data validation.

Other studies, however, set up strict criteria for site observations to facilitate quality control [10], [11]. During training workshops, Shupe et al. [12] instructed citizens to provide observations of hydrological conditions, water flow, land use etc.

In situ measurements are also very common. Generally, professional scientists provide citizens with measurement kits. These kits can be developed by the researchers to suit the project objective or can be supplied by third party organizations, such as the FreshWater Watch [8] or EarthEcho [13]. The volunteers are trained and, in most cases supervised, by professional researchers to do the measurements [12], [14], [15]. Common water quality measurements include the concentration of nutrients, pH, turbidity and conductivity. For water level measurements, professional researchers install water gauges, near public bridges, and ask citizens to send the observations via text messages or smartphone applications [16], [17]. Data validation is usually performed by comparing the data with sensors installed on site or with measurements made by professional scientists.

In addition to measurement kits, devices can also be used to determine the quality of surface water. Simple devices (Table 2) can be constructed by high school students during school projects. Such activities will not only increase their knowledge on environmental issues, but also on the basic theory of optics and spectroscopy.

Table 2. Examples of devices that can be constructed and/or used by citizen scientists for water quality data.

Device	Measurement	Reference
Foldable Mini Spectrometer	Light spectrum	[18]
KnoWare	Light spectrum	[19]
KdUINO	Tranparency	[20]

In the case of Romania, urban citizens may be targeted to deliver water quality observations. The high-density population in urban areas ensures a greater pool of volunteers, compared to rural areas. Also, urban citizens may be willing to engage in outdoor hobbies and may have leisure time that they can sacrifice for training and data collection. In addition, urban citizens are more likely to travel for touristic purposes around the country and may submit data along the way. In such case, the use of smartphone applications is particularly feasible for observations such as water bank profiles, aquatic vegetation, land use or water level. However, this urban approach limits the involvement to only one socio-economic group.

2.2. Sample collection

Citizens may collect and send water samples to research laboratories for investigations. These programs are developed by professional researchers, with the help of local coordinators. Such programs reduce the time for water sample collection, while covering a large geographical area [21]. Samples may also be collected by citizens during in situ observations, which can then be used for data validation or additional measurements [22].

This approach may be feasible for both urban and rural communities in Romania, provided that motivated local coordinators, such as authorities or schools, can commit the time and effort to ensure the supply of samples to laboratories. In addition, it requires less training for sample collection and limited effort for rural citizens, who are mostly engaged in agricultural activities, or for those who have multiple jobs.

2.3. Social media mining

Social media mining is an additional information source to site observations and may be a complementary source to traditional monitoring. This approach is suited to remote areas or in locations with scarce data. However, the method is limited in accuracy and temporal resolution [23]. For example, Michelsen et al. [23] have analyzed YouTube videos to extract data regarding water level in caves, at temporal scale. Also, social media mining can be used to collect fast data in areas prone to floods. Fohringer et al. [24] were able to determine spatial flood patterns and depths in Dresden.

Social media may be used by professional researchers as platforms where citizens can send data. For example, on a dedicated account, citizens can post photographs or alerts of pollution events or natural disasters [6]. This is a mixed model of structured and unstructured data.

In 2019, in Romania there were over 43,000 active Facebook accounts and on Instagram, users posted 1.6 million photographs, 107,000 videos and over 5 million comments [25]. The increasing use of social media may ensure the supply of additional data on litter pollution or water level, especially in touristic locations. However, the information may be biased as citizens decide what to photograph.

3. Conlusions

This study showed that all approaches, site observations, sample collection and social media mining can be implemented in citizen science projects in Romania. However, site observations may have a greater success in the urban environment, compared to rural areas. Urban citizens have greater access to information on environmental issues and may engage during their leisure time in training and monitoring activities. The sample collection approach may be applied throughout the country. However, it requires the involvement of local authorities or schools to ensure that the samples are collected and supplied to professional researchers. The last approach, social media mining, may be complementary to the other approaches, but the data may be biased, as the citizens may not provide the full picture of the environmental issue. In addition, the data may have low temporal resolution and limited accuracy.

Acknowledgements

The authors acknowledge the support of the support of the Ministry of Research and Innovation, CNCS - UEFISCDI, project number PN-III-P1-1.1-TE-2019-0789, within PNCDI III, and by the Core Program OPTRONICA VI, project number 18N/2019, project number 19PFE/17.10.2018 and project number 152/2016, SMIS 108109.

References

[1] A. Miller-Rushing, R. Primack, R. Bonney, Front. Ecol. Environ., **10**(6), 285 (2012).
[2] C. C. Conrad, K. G. Hilchey, Environ. Monit. Assess., **176**(1–4), 273 (2011).
[3] A. H. Toomey, L. Strehlau-Howay, B. Manzolillo, C. Thomas, Landsc. Urban Plan., **200**, 103824 (2020).
[4] L. Rambonnet, S. C. Vink, A. M. Land-Zandstra, T. Bosker, Mar. Pollut. Bull., **145**, 271 (2019).
[5] A. San Llorente Capdevila, A. Kokimova, S. Sinha Ray, T. Avellán, J. Kim, S. Kirschke, Sci. Total Environ., **728**, 137843 (2020).
[6] S. Becken, R. M. Connolly, J. Chen, B. Stantic, Ecol. Inform., **52**, 35 (2019).
[7] N. Njue, J. Stenfert Kroese, J. Graf, S. R. Jacobs, B. Weeser, L. Breuer, M. C. Rufino, Sci. Total Environ., **693**, 133531 (2019).
[8] "FreshWater Watch, Earthwatch Europe," 2020. [Online]. Available: https://freshwaterwatch.thewaterhub.org/our-data/explore-our-data. [Accessed: 08-Oct-2020].
[9] C. C. Chiu, C. P. Liao, T. C. Kuo, H. W. Huang, Mar. Pollut. Bull., **157**, 111301 (2020).
[10] T. Kiessling, K. Knickmeier, K. Kruse, D. Brennecke, A. Nauendorf, M. Thiel, Environ. Pollut., **245**, 545 (2019).
[11] A. M. Gurnell, J. England, L. Shuker, G. Wharton, River Res. Appl., **35**(8), 1359 (2019).
[12] S. M. Shupe, Sci. Total Environ., **603–604**, 745 (2017).
[13] "EarthEcho Water Challenge," 2020. [Online]. Available: https://www.monitorwater.org/. [Accessed: 09-Oct-2020].
[14] E. McGoff, F. Dunn, L. M. Cachazo, P. Williams, J. Biggs, P. Nicolet, N. C. Ewald, Sci. Total Environ., **581–582**, 105 (2017).
[15] L. Quinlivan, D. Chapman, T. Sullivan, Sci. Total Environ., **699**, 134255 (2019).
[16] B. Weeser, J. Stefert Kroese, S. R. Jacobs, N. Njue, Z. Kemboi, A. Ran, M. C. Rufino, L. Breuer, Sci. Total Environ., 631–632, 1590 (2018).
[17] S. Etter, B. Strobl, I. van Meerveld, J. Seibert, Hydrol. Process., **34**(22), 4365 (2020).
[18] " Public Lab: Foldable Spectrometry Starter Kit." [Online]. Available: https://publiclab.org/wiki/foldable-spec. [Accessed: 27-Oct-2020].
[19] J. Storer, J. Chao, A. Torelli, A. Ostrowski, Informing Sci., **19** (1), 125 (2016).
[20] R. Bardaji, A. M. Sánchez, C. Simon, M. R. Wernand, J.

Piera, Sensors, **16**(3), 1 (2016).
[21] L. Breuer, N. Hiery, P. Kraft, M. Bach, A. H. Aubert, H. G. Frede, Sci. Rep., **5**, 1 (2015).
[22] A. Jollymore, M. J. Haines, T. Satterfield, M. S. Johnson, J. Environ. Manage., **200**, 456 (2017).
[23] N. Michelsen, H. Dirks, S. Schulz, S. Kempe, M. Al-Saud, C. Schüth, Sci. Total Environ., **568**, 189 (2016).
[24] J. Fohringer, D. Dransch, H. Kreibich, K. Schröter, Nat. Hazards Earth Syst. Sci. Discuss., **3**(7), 4231 (2015).
[25] "EurActiv," 2020. [Online]. Available: https://www.euractiv.ro/infosociety/aproape-zece-milioane-de-utilizatori-facebook-in-romania-13323. [Accessed: 28-Oct-2020].

*Corresponding author: elfrida.carstea@inoe.ro

Assessing environmental factors related to COVID-19 transmission in Bucharest city, in Romania

M.ZORAN, R. SAVASTRU, D. SAVASTRU, M. TAUTAN, L. BASCHIR, D. TENCIU,

National Institute of R&D for Optoelectronics, Atomistilor Street 409, Magurele, Romania

Abstract: The relationship between air quality and main climate variables with incidence of SARS-CoV-2 viral infection transmission and COVID-19 pandemic disease in Bucharest, metropolitan region of Romania was quantified, with a focus on inhalable particulate matter PM10 and ground levels of ozone and nitrogen dioxide. The analysis of 15 March- 15 October 2020 time period found positive correlations of COVID-19 incidence with air quality index, ground level ozone, and air temperature and negative correlations with planetary boundary layer height, air relative humidity, net solar radiation and wind speed intensity, which suggest possible airborne pathway of viral infection.

Keywords: Coronavirus COVID-19; Air Quality Index; particulate matter PM10; ozone and nitrogen dioxide; climate variables and Planetary Boundary Layer.

1. Introduction

The novel coronavirus disease (COVID-19) is a highly pathogenic, transmittable and invasive penumocaoccal disease caused by Severe Acute Respiratory Syndrome Coronavirus 2 (SARS-CoV-2), which emerged in December 2019 and January 2020 in Wuhan city, Hubei province, China and fast spread later on the middle of February 2020 in the Northern part of Italy and Europe. During COVID-19 pandemic global outbreak ongoing progression at an accelerating rate worldwide, viral infection transmission risks depend on spatio-temporal distribution of pathogens in some complex environmental conditions. Is well known that aerosols might transport bioaerosols (viruses, bacteria and fungi) and facilitate infection [1], while air pollution and climate parameters (air temperature, air relative humidity, wind speed intensity, air pressure and planetary boundary layer height) variation might decrease the human immune and cardiorespiratory systems defenses [2]. Due to oxidative potential of air pollutants like as particulate matter PM2.5 and PM10, ozone (O_3) and nitrogen dioxide (NO_2), several epidemiological and toxicological studies demonstrated their adverse effects on air airway inflammatory and cardiovascular diseases. At the near-surface atmosphere, particulate matter can attach different viruses, which can damage innate immune recognition receptors that respond to unique pathogen-associated molecular patterns [3]. Regarding seasonality of SARS-CoV-2, the genetic drift is currently unknown, and according to previous viral infections pandemic known as SARS and MERS-CoV, new waves infections are likely to occur, with unpredictable height and breadth of the waves [4]. This paper investigates the impact of poor urban air quality described by high values of air quality index (AQI) together climate conditions on COVID-19 pandemic increased incidence in Bucharest metropolitan area during 15 March-15 October 2020 time period, aiming to provide scientific evidence regarding the relationship with air temperature, air relative humidity and air quality index with fast diffusion of SARS-CoV-2 viral infections for epidemiological studies.

2. Background and Methods

2.1. COVID-19

The new coronavirus, SARS-CoV-2, is an enveloped, positive-sense, single-stranded RNA virus associated with a nucleoprotein within a capsid comprised of matrix protein and is in the betaCoV genus [5]. Its associated fatalities might be related to cytokine storm syndrome, also known as hypercytokinemia, which is characterized by an uncontrolled release of pro-inflammatory cytokines, being a severe reaction of the immunity system, leading to death. Like previous coronaviruses versions SARS-CoV and MERS-CoV, SARS-CoV-2 has high mutation rates that result in viral genetic diversity, plasticity, and adaptability to invade a wide range of hosts. SARS-CoV-2 viruses are roughly spherical or moderately pleomorphic virions of approximately 60 to 140 nm with an average to 0.1µm in diameter. SARS-CoV-2 viral genome contains distinctive features, including a unique N-terminal fragment within the spike protein, which allows coronavirus attachment on ambient air pollutants. Presently the main considered routes of COVID-19 transmission in humans are: 1) inhalation of respiratory droplets sprays (sneeze or a cough) - typically greater than 5 µm in diameter [6]; 2) direct contact with infected persons and 3) contact with contaminated surfaces. In confined spaces, like hospitals was found the bioaerosols transmission of SARS-CoV-2 pathogens in two distinct size ranges (0.25 to 1.0 µm), and with diameter larger than 2.5 µm [7]. SARS-CoV-2's capacity to be attached on airborne particulate matter supports the hypothesis of outdoor airborne viral diffusion as a possible pathway of COVID-19 viral infection transmission. Also, outdoor specific climate conditions (as temperature, wind speed, humidity) can be top predictors of airborne coronavirus illnesses diffusion [8]. The epidemiological dynamics of COVID-19 has changed dramatically over the course of months. The key to decrease transmission and combating COVID-19 virus is to create awareness of the facts that it typically causes the disease and how well it spreads.

2.2. Air pollution

Both indoors and outdoors, the air we breathe, is contaminated by particles, gases, bacteria and viruses originating from natural and anthropogenic sources that can reach the eyes, the nose, the upper and lower airways, and the lung parenchyma [9]. Exposure to ambient near-ground hazardous atmospheric pollutants primary particulate matter PM, Black Carbon (BC), ozone (O_3), nitrogen dioxide (NO_2), carbon monoxide (CO), volatile organic compounds (VOCs) and various heavy metals is associated also with a wide range of adverse environmental and health effects especially in large cities [10]. Particulate matter (PM) air pollution consists of a multi-component matrix originating from various anthropogenic sources (power generation, traffic-related, etc.) and natural sources (biomass combustion, dust, etc.) with a great spatio-temporal variability, being subject to several atmospheric processes of transport and removal. In metropolitan agglomerated regions like Bucharest, PM concentration is normally dominated by different size fractions (the ultrafine particles PM0.1 with diameter < 0.1 µm; fine particles PM2.5 with diameter ≤ 0.2.5 µm; coarse particles PM10 with diameter > 0.2.5 µm and ≤ 10 µm. PM2.5 mainly originating from combustion processes, are considered most toxic for respiratory and cardiovascular system, with strong inflammatory potential [11], being associated with increased morbidity and mortality. If coarse PM10 deposit mainly in the upper and large conducting airways, being used as air quality indicator, fine PM or PM2.5 µm deposit throughout the lower respiratory tract, particularly in small airways and alveoli [12].Due to chemical composition and sometimes associated bacteria and viruses, PM might have toxic heavy metals on their surface, which can enhance their toxicity. Also, epidemiological studies revealed their important impacts on infectious disease spread, serving as transmission items for numerous and diverse types of viruses, including influenza viruses, and lethal coronaviruses viruses. Long-term chronic or just short –term exposure to air pollutants in metropolitan regions might have a significant role in the spread of Covid-19, being associated with a reduction in lung function and induction of respiratory symptoms including cough, shortness of breath and pain on deep inspiration [13]. As a secondary air pollutant, ambient ground-level O_3 is a known respiratory irritant of great concern due to its widespread pollution and adverse health effects proven by several environmental epidemiological studies, which focused on its toxicity and negative impacts on respiratory and cardiovascular systems respiratory [14]. O_3 is a gas that occurs both in the Earth's upper atmosphere (stratosphere) and at ground-level. While stratospheric ozone is considered to be "good" acting as a barrier for ultraviolet rays, in the troposphere and at the ground-level it is a secondary air pollutant generated through a series of complex photochemical reactions involving solar radiation and ozone-precursors. NO_2 is a ubiquitous atmospheric gaseous pollutant which contributes to respiratory inflammation, responsiveness, infections and symptoms [15]. The anthropogenic NO_2 in the ambient air is mainly from the combustion processes primarily from traffic-related sources road transport, energy production, industry, etc. Long-term and short-term exposure to O_3 and NO_2 is associated with increased morbidity and mortality risk. Climate change is expected to increase O_3 and NO_2 concentrations as well as the number of high ozone days in urban areas around the globe, potentially heightening adverse impacts on respiratory health [16-17].

2.3. Investigation test site

Bucharest metropolitan (44.43°N, 26.09 °E) area (Figure 1) is located in the South-Eastern part of Romania in a flat region, with a total surface of 5,080 km^2 and and has about 1.9 million inhabitants. The metropolitan area of Bucharest is made up of 7 counties. Bucharest's traffic follows an increasing trend, mainly due to the extended car use. Cars are becoming more and more numerous, ~1.5 million vehicles per day present in Bucharest for 1.85 million inhabitants, compared to EU average of 505,000 passenger cars per 1 million inhabitants. Thirdly, another source for air pollution within the city is heating based on fossil fuels such as coal and natural gas. Traffic related pollution to extensive use of old cars is responsible of recorded high concentration levels of air pollutants like as NO_2, O_3, CO_2, SO_2 and particulate matter PM2.5 and PM10, which sometimes exceed critical standard limits for Romania and European Union (Zoran et al., 2019a). Despite general downward trends in emissions over recent years, all European metropolitan regions still presents exceedances of air quality legal limits according to the Directive 2008/50/EC in Europe Standards.

Figure 1.Test site Bucharest metropolitan zone on Landsat 8 OLI 19/07/2020 image

2.4. Data and statistical analysis used

Time series data of daily average air pollutants PM10, O_3 and NO_2 for selected monitoring station Bucharest in Romania have collected from https://aqicn.org/. Time series meteorological data, including daily average temperature (T), daily average relative humidity (RH),daily average wind speed were retrieved from (https://www.wunderground.com/ and meteoromania.ro). Planetary Boundary Layer PBL heights data were collected from the archived data of NOAA's Air Resources Laboratory (https://ready.arl.noaa.gov). Origin 10 software was used for time series data analysis. In order to describe urban air quality of selected metropolitan area of Bucharest, this paper considered daily Global Air Quality Index (AQI) according to classification of air quality (http://www.eurad.uni-koeln.de) and EU regulations, which is defined function of the main air pollutants concentrations (O_3, PM10, NO_2, SO_2, CO) and classified in six classes from very good to very poor. Almost real time data for coronavirus COVID-19 Total, Daily New and fatalities cases recorded for Romania and Bucharest have been retrieved from www.statista.com and https://www.worldometers.info/. On 29 October 2020 in Romania have been recorded 229,040 COVID-19 positive confirmed cases and 6,764 deaths, of which in Bucharest metropolitan region 14.58% cases. In this study, to assess the relationship between main air pollutants PM2.5, PM10, O_3 and NO_2, climate variables data and COVID-19 infections and fatalities, Spearman correlation test was used. Spearman correlation coefficient was selected as a proper measure of the strength of the linear relationship between pairs of two variables. To compare each air pollutant data with data of climate signals, all the data have been standardized. The value of Spearman coefficients varies from 1 - to 1. If the two variables are in perfect linear relationship, the correlation coefficient will be either 1 or –1. The sign depends on whether the variables are positively (directly) or negatively (inversely) related. The correlation coefficient is 0 if there is no linear relationship between the variables. Also, the p-values, with 0.05 significance level, were calculated to accept (reject) the statistical significance of the correlation between pairs of two variables. Correlation coefficients and p-values were calculated using ORIGIN 10 software. For a better correlation analysis, also a simple regression analysis (quadratic model) was used.

3. Results and discussion

3.1 Impact of air quality on COVID-19 pandemic incidence

Humans consume daily: ~ 1.3 kg food; 2 l water and 10.8 l air. Urban areas are affected by air pollution due to natural (dust, pollen, mold, etc.) and anthropogenic sources (traffic-related, old cars, industrial, etc.). In spite of EU, and Romanian legislation as well as of control regulation by World Health Organization, threshold limits for different pollutants recorded exceedances, which became a major problem in Romania and Bucharest. Main air pollutants in the surface air with harmful effects on cardio-respiratory and immune system: particulate matter in different size fractions (PM1, PM2.5, and PM10) and gaseous pollutants-ozone, nitrogen dioxide NO2. The temporal analysis of ground level air pollutants has been conducted on a regional scale for Bucharest capital of Romania, and combined with the recorded number of COVID-19 cases per city. To analyze short- and medium-term effects of air pollution on fast COVID-19 virus diffusion, and quantify the lockdown effect on air pollutants levels, the daily average concentrations of PM10, O_3 and NO_2, were computed for two time windows periods pre-lockdown (from 1st January 2020 - 15 February, the start date of the lockdown for Bucharest and beyond lockdown for each selected town till 15 October 2020). Several sanitary restrictions (industry, travel, aerial-road traffic) during lockdown (15 March 2020) in Romania, were related with drop in air pollution emissions during COVID-19 lockdown period (15 March 2020 and beyond): NO2 clearly reduced by 42% compared with the same period 2015-2019, PM10 recorded not much change and O3 increased by 1.57 factor due to reduction of related traffic NOx emissions leading to a lower O3 titration by NO in synergy with spring seasonal variation. This study found that during investigated period, daily average ground-level ozone concentrations values were positive correlated with all COVID-19 cases (confirmed Total, confirmed Daily New positive and Total Deaths) for Bucharest analyzed city. Particulate matter as well other aerosols could act as carriers for viruses and the increasing quantity of PM offered more medium for airborne microbes to adhere. Furthermore, the main sources of airborne microbes and viruses come from local, regional or transboundary sources. Low positive correlations between Daily New COVID-19 cases and PM10 and AQI have been recorded during invetigated period. In good accordance with scientific literature, daily average ground level ozone concentrations were negative correlated with daily average concentrations of particulate matter PM10 for Bucharest r= -0.37 with p-value <0.01, while daily average NO_2 was positively correlated with PM10, namely r= 0.25 with p-value <0.01. Figure 2 presents temporal variation of the daily average concentrations of the main air pollutants PM10, O_3 and NO_2 together with AQI and Daily New COVID-19 cases recorded in Bucharest during 15 March – 15 October 2020.

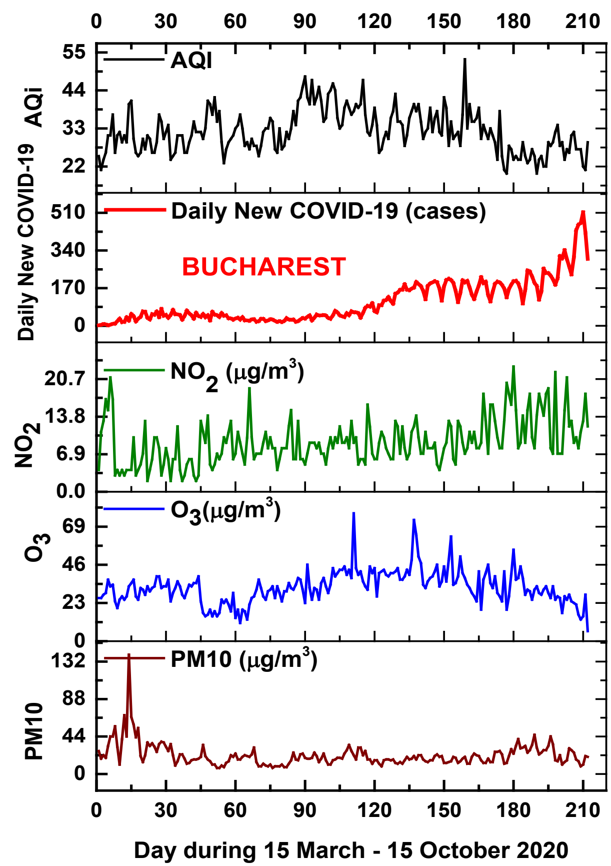

Figure 2. Temporal variation of the main air pollutants and AQI and Daily New COVID-19 cases recorded in Bucharest during 15 March – 15 October 2020.

3.2 Association between atmospheric variables and COVID-19

Presently, the pathogenesis of COVID-19 deadly epidemics is not yet very clear, but its existence as viral bioaerosol indoors and outdoors explains its pathogenicity. Scientific evidence linked short- and long-term exposure to high levels of ambient air pollution with a consistently higher risk for respiratory and cardiovascular systems, and viral infectious diseases transmission observed at time-lag 0-1 day [18-19]. Airborne microbial communities (bacterial, fungal, viral), known as bioaerosols and their seasonal shift in both the concentration and biodiversity have been systematically observed in the planetary boundary layer (PBL) and especially in urban areas[20]. The seasonal variability was associated to changes in surface air conditions at landscape interactions, meteorological conditions, and/or changes in the global air circulation [21-22]. With increasing the amplitude of seasonal fluctuations in air temperature and relative humidity, and wind intensity regimes lead to more intense epidemics and elevated base transmission potential in metropolitan areas. In its relation with COVID-19 viral infections transmission incidence, air temperature is a very important climate variable. In the densely built-up urban areas air temperature can be warmer than that of rural surroundings by up to several degrees Celsius, especially during the night. This heating phenomenon being known as the urban heat island (UHI), not only impacts the thermal stability of PBL directly but also affects the transport of PM and gaseous pollutants by inducing local thermal circulation, microclimate, and dispersion, and deposition of pollutants within street canyons. The results iof this study indicate positive correlations of SARS-CoV-2 viral infection spreading with daily average air temperature in Bucharest, Spearman rank correlation coefficients having positive values with all COVID-19 cases namely: $r=0.66$, $p=0$ for Total COVID ; $r=0.66$, $p=0$ for Total Deaths and $r=0.51$, $p<0.01$ for Daily New COVID confirmed positive cases during 15 March -15 October 2020. Negative Spearman correlation coefficients with planetary boundary layer heights-PBL have been recorded with COVID-incidence all cases in Bucharest during investigated period ($r= -0.33$, $p<0.01$ for Total COVID; $r= -0.28$ for Total Deaths and $r= -0.29$, $p<0.01$ for Daily New COVID confirmed positive cases). Also, this study found negative correlations of COVID-19 incidence with daily average air relative humidity, namely: $r= -0.37$, $p<0.01$ for Total COVID;$r= -0.48$ for Total Deaths and $r= -0.21$, $p<0.01$ for Daily New COVID confirmed positive cases. Spearman rank correlation coefficients having negative values with all COVID-19 cases have been recorded for daily maximum net solar radiation namely: $r= -0.27$, $p<0.01$ for Total COVID; $r= -0.25$ for Total Deaths and $r= -0.24$, $p<0.01$ for Daily New COVID confirmed positive cases. Negative correlations have been registered for daily average wind speed intensity and planetary boundary layer heights. Figure 3 presents temporal pattern of Daily New COVID-19 confirmed positive cases in relation with daily climate variables during 15 March- 15 October 2020 period in Bucharest. Associated with hot summer air temperatures (atributed to heat waves in synergy with urban heat island phenomena), from late June 2020 till the beggining of September was recorded was recorded a sharp „start-up" of second COVID-19 viral infection wave in Bucharest. This moment was marked by a blue arrow on graphic. Spearson correlation coefficients between daily mean ground-level particulate matter PM10 concentrations were negative correlated with daily average air temperature and Planetary Boundary Layer height and positive correlated with daily average relative humidity and Air Quality Index. Is well recognized that both indoor as well as outdoor air relative humidity is an important factor in determining respiratory diseases severity.This study supports the hypothesis that air relative humidity is an essential climate factor for COVID-19 virus viability, dry weather conditions being favorable for COVID-19 viral infection spreading, while humid weather conditions have an opposite effect.

According with present literature in the field of virusology and epidemiology, this research can play an important role of air relative humidity in understanding COVID-19 viral infectivity and transmission, which is negatively correlated with all COVID-19 cases registered in Bucharest. Based on these information, we hypothesize that air pollutants could enhance the transmission capability of SARS-CoV-2 through cluster of aerosols, which disrupt the integrity of human respiratory barrier and form condensation nuclei for viral attachment [7-8]. Infections caused by airborne pathogens like viruses and bacteria are dependant on several factors:

1) the emission rate of pathogens, function of pathogen availability and the aerosolization rate; meteorological (wind speed, wind direction, solar radiation, atmospheric stability, wet or dry deposition) effects;

2) inactivation of pathogenic bioaerosols like viruses or bacteria that is a function of time or meteorological

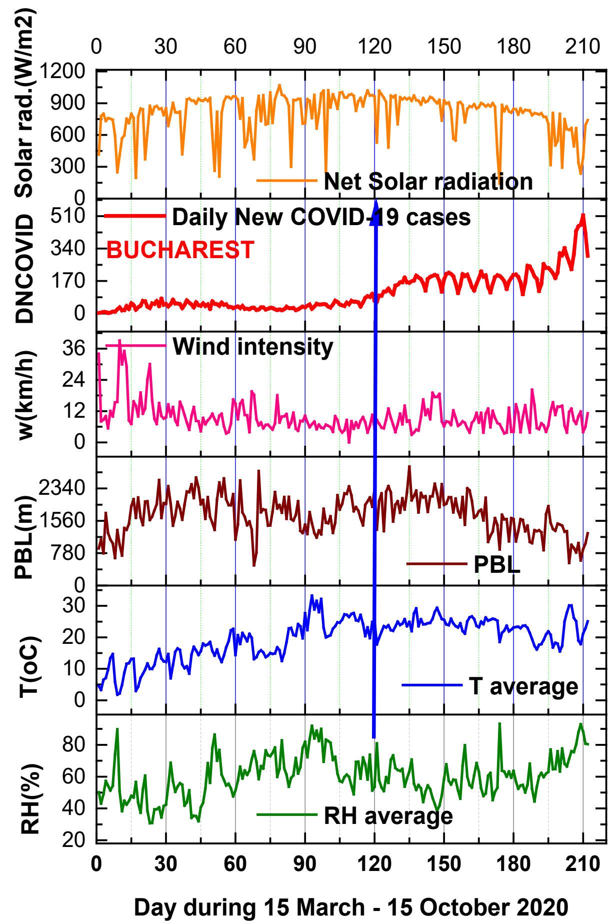

Figure 3. Temporal pattern of Daily New COVID-19 incidence in relation wih daily variation of climate variables.

conditions, such as temperature and humidity, and may be in the time range of minutes to hours or days;

3) the amount of inhaled pathogens, with breathing rate, lung volume, and particle size being important factors; the host's health response as a function of inhaled dose [23].

All these factors can affect the degree of viability and spread of contagious viruses like COVID-19. Viral aerosol diffusion considers the possibility that fine virus particles, called droplet nuclei, to remain airborne for prolonged periods. This viral aerosol transmission involves particles of diameter < 5 µm [24]. For coronavirus, the airborne transmission has not yet been clearly established but there is growing evidence for aerosol-driven infection. Production of infectious droplets and subsequent spread to surrounding environment is determined by generation and annihilation processes and may be affected by many variables such as air temperature, relative humidity, air mass concentrations, wind intensity, etc. Inactivation of pathogenic bioaerosols like viruses or bacteria is function of time or meteorological conditions (such as air temperature and humidity), and may be in the time range of minutes to hours or days, while spores are generally highly persistent [25]. Statistical analysis provided by this research shows that daily average ground level PM10 concentrations in selected city were negative correlated with daily average air temperature and Planetary Boundary Layer, in good accordance with other studies [26-29] and positive correlated with daily average air relative humidity and Air Quality Index. As higher humidity levels are associated with large cloud cover and atmospheric instability, PM are depleted by wet deposition on water droplets. Furthermore, air temperature also contributes towards the transmission of the virus [28], suggesting that air humidity and temperature will play an important role in mortality rate from COVID-19, as climate variables are direct correlated with the spread of COVID-19. Several papers had provided experimental evidence that transmission of some viral infectious diseases via the airborne route is very important step in viral transmission [30-33]. Furthermore was evidenced that there is a relationship between incidence or transmission and air humidity, because the viruses in droplets and aerosols survive well at low relative humidity below approximately 50%, and opposite for high levels of humidity [34-35]. The trend analysis by polynomial regression of Daily New COVID-19 confirmed cases in relation with daily average relative humidity, shows a strong positive correlation (R^2 = 0.7978).

Conclusion

This study provide scientific evidence regarding the influence of ground surface air pollution and climate factors on COVID-19 diffusion in Bucharest. Were found positive correlations of AQI and O_3 concentrations, and negative correlations of NO_2 with the increased rates of COVID-19 infections (Total confirmed positive, Daily New and Total Deaths cases), which can be attributed to airborne bioaerosols distribution and climate conditions. Also, this study found positive correlations of COVID-19 infections with air temperature and PBL heights, and negative correlations with relative humidity and wind speed, that means the new coronavirus might be ongoing during summer conditions associated with higher air temperatures and PBL heights, and low relative humidity levels. COVID-19 lockdown resulted in a large drop of NO2 and PM emissions.

Acknowledgements

This work was supported by Romanian Ministry of Research and Innovation Contract nr.18 PCCDI/2018- VESS-3PIMS, Project MCI CDI Contract nr.19 PFE/17.10.2018 and Program NUCLEU Contract 2020.

References

[1] R. Lu, X. Zhao, J. Li, et al. Lancet **395** (10224), 565-574 (2020).
[2] L.Mousavizadeh, S.Ghasemi, Journal of Microbiology, Immunology and Infection, https://doi.org/10.1016/j.jmii.2020.03.022, (2020)
[3] F. Rivellese and E. Prediletto, Autoimmunity Reviews, (2020) https://doi.org/10.1016/j.autrev.2020.102536
[4] Shang J, Ye G, Shi K, Wan Y, Luo C, Aihara H, et al., Nature **1–8**. (2020) https://doi.org/10.1038/s41586-020-2179-y
[5] H.Nishiura, N.M.Lintona, A.R.Akhmetzhano, International Journal of Infectious Diseases **93**, 284-286, (2020).
[6] X.Seposo, K.Ueda, S.Sugata, A.Yoshino, A.Takami, Science of the Total Environment, (2020) https://doi.org/10.1016/j.scitotenv.2020.138934.
[7] L.Setti, F.Passarini, G. De Gennaro, P.Barbieri et al., Int J Environ Res Public Health **17**(8), 2932, (2020a)doi: 10.3390/ijerph17082932.
[8] L.Setti, F.Passarini, G. De Gennaro, P.Barbieri et al., Environmental Research **188** 109754, (2020b) https://doi.org/10.1016/j.envres.2020.109754
[9] S.K.Pani., H.H.Lin, S.Ravindra Babu, Science of the Total Environment **740**,140112, (2020).
[10] W. Smets, S. Moretti, S. Denys, S. Lebeer, S. Atmos. Environ. **139**, 214-221 (2016).
[11] JS.Silva, JP.Rojas, M.Norabuena, RJ.Seguel. Atmosphere & Health **11**, 993-1008 (2018).
[12] Sugiyama J.T., Ueda K., Seposo X.T.,et al. Science of the Total Env.**709**, 136023 (2020).
[13] J.Burns, H. Boogaard, S. Polus, L.M. Pfadenhauer, et al.Environ. Int. **135**, 105400 (2020).
[14]Y.Cao, M. Chen, D. Dong, S. Xie, M. Liu, M. Thorac. Cancer. **11**, 505–510 (2020).
[15] M.Carugno, F. Dentali, G. Mathieu et al. Environ. Res. **166**, 452–457 (2018).
[16] CK.Chan, X, Yao X. Atmos Environ. **42**, 1–42 (2008).
[17] M.Z. He, P.L. Kinney, T. Li,et al. Environ. Pollut. **261**, 114165 (2020).
[18] R.Tignat-Perrier, A. Dommergue, A.Thollot, et al. Science of The Total Environment **716**, 137129 (2020).
[19] T. Ruiz-Gil, J. Acuna, S. Fujiyoshi, et al. Environment International **145**, 106156 (2020).
[20] Y. Miao, X.M. Hu, S. Liuet al. J. Adv. Model. Earth Syst. **7**, 1602-1626 (2015).

[21] E. Innocente, S. Squizzato,F. Visin et al. Science of The Total Environment **593–594**, 677-687 (2017).
[22] J.Uetake, Y.Tobo,Y. T.C.J.Hillet al. bioRxiv, **542001** (2019).
[23] N.Sundell, L.M.Andersson, R.Brittain-Long, et al. Journal of Clinical Virology **84**, 59–63 (2016).
[24] I. B.Tager et al. Epidemiology **16**, 751-759 (2005).
[25] J.Tan, L.Mu, J. Huang et al. J. Epidemiol. Community Health **59**, 186–192 (2005).
[26] A.Tobias, X.Querol, et al. Sci. Total Environ. **726**, 138540 (2020).
[27] R.Tosepu, J.Gunawan et al. Sci. Total Environ. **725**,138436 (2020).
[28] N. van Doremalen, T. Bushmaker, DH Morris DH et al. N Engl J Med **382**(16), 1564-1567 (2020).
[29] L.C Marr, J.W Tang et al. Journal of the Royal Society, Interface, **16** (150), 20180298 (2019).
[30] E.P.Vejerano, L.C Marr. J. R. Soc. Interface **15**, 20170939 (2018).
[31] Y.Wan, J.Shang,S.Sun et al. J.Virol.**94**(5) (2020).
[32] D.Wang, B. Hu, C. Hu et al.. JAMA, **323**(11) (2020).
[33] Q.Wang, M.Su. Science of The Total Environment **728**, 138915 (2020).
[34] M.Zoran, R.Savastru, D.Savastru, M.Tautan. Science of The Total Environment **738**, 139825 (2020).
[35] M.Zoran, R.Savastru, D.Savastru, M.Tautan. Science of The Total Environment **740**, 140005 (2020).

*Corresponding author: mzoran@inoe.ro

Determination of the optimal frequency for the detection Cherenkov cone of electromagnetic radiation in saline environment

V. SAVU 1[a], M. I. RUSU 1[a*]
1[a] National Institute of Research and Development for Optoelectronics – INOE2000, 409 Atomistilor Street, PO BOX MG-5, RO 077125, Magurele – Ilfov, Romania

Abstract: Cherenkov cone moves in the same direction as the neutrino, keeping its angle at the top of the cone. The electromagnetic effect of the Cherenkov cone is perpendicular to the lateral surface of the cone and has direct the energy proportional to the energy of the neutrino. The optimal propagation of electromagnetic waves generated by the Cherenkov cone in the saline environment is achieved for a frequency specific to this environment. In this article we aim to develop a method by which to determine this optimal frequency. The determination of the Cherenkov cone brings new information about the Universe.

Keywords: Cherenkov, cone, frequency, saline, environment, radiation, electromagnetic

1. Introduction

Cosmic radiation began to be studied between 1911 and 1913. During this period, the Austrian physicist Victor Hess, flying with balloons, measured the variation of ionization present in the air with altitude [1]. Neutrinos transported by cosmic radiation have very high energies of the order ($10^{15} \div 10^{23}$) eV, those with energy between ($10^{15} \div 10^{21}$) eV can be detected in saline environment, and those with energies higher than 10^{21} eV cross the terrace.
Following the analysis of the experimental results, it was possible to take the first step in knowing and understanding the origin of cosmic radiation [2]. Today, cosmic radiation detectors placed in different environments (salt, silicon sand, ice from poles, etc.) are used. Cosmic radiation that propagates through these environments can interact producing effects in the acoustic, radio and optical fields [3]. The detection of cosmic radiation in the case of energies up to 10^{14} eV can be performed directly, i.e. using measurements by placing instruments on satellites or balloons. In the case of cosmic radiation with high energies (particles with energies > 10^{14} eV), their detection is performed by indirect experiments, i.e., the primary particle is no longer directly detected, but the effect of secondary particles is created as a result of the interaction of the primary particle with the environment through which it passes. The results of experimental measurements at very high energies are, so far, relatively few, due to the fact that the occurrence of these cosmic phenomena is very rare [4], [5], [6], [7].
In order to observe very high energy neutrinos in the case of

a cosmic radiation detector (it occupies a large volume) it is necessary to place it in a salt mine and in this case, we can identify the origin of extragalactic sources that produce these neutrinos [8]. Determining neutrinos with energies higher than 10^{12} eV can lead to discover new astrophysical systems and new physical processes [9]. The direction from which these very high energy neutrinos come is a direct indicator of the source that generates them, so a cosmic radiation observer in a salt mine will have to fulfil this goal [9].

The phenomenon by which high-energy charged particles are detected due to the interaction with the environment is called the Askaryan effect and consists in the coherent emission of Cherenkov radiation in the radio frequency domain, through an excessive electrical overload that occurs during the development of an electron cascade. . Cherenkov radiation occurs in the case of particles moving through an environment at a higher speed than the speed of light through that environment [10].

The interaction between a neutrino with a very high energy and a dense and dielectric medium (salt block) is represented by an avalanche of relativistic particles [9]. When referring to neutrinos with energy higher than 10^{15} eV, only about 20% of it appears as a cascade of hadronic particles, and this cascade has an electromagnetic component [9]. The electromagnetic cascade consists of electrically charged particles (about 70% of the particles) [11]. These particles contribute to the generation of total electromagnetic energy of the waterfall [11]. Particles having a speed of movement higher than the speed of light through a transparent and dense medium (salt block) will produce the Cherenkov (electromagnetic) radiation effect in this medium [10].

Knowing the effects related to the propagation of electromagnetic waves in dielectric media with impurities (saline environment) [12], then, by eliminating the influences of the parameters of the propagation medium, the basic parameters of the transmitting and receiving antennas used in measurements can be inferred. By performing a sufficient number of measurements, these basic parameters of the transmitting and receiving antennas can be determined.

Knowing the electrical parameters of the transmitting and receiving antennas, the electromagnetic radiation of the Cherenkov cone (which is known to be perpendicular to the cone generator) can be detected with much higher accuracy. Then it will be possible to determine the direction and energy level of the neutrino that generated the Cherenkov cone with the same level of precision.

Low energy cosmic radiation is very abundant. On average, about 200 particles with energies of the order of 10^6 eV fall in a second on every square meter of the Earth’s surface [13]. These particles being electrically charged, will be captured by the Earth’s magnetic field and will rotate around the planet and will be pushed slightly towards the poles. Here, they give rise to the northern lights [14].

Neutrinos are almost massless subatomic particles. They are recognized by the fact that they rarely interact with other forms of matter. They are electrically neutral and have a semi-whole spin (own kinetic moment). Being free of electrical charge, neutrinos are not affected by electromagnetic radiation.

Neutrinos are influenced only by the weak subatomic force (fundamental force that governs the interactions between hadrons and leptons) and by gravity [15].

In order to detect cosmic radiation with energies higher than $10^{19.5}$ eV, there must be a neutrino energy flow that has the energy between ($10^{17} \div 10^{19}$) eV [10], [16], [17].

The appearance of a neutrino with this energy range is 10/ km^2/century [10]. For this reason, the neutrino detectors must have an equivalent volume of hundreds of km^3 in order to be able to detect a significant number of events.

Askaryan first predicted the appearance of radio pulses when an ultra-high energy neutrino (UHE) interacts with dense dielectric media [18]. The radio pulses come as a result of the appearance, in the propagation medium, of an excessive negative charge due to a charge asymmetry. This asymmetry occurs as a result of electron and photon scattering processes. Askaryan also proposed some natural materials as volumetric detectors (the salt present in saline environment, ice at the poles and the soil of the moon) [19].

The interaction of a neutrino with UHE energy in a dielectric medium gives rise to charged primary particles (electrons). These electrons produce electromagnetic radiation and at the same time produce other charged particles [20].

The Askaryan effect is the phenomenon by which a particle travels through a solid and dense dielectric medium faster than light through this medium. Then there is a "rain" of anisotropic elements in the form of secondary particles emitting a radio coherent radiation cone (Cherenkov cone) in the electromagnetic spectrum [21].

Following the detection of the Askaryan effect (it is a relatively rare phenomenon) a radio radiation cone appears in the form of pulses (Cherenkov cone). The solid angle of the cone is the measure of the energy of the incident primary particle. To determine the energy of electromagnetic waves, antennas with very high frequency bands are used. These antennas will be placed in a cube with a side of 1000 m (example) as shown in **Figure 1**. [22].

In order to increase the chances of neutrino interaction processes (in order to be able to detect them), they will have to cross a mass of matter as consistent and homogeneous as possible [23]. For this we could use as natural detectors massive blocks of salt deposits or even massive blocks of ice in Antarctica (Figure 3). For the detection of ultra-high energy

Fig. 1. Neutrino detector in salt block, consisting of antennas placed in a cube with a side of 1km [22].

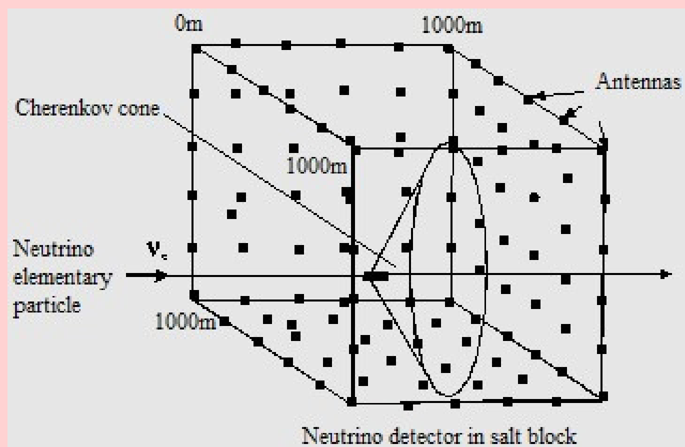

neutrinos, it would be useful to choose salt deposits that can contain blocks with a size of 3 km × 3 km × 3 km (27 km^3) and thus reach masses of the order of 50 Gt [24], [25].

The principle of Cherenkov detectors is based on the fact that when a particle passes through a medium and moves at a speed higher than the speed of light through that medium, an electromagnetic radiation will be emitted (Cherenkov Effect). Cherenkov detectors have the property that they can discriminate particles at different speeds. Being possible to measure the impulses of these particles, then we can say that discrimination can be made after the mass of the particles [26], [27], [28].

Due to an inhomogeneous distribution of impurities in the saline environment, it is not possible to make a theoretical approach to the phenomenon of electromagnetic wave propagation in this environment, so it is necessary to make an antennas system (a transmitting antenna and a receiving antenna) with adaptation and symmetrisation for coupling the antennas to the necessary equipment (a signal generator as transmitter and a signal analyser as receiver) [29], [30].

To determine the spatial position and energy level of the Cherenkov electromagnetic radiation cone it is necessary to make a cosmic radiation detector in a saline environment because the noise level is very low [25], [31].

The detection of the Cherenkov cone generated by the interaction of a neutrino with very high energy (10^{15} eV ÷ 10^{21} eV), the case of the saline environment), brings new information about the very distant Universe

In order to detect as accurately as possible, the Cherenkov cone (the energy level of the electromagnetic radiation and the spatial position of the Cherenkov cone) in saline environment it is necessary to find an optimal frequency of propagation of electromagnetic waves through this environment.

2. Experimental

High-energy cosmic radiation particles generate electromagnetic waves when they collide with ionosphere molecules. This phenomenon was highlighted by Cherenkov. The Askaryan effect [32] assumes that the average density of the avalanche of particles produces microwave pulses in Cherenkov radiation.

If we take into account the cosmic radiation with very high energies (UHE - Ultra High Energy) then we can determine the electromagnetic effect generated by them. This phenomenon is formed on the basis of two different mechanisms that generate radio frequency signals. The first mechanism is called geosynchrotron radiation. It consists of generating radio waves in the Earth's atmosphere. The generation of radio waves is given by the synchrotron acceleration of electrons and positrons due to the geomagnetic field [33]. The second mechanism is formed when an excess of negative charges occurs in the propagation medium. This excess of negative charges generates Cherenkov radiation where electromagnetic radiation appears perpendicular to the generator of the cone that is formed. The appearance of such radio pulses following the interaction between a UHE neutrino and a dense dielectric medium is called the Askaryan effect [33].

To demonstrate the Askaryan effect, many experiments were performed in dense environments such as: ice block, salt and lunar soil. All these experiments sought to find a frequency at which we have the maximum intensity of radio waves for coherent radiation [18].

To detect the energy of the particle that generates electromagnetic radiation we will use the Askaryan effect applied in a saline environment (Cherenkov radiation produced in saline environment, which generates electromagnetic waves perpendicular to the cone generator). The detection of such elementary particles is particularly difficult. Being neutrinos, they will interact with the environment they come in contact with only through the weak fundamental interaction. In this situation, neutrinos with high energies above 10^{21}eV that reach the Earth, can cross the entire mass of the Earth and will not interact with it, coming out on the opposite side and traveling further through the Universe [23].

A solid block of salt has been shown to be a very good candidate for such detectors, as it undergoes significant changes in its electrical properties, on the basis of which neutrinos passing through the block of salt can be detected. In saline environment, high energy neutrinos (10^{15} eV ÷ 10^{21} eV), interact with this environment producing as final phenomenon, the Cherenkov cone. From the radiation spectrum of the Cherenkov cone we are interested in the radio frequency component of the electromagnetic radiation for which we have an optimal frequency of propagation of these waves.

For the saline environment, a strong coherence of the radio pulses in the frequency band (0.1 ÷ 15) GHz) was observed. In order to determine the optimal frequency of propagation of electromagnetic waves through the saline environment, we designed an antenna system (transmission and reception), for which the working impedance and their physical length were calculated knowing that they work in saline environment.

The behavior of the dipole antenna in dielectric mediums for the propagation of electromagnetic waves is similar to the behavior in vacuum or air except that the impedance and the calculation of the length of the antenna arms change depending on the relative permittivity of the environment in which the antenna is located.

If a group of antennas is introduced into a salt block, then the input resistance and the length of the dipole antenna in $\lambda/2$ will be changed with the real value of the salt permittivity and the penetration depth of electromagnetic waves will depend on tgδ which is exactly the ratio between the imaginary part and the real part of the permittivity.

Antenna parameters are influenced when the antenna switches from working in a vacuum or air environment to working in an environment with a different permittivity to vacuum. Therefore, in the calculation of antennas working in environments with different permittivity than that of vacuum (generally higher), the permittivity of the environment in which the antenna works is taken into account. Media such as salt is an unconventional medium for antennas and therefore the dielectric parameters of the salt for a frequency range between 100MHz and 5GHz must be known.

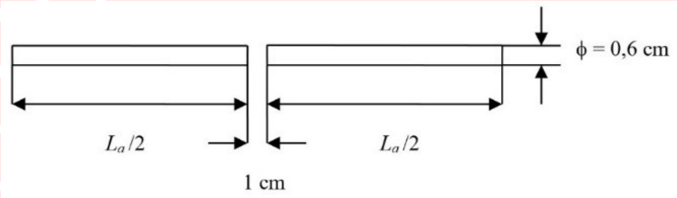

Fig. 2. Antenna dimensions [34].

We used dipole antennas in λ/2 and for the calculation we took into account the fact that they work in a saline environment. The calculation formula is as follows:

(1)

represents the length of the antenna in λ / 2 [m], c = 3 · 108 m / s **λ**/2 [m], c = $3{\cdot}10^8$ and f = the resonant frequency of the antenna [Hz].
Knowing ε_r=5.981 + j0.0835, we will take into account the real part [67]. **Figure 2** shows the antenna shape and dimensions [12], [25], [34], [35], [36], [37] determined by formula (1).

The formula for calculating the radiation resistance of antennas for working in salt is [67]:

(2)
where:
wavelength in the air.

Table 1 shows the lengths calculated for the arms of the antennas with which the measurements were made at the "Cantacuzino" salt mine from Slănic Prahova for different working frequencies (100 MHz ÷ 1GHz). These antennas are needed to determine the frequency at which we have an optimal propagation of electromagnetic waves through saline medium (the minimum attenuation introduced by saline medium). Also here is the value of the resistance and radiation reactance of the antenna (R_{rad} and X_{rad}).

Table 1. Determination of dipole antenna arm lengths in ***λ/2*** *(L_a) as a function of frequency and of the real and imaginary part of the radiation impedance (R_{rad} and X_{rad}).*

f [MHz]	100	300	400	800	900	1000
L_a [m]	0,612	0,204	0,153	0,077	0,068	0,061
R_{rad} [Ω]	29,853	X_{rad} [Ω]	j17,358			

Transformers with transmission lines (balloon) were used to adapt the radiation resistance of the antenna to the impedance of the coaxial cable (RG58LL) of 50Ω. These were made on torches with two holes and for the symmetrization of the antenna power supply were used symmetry transformers. The electrical diagram of the transformer (balloon) with transmission lines and of the symmetrizer is presented in **Figure 3** [12], [25], [35].

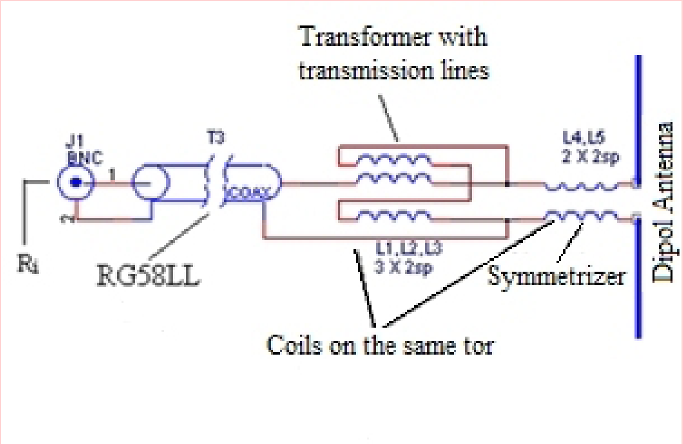

Fig. 3. Wiring diagram of the antenna supply through the transformer with transmission lines and symmetrizer [12], [25], [35].

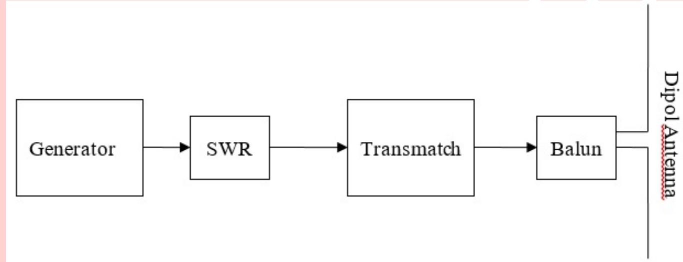

Fig. 4. Method for determining the adaptation of antennas to work in a saline environment.

The transformation ratio of the symmetrization transformer is 1: 1 and of the transformer with transmission lines (balun) is 9: 4 so the resistance seen at the input to the antenna is [12], [25], [35] approximately 30 Ω.

The scheme in **Figure 4** is used to determine the adaptation of the antennas to the working conditions in the saline environment.

An unmodulated signal in the 100 MHz ÷ 1 GHz frequency range was injected from the generator and a unitary standing wave factor (σ = 1) was tracked on the reflectometer (SWR) by adjusting the impedance adapter (Transmatch) to cancel the imaginary part of the antenna impedance and adaptation of the real part to 50 Ω (output impedance of the SIGLENT Generator). The balun is used for the symmetrical loading of the dipole antenna arms in λ/2 of transmission and reception. This assembly was used in the laboratory and at reception a standard antenna was used (multiband with several elements in the vertical plane and with the working impedance of 50 Ω) which was connected to an oscilloscope (Tektronix) with which the maximum signal was measured on frequency for which the antennas were calculated. The table below shows the determination of the antennas length for working in saline environment for the frequency range 100 MHz ÷ 1 GHz.

In order to pass from the 30 Ω impedance to the 50 Ω impedance of the signal generator, an impedance adapter in Π (transmatch) was designed and made. The adjustment of the adapter in Π to the impedance of the generator was made with a circuit to check this adaptation. The minimum indication of the digital measuring instrument (0 mV) indicates that the adapter in Π is set. **Figure 5** shows the antenna, the Π adapter, the Π adapter adjustment check circuit and the digital measuring instrument.

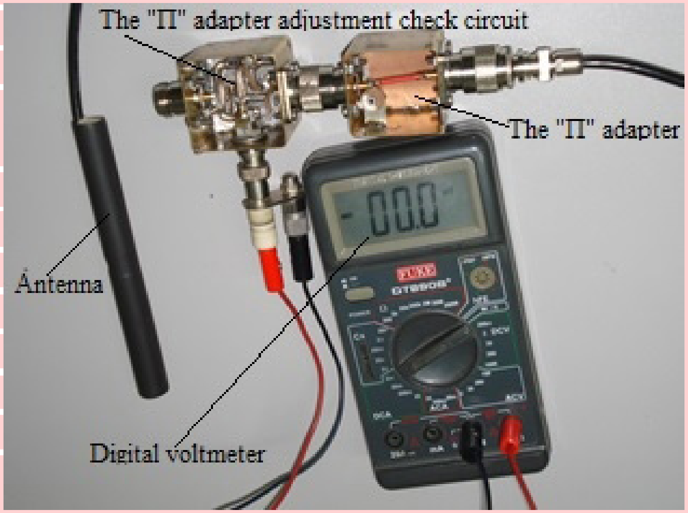

Fig. 5. Adjusting the adapter in Π to the impedance of the generator.

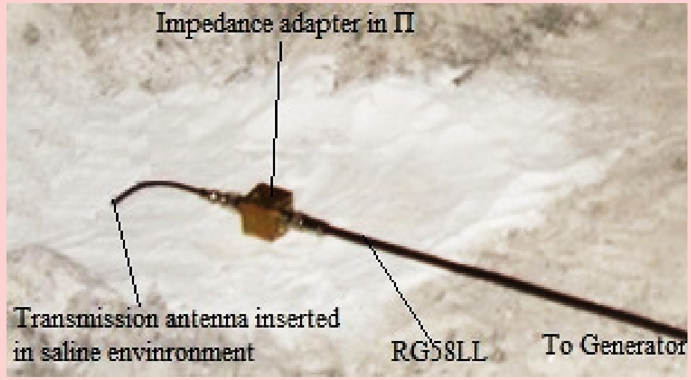

Fig. 6. Realization of the system of measurements in salt.

The adjustment of the adapter in Π is made when the impedance of the generator of 50 Ω is transformed to a value equal to the real part of the antenna impedance of 30 Ω and when the imaginary part is canceled by the impedance adapter in Π by entering by the adaptation circuit an imaginary value so as to cancel the imaginary part of the antenna. So the impedance of the generator will be adapted to the real part of the antenna impedance: $Z_G = 50\ \Omega \rightarrow R_{rad} = 29.853\ \Omega$ and the imaginary part inserted by the adapter in Π will cancel the imaginary part of the antenna: $X_G = 0 \rightarrow X = X_{rad} - X_{trsm} = j17.358 - j17.358$ where X_G represents the total impedance of the signal generator impedance, X_{trsm} represents the reactance introduced by the adapter in Π after adjustment.

3. Results

After making the adjustments, the adapters of the transmitting and receiving antennas, measurements were made in a saline environment (Cantacuzino mine from Slănic Prahova). **Figure 6** shows the transmitting antenna placed in the salt at a depth of 1 m from the floor and 208 m from the surface (entrance to the salt mine). It is connected to the RF generator (radio frequency) via the shielded cable RG58LL with impedance of 50 Ω and the impedance adapter in Π (transmatch) set to adapt the impedance from the dipole antenna terminals in λ/2 of 30 Ω to the impedance 50 Ω signal generator.

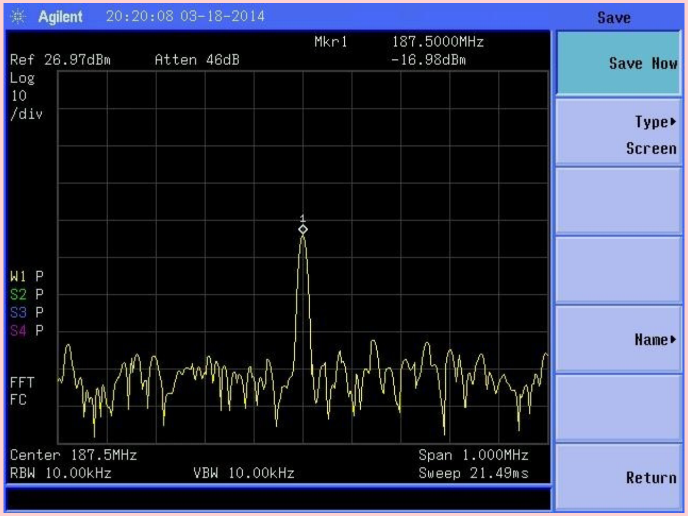

Fig. 7. Measurement of signal amplitude in saline environment with the receiving antenna on the frequency of 187.5 MHz at a distance of 12.1 m from the transmitting antenna.

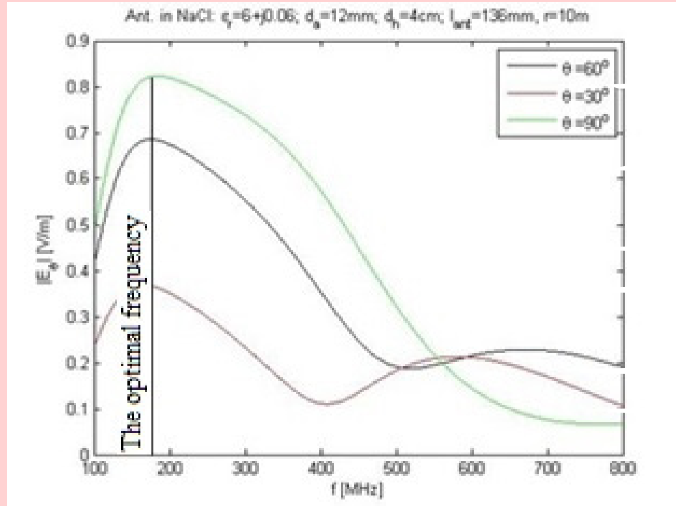

Fig. 8. The electric field generated on average by a dipole antenna as a function of frequency having as parameter the angle with respect to the vertical, ϑ.

A 0 dBm (224 mVpp) signal was injected into the transmitting antenna and at a distance of 12.1 m a signal was received with the receiving antenna placed in a saline environment in the same way as the transmitting antenna. A signal of -16.98 dBm (31.6 mVpp) was measured with the receiving antenna as shown in **Figure 7**.

The field measurements were made according to **figure 6**, where the adapter in Π from **figure 6**, replaces the Transmatch from **figure 4** and the symmetric together with the balloon are located in the space between the two arms of the dipole antenna in λ/2. The transmitting and receiving antennas (for several measurement frequencies) were connected to an Anritsu MS2690A signal analyzer. The field measurements were carried out horizontally and vertically. The receiving antenna moved at different points and at different distances for the two planes keeping the transmitting antenna for the vertical and horizontal plane at a fixed point.By means of these measurements, was determined the propagation of electromagnetic waves through the saline environment (minimum attenuation of electromagnetic waves).

Figure 8 shows the electric field determined in saline environment by a dipole antenna as a function of frequency

having as parameter the angle to the vertical, θ.
This graph shows a maximum reception for all three angles to the vertical θ (30 °, 60 ° and 90 °). The frequency at which the maximum was obtained is around 187.5 MHz and is specific to the saline environment at the Cantacuzino mine in Slănic Prahova at a depth of 208 m from the surface.
The measurements were repeated under the same conditions with several pairs of antennas (transmission - reception). Following the calculations of the measurements, it was established that for the saline environment from the Cantacuzino mine in Slănic Prahova (Romania) the optimal frequency of propagation of electromagnetic waves through saline environment is 187.5 MHz (minimum attenuation of electromagnetic waves).

4. Conclusions

This frequency (187.5 MHz) represents the optimal frequency (minimum attenuation) of propagation of electromagnetic waves through saline environment (Cantacuzino mine from Slănic Prahova, Romania) for the determination of the Cherenkov cone in this type of environment.
By determining the Cherenkov cone in saline, we can extract information about the energy, direction and meaning of neutrinos that interact with saline. Extracting this information provides us with data about the phenomena in the Universe that took place at very great distances from the Earth (much greater than the distances at which the best telescopes can work). These data will increase the horizon of knowledge and will contribute to the development of information about the Universe (astrophysics and astronomy).

Acknowledgements

This work has been carried out on the Core Programme of the Romanian Ministry of Education and Research, National Authority for Scientific Research, PN-19-18 (18N/08. 02. 2019).

References

[1] V.F. Hess, Convection phenomena in ionized gas-ion winds, Phys. Zeit. **13**, (1912), pp. 1084–1091.
[2] I. Bacioiu, The theoretical interpretation of some cosmic rays reaching the sea-level and the meson theory, Romanian Reports in Physics, Vol. **63**, No. 1, (2011).
[3] I. Nuțescu (Băcioiu), Studiul radiației cosmice, Teză de doctorat, București, (2012).
[4] R. Abbasi, Y. Abdou, et. al., An Absence of Neutrinos Associated with Cosmic Ray Acceleration in Gamma-Ray Bursts, arXiv:1204.4219v2 [astro-ph.HE] **11** (2013).
[5] A. Watts, IceCube Neutrino Observatory provides new insights into origin of cosmic rays, (2012).
[6] A. J. Aguilar, IceCube neutrino results and its inplications on astrophysical models, (2013).
[7] A. V. Avrorin, et al., Search for neutrinos from gamma-ray bursts with the Baikal neutrino telescope NT200. Astronomy Letters, **37**, (2011).
[8] E. Waxman, Extra galactic sources of high energy

neutrinos, New J. Phys. **6** 140, (2004).
[9] A. Bădescu, Radio technologies used in cosmic particle detection, Doctor thesis, The Polytechnic University of Bucharest, Romania, (2011).
[10] R. Engel, D. Sekel, T. Stanev, Neutrinos from propagation of ultra-high energy protons, Phys. Rev., **D64**, (2001), pp. 093010.
[11] B. Carroll, D. Ostlie, An introduction to modern astrophysics, Ed. Pearson Addison-Wesley, San Francisco, (2007), pp. 18.
[12] V. Savu, Contributions to the selection and processing of radio pulses produced by cosmic radiations in the specific conditions of an observer built in a saline environment, Doctor thesis, (2014), The Polytechnic University of Bucharest, Romania.
[13] G. Frichter, J. Ralston, D. McKay, On Radio Detection of Ultra High Energy Neutrinos in the Antarctic Ice, Phys. Rev. **D53**, (1996).
[14] R. H. Eather, Majestic Lights - The Aurora in Science, History, and The Arts, American Geophysical Union, Washington DC., (1980), ISBN 0-87590-215-4.
[15] http://zalmoxyss.blogspot.ro/2011/11/neutrinii-viteza-luminii-si-teoria.html
[16] R. Surman, J. Engel, Changes in r-process abundances at late times, Phys. Rev. **C64**, 035801 (2001).
[17] G. Decerprit, D. Allard, Constraints on the origin of ultra-high-energy cosmic rays from cosmogenic neutrinos and photons, A&A 535, **A66** (2011).
[18] D. Saltzberg, P. Gorham, et al., Observation of the Askaryan Effect: Coherent Microwave Cherenkov Emission from Charge Asymmetry in High-Energy Particle Cascades, Phys. Rev. Lett. **86**, 2802, (2001).
[19] I. Kravchecko, et al., RICE Limits on the Diffuse Ultra-High Energy Neutrino Flux, Phys. Rev. **D73**, 082002, (2006).
[20] N. Shaviv, On climate response to changes in the cosmic ray flux and radiative budget, J. of Geophysical Res., **110**, 8105, (2005).
[21] E. R. Lusczeka, Radio Pulse Emission in Air Showers and Dense Media, 29th International Cosmic Ray Conference Pune **8**, 331, (2005).
[22] T. Kamijo, M. Chiba, Microwave Properties of Rock Salt and Lime Stone for Detection of Ultra-High Energy Neutrinos, SPIE, Vol. **4858**, (2003).
[23] http://destepti.ro/neutrini-de-origine-extraterestra-identificati-la-polul-sud
[24] M. Chiba, et. all, Radar for salt ultra-high-energy neutrino detector and contribution of W-gluon fusion process to collision of neutrinos against protons, Nuclear instruments & methods in physics research, ISSN 0168-9002, (2009).
[25] V. Savu, I. Marghescu, O. Fratu, S. Halunga, A. Bădescu, Antenna Design for Electromagnetic Waves Propagation Studies Through the Salt Ore, U.P.B. Sci. Bull., Series C, Vol. **75**, Iss. 2, 2013 ISSN 2286 – 3540, (2013), pp. 143 – 156.
[26] T. Farbel, Experimental Techniques in High Energy Nuclear and Particle Physics, World Scientific, Singapore, (1991).
[27] W. R. Leo, Techniques for Nuclear and Particle Physics Experiments, Springer Verlag, Berlin, Heidelberg, New York, London, Paris, Tokyo, (1995).

[28] W. H. Tait, Radiation detection, Butterworths, London, Boston, Sydney, Wellington, Toronto, Durban, (1980).
[29] D. Sjoberg, Determination of propagation constants and material data from waveguide measurements, Progress In Electromagnetics Research B, Vol. **12**, 163, (2009).
[30] D. A. Hill, Fields of horizontal currents located above the earth, IEEE Trans. Geosci. Remote Sensing, vol. **GE-26**, no. 6, (1989).
[31] V. Savu, O. Fratu, M. I. Rusu, D. Savastru, D. Tenciu, A. Vulpe, R. Craciunescu, Determination of the electromagnetic wave propagation for the detection of the Cherenkov radiation cone in salt environment, U.P.B. Sci. Bull., Series A, Bucharest, Romania, **80** (1), 251 (2018).
[32] P. W. Gorham, et al., Experimental limit on the cosmic diffuse ultrahigh-energy neutrino flux, Phys. Rev. Lett. **93**, 041101 (2004).
[33] P. McIntyre, A. Sattarov, Tripling the LHC: The Path from Technology to Discovery, Dark Matter in Astro- and Particle Physics, (2004).
[34] V. Savu, M. I. Rusu, D. Savastru, Chaper - Optimization of Cosmic Radiation Detection in Saline Environment, Editure IntechOpen Limited, 5 Princes Gate Court, London, SW7 2QJ, UK, (2020), DOI: http://dx.doi.org/10.5772/intechopen.91156.
[35] V. Savu, Book – Detecția Conului Cherenkov în Mediu Salin, Editure Tehnopress 700109 Iași, (2019), ISBN 978-606-687-379-6.
[36] D. Toader, M. L. Munteanu, N. Banu, A. Scurtu, C. M. Ticos, Evaluation of submillimeter electromagnetic waves scattering on dust particles in plasma, JOAM Vol. **15**, No. 3-4, (2013), p. 294 – 298.
[37] M. Z. Yaqoob, A. Ghaffar, I. Shakir, M. Y. Naz, Q. A. Naqvi, Electromagnetic scattering from perfect electromagnetic conductor (PEMC) sphere placed in isotropic plasma, JOAM, Vol. **17**, No. 1-2, (2015), p. 177 – 181.

*Corresponding author: Madalin Ion RUSU, madalin@inoe.ro

A practical approach to the design of a vertical axis wind turbine

V. DULGHERU1 [a], C. DUMITRESCU2[a],
I. RABEI3 [b], M. GUTU4 [b], O. CIOBANU5 [a*]
[a] *Hydraulics and Pneumatics Research Institute INOE 2000-IHP, Romania*
[b] *Technical University of Moldova*

Abstract: The article presents the steps taken for designing a vertical axis wind turbine. Firstly, hand calculations were performed for determining the geometrical dimensioning and the corresponding performance indicators (power coefficient and rpm). Here a set of assumptions were made the main one being related to the power coefficient. Secondly, some of the output parameters were used as input for the numerical analysis using QBlade and ANSYS software. The estimated parameters (rpm, power coefficient and TSR) set by previous calculations were verified, corrected and updated. Finally, a rotor design is proposed to be manufactured and tested based on determined parameters.

Keywords: *airfoil, simulations, wind energy.*

1. Introduction

The vertical axis wind turbines (VAWTs) are defined mainly by four parameters: the rotor's diameter and height, airfoil type and chord length. From these a series of different parameters can be derived for example: swept area, rotor's aspect ratio, solidity, blade's aspect ratio. Each of these parameters affects the behavior and efficiency of the turbine and subsequently its power output. For example the solidity strongly affects the tip speed ratio that subsequently determines the rotor's number of revolutions per minute. However there are other features that affect the turbine's performance for example blade shape where a few options exist among which are the straight, curved or helical blades. Having a fixed or variable pitch angle or end plates covering the tips of the blades will also affect the efficiency. Therefore by the end of designing process a list including all these parameters and information should be set. Above this the presumed torque and number of rotation for certain wind speeds should be evaluated.
There are different methods of designing and studying vertical axis wind turbines among which the experimental approach, numerical methods that comprise the stream tube models [1, 2], CDF simulations etc. In this paper a particular approach was taken for designing a 1 kW VAWT ending with list of geometrical parameters and performance indicators. A turbine for research purposes is planned to be built based on these results.
In the first section hand calculations were done where a few assumptions regarding the power coefficient and solidity

value were made. The output data from this stage were then analyzed using QBlade and ANSYS software and the assumptions were adjusted.

2. Preliminary calculations

The process starts by splitting the information that it's known or is to be determined into three categories: the input, the equations or/and reference data and the output. For our specific case the input box consists of the following parameters: the turbine rated power, rotor's height, rated wind speed, air density, presumed power coefficient, airfoil, blade number and solidity (**Table 1**). The data that is to be determined comprises: the rotor's swept area, diameter, rotor's aspect ratio, blade's chord length, tip speed ratio, blade's tangential and angular velocity and the number of revolutions per minute.

Table 1. Input data

The parameter, (unit)	Value
Rated power, (W)	1000
Rotor's height (m)	2.7
Rated wind speed, (m/s)	11
Air density, (kg/m^3)	1.225
Presumed power coefficient, (/)	0.2
Airfoil	FX 63-137
Blade number, (/)	3
Solidity, (/)	0.4

In general, depending on the particular requirements or information available the data in the input box might be slightly or completely different than the one presented. So the information that is known in one case is to be determined in a different scenario. The specific parameters listed in the **Table 1** are motivated by the following considerations.

The rated power comes from the required energy for a specific application.

As the turbine that is to be built has a specific limitation of the maximum height, this parameter was set in the input box. A common thing is to determine it as an output data by setting the rotor's aspect ratio.

For the case of rated wind speed the common values lay between 10 and 14 m/s. These values can be noticed from the data sheets of the products sold by companies. Usually the wind turbines operate for wind speeds with magnitudes up to 5 - 8 m/s called operational wind speeds. In such conditions the power output is lower as it can be deduced form the **eq. 1**:

(1)

where P – rated power; C_p – power coefficient; ρ – air density; A – turbine's swept area; U – rated wind speed.
In order to get the necessary energy for lower wind speeds a turbine with a larger swept area is needed. This implies higher costs so a compromise between the established rated wind speed and the rotor's size is pursued.
The value of air density is used for further calculations and depends on the air pressure and temperature. For simplicity

Fig. 1. The performance of two turbines based on NACA 0018 and FX 63-137 (concave side out) airfoils [7].

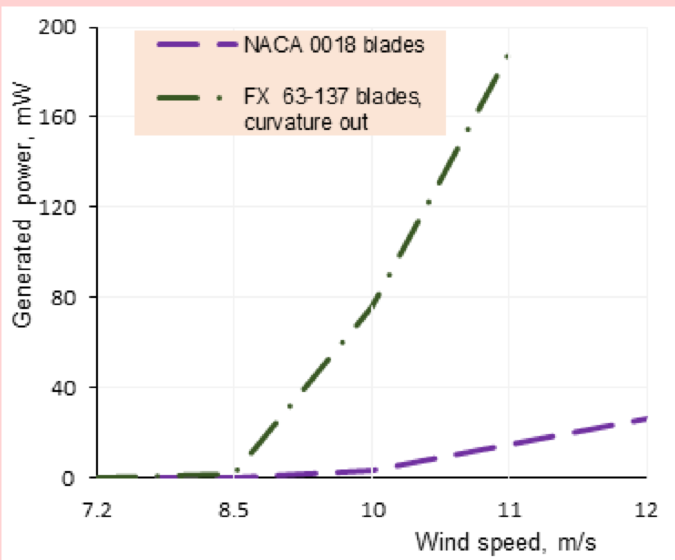

Fig. 2. Two possibilities of orienting the asymmetrical airfoils

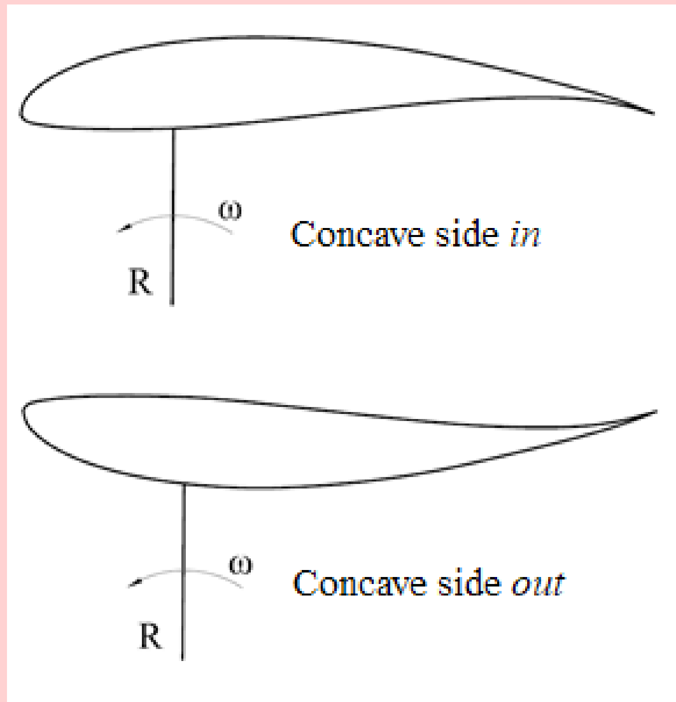

the value for normal conditions is considered.

The most important assumption is in regard to the power coefficient which for VAWTs lays normally between 0.1 and 0.4, depending on how optimized the turbine's parameters are, the rotor's size, operational wind speeds etc. For this case a starting value equal to 0.2 was considered.

The airfoil is one of the most confusing parameters of a vertical axis wind turbine. It is rather difficult to decide based on references which version is better as the results seem to be motley and not conclusive. It is also unclear how the wind tunnel results involving blade segments of a specific airfoil relate to the performance of the VAWTs with blades based on the same airfoil. Historically the most used airfoils were part of the NACA family, especially NACA 0012, NACA 0015 and NACA 0018 versions [4, 5]. However nowadays many other versions are adopted, both of symmetrical and asymmetrical shape. For this specific application the asymmetrical FX 63-137 was chosen from the list proposed by Bostan et al [6].

Table 2. Necessary relations

Eq. number	Equation	Caption
2		*P* – rated power; *Cp* – power coefficient; ρ – air density; *A* – swept area; *U* – rated wind speed.
3		*RA* – rotor's aspect ratio, *h* – rotor's height, *D* – rotor's diameter.
4		
5		σ – solidity; *N* – blade number; *c* – chord length.
6		λ_{opt} – optimal tip speed ratio.
7		*Vt* – blade's tangential speed.
8		ω – blade's angular speed; *R* – rotor's radius.
9		*rpm* – revolutions per minute.
10		*RAb* – blade's aspect ratio.

This is based on the experimental results that involved NACA 0018 and FX 63-137 airfoils where the last version was more efficient (**Figure 1**) [7].
For asymmetrical airfoils the orientation is very important as these types can be oriented in two modes: the concave side *in* and *out* (**Figure 2**). The FX 63-137 showed much better results when oriented with the concave side *out* [8]. Normally the choice of the optimal airfoil is established by running CFD simulations or experimental testing thus it is considered as the output data. In this case however, given the reference above the airfoil is chosen and listed in the input box. Once the list is complete the necessary equations can be applied for obtaining the output parameters. The equations are depicted in the **Table 2**.
Firstly the swept area can be determined using the **eq. 2**. Having the terms specified in the **Table 1** we get a value equal to 6,13 m^2.
For the same swept area many options exist in regard to the rotor's diameter and height. These possibilities are controlled by the aspect ratio which is calculated by dividing the height over the diameter (**eq. 3**). The parameter can take values larger, equal or smaller than 1. The influence of the aspect ratio on turbine's efficiency was addressed by several authors [9, 10] that showed a higher power coefficient for higher aspect ratios. However Brusca et al [11] recommended lower values as these facilitate higher Reynolds numbers.
The rotor's diameter was calculated using the **eq. 4** thus for a swept area of 6.13 m^2 and a height of 2.7 m a value equal to 2.27 m was obtained which was rounded to 2.5 m. With the new dimension the swept area value was updated to 6.75 m^2. Consequently the obtained aspect ratio is equal to 1.08.
Having set the solidity, number of blades and rotor's diameter the blade's chord length can be calculated by applying the solidity equation (**eq. 5**). The value obtained is equal to 330 mm.
The tip speed ratio (TSR) is the ratio between the blades tangential speed and the wind speed. This parameter is strongly related to the solidity. Rezaieha et al [12] established a mathematical relationship (**eq. 6**) between the two based on an extensive study of different VAWTs. Applying the corresponding equation a number equal to 2.05 was obtained. Once the TSR is set and involving the rated wind speed the blade's tangential and angular speeds can be calculated using the **eqs. 7** and **8**. The values obtained are equal to 22.5 m/s and 18 rad/s respectively.
The next step is calculating the number of revolutions per minute using the **eq 9**. This number is particularly important when the electrical generator is to be chosen or designed. For this specific case at 11 m/s about 172 rpm is expected.
All calculated parameters are listed in the output **table 3**. For facilitating the manufacturing process straight blades were chosen. The blade's aspect ratio computed with the **eq. 10** is 8.18. In order to avoid tip losses Kirke [4] recommends a value higher than 7.5 and Ahmadi et al [13] values between 10 and 20. So in this case end plates can be considered but attention is to be paid to their shape as this aspect is important [14].
Some of the obtained output data is used in the next section as input for estimating the aerodynamic performance and

suppositions above adjusted accordingly.

Table 3. Output data

Parameter, (units)	Obtained value	Applied equation
Swept area, (m^2)	6.75	2, 3
Rotor's diameter, (m)	2.5	3, rounded value
Aspect ratio, (/)	1.08	4
Chord length, (m)	0.33	5
Tip speed ratio, (/)	2.05	6
Blade's tangential speed, (m/s)	22.5	7
Blade's angular speed, (rad/s)	18	8
rpm	172	9
Blade's aspect ratio, (/)	8.18	10

2. Numerical analysis of aerodynamic performance of the turbine rotor

2.1. Rotor analysis using QBlade software

In order to estimate the theoretical performance of the rotor QBlade software was used. The rotor geometry was created according to the design parameters obtained by hand calculation (**Figure 3**).

The QBlade software contains a module for unsteady aerodynamic simulations of wind turbines based on a nonlinear lifting line free vortex wake algorithm (LLFVW) [15].

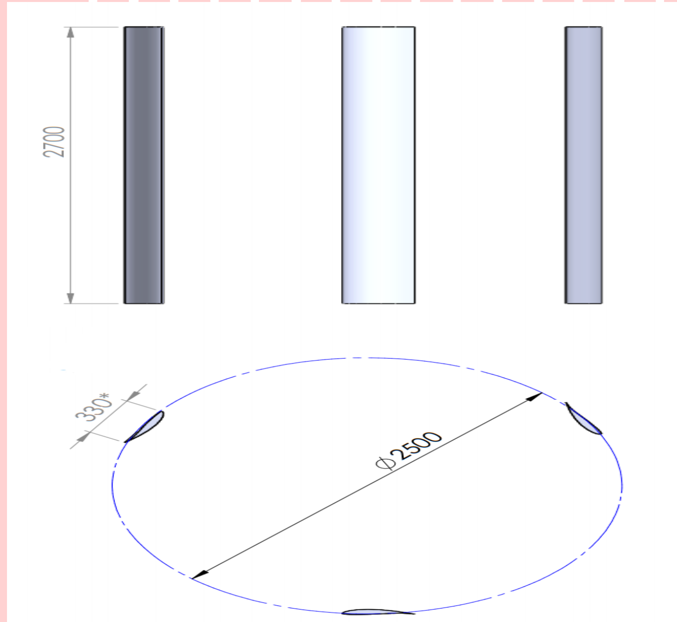

Fig. 3. Rotor geometry (Continued next page)

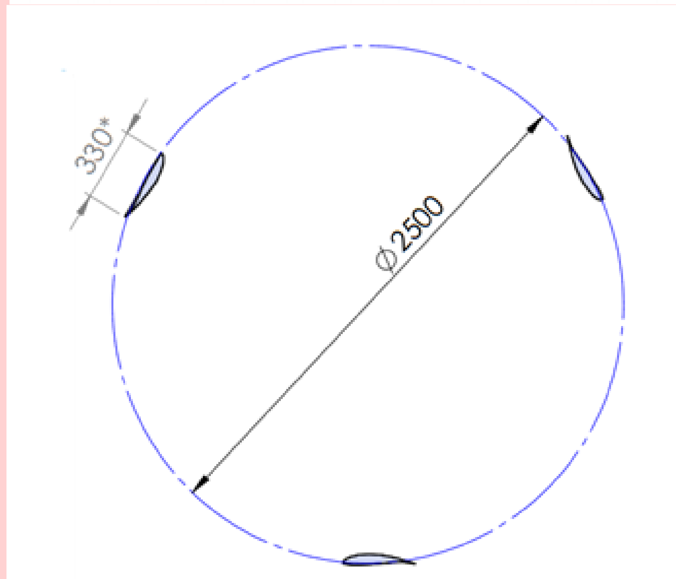

Fig. 3. Rotor geometry

Especially for the simulation of vertical axis wind turbines the lifting line method presents a large improvement over the double multiple stream-tube method. The lifting line does not have any convergence problems and the accuracy is drastically enhanced. The wind turbine analysis algorithm using QBlade software was applied according to the diagram presented by Alaskari et al [16].
For a maximum power coefficient it was estimated a tip speed ratio of 2.5 (versus 2.05 obtained by previous calculation). The **figure 4** shows the power coefficient dependence on the TSR and the **figure 5** presents the variation of the power output in with the TSR.

Finally, a complex simulation of the wind rotor was performed which contained different values of wind speed, rpm and blade pitch angle. A comparative diagram with the results is presented in the **figure 6**. As it can be noticed from the graph for the nominal wind speed of 11 m/s the rotor delivers over 800 W of power. This value corresponds to 200 min^{-1} (versus 172 revolutions per minute calculated previously) with the blades pitch angle equal to minus 1 deg. Blades pitch angle equal to 0 is considered when the angle between the supporting strut and the chord line is equal to 90°.
The negative angle is considered when the angle between supporting struts and the chord line larger than 90° and vice versa for the positive angle.

Fig. 4. Power coefficient and tip speed ratio dependence

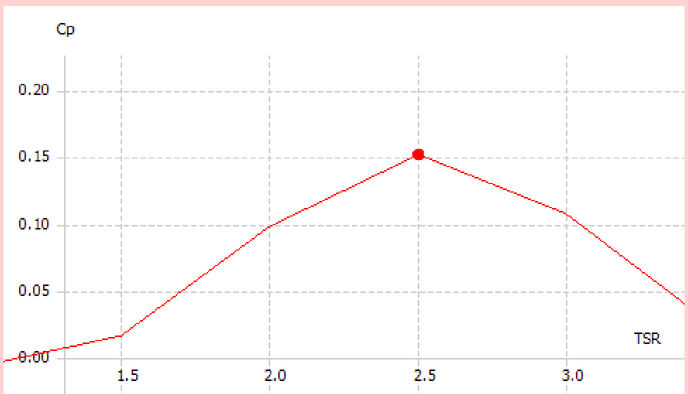

Fig. 5. Rotor power and tip speed ratio dependence

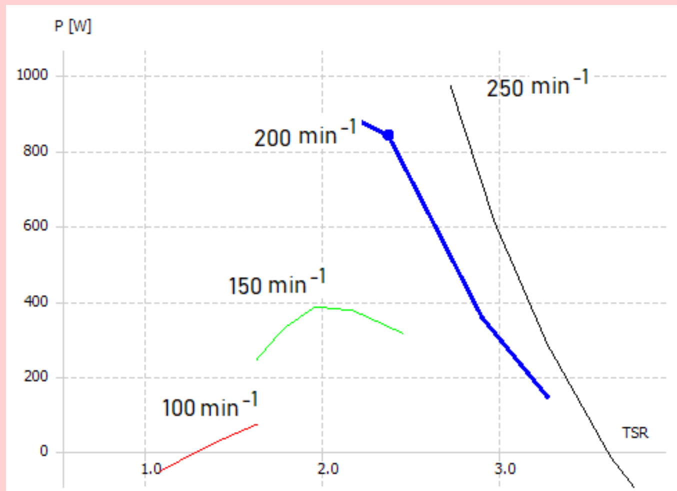

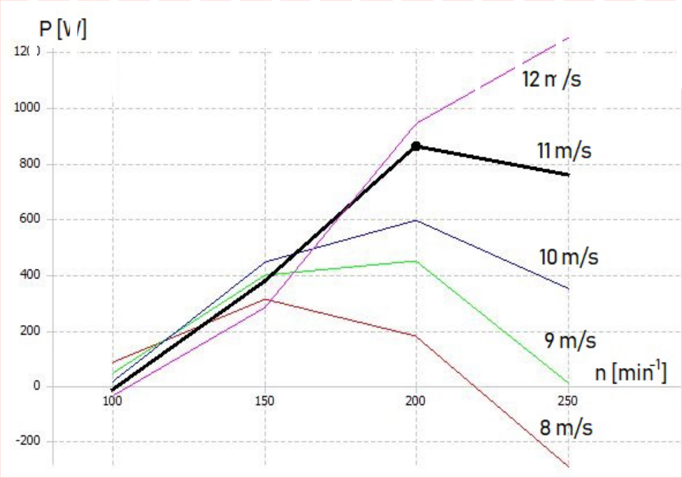

Fig. 6. Comparative power curves of the rotor.

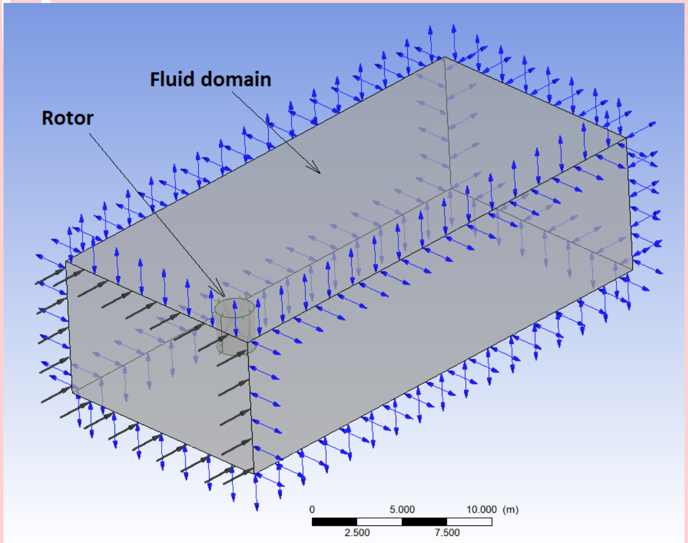

Fig. 7. Model of computational fluid domain

2.2. Rotor CFD analysis using ANSYS CFX software

In order to verify the rotor efficiency or the power coefficient a CFD model was developed using finite element analysis software ANSYS CFX.
As it is well known, the mathematical model in ANSYS CFX software is based on the continuity and momentum equations and it is solved using the k-epsilon turbulence model (solving the non-stationary Navier-Stokes equation).
The rotor geometry, designed using SolidWorks, was then imported into the ANSYS Design Modeler software.
The dimensions of the computational fluid domain were chosen taking into account the recommendations of Mohamed et al. [17] so that the boundaries of the field do not influence the free flow of the air. The simulated fluid domain was divided into two subdomains: the Stator (static) subdomain and the Rotor subdomain inside (of cylindrical form which rotates around its axis). **Figure 7** shows the considered fluid domains.
After importing the geometric model the following regions were defined as recommended by Bostan [18]: (Inlet – the face with black arrows on the perimeter), (Outlet – the opposed face to the Inlet), (Openings – the four side faces) and the common regions between *Fluid_stator* and *Rotor* (Fluid-Fluid).

Simulations were performed for a nominal wind speed of 11 m/s and 200 min^{-1} rotational speed.

Using ANSYS CFX Expression Language (CEL) the following variables of interest were defined: torque appearing on the rotor shaft (*Mz = torque_z()@Pale*) and the power (*P = Mz*pi*n/30*).

The mesh of the rotor was generated using the ANSYS Meshing Workbench. This is an integrated software that offers optimized meshing strategies and features regarding mesh control, type, sizing etc.

In order to capture the effects of the boundary layer on the surface of the blades the edges were finely discretized in 9 layers using the function *inflation*. The transition from the fine-meshed areas to the gross meshed ones (**figure 8**) was done by specifying the Growth Rate = 1.1. The maximum variation of the characteristic dimensions of two adjacent elements was not bigger than 5%. The entire domain was meshed into approx. 5 500 000 finite elements.

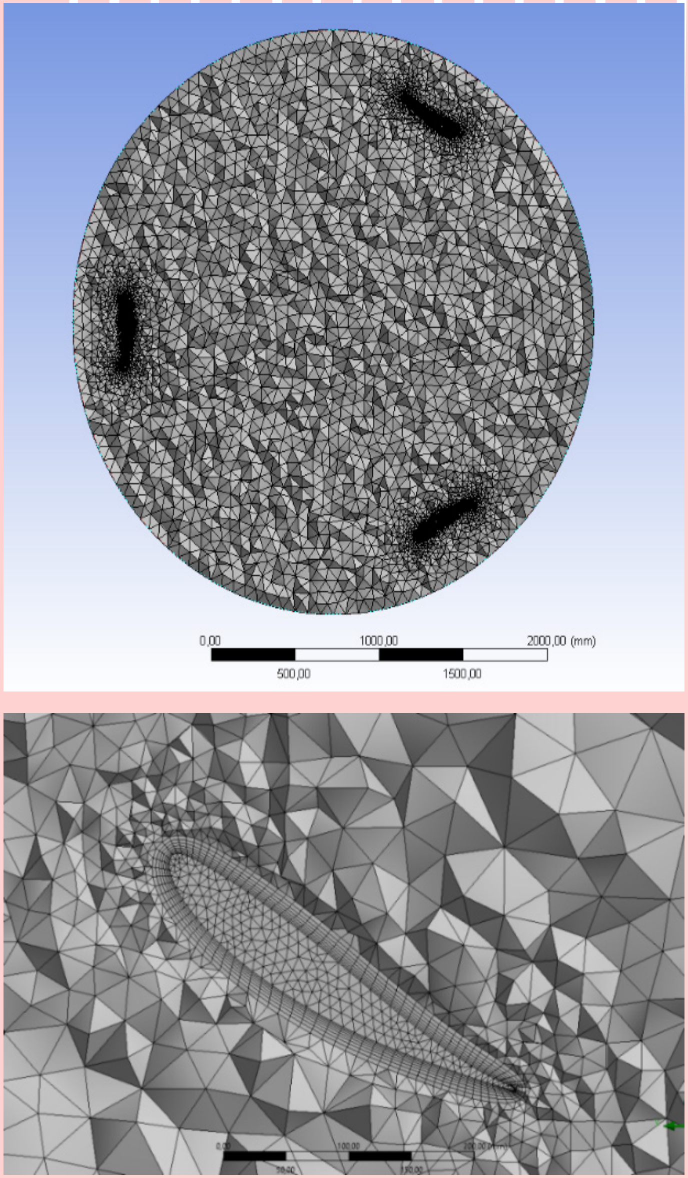

Fig. 8. Rotor mesh details (a) and inflation layers around the blade surface (b).

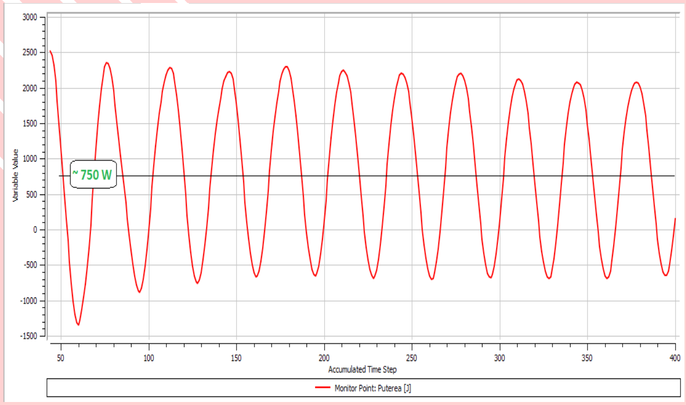

Fig. 9. Generated power diagram at 11 m/s wind speed.

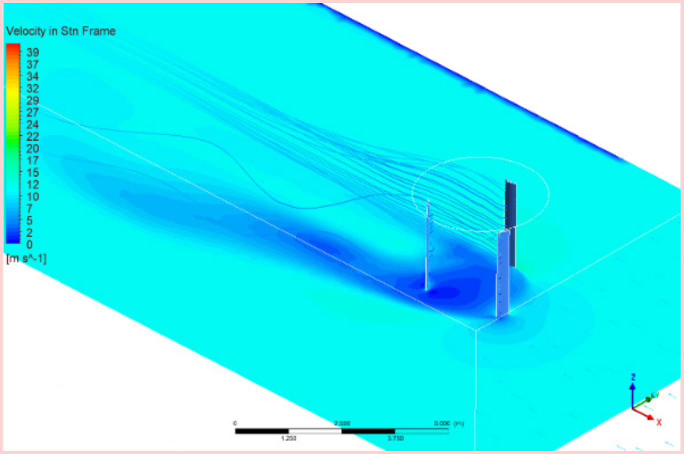

Fig. 10. Fluid velocity distribution around the rotor

In order to obtain the rotor power curve a monitoring point with *Power* as a variable of interest was created (**fig. 9**). The power diagram is variable because of the variable torque developed on the rotor shaft.
In order to check the flow field around the rotor, the velocity distribution was analyzed. Velocity contour section for 11 m/s wind speed is depicted in the **figure 9.**
When interacting with the air, the blade experiences turbulences that are formed at the trailing edge and at the tips of the blade. The last ones are the most detrimental in regard to the blade's performance so they should be minimized. The simplest method for doing so is endowing the blades with endplates however this option was not simulated. Validation of the CFD model is to be performed after manufacturing the experimental prototype of the rotor and testing it in real operating conditions. The results of the simulations in ANSYS CFX showed good accordance with the results obtained in the dedicated QBlade application.
The value of the power obtained in ANSYS CFX for the given parameters of the rotor is 8-10 % lower than the one estimated with the QBlade software (825 W versus 750 W). For this reason, the power coefficient should be corrected to the value of approx. 0.15 (versus 0.2 estimated before). According to Hilewit et al [19] the empirical Cp for small vertical axis wind turbines and low tip speed ratio is between 0.1 - 0.23. The key parameters changed from the **Table 3** are depicted in the **Table 4**.

Table 4. Updated output parameters

Parameter, (units)	Obtained value
Estimated power, (W)	750 - 820
Tip speed ratio, (/)	2.50
Rotor speed, (min^{-1})	200

Conclusions

There is a difference between the power obtained by simulations and the power initially accepted. The parameters that directly influence the delivered power are the swept area, airfoil and the solidity of the rotor. In this sense, another iteration could be performed with the focus on optimizing especially the solidity and swept area so that power initial desired was obtained. However because of the size limitations the turbine that is to be built will be based on the geometrical dimensions depicted in **Tables 1 and 3** and a lower rated power is expected.

Acknowledgements

This paper has been funded by the Romanian Ministry of Research and Innovation under Programme I-Development of national R&D system, Subprogramme 1.2–Institutional performance–Projects financing excellence in R&D&I, Project acronym: PRO-INSTITUTIO, Financial Agreement no. 19PFE/17.10.2018, Phase 5, and is based on results obtained within the CONVENER project, financing contract 37/2016 from the POC 2014 - 2020 program.

References

[1] J. H. Strickland, The Darrieus turbine, a performance prediction model using multiple streamtubes. Energy report, Sandia Laboratories, 1975.

[2] I. Paraschivoiu, Wind turbine design with emphasis on Darrieus concept. Ecole Polytechnique de Montréal, 2002, ISBN 2-553-00931-3.

[3] V. Bostan, I. Bostan, I. Rabei, M. Gutu, V. Dulgheru, Vertical Axis Wind Turbines. Optimal Positioning of the Blades Defined by Asymmetrical Airfoils. In: Visa I., Duta A. (eds) Solar Energy Conversion in Communities, pp 207-213. Springer Proceedings in Energy. Springer, Cham. (2020). doi.org/10.1007/978-3-030-55757-7_15

[4] B. K. Kirke, Evaluation of self-starting vertical axis wind turbines for stand-alone applications. PhD thesys, Griffith University, 1998.

[5] M. Islam, A. Fartaj, R. Carriveau, Analysis of the design parameters related to a fixed-pitch straight-bladed vertical axis wind turbine. Wind engineering, volume 32, No. 5, 2008 pp 491–507.

[6] I. Bostan, V. Dulgheru, R. Ciuperca, Theoretical aerodynamic analyses of airfoils for use on small wind turbines and selection of optimal profiles for the wing of helical wind turbine functional model (Part I). Bulletin of the Polytechnic Institute of Jassy, Machine Building section LII (LVI), Fasc. 5D, 2006. pp. 1280 - 1284.

[7] V. Bostan, I. Bostan, I. Rabei, V. Dulgheru, R. Ciuperca, Vertical Axis Wind Turbines: The behavior of lift and drag

airfoils. In: Visa I., Duta A. (eds) Solar Energy Conversion in Communities. Springer Proceedings in Energy (2020). Springer, Cham. DOI.org/10.1007/978-3-030-55757-7_14.

[8] V. Bostan, I. Bostan, I. Rabei, M. Gutu, V. Dulgheru, Ciuperca R. Vertical Axis Wind Turbines. Optimal Positioning of the Blades Defined by Asymmetrical Airfoils. In: Visa I., Duta A. (eds) Solar Energy Conversion in Communities. Springer Proceedings in Energy (2020). Springer, Cham. DOI.org/10.1007/978-3-030-55757-7_15.

[9] R. D. Ionescu, S. Vlase, M. Ivanoiu, Rotor design for vertical axis wind turbines, suitable for urban seashore environment or naval industry implementation (numerical methods and analytical calculus). Special issue of JIDEG Volume 9, International Conference ISTM 2014 papers.

[10] F. Scheurich, R. E. Brown, Vertical-axis wind turbines in oblique flow: sensitivity to rotor geometry. University of Glasgow, Glasgow, UK.

[11] S. Brusca, R. Lanzafame, M. Messina, Design of a vertical-axis wind turbine: how the aspect ratio affects the turbine's performance. International Journal of Energy and Environmental Engineering (2014) 5:333–340, DOI 10.1007/s40095-014-0129-x.

[12] A. Rezaeiha, H. Montazeri, B. Blocken, Towards optimal aerodynamic design of vertical axis wind turbines: Impact of solidity and number of blades. Energy, 165(B) (2018), 1129-1148. DOI.org/10.1016/j.energy.2018.09.192.

[13] M. Ahmadi-Baloutaki, R. Carriveau, D. S-K. Ting, Straight-bladed vertical axis wind turbine rotor design guide based on aerodynamic performance and loading analysis. DOI: 10.1177/0957650914538631, SAGE Journals, 2014.

[14] R. Gosselin, G. Dumas, M. Boudreau, Parametric study of H-Darrieus vertical-axis turbines using uRANS simulations. 21st Annual Conference of the CFD Society of Canada, Sherbrooke, Canada, May 6–9, 2013.

[15] D. Marten, M. Lennie, G. Pechlivanoglou, C. N. Nayeri, C. O. Paschereit, Implementation, Optimization and Validation of a Nonlinear Lifting Line Free Vortex Wake Module Within the Wind Turbine Simulation Code QBlade. Journal of Engineering for Gas Turbines and Power, December 2015.

[16] M. Alaskari, O. Abdullah, M. H. Majeed, Analysis of wind turbine using QBlade software, 2019 IOP Conf. Ser.: Mater. Sci. Eng. 518 032020.

[17] M. H. Mohamed, A. M. Ali, A. A. Hafiz, CFD analysis for H-rotor Darrieus turbine as a low speed wind energy converter. Engineering Science and Technology, an International Journal. Volume 18, Issue 1, March 2015.

[18] V. Bostan, Mathematical models in engineering, contact problems, modelling and numerical simulations in aero-hydrodynamics. Chisinau, Editura Bons Office, 2014.

[19] D. Hilewit, E. A. Matida, A. Fereidooni, H. Abo el Ella Fred Nitzsche, Power coefficient measurements of a novel vertical axis wind turbine. Energy Science and Engineering, 2019. DOI: 10.1002/ese3.412.

*Corresponding author: O. CIOBANU
oleg.ciobanu@bpm.utm.md.

Monitoring the wear of the hydraulic gear pumps in endurance through modern methods of predictive and proactive maintenance

AL.-D. MARINESCU1[a,*], AL.-V. RĂDULESCU2[b] ,
I. RĂDULESCU3[b], A.-M. C. POPESCU4[a], ȘT. M. ȘEFU5[a]
[a] *Hydraulics and Pneumatics Research Institute INOE 2000-IHP Bucharest*
[b] *Politehnica University of Bucharest, Machine Organs and Tribology Department*

Abstract In this paper the authors analyze oil samples from the endurance stands of two hydraulic gear pumps in order to determine the optimal rheological model and the related rheological parameters. The results obtained in the laboratory with the help of a modern viscometer come in addition to other experiments performed with the help of an impurity particles analyser, that monitored the slow wear of the studied pumps. These researches focused on oil analysis represent concrete ways to apply predictive and proactive maintenance to the hydraulic gear pumps, but also to other hydrostatic equipment.

Keywords: predictive maintenance, proactive maintenance, oil analysis, hydraulic gear pumps, wear

1. Introduction

Monitoring the degree of wear of hydraulic gear pumps is a specific activity to industrial maintenance operations. The oil analysis is one of the basic activities of predictive and proactive maintenance of hydraulic drive systems and components. In 85% of cases, hydraulic system failures occur due to impurities in the oil. According to the provided information by the equipment manufacturers, 70% of the components are sold to replace the defective ones. 90% of component failures occur due to maintenance errors, as well as due to malfunction of the hydraulic system. To ensure the reliability of the components of the hydraulic system it is necessary to choose an optimal filtration solution. Modern equipment have increased their performance due to the reduction of the clearance between the moving elements (spool valve-body), which leads to the obligation of a significant increase of the oil purity class. Equipment manufacturers usually indicate the required level for the oil purity class. Filtration-cooling systems as well as the special oil diagnostic devices are important elements to be taken into account in the struggle to reduce maintenance costs.[1]
In the experiments covered by this paper, the authors used two such devices, namely: a **Parker CM** Laser Particle Analyzer and a **Brookfield 2000+** viscometer. One of the causes of malfunction of hydrostatic equipment is the contamination

of the installation used oil. The maintenance specialists distinguish three types of contamination: gaseous (air), liquid (water), solid (metal particles, abrasive particles, rust, textiles, etc.). Contamination with solid particles can be found when at the oil analysis (specific proactive maintenance operation) one detects the following elements: metallic and non-metallic particles (bronze, brass, aluminium).

These lead to the rapid degradation of the oil by the formation of gelatinous or muddy precipitation.

Types of solid contaminants:

- abrasive particles; These are very harmful and lead to rapid degradation of components
- fibers, textiles, rubber, oxides, traces of paint;

The consequences of this type of contamination are reflected in the high increase in maintenance costs, as the presence of solid particles in the oil leads to wear and blockage of the hydraulic equipment.[1]

In the below described experiments, the authors monitored the endurance operation of two hydraulic gear pumps, analyzing oil samples from the stands on which they were mounted, in order to identify wear after several work cycles.

2. Experiments

2.1. Brief description of monitored pumps and of endurance stands

The experimental researches aimed to monitor two types of hydraulic gear pumps in endurance tests at the manufacturing company, **SC Hesper SA Bucharest**. More specifically, these are the following pumps from group 05 with the following manufacturing codes and series: -HP0505-0,5 + 1,5-1-0,2-6-C-06-2, series 11UA -BHP 05- 05-010 UB, 01TC series. For simplification, in the following lines, they will be marked **P1** and **P2** respectively. Fig.1 and Fig.2 present the pump P1, respectively its endurance stand.

Fig. 1. Pump P1; [2]

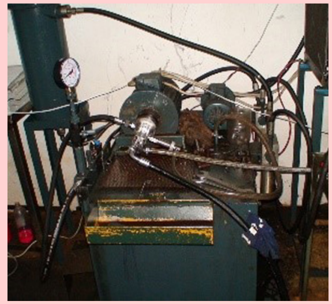

Fig. 2. Endurance stand of pump P1

Fig. 3. Pump P2; [2]

Fig. 4. Endurance stand of pump P2

nalogously, pump P2 and the corresponding endurance stand are shown in Fig. 3 and Fig. 4.

P1 type pumps have a compact construction consisting of two parts (body and cover), and the fastening is done with two screws through the pump body. The **P2** type pumps have a compact two-part construction (body and cover), with two screws through the pump body. They are bidirectional pumps, built on the design line of the **P1** type pump family. In contrast, they can operate in both directions of rotation, having two identical suction / discharge on the pump clamping flange and an external drain [2] To ensure the quality of the working fluid, both endurance stands are equipped with 3 hydraulic filters mounted in cascade.

2.2. Used working fluid

For endurance testing of pumps **P1** and **P2**, the tanks of the stands were loaded with H46 EP mineral oil. This is an additive hydraulic oil for extreme pressure, obtained from refined base oil and the addition of additives that thus give it antioxidant, anti-rust, anti-wear, anti-foaming and demulsifying properties. According to the manufacturer's catalog [3] this product meets the requirements of the specifications: DIN 51524 / Part 2 HLP, AFNOR NF E 48-603 HM, Sperry Vickers I-286-S; Denison Filterability TP 02100, US Steel 127, STAS 12023-82. The manufacturer also recommends it as a working fluid in hydraulic power transmission systems, equipped with pumps and motors for high pressures, with axial or rotary pistons, for high speed gears, hydraulic couplings and speed variators, according to the working instructions. The quality conditions are in accordance with standard ST-16/2007.

2.2.1 Classification of the used working fluid in the purity class of the oils

The ISO classification, mentions ten classes of purity oils as follows [1]:

- Class 1: 23/21/19;
- Class 2: 22/20/17;
- Class 3: 21/19/16;
- Class 4: 20/28/15;
- Class 5: 19/17/14; (for lubrication systems); -

Class 6: 18/16/13; (for conventional hydraulic systems ON-OFF, with filtration fineness of (15-16) µm.

- Class 7: 17/15/12; (for classical hydraulic systems at high pressures, with filtration fineness of (10-15) µm -

Class 8: 16/14/11; (proportional apparatus, with fineness of filtration of (5-10) µm; -

Class 9: 15/13/10 (servo apparatus with fineness of filtration of (3-15) µm;

- Class 10: 14/12/9 (aeronautical equipment and special applications). H46 EP oil, used for the endurance of pumps P1 and P2, falls into purity class 6.

2.3 Experiments with the Laser CM Parker particles analyzer

Contaminants can appear in the working fluid - hard or soft particles, but also air, water, heat or various substances that influence its physical-chemical properties are also contaminants. As it is known, the wear of hydrostatic devices is accelerated by particles contamination, and the speed of this phenomenon is influenced by the internal distance from the system, by the size and number of particles in the oil, but also the pressure in the installation. Usually, the particles having a larger diameter than the internal clearances do not present any danger for the proper functioning of the system, but those that have the same size as the internal distances give rise to wear by friction. Particles that have a smaller diameter than the internal releases of the analyzed hydrostatic component create major system problems over long periods of time. Particles that have a diameter lower than the limit of 5 µm are particularly abrasive, and in the situation where they look like mud, wear occurs quickly which leads to the destruction of pumps and other hydrostatic components. However, this type of failure is not often found in a well-designed and maintained hydrostatic system. The authors presented the example above to show the important role that regular monitoring of the purity level of hydraulic oil has. If high levels of sludge particles are observed in the working fluid, the fault can be removed within a reasonable time, avoiding damage to the pumps and greatly reducing the costs required to repair them. In order to conduct the experiments, the oil samples taken from the company **SC Hesper SA** Bucharest were first monitored at **INOE 2000-IHP** Bucharest, using a laser analyzer, from the Fluid Mechanics Laboratory.

2.3.1. Brief description of the analyzer and how it works

The **Laser CM 20** portable laser analyzer (Fig. 5) used for experiments is a product of **Parker** company (USA) that incorporates the most modern technology in the field for the analysis of solid particle contamination. The appliance is particularly complex and reliable and is designed to be easy to handle [4].

Fig. 5. Analyzer Laser CM *Fig. 6. Keyboard analyzer*

The average time to perform a test is about 2 minutes. In addition to the analyzer printer that is mounted in its body, the appliance also consists of a keyboard with a display to show the obtained data (Fig. 6) and a sampling module (Fig. 7) equipped with two oil recipients that can work separately, except for a pressure tap.

Fig. 7. Sampling module and its recipients

100 ml of hydraulic oil samples from the monitored endurance stands were placed in the recipient on the left side of the appliance. At the beginning of any analysis, the **Flush** command must be activated so that the oil sample is filtered and cleaned of impurities [4]. The amount of oil that has been processed in this way is then transferred to the recipient in the right of the appliance. Immediately after the operation of calibrating the analyzer printer, the **Print** command was given, which allowed the printing of a receipt indicating the number of solid particles of corresponding impurities in the ascending order of their diameters: > 4 µm, > 6 µm, > 14 µm, > 21 µm, > 38 µm, > 70 µm. An example is shown in Fig. 8.

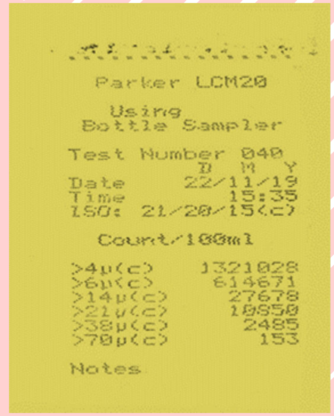

Parker LCM20

Using
Bottle Sampler

Test Number 040
D M Y
Date 22/11/19
Time 15:35
ISO: 21/20/15(c)

Count/100ml

>4µ(c) 1321028
>6µ(c) 614671
>14µ(c) 27678
>21µ(c) 10950
>38µ(c) 2485
>70µ(c) 153

Notes

Fig. 8. Receipt for analysis of the oil sample

2.3.1. Monitoring of the pump P1; Results and interpretations

Between February and July 2020, several oil samples were analyzed and the results were summarized in Table 1 below:

Table 1. Pump P1 test results

Conținut ulei /100 ml									
Nr. crt.	Nr. probă	Conformitate	Data	Număr particule impurități cu diametrul					
				>4µm	>6µm	>14µm	>21µm	>38µm	>70µm
1	P50	ISO 21/20/19 (c)	05.02.2020	1403664	974014	259064	116878	18192	1125
2	P51	ISO 21/20/17 (c)	07.02.2020	1366371	887264	96842	16578	4192	259
3	P54	ISO 21/20/18 (c)	17.02.2020	1400614	905721	143964	45907	5521	341
4	P56	ISO 21/20/16 (c)	24.02.2020	1327150	759992	52257	12528	1600	98
5	P58	ISO 21/20/17 (c)	06.03.2020	1606700	926778	65307	13828	1664	102
6	P60	ISO 21/20/15 (c)	13.03.2020	1585857	821485	23807	3535	700	43
7	P62	ISO 21/20/15 (c)	20.03.2020	1630407	868892	26871	4335	607	37
8	P72	ISO 22/20/14 (c)	15.07.2020	2039592	775442	12742	2671	485	30
9	P75	ISO 22/21/17 (c)	17.07.2020	2641414	1455735	76507	10264	857	53

The obtained results in the above table were used to draw diagrams that illustrate the evolution over time of contaminant particles with diameters greater than the values above specified. As examples, two diagrams corresponding to the evolution over time of the number of oil contaminant particles with diameters greater than 4 µm, respectively 6 µm, are shown in Fig. 9 and Fig 10. On the abscissa of the diagrams the current numbers corresponding to the tests performed in the data from the interval (February-July) 2020 are written, and on the ordinate the number of contaminant particles measured with the analyzer is written. From the analysis of these graphs it results that the number of oil contaminant particles with d > 4 µm, respectively d > 6 µm increased during the whole endurance cycle. The polynomial curves of the 2nd order, represented by dots on the two diagrams by interpolation, provide a clearer picture of the increasing trend of the number of contaminants in the oil.

Fig. 9. Evolution over time of contaminants with d > 4 µm

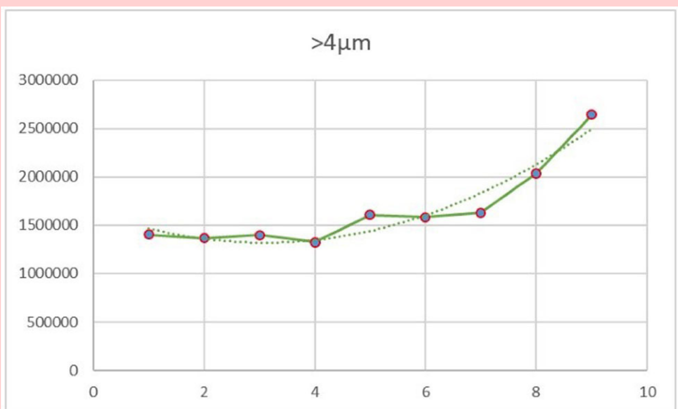

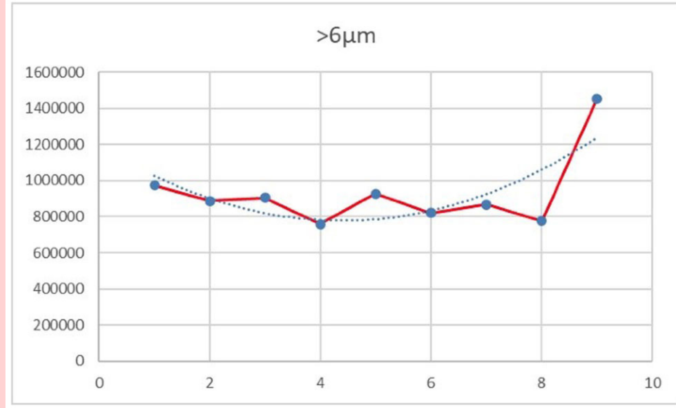

Fig. 10. Evolution over time of contaminants with d > 6 µm

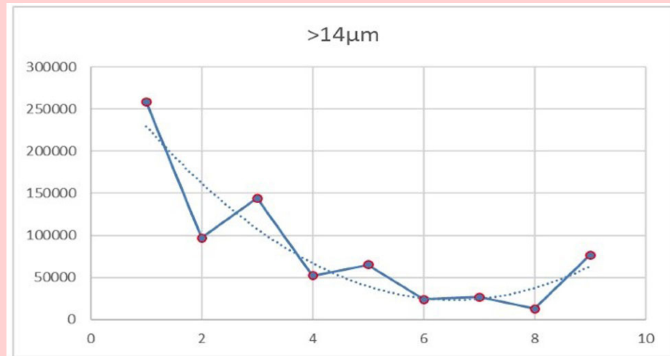

Fig. 11. Evolution over time of contaminants with d > 14 µm

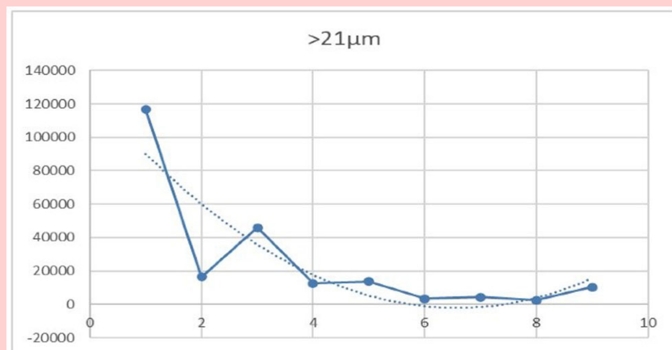

Fig. 12. Evolution over time of contaminants with d > 21 µm

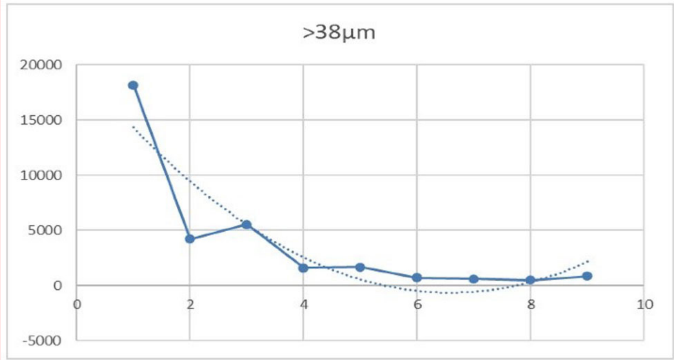

Fig. 13. Evolution over time of contaminants with d > 38 µm

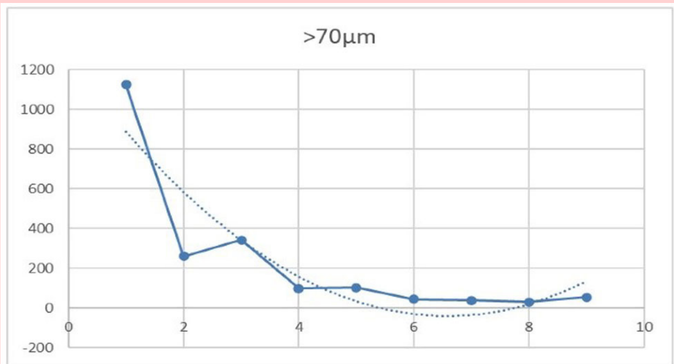

Fig. 14. Evolution over time of contaminants with d > 70 µm

Analogously, Fig. (11÷14) present 4 diagrams corresponding to the evolution over time of the number of particles of oil contaminants having diameters larger than: (14, 21,38,70) µm.
The analysis of these diagrams shows that the number of oil contaminant particles with d > (14, 21,38,70) µm decreased throughout the endurance cycle. The polynomial curves of the 2nd order, represented by dots on the two diagrams, by interpolation provide a clearer picture of the decreasing trend of the number of oil contaminants. Monitoring of the pump **P1** showed that its wear occurred slowly between

Table 2. Pump P2 test results

Conținut ulei /100 ml									
Nr. crt.	Nr. probă	Conformitate	Data	Număr particule impurități cu diametrul					
				>4µm	>6µm	>14µm	>21µm	>38µm	>70µm
1	P14	ISO 21/19/14 (c)	04.06.2019	1308178	400542	9085	3185	1121	69
2	P15	ISO 21/21/19 (c)	10.06.2019	1430071	1094278	457542	210392	59314	3669
3	P16	ISO 21/21/19 (c)	10.06.2019	1363457	1024407	422328	189150	52414	3242
4	P17	ISO 21/19/14 (c)	10.06.2019	1559421	487650	13921	4357	1007	62
5	P18	ISO 21/19/14 (c)	10.06.2019	1561271	487835	12350	3542	764	47
6	P19	ISO 21/19/16 (c)	24.06.2019	1349300	383728	32428	12764	3292	203
7	P20	ISO 21/19/16 (c)	24.06.2019	1307342	345814	34164	13735	3835	237
8	P21	ISO 21/19/16 (c)	02.07.2019	1346250	408171	45650	17007	5600	346
9	P22	ISO 21/19/16 (c)	02.07.2019	1336057	408578	47250	16864	5357	331
10	P23	ISO 21/19/13 (c)	11.07.2019	1236678	291721	7678	2814	642	39
11	P24	ISO 21/19/14 (c)	23.07.2019	1248728	334685	9764	3192	585	36
12	P25	ISO 21/19/14 (c)	22.08.2019	1243300	314607	12557	4557	864	53
13	P26	ISO 21/19/15 (c)	05.09.2019	1152842	319300	27464	11514	2278	140
14	P28	ISO 21/19/14 (c)	10.09.2019	1154557	290657	13500	4957	914	56
15	P29	ISO 22/21/17 (c)	19.09.2019	2453142	1339885	65164	13992	2121	131
16	P32	ISO 21/19/14 (c)	27.09.2019	893692	216971	10657	4064	850	52
17	P34	ISO 22/19/15 (c)	18.10.2019	1062800	389142	31521	11871	2635	163
18	P36	ISO 20/18/15 (c)	01.11.2019	737407	236314	19035	7935	2107	130
19	P38	ISO 20/18/13 (c)	22.11.2019	591578	164757	6792	2485	550	34
20	P42	ISO 21/21/19 (c)	13.12.2019	1420257	1049650	350835	149642	11092	686
21	P45	ISO 21/20/16 (c)	18.12.2019	1124900	623764	54964	15871	3242	200
22	P47	ISO 21/20/16 (c)	10.01.2020	1016107	578250	52542	23178	10135	626
23	P49	ISO 21/20/15 (c)	05.02.2020	1151692	550957	21528	7157	2542	157
24	P52	ISO 21/20/16 (c)	07.02.2020	1188914	690671	61157	14485	2942	181
25	P53	ISO 21/20/16 (c)	17.02.2020	1144214	637850	40507	7107	2300	142
26	P55	ISO 20/19/15 (c)	24.02.2020	957750	444607	20521	7214	2414	149
27	P57	ISO 21/20/16 (c)	06.03.2020	1335950	681400	40657	10650	2314	143
28	P59	ISO 21/20/16 (c)	13.03.2020	1353321	691785	48628	23014	15814	978
29	P61	ISO 21/20/16 (c)	20.03.2020	1279535	640528	53292	23300	9357	578
30	P73	ISO 21/20/17 (c)	15.07.2020	1558407	589071	67414	28078	4207	260
31	P74	ISO 21/19/15 (c)	08.09.2020	1080121	324278	28700	12335	2442	151

Observație: P15 și P16 sunt probe de ulei prelevate direct din containerul cu ulei H46 EP neuzat

(February and July) 2020, mainly due to impurity particles having diameters d > 4 µm and d > 6 µm, while the input of particles with d > (14, 21, 38, 70) µm was a negligible one.

2.3.2. Monitoring of the pump P2; Results and interpretations

Between February and July 2020, several oil samples were analyzed and the results were summarized in Table 2 below. The obtained results in this table were used to draw diagrams that illustrate the evolution over time of contaminant particles with diameters greater than the values specified above. As examples, two diagrams corresponding to the evolution over time of the number of particles of oil contaminants with diameters greater than 4 µm, respectively 6 µm, are shown in Fig. 15 and Fig.16. The current numbers corresponding to the tests performed in the interval (June 4, 2019-7 February 2020) are written on the abscissa of the diagrams, and on the ordinate the number of contaminant particles measured with the analyzer is written.

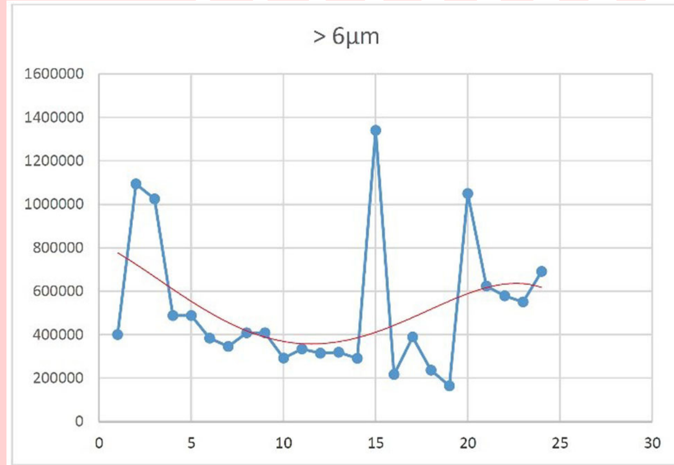

Fig. 16. Evolution over time of contaminants with d > 6 µm

Fig. 15. Evolution over time of contaminants with d > 4 µm

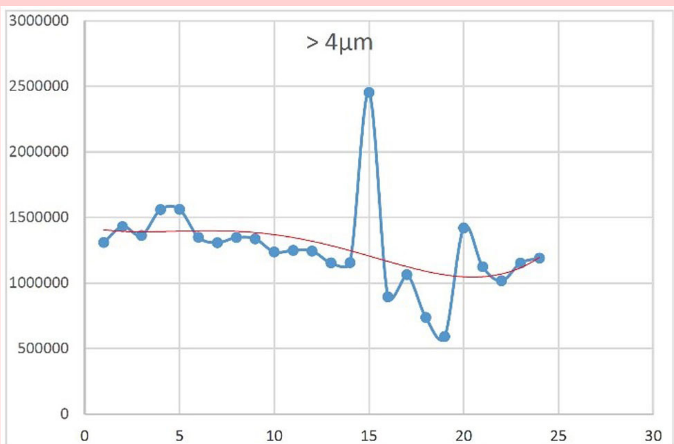

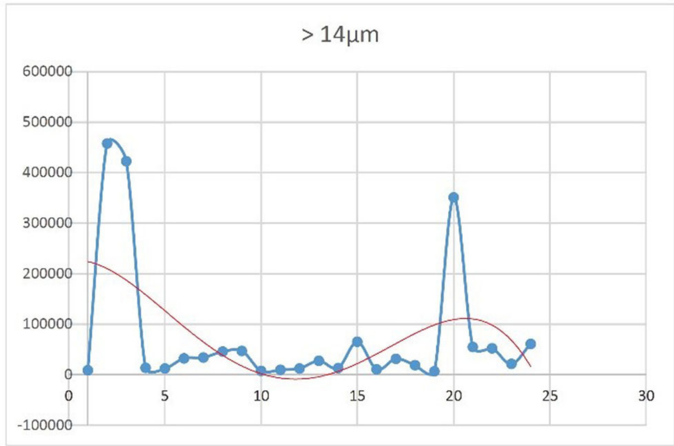

Fig. 17. Evolution over time of contaminants with d > 14 µm

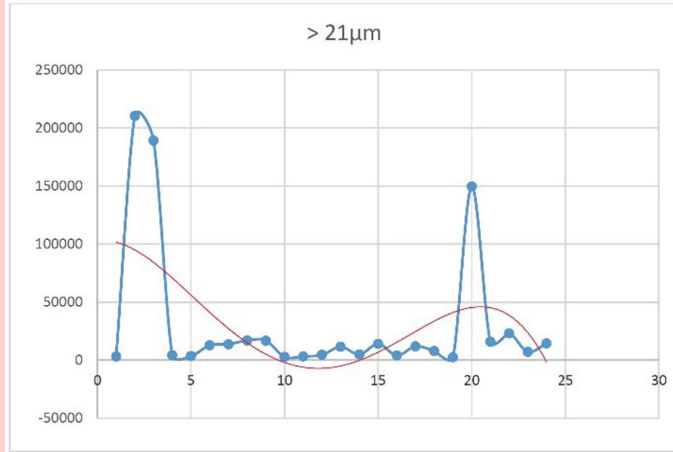

Fig. 18. Evolution over time of contaminants with d > 21 µm

Fig. 19. Evolution over time of contaminants with d > 38 µm

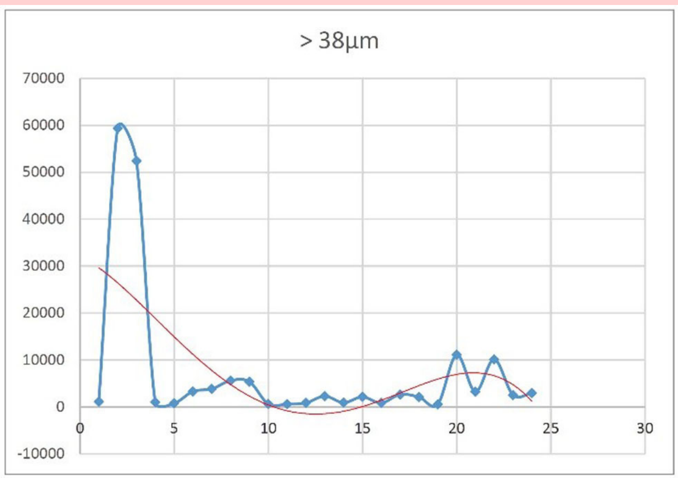

Fig. 20. Evolution over time of contaminants with d > 70 µm

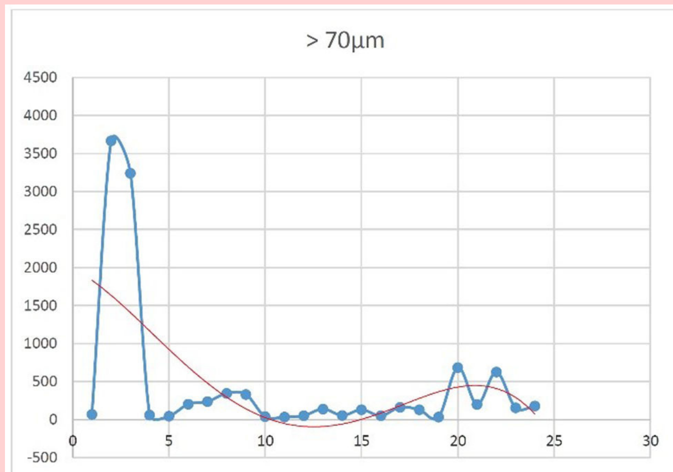

From the analysis of these diagrams it results that the number of oil contaminant particles with d > 4 µm, respectively d > 6 µm increased during the whole endurance cycle. The polynomial curves of the 4th order, represented by dots on the two graphs by interpolation, provide a clearer picture of the increasing trend of the number of contaminants in the oil.

Analogously, in Fig. (17÷20) 4 diagrams corresponding to the evolution in time of the number of particles of oil contaminants having diameters bigger than: (14, 21,38,70) µm are presented.

From the analysis of these diagrams it results that the number of oil contaminant particles with d > (14, 21,38,70) µm, decreased during the endurance monitoring period from the above indicated interval. The polynomial curves of order 4, represented by points on the two diagrams, by interpolation, provide a clearer picture of the declining trend in the number of oil contaminants. Monitoring of the pump **P2** showed that its wear occurred slowly between 4 June 2019 and 7 February 2020, mainly due to impurity particles with diameters d > 4 µm and d > 6 µm, while the input of particles with d > (14, 21, 38, 70) µm was a negligible one.

2.4. Oil analysis with the Brookfield viscometer

With the help of a high-performance viscometer (**Brookfield CAP 2000+**), samples of unused and used oil taken from the endurance stands of pumps **P1** and **P2** were analyzed.

Fig. 21. Brookfield CAP 2000 Plus Viscometer

2.4.1. Brief description of the viscometer and the working method

The **Brookfield CAP 2000 +** viscometer (Fig. 21) is a compact analysis laboratory instrument that can be used to test products over a wide range of temperatures and viscosities. It operates with small sample volumes (less than 1 ml) and provides precise thermal control during experiments. The viscometer used has a robust construction and ensures resistance in difficult working conditions. It is recommended in research and development activities and for thorough testing in the field of quality control. According to the appliance’s technical book, **CAP 2000+** offers lower shear rates, making it suitable for many applications where a small sample volume and good temperature control are required.

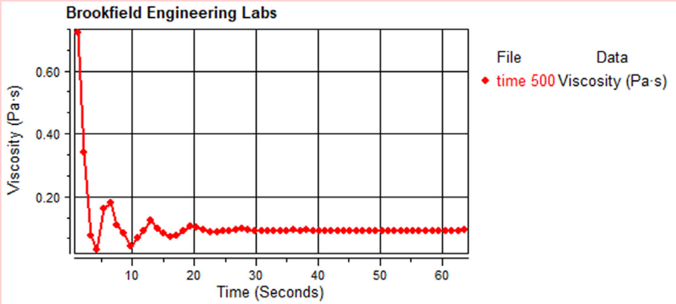

Fig. 22. Stabilization of the oil sample at n = 500 rpm

Among the most important technical specifications we can list the following:

- viscosity range: 0.2 ... 15 Poise
- shear rate: 10 ... 13 s^{-1}
- temperature: 5-75 ° C or 50-235 ° C
- rotation speed: 5-1000 rpm

Fig. 23. Comparative rheograms for 3 samples of analyzed oil (fresh oil / P1 pump oil / P2 pump oil)

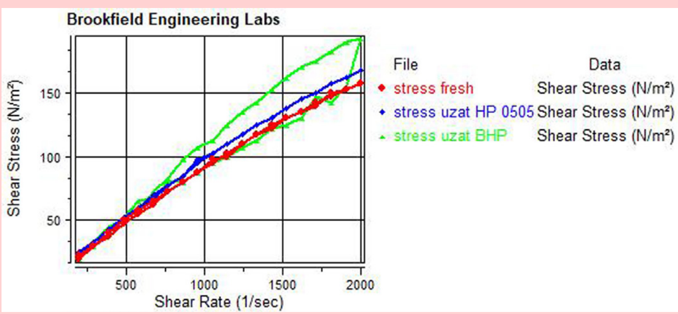

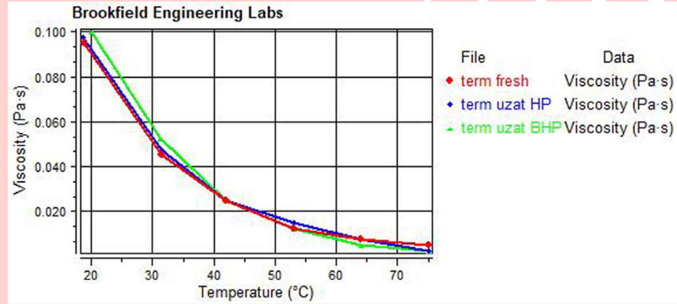

Fig. 24. The viscosity variation with temperature - comparative results for 3 samples of analyzed oil (fresh oil / P1 pump oil / P2 pump oil)

- meets industry standards: ASTM D4287; ISO 2884; BS 3900
- small sample: <1 ml;
- integral temperature control;
- optional CAPCALC 32 software for complete control and data analysis [5].

For the brought oil samples, three types of tests were performed:

- Test 1 (homogenization);
- Test 2 (for determining the parameters of the rheological model;
- Test 3 (for varying the parameters of the rheological model).

The authors of the paper specify that the Brookfield 2000+ viscometer is an equipment of the Tribology laboratory of the Department of Machine Organs of the University Politehnica of Bucharest, where the experiments were performed in September 2020.

2.4.2. Test 1 (homogenization test)

This test was performed for the fresh oil sample, H46 EP. This is a time test that was done at different speeds of the viscometer and the following were found:
- at 100 rpm, after 25 s, the oil sample was homogenized;
- at 200 rpm, after 25 s, the oil sample was stabilized;
- at 500 rpm, after 30 s, the oil sample was stabilized and the measurements continued (Fig. 22).

2.4.3. Test 2 (for determining the parameters of the rheological model)

This test meant tracing the rheograms of the oil samples and obtaining the corresponding rheological models. For this purpose, the following parameters were determined:
-tangential tension
- shear stress (Oy axis) $\tau = m\dot{\gamma}^{n}\tau = m\dot{\gamma}^{n}$ where m = consistency index [Pas^{-n}], n = flow index (dimensionless);

$\dot{\gamma}$ $\dot{\gamma}$ = speed gradient - shear rate (Ox axis).
The comparative rheograms of the three oil samples are shown in Fig. 23.

Lubricant type	Newtonian model		Law power model		
	Viscosity [Pa·s]	Confidence of fit	Consistency index [$Pa{\cdot}s^n$]	Flow rate	Confidence of fit
H46 fresh	0.085	97.8%	0.210	0.877	97.9%
Used Oil H46 Pump P1	0.090	97.5%	0.250	0.861	98.2%
Used Oil H46 Pump P2	0.095	92.3%	0.177	0.915	91.4%

Table 3. Rheological parameters of the 3 oil samples

2.4.4. Test 3 (variation of the parameters of the rheological model with temperature)

This last test, concretely, aimed to graphically illustrate the variation of the viscosity of the 3 oil samples with temperature. Fig. 24 presents the comparative results of the variation of the viscosity of the 3 oil samples with temperature.

2.4.5. Obtained results - Rheological parameters of the tested oils

Table 3 shows the calculated values of the rheological parameters corresponding to the Newtonian model, respectively the Law of Power model for the three oil samples analyzed with the **Brookfield 2000+** viscometer. In the case of obtained both models, the correlation coefficient (Confidence of Fit) represents the statistical correlation coefficient of the data and shows how close the values obtained are to the obtained model.

3. Conclusions

In predictive and proactive maintenance, oil analysis is a particularly important activity for verifying the proper functioning of hydraulic equipment and systems. In particular, the authors of this paper studied the influence of wear of solid contaminant particles on two hydraulic gear pumps in endurance, using two ultramodern laboratory appliances.

- Oil analysis performed with **a Laser CM Parker** analyzer showed that high wear in pumps are caused by contaminant particles with diameters d > 4 μm and d > 6 μm, while the contribution of particles with diameters d > 14 μm, d > 38 μm, d > 70 μm is negligible.
- The analysis of the oil performed with **Brookfield 2000 +** viscometer indicated an increase in dynamic viscosity, in the case of the oil used by pumps P1 and P2, which can be explained by the appearance of solid contaminants in the oil as a result of their running-in.
- The **Law Power** rheological model was preferred in the case of the oil sample corresponding to pump **P1** and the fresh oil sample H46 EP while the **Newtonian** rheological model was preferred in the case of the oil sample corresponding to pump **P2**.

For this reason, the parameters of interest in evaluating the contamination of the **P1** pump oil were the consistency index, respectively the flow index, while for the evaluation of the **P2** pump oil contamination, the kinematic viscosity was the indicator of the appearance of impurities.

- The occurrence of wear in the monitored pumps as a result of the erosive action of solid particles in the corresponding oil samples was demonstrated by laboratory methods that on the one hand allowed the quantification of impurities and on the other hand indicated the rheological models to follow in the predictive and proactive analysis of them.

Acknowledgements

This paper has been funded by the Romanian Ministry of Research and Innovation under Programme I-Development of national R&D system, Subprogramme 1.2–Institutional performance–Projects financing excellence in R&D&I, Project acronym: PRO-INSTITUTIO, Financial Agreement no. 19PFE/17.10.2018, Phase 5.

References

[1] A. D. Marinescu, Menținerea eficienței energetice în timp a sistemelor hidraulice prin utilizarea unor metode moderne de mentenanță predictivă, Rap.Științific nr. 3, Universitatea Politehnica din București, 12.07.2017.

[2] https://www.hesper.ro/categorie-produs/pompe-si-motoare-cu-roti-dintate/.

[3] https://www.sigma-distributie.ro/ulei-lukoil/lubrifianti-industriali/ulei-hidraulic/ulei--lukoil-h-100-ep/files/fisa_produs/1-4%20HIDRAULICE%20ADITI VATE%20PENTRU%20 EXTREMA%20PRESIUNE%20H_EP.pdf.

[4] https://manualzz.com/doc/6598462/laser-cm20__ park Erhfde.

[5] http://www.huntercaprez.com/view/data/3906/ Brookfield/Manual/CAP2000plus.pdf.

*Corresponding author: AL.-D. MARINESCU marinescu.ihp@fluidas.

Applications of hydraulics in wind power generation

I.-M. BACIU1[a*], AL. HRISTEA2[a], C. DUMITRESCU3[a]

[a] *Hydraulics and Pneumatics Research Institute INOE 2000-IHP Bucharest*

Abstract: The article presents some hydraulic systems that are found in wind energy conversion facilities (wind turbines). These systems intervene in the positioning of the turbine platform, the orientation of the blades, the braking at high wind speeds. Also, a system for hydraulic energy transmission from the turbine rotor to the electric generator is presented, which is the subject of the doctoral thesis of the main author.

Keywords: positioning, blade, nacelle orientation system; braking system; wind power.

1. Introduction

Global warming is a growing global concern, as it causes drastic climate change with disastrous effects on humanity such as floods, desertification, extinction of wildlife, lack of food, etc. This change in global temperature is caused by emissions of CO2 and other toxic gases, resulting from the burning of fossil fuels (oil, gas and coal) to produce electricity, heat, etc.[1]

A non-polluting alternative in electricity production is wind energy. The advantages of producing electricity through wind energy are: lack of environmental pollution; no toxic waste of any kind is produced; low decommissioning costs. [2]

Energy conversion is accompanied by a loss of energy which leads to a decrease in energy efficiency. Taking into account the area crossed by the air current **A**, the wind speed **v** and the air density **ρ**, the power and energy of the air flow can be determined as follows:

$$P = \frac{16}{27} \cdot \frac{p \cdot v^3 \cdot A}{2} = \frac{8}{27} \cdot p \cdot v^3 \cdot A$$

$$P = \frac{16}{27} \cdot \frac{p \cdot v^3 \cdot A}{2} = \frac{8}{27} \cdot p \cdot v^3 \cdot A \quad [3] \qquad (1)$$

$$E = \frac{m \cdot v^2}{2} = \frac{(A \cdot v \cdot t \cdot p) \cdot v^2}{2} = \frac{A \cdot v \cdot t \cdot p \cdot v^3}{2}$$

$$E = \frac{m \cdot v^2}{2} = \frac{(A \cdot v \cdot t \cdot p) \cdot v^2}{2} = \frac{A \cdot v \cdot t \cdot p \cdot v^3}{2} \quad [3] \qquad (2)$$

where: ***P*** - wind power; ***ρ*** – air density; ***A*** – rotor area; ***v*** – wind speed; ***E*** - energy [3]

As can be seen from the two relationships, both power and energy are mainly influenced by air speed.
Betz's law, published in 1919, sets the theoretical limit of efficiency for a wind turbine and is based on the law of conservation of mass and the moment of air flow. Following the calculations, Betz determined that a wind turbine can extract a maximum of 59.3% of the kinetic energy of the wind. [3]
In reality, the most efficient wind turbines have a Betz factor equal to 0.45… 0.50.
In addition, there are losses due to incorrect orientation of the platform or blades.
To increase efficiency, it is possible to intervene on the orientation of the turbine during operation. There are two ways to act on the orientation: through a nacelle orientation actuation system, respectively through a blade positioning system. Such systems are only required for horizontal shaft turbines. In this article, the systems with hydraulic drive and braking will be discussed.
The blade positioning system and the nacelle orientation system can be hydraulically or electrically operated in the case of low power turbines. For high power turbines, positioning, wind orientation and hydraulic braking systems are used. In this article, the systems with hydraulic actuation and braking will be discussed.

The advantages of hydraulic systems:

- ✓ Wide range of torque / speed
- ✓ Transmission of high power with low inertia
- ✓ They allow to change the speed much faster because they have lower inertia
- ✓ They remain blocked and are not damaged under maximum load
- ✓ Power density
- ✓ Increase turbine operating time
- ✓ Higher stability of the system to which they belong
- ✓ Fast response, compact structure, small volume, light weight
- ✓ Good dynamic response

2. Yaw systems

Yaw is the rotation that orients the turbine nacelle around the tower, while orienting the rotor in the wind direction according to the data provided by the sensors, which leads to a maximum energy production efficiency. The turbine platform and its tower perform relative movements relative to each other through subassemblies connected to the turbine tower and the platform, respectively. [4]
Yaw can be used to adjust the power to exceed the rated wind speed for which the turbine was designed, by reducing the swept area of the rotor positioned in the wind direction. The yaw torque must take into account the strong torque due to the high moment of inertia of the nacelle and the rotor. [4]

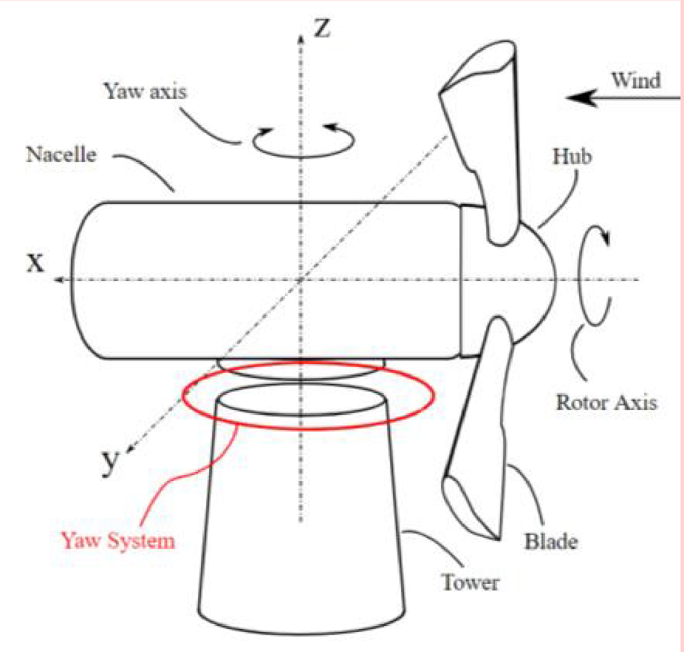

Fig. 1. Schematic representation of a wind turbine [4]

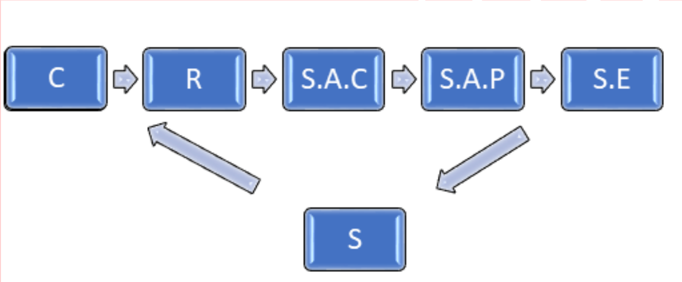

Fig. 2. Block diagram of the nacelle orientation system

The orientation of the nacelle is done by means of a simple hydraulic system (Fig. 2):

- C - comparator;
- R - regulator (data processing block);
- S.A.C - drive and control system;
- S.A.P - gear and lever system;
- S.E - execution system;
- S – sensors.

Figure 1 shows schematically the side view of a wind turbine; in this representation one can see the 3 axes: nacelle axis of rotation (Z); rotor axis of rotation (X) and Y-axis.

The comparator receives data from the sensors and compares them with the reference values that were established following previous field research. The controller is the one that receives the information from the comparator and further determines which control signal to transmit to the drive system. The drive system consists of: hydraulic pumps and motors, proportional directional valves and auxiliary elements. The execution element is one or more rotary hydraulic motors that perform the rotational movement of the nacelle relative to the tower; another important element in the orientation of the nacelle is the system of levers, gears and braking equipment. As the wear of mechanical elements by friction occurs, it is necessary to install a lubrication system proposed following the tribological analysis. The sensors provide information about the parameters and coordinates of the rotor axis relative to the wind direction, the values obtained are compared with reference, and depending on the result of the comparison, the angular adjustment is ordered. The relative movement of the nacelle relative to the tower is produced by the action of one or more hydraulic motors which are mounted between the two components of the turbine. This movement is performed when the wind changes direction, the main controller of the system sends a command through which the nacelle changes its position. An advantage of using hydraulic drive is the reduction of mechanism fatigue and damping of rotational movements.

Fig. 3. Hydraulic diagram of the nacelle orientation system [5]

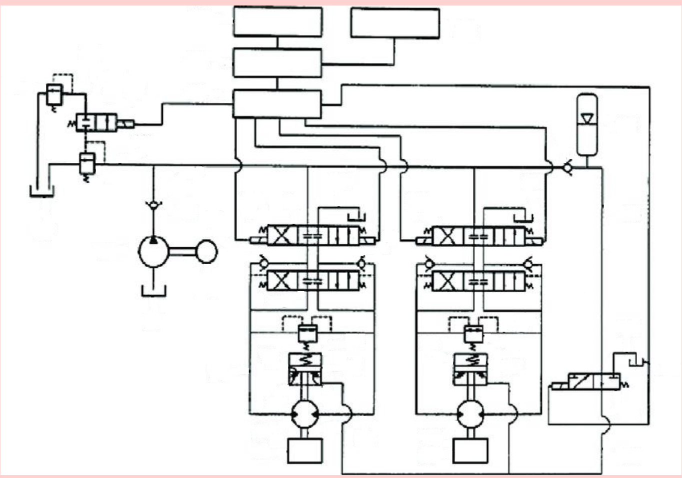

3. Pitch system

The blade orientation system is found in most wind turbines today. It adjusts the rotational speed of the rotor and the power generated by the electric current generator. As the wind speed increases or decreases this system adjusts the blade angle to ensure a constant rotor speed. The turbine blades can be driven simultaneously by a hydraulic system, consisting of a cylinder on which a plate is fixed, which rotates the blades simultaneously. The pitch system rotates the blade axis with a maximum angle of 5 degrees to ensure the best possible capture of wind energy; if an angle greater than 5 degrees is desired, one shall operate with a hydraulic actuator whose movement is very precisely controlled. [3] [6]

The hydraulic installation for driving the pitch system includes:

- C – comparator;
- R – regulator;
- S.A.C - drive and control system;
- S – sensors;
- S.F - braking system.

Figure 4 shows the block diagram of the pitch hydraulic system. The blade position adjustment system allows the turbine

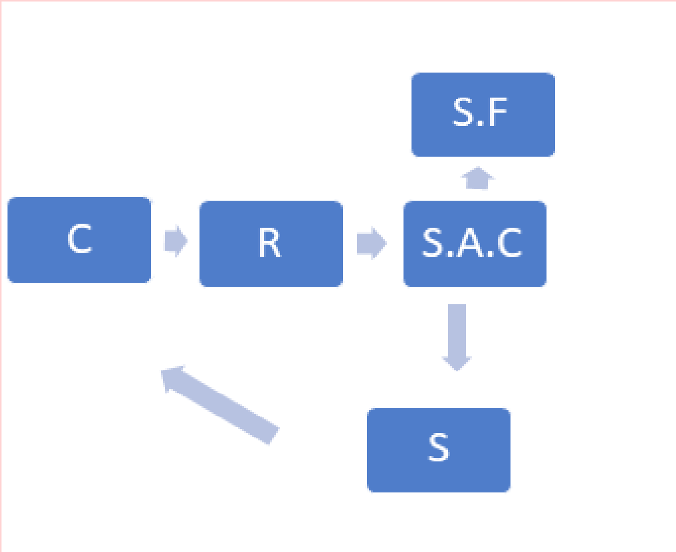

Fig. 4. Block diagram of the pitch system hydraulic installation

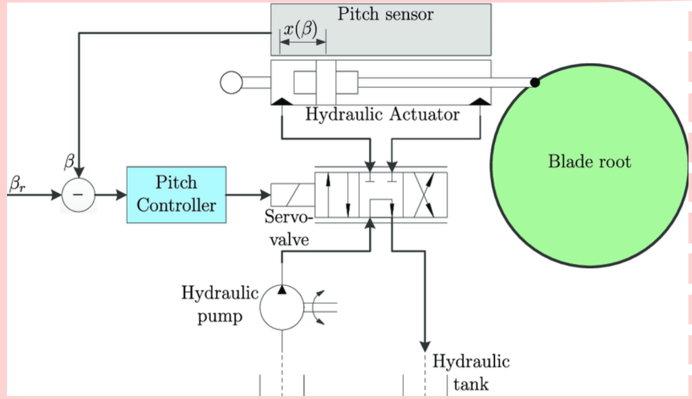

Fig. 5. Extended hydraulic diagram of the blade positioning system [5]

rotor speed to be kept constant, and is accompanied by the braking system, as changing the angle of attack of the blade increases the rotor speed. The platform orientation system allows coarse adjustment of the orientation, while the blade orientation system is operated by a hydraulic system that offers high precision.[6]

The advantages of the hydraulic drive of such a system are: long service life, short response time and high driving forces. The costs with the blade positioning system are low, below 3%, compared to the costs for the construction and installation of a turbine, but 23% of the failures that cause the turbine to stop operating are caused by this system.

The hydraulic system must be designed taking into account aspects related to the climate and the environmental conditions in which it is installed. The hydraulic installation must be designed taking into account aspects related to the climate and the environmental conditions in which it is installed. The oil temperature must be maintained in the range of 30 ... 50°C

4. Braking system

Wind turbines are equipped with braking systems to control factors such as: overspeed, system overheating and vibration. In the event of a fault, the rotor is stopped by braking; the braking torque must exceed the aerodynamic torque and absorb the energy of the rotational mass and the wind energy. The most used braking systems are the hydraulic ones because they are precise and can generate a large braking torque; electro-mechanical systems are also used but they have the disadvantage that for a high torque the electric motor must have a suitable size. [7]
The wind changes its direction and speed, consequently the braking system must work continuously, which leads to a permanent friction of the brake discs, and the energy taken is transformed into heat, with the possibility of starting a fire. To prevent such incidents, the amount of heat generated (energy lost through friction) must be kept to a minimum. For this purpose, measures were taken such as: the use of proportional hydraulics, adjustable pumps, special fluids, etc. The brake discs are made of special materials that increase the reliability of the braking system and reduce oscillations.

Fig. 6. Block diagram of the braking system [7]

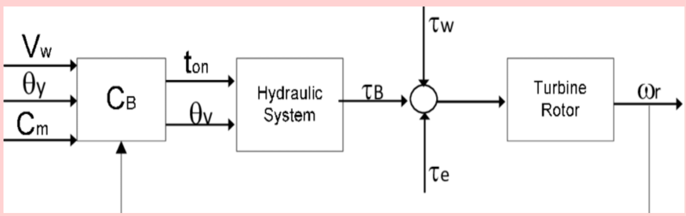

5. Hydrostatic transmission

In modern wind turbines, with powers of up to a few Megawatts, the nacelle together with the components and systems it contains weighs between 20 and 35% of the total weight of a turbine. For example, on the VESTAS V90-3MW turbine, the assembly weighs 271 tons for a height of 80 m or 346 tons for a height of 105 m. Regardless of the height, the platform weighs 70 tons and the rotor weighs 41 tons. , which leads to a percentage of 25.8% and 20.2%, respectively. A failure of the nacelle components brings special problems, especially for offshore turbines. To reduce the impact, the components are subject to preventive maintenance, which involves, among other things, replacement or overhaul every 4 years. It should be added that the speed multiplier represents 10% of the price of a turbine. So repairing or replacing it leads to significant expenses. The hydraulic transmission between the rotor and the generator offers a solution to all these problems. [8]
A hydrostatic transmission (HST), figure 7, transfers the rotor power $\boldsymbol{P}_{Rotor}$ to the generator while transforming the variable rotor speed $\boldsymbol{n}_{Rotor}$ into the required constant generator speed $\boldsymbol{n}_{Gen}$. The rotor speed is regulated using the motor's displacement setting $\boldsymbol{\alpha}_m$ [3]. Low wind speeds require low displacement settings as less flow is generated by the rotor, while higher wind speeds generate more flow and require larger motor displacements. [8]

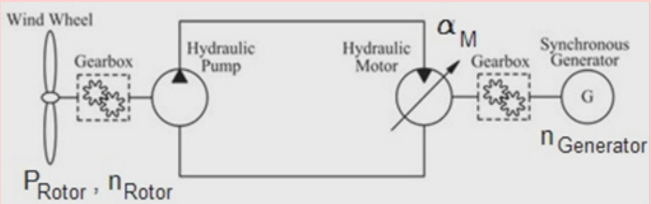

Fig. 7. Basic principle of hydrostatic transmission (HST). [8]

At the moment, the work team from Hydraulics & Pneumatics Research Institute (INOE 2000 - IHP Bucharest) is involved in the realization of a hydraulic transmission for a medium size turbine, with a power between 20 and 50 kW. The next step after developing the transmission is to develop a pneumatic storage system, where the compressor is also driven by a hydraulic motor. After compression, the air is stored in a pressure tank, to be used for electricity generation using a pneumatic engine or for other purposes. The electricity thus obtained can be combined with that obtained in the main branch (hydrostatic transmission), but can also be used for auxiliary purposes (for auxiliary systems of the closed-loop hydrostatic transmission: cooling, additional pump drive, etc.). The diagram of the entire proposed installation, in parallel with the principle diagram of a classical wind turbine, is presented in figure 8. The pneumatic storage facility was approached at theoretical level and by physical realization within INOE 2000-IHP in 2016.

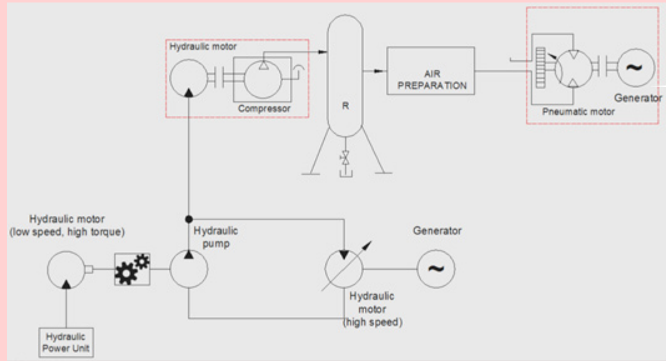

(a)

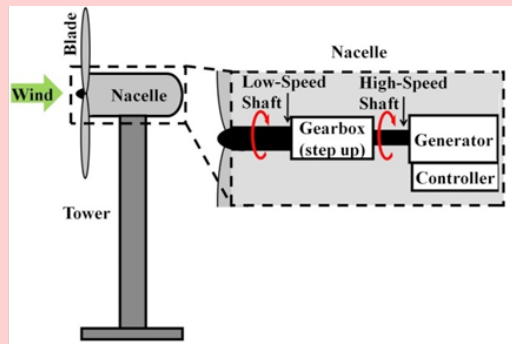

(b)

Fig. 8. HST combined with energy pneumatic storage system (a), compared to a classical turbine (b).[8]

Figure 9 shows the location of the main components of the wind turbine equipped with HST: the rotor and the main pump - in the nacelle; the hydraulic lines - inside the tower; the electric generator and the rest of HST components at the base of the tower.

Figure 10 shows the main subassemblies of the stand where the hydrostatic transmission will be tested. In testing phase, the rotor which drives the hydraulic pump could be simulated

Fig. 9. The main components of the wind turbine with HST [8]

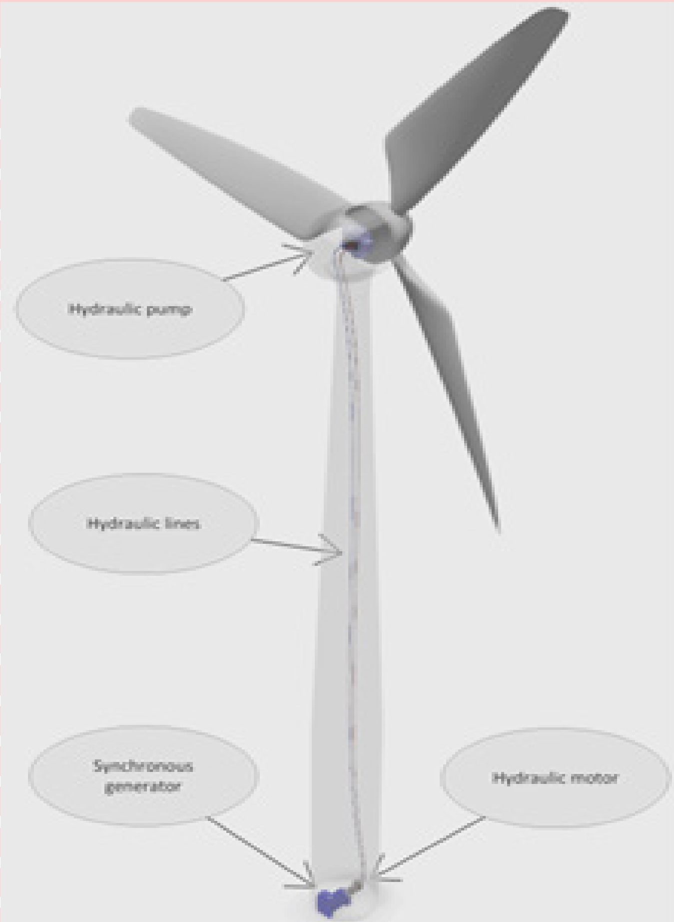

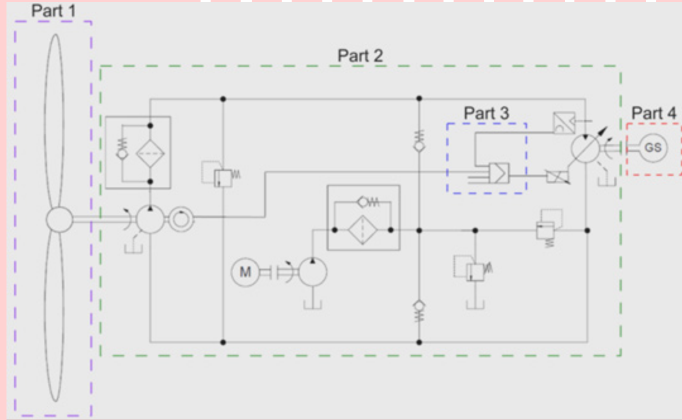

Fig. 10. The subassemblies of the HST:
***Part 1** = wind turbine simulated with variable electric/ hydraulic motor; **Part 2** = HST for low-power turbines**; Part 3** = HST controller; **Part 4** = synchronous generator.[8]*

with an electric motor, with variable speed. The hydraulic transmission is essentially a closed-loop hydraulic drive system. The main components are: a fixed capacity main pump, a variable-capacity main motor, hydraulic circuits, hydraulic accumulators, safety valves, sensors, filters, heat exchanger, anti-cavitation volume loss compensation pump, hydraulic motor capacity controller with hydraulic circuit with feedback from the high pressure hydraulic circuit, aerodynamic rotor speed and wind speed. [8]

5. Conclusions

- ✓ Wind energy is a green energy type.
- ✓ Hydraulic drive systems can be found in yaw system, pitch system and brake system.
- ✓ Yaw system main advantages are: the reduction of the mechanism fatigue and the damping of the turning movements.
- ✓ The pitch system allows the turbine rotor speed to be kept constant.
- ✓ Accidents can be avoided by using proportional hydraulics, which also ensures high positioning accuracy.
- ✓ Orientation and positioning systems can prevent the destruction of the turbine but at the same time contribute to increasing energy performance.
- ✓ Among the ways of transmitting wind power is the hydrostatic transmission, which has the advantage of reducing the mass of the nacelle.

Acknowledgements

This paper has been funded by the Romanian Ministry of Research and Innovation under Programme I-Development of national R&D system, Subprogramme 1.2–Institutional performance–Projects financing excellence in R&D&I, Project acronym: PRO-INSTITUTIO, Financial Agreement no. 19PFE/17.10.2018, Phase 5.

References

[1] ***, Renewables 2018. Global Status Report, https://www.ren21.net/wpcontent/uploads/2019/05/GSR2018_Full-Report_English.pdf (2018)

[2] E. MAICAN, Sisteme de energii regenerabile (Renewable energy systems), Printech, Bucharest, 2015, ISBN 978-606-23-0359-4

[3] I. BOSTAN, V. DULGHERU, I. SOBOR, V. BOSTAN, A. SOCHIREANU, Sisteme de conversie a energiilor regenerabile (Renewable energy conversion systems), Tehnica-Info, Chişinău, 2007, ISBN 978-995-63-076-4

[4]-https://www.windturbin.com/wind-turbine-yaw-controlling/, accessed 10 october 2020

[5] H.C. Pedersen, S. Stubkier, Design, Optimization and Analysis of Hydraulic Soft Yaw System for 5 MW Wind Turbine, Wind Engineering, 35(5), 529 (2011).

[6] - https://en.wikipedia.org/wiki/Blade_pitch, accessed 12 october 2020

[7] E. Rijanto, A.S. Nugraha, A. Muqorobin, Development of a Hydraulic Brake Control System for 100 kW Horizontal Axis Wind Turbines using Pressure Relief and Directional Valves, International Journal of Applied Engineering Research, Volume 7(4), pag. 383 – 396, 2012.

[8] R. Radoi, I. David, A.-P. Chirita, A.-M. Popescu, Considerations regarding the use of hydraulic drive systems in the construction and maintenance of wind turbines, Journal of Research and Innovation for Sustainable Society (JRISS), Volume 2, Issue 1, 2020, ISSN: 2668-0416, Thoth Publishing House

*Corresponding author: I. M. BACIU, baciu.ihp@fluidas.ro

Digital hydraulic used to reduce energy losses in hydraulic systems

B. TUDOR1[a], M.A. HRISTEA2[a*], S. SEFU3[a]
[a] - *Hydraulics and Pneumatics Research Institute INOE 2000-IHP, Romania*

Abstract: Digital hydraulics has begun to take a significant lead in recent years, with the need to reduce energy losses in hydraulic systems and make them more efficient. Currently, there are several research teams in the world located in universities or research institutions that deal with digital hydraulics such as the Universities of Linz, Aachen, Tampere and the INOE 2000-IHP research institute in Bucharest. There are also companies that have invested in this field of digital hydraulics, coming on the market with digital hydraulic equipment, such as Bosch-Rexroth, Artemis and Sauer Danfoss [1].

Keywords: digital hydraulics, energy efficiency, digital solutions

1. Introduction

Defining digital hydraulics

Hydraulic systems have been operating with high energy losses since their inception. As technology advanced, new equipment emerged that increased the performance of hydraulic systems and reduced energy losses. Among these developments, we can mention proportional and servo equipment, and currently we can discuss the concept of digital hydraulics.

The term digital hydraulics is a term that appeared recently in the literature and tries to introduce in the field of hydraulics, a series of new hydraulic equipments, with the help of which to achieve good performances and small energy losses.

In the construction of digital hydraulic equipment, components with low energy losses are used, so that the energy losses of the system are reduced by using such equipment, compared to the existing hydraulic systems that use proportional and servo components.

The idea of digital hydraulics does not refer in any case to the connection of classical hydraulic devices to a computer, but is defined as follows:

- Digital hydraulic equipment uses on/off type distributors;
- Performance comparable to that of existing proportional and servo equipment;
- A flexible and programmable controller;
- Redundant circuits so that the system can operate, even at a reduced capacity, and in case one or more distributors fail.

2. Types of digital hydraulic equipment

- Digital distributors
- Digital pumps
- Digital hydraulic cylinders
- Digital power management system

2.1 Digital distribution

The digital distribution is of two types, switching and parallel.

2.1.1 Digital switching distribution

It is based on the idea of controlling an on/off type distributor by a permanent and high frequency switching between the closed and the open position, with the help of a PWM (pulse width modulation) signal [2]. The flow resulting from leaving the distributor is the result of the ratio between its closing and opening periods.

Figure 1. PWM signal controlled on / off distributor [2]

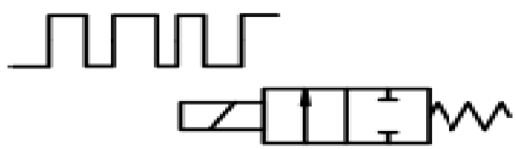

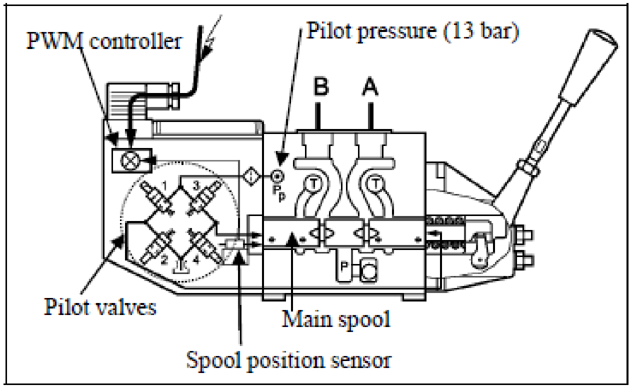

Figure 2. Proportional distributor with PWM controlled pilot [3]

The foundations of this concept were laid by researchers at the mechatronics center in Linz.
Figure 1 shows the symbol of such a switching distributor. Because switching distributors require high frequencies and special materials for the construction of the hydraulic spool and the electromagnet, so far they have not been used in series production, except for small distribution and/or small pressures. Such an example of the hydraulic equipment manufacturer Sauer Danfoss is shown in figure 2. The figure shows in section a proportional distributor for mobile equipment, which has been replaced by the proportional electromagnet with and the servo controller with a system of small switching distributors.

2.1.2 Digital parallel distribution

Digital distribution in parallel is achieved by connecting in parallel several on/off distributors and this system is called Digital Flow Cntrol Unit or DFCU for short.
Figure 3 represents the symbol of a DFCU, where n is the number of distributors.

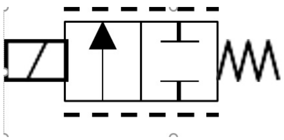

Figure 3. symbol of a DFCU [2]

This method is based on several types of distributor coding such as:
- Coding using the Pulse Number Mdulation or PNM method, where several distributors of the same type are used;
- Coding using Fibonacci series (1,1,2,3,5 … etc);
- Coding using the Pulse Code Modulation method based on the binary series (1,2,4,8 … etc or 2^n).

By coding the distributors, it is understood that the flow areas of the distributors connected in parallel is in a certain progression, as defined above.
The use of distributor coding leads to a step flow curve, where the step size for each step is constant, as we can see in Figure 4.
A DFCU with a number of 200 different flow rates offers the same controllability as a good servovalve. Obtaining 200 different flows can be done using 200 distributors of the same

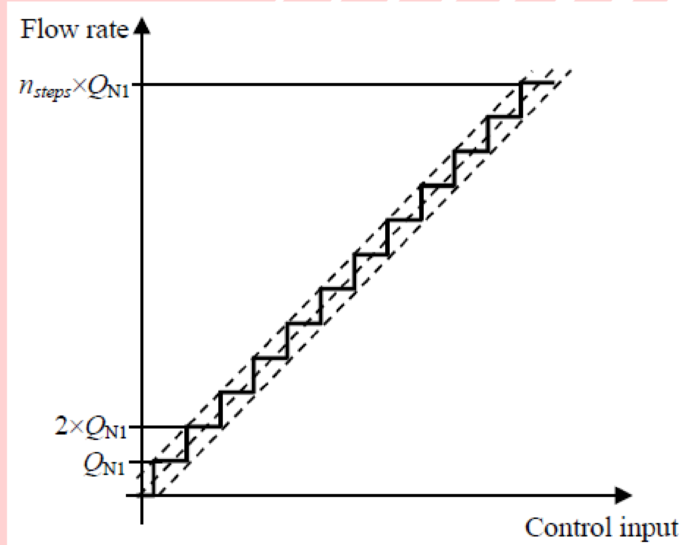

Figure 4. Flow curve for a DFCU [4]

Figure 5. Example of binary coded DFCU with 5 distributors and 31 different flow rates that can be obtained.

type, or 11 distributors coded in the Fibonacci series, or 8 distributors coded binary. An example of a DFCU can be seen in Figure 5.

2.2 Digital pumps

As in the case of digital distribution, digital pumps are based on the same principles and are also two types, switching and parallel.

Digital switching pumping systems consist of fixed flow pumps to which a switching distributor is connected and the flow is the result of its closed and open periods, and are shown in Figure 6 (a).

Figure 6 (b) shows a digital pumping system solution consisting of 3 fixed flow pumps, 3 on/off type distributors and 3 directional valves. Flow variation is achieved by opening in a certain combination of distributors. When the flow provided by one of the pumps is not necessary for the system, it flows to the tank with a small Δp.

Another method of implementing the digital pumping system in parallel, is by controlling the piston with an on/off distributor, so that the flow provided by each piston of the pump can be directed to the tank or to the system. Figure 7 (a) shows this type of pump, and Figure 7 (b) shows a reversible pump that can function both as a pump and as a motor. Each piston of the reversible machine can have 3 states, pumping in the system, running with no-load, or functioning as a hydraulic motor.

An example of a digital pumping system connected in parallel and having the control of each piston, is a system developed by the company Artemis [5], in order to use it at wind farms.

Figure 6. Switching pump (a), Parallel connected pumps (b) [4]

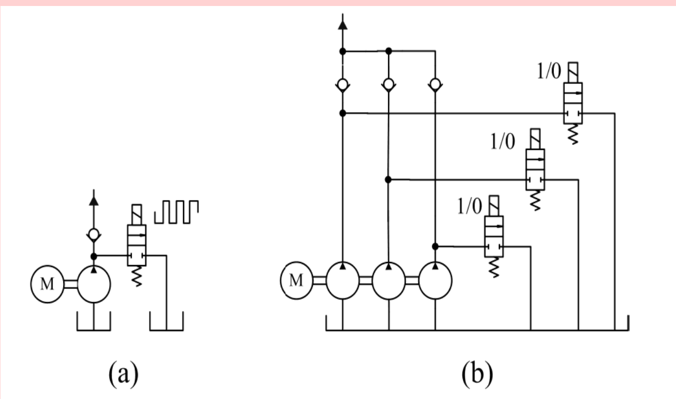

Figure 7. - Digital pumps with independent pistons [4]

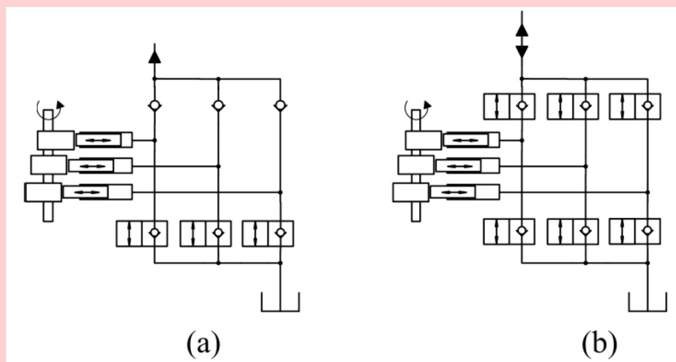

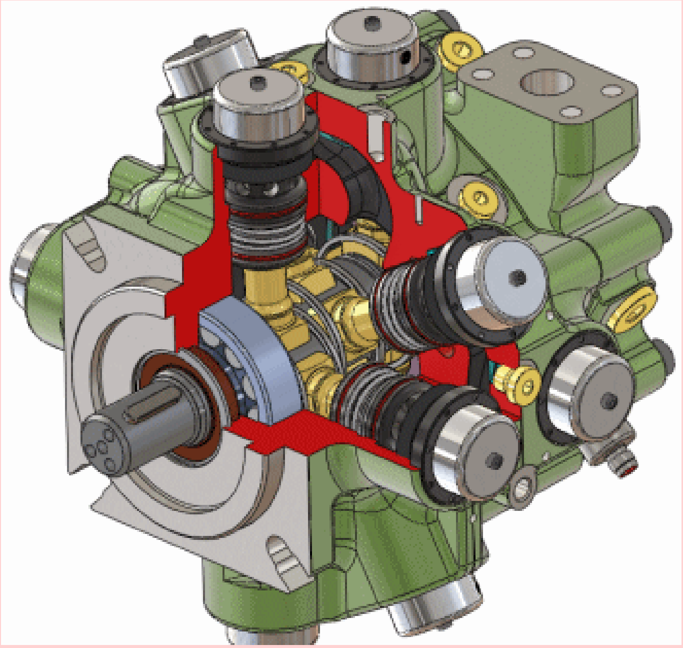

Figure 8. Section by digital pump developed by Artemis [5]

Figure 9. Digital switching motor (a), Digital motors connected in parallel (b) [4]

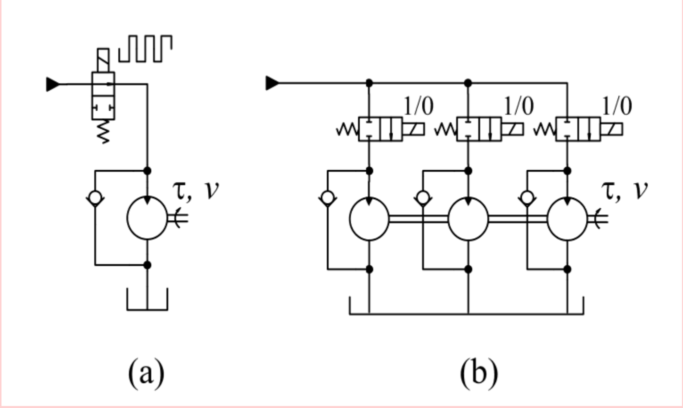

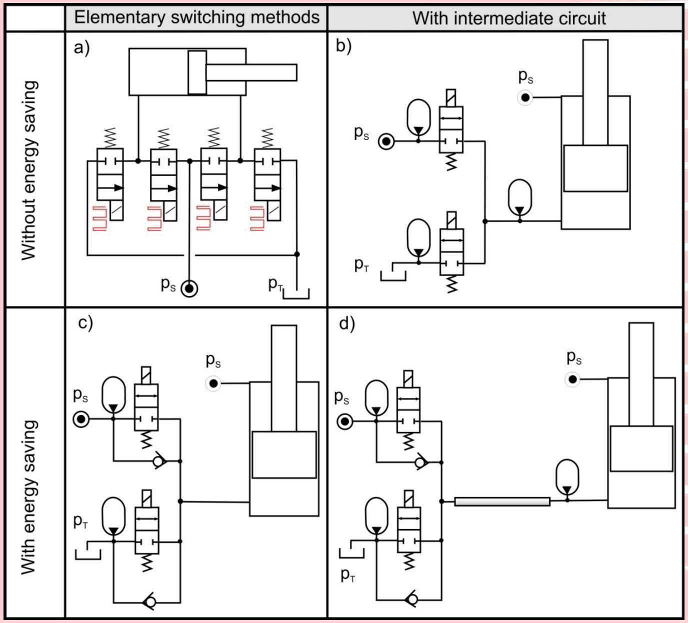

Figure 10. Switching methods [6]

Figure 11. Variable displacement Linear Actuator (VDLA) [6]

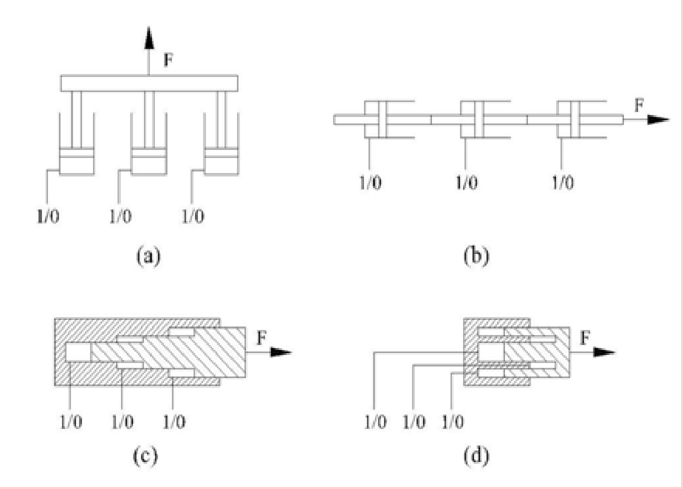

This example can be seen in Figure 8.

2.3 Digital hydraulic actuators

Digital hydraulic actuators are of two types: rotary hydraulic motors and linear hydraulic motors.
Rotary hydraulic motors are based on the same principle as pumps, having two types, switching 9 (a) and parallel 9 (b).

2.3.1. Variable Displacement Linear Actuator (VDLA)

It is also presented in two variants, switching and parallel. The type of linear digital switching hydraulic actuator is made by simply connecting to a cylinder a digital switching distributor, figure 10. The type of digital hydraulic actuator in parallel can be made in several ways, or by connecting several cylinders in parallel of the same size and rod joined at the end, either by making a cylinder with several actuating surfaces, in a progression such as the binary one, the Fibonacci series or PNM; the examples are shown in figure 11.

2.4 Digital Hydraulic Power Management System (DHPMS)

DHPMS is a solution of an integrated variable flow equipment, which has a certain number of independent outputs. The pressure and flow (including the direction of the fluid) of each outlet can be controlled independently, so there is no limitation in terms of pressure gain, which allows the use of a hydraulic accumulator to store fluid energy. One of the

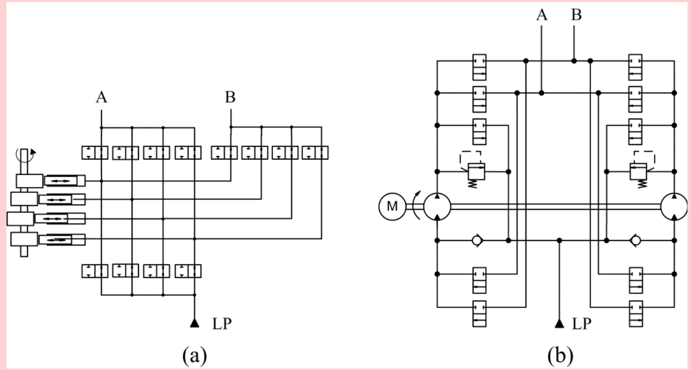

Figure 12. Examples of digital power management systems (DHPMS) [4]

disadvantages of this DHPMS is that, by its centralized nature, it introduces the need to use long hoses in many applications. Figure 12 shows two methods of implementing a DHMPS. Figure 12 (a) shows the DHMPS version with in-line pistons and distributors connected in parallel, while Figure 12 (b) shows the version using reversible machines of the fixed cylinder/pump type, connected on the same shaft. rotation.

3. Digital hydraulic equipment systems developed within INOE 2000 - IHP

Numerous equipment designs for which patent applications have been filed have been developed within the INOE 2000 IHP research institute, and some of them have been developed and tested, and others are under construction.

3.1 Examples of digital distribution

3.1.1 Digital switching distributors

The digital switching distributors developed by the INOE 2000 - IHP Research Institute are of two types, normally closed and normally open. [7]
Figure 13 shows a normally closed switching distributor, and Figure 14 normally open. This type of digital switching distributors are made using the closing of the cone flow hole on a circular seat. Lifting the cone from the seat is done with the help of the electromagnet in the normally close version, while in the normally open version the electromagnet pushes the cone on the chair, thus closing the fluid flow area.

Figure 13. Normally closed digital switching hydraulic distributor [7]

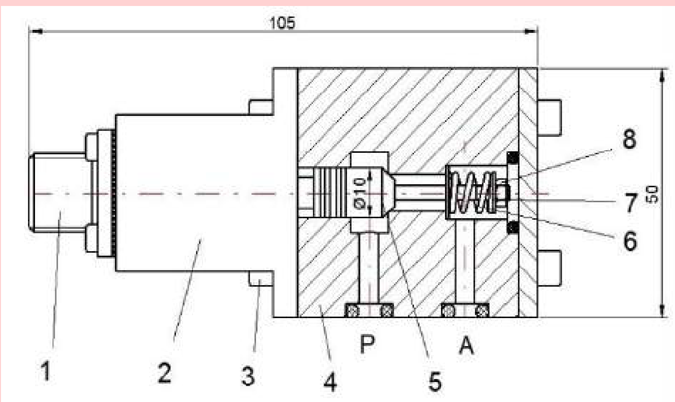

3.1.2 **Example of Digital Flow Control Unit (DFCU)**

The figure below shows a DFCU containing 5 2/2 on/off distributors, binary coded after the next progression 2, 4, 8, 16, 32 liters. The pressure drop on such a distributor is Δp = 14%. The system thus composed can achieve 2^5-1 = 31 discrete values, different for regulating the flow in the system. The flow variation resolution of this system is 2 liters.
The system in figure 15 consists of 1 bilateral single cylinder, 2 distributor 4/3, 3.1. DFCU with 5 binary coded on/off distributors and 3.2. DFCU consisting of 5 binary coded on/off distributors. DFCU 3.1 performs the flow variation and 3.2. performs controlled lowering of the cylinder in case

Figure 14. Normally open digital switching hydraulic distributor [7]

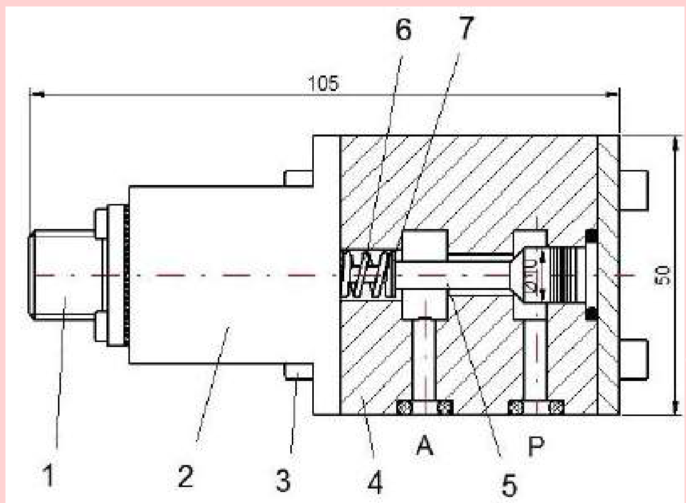

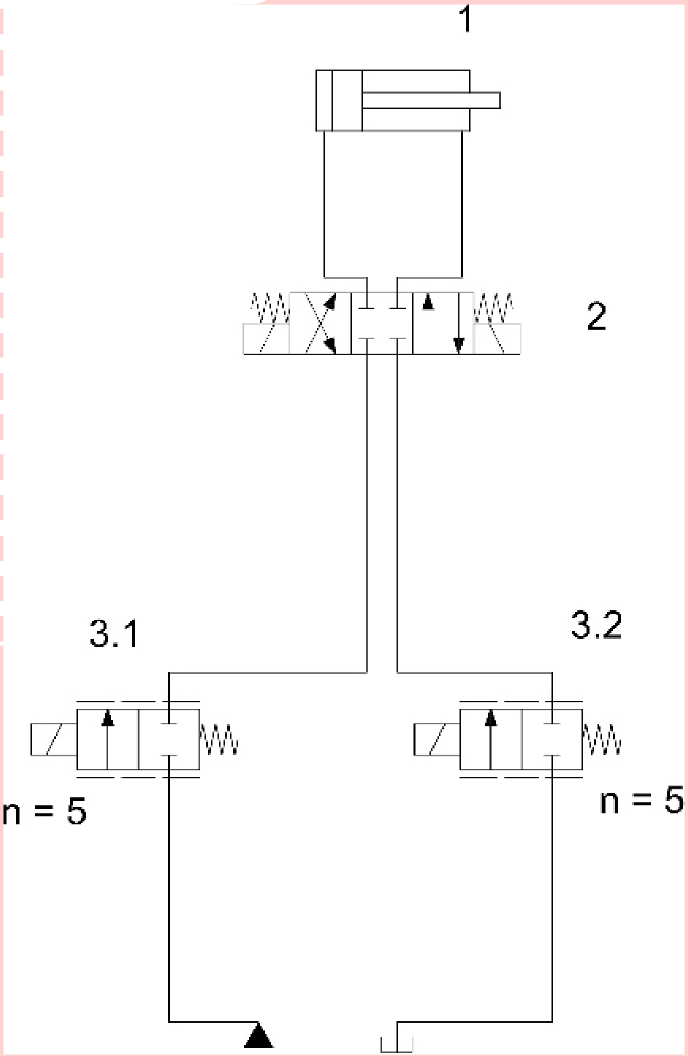

Figure 15. DFCU

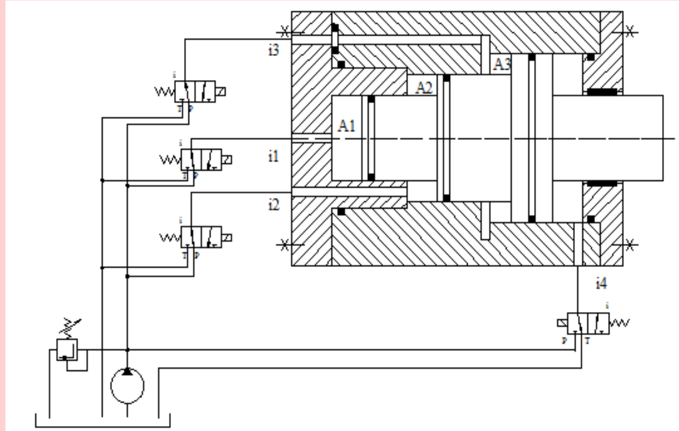

Figure 16. Digital linear hydraulic actuator [9]

of negative forces and 2. performs switching between the cylinder chambers.

3.2. Digital hydraulic cylinders

Within a 200 IHP, 2 types of VDLA have been designed, one with binary encoded surface areas and one that uses a hybrid encoding between PNM and PCM.

3.2.1. VDLA with binary coded areas [8]

Figure 16 shows a VDLA with 3 concentric areas, binary coded, as follows, A2 = 2A1, A3 = 2A2, thus obtaining 2^3-1 = 7 different variations of force and speed. This type of

VDLA allows that by supplying separately the 3 concentric areas, using on/off type distributors, to obtain a relatively linear curve of variation of force and speed.

3.2.2. Hybrid VDLA

Figure 17 shows a hybrid VDLA [10]. It was named so because its construction uses two types of coding, namely PNM coding and PCM coding and consists of a large diameter piston, driven by 9 pistons with a smaller diameter, and their operation is performed according to table 1.

Table 1. Digital hydraulic actuator actuation diagram [10]

Elmg. / Motion	E1	E2	E3	E4	E5
Advance 1	+	-	-	-	-
Advance 2	-	+	-	-	-
Advance 3	+	+	-	-	-
Advance 4	-	-	-	+	-
Advance 5	+	-	-	+	-
Advance 6	-	+	-	+	-
Advance 7	+	+	-	+	-
Advance 8	-	+	+	+	-
Advance 9	+	+	+	+	-
Withdrawal	-	-	-	-	+

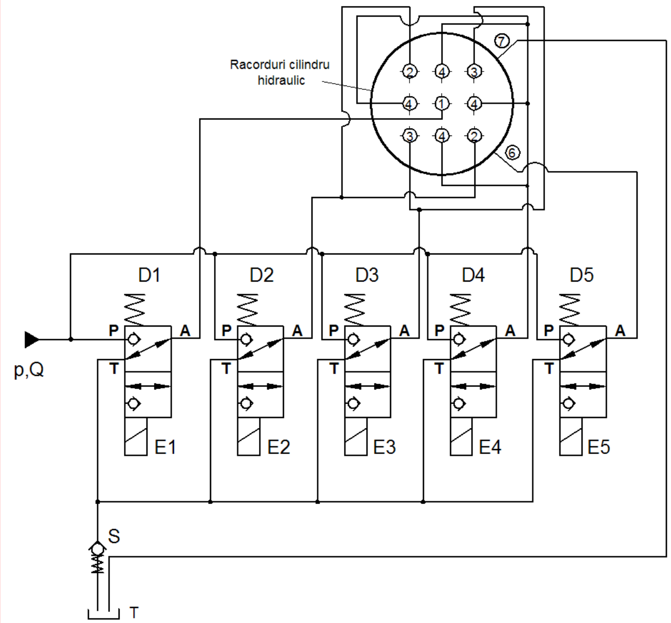

Figure 17. Digital hydraulic actuator actuation diagram [10]

As can be seen in figure 17 the 9 cylinders are connected as follows, cylinder 1 to distributor E1, the 2 cylinders numbered 2 to distributor E2, the 2 cylinders marked with 3, to distributor E3, the 4 cylinders numbered 4 to distributor E4, and the E5 distributor is used to retract the cylinder. As can be seen in Table 1, 9 different variations of forces and speeds are obtained.

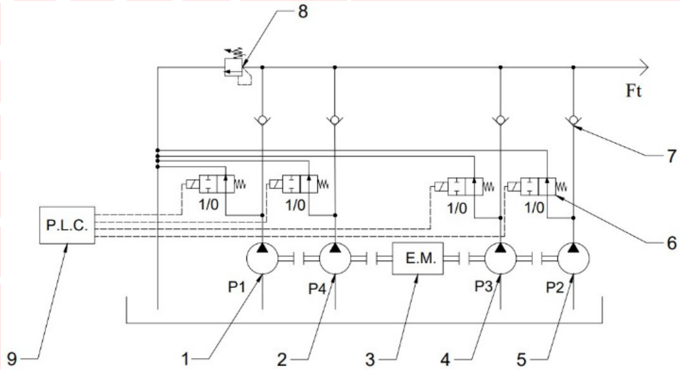

Figure 18. Hydraulic system with 4 fixed displacement pumps consists in: (1, 2, 4, 5) fixed displacement pumps, (3) biaxial electric motor, (6) 2/2 directional valve, (7) one-way valve, (8) pressure relies valve [11]

3.3. Digital pumping systems

Hydraulic systems which use pumping units with 4 coaxial pumps [11] (Figure 18) connected to an electric motor (3). The pump selection is made with a normal open on/off valve (6). When one of the on/off valve is switched to the close position, the flow is directed form the tank to the consumer through the directional valve (7). The safety valve (8) ensures system protection for system overload. Each pump has its own flow (Q1, Q2, Q3, Q4) of which we can select for the system one, two or even all for, getting the flow rates with the help of a programable logic controller 9 (P.L.C.).
Q1=First pump with the flow displacement of 4 (1)
Q2= Second pump with the flow displacement of 8 (2)
Q3= Third pump with the flow displacement of 16 (4)
Q4= Forth pump with the flow displacement of 32 (5)
The digital systems presented in points 3.1.2, 3.2.1 and 3.3 are ongoing research works of the authors and will concretize the results of these researches in other future articles.

4. Conclusions

By using on/off type distributors in the composition of digital hydraulic equipment, the energy losses from the hydraulic systems are reduced, because at the type of on/off devices they have a much lower pressure frames compared to the already consecrated equipment. Conventional hydraulic devices have pressure drops on devices between 20 and 40%, while digital hydraulic systems have obtained pressure losses of 14%.
By using simple equipment, on / off type distributors, fixed capacity pumps, in digital hydraulic systems, a good functioning of the system is ensured even if one of these equipment fails. In digital hydraulic systems the adjustment of different parameters (force, speed and flow) is done without high energy losses, due to the fact that the system is always connected to the tank when it does not adjust any parameter.

Acknowledgements

This paper has been funded by the Romanian Ministry of Research and Innovation under Programme I-Development of national R&D system, Subprogramme 1.2–Institutional performance–Projects financing excellence in R&D&I, Project acronym: PRO-INSTITUTIO, Financial Agreement no. 19PFE/17.10.2018, Phase 5.

5. Bibliography

[1] Luke WADSLEY," Optimal System Solutions Enabled by Digital Pumps" The 52nd National Conference on Fluid Power, **pp.7-13** (Las Vegas, March 23-25, 2011)

[2] Rudolf SCHEIDL, Helmut KOGLER, Bernd WINKLER, Proceedings of 2012 International Conference on Hydraulics and Pneumatics – HERVEX, November 7-9, Baile Govora, Romania, ISSN 1454 - 8003 - Hydraulic Switching Control – Objectives, Concepts, Challenges And Potential Applications,

[3] The Eighth Scandinavian International Conference on Fluid Power, SICFP'03, May 7-9, 2003, Tampere, Finland, IS IT TIME FOR DIGITAL HYDRAULICS? Academy. Research Fellow Matti Linjama, M. Sc. Arto Laamanen and Professor Matti Vilenius, **pp.347-366**.

4] The Twelfth Scandinavian International Conference on Fluid Power, May 18-20, 2011, Tampere, Finland, DIGITAL FLUID POWER – STATE OF THE ART, Matti Linjama, **pp. 331-334**.

[5] **http://www.artemisip.com/technology/,** accessed on 16.10.2020

[6] Petrin DRUMEA, Radu RĂDOI, Bogdan TUDOR, Ilare BORDEAȘU, Proceedings of 2016 International Conference on Hydraulics and Pneumatics – HERVEX, November 9-11, Baile Govora, Romania, ISSN 1454 - 8003 - DIGITAL HYDRAULICS SOLUTIONS,.

[7] Cerere de brevet numărul. A/00432/2016, "Distribuitor hidraulic cu comanda electrica, comutațional de înaltă frecvență și debite mici

[8] Petrin DRUMEA, Ionel Pavel, Gabriela MATACHE, Proceedings of 2016 International Conference on Hydraulics and Pneumatics – HERVEX, November 9-11, Baile Govora, Romania, ISSN 1454 - 8003 - DIGITAL HYDRAULIC motors.

[9] Cerere de brevet nr.A/00779 – 01.11.2016, Actuator hydraulic cu arii multiple, autori Drume Petrin, Pavel Ioan, Matache Gabriela

[10] Cerere de brevet nr. A/00648 – 14.09.2017, Cilindru digital compact, autori, Bălan Ioan, Rădoi Radu, Hristea Alexandru, Pavel Ioan

[11] A.M. Hristea, B.A. Tudor, S.M. Sefu, M. Gabriela, 9th International Conference on Thermal Equipments, Renewable Energy and Rural Development (TE-RE-RD 2020), **Volume** 180, article number 04020, Mechano-hydraulic pumping solutions for reduction off energy losses in agricultural mobile machinery.

*Corresponding author: M.A. HRISTEA, hristea.ihp@fluidas.ro

CHAPTER V

Optoelectronics in Heritage Science

Physico-chemical exploration of the pioneering photography and electrotyping reproduction developed around 1840 in Vienna

V. LJUBIĆ TOBISCH, W. KAUTEK

University of Vienna, Department of Physical Chemistry,
Währinger Strasse 42, A-1090 Vienna, Austria

Abstract: A physico-chemical investigation of the world's first high-sensitivity photographic technique enabling manifold reproductions is presented based on an etched daguerreotype produced in Vienna around 1840 (Technisches Museum Wien, Austria). Surface analyses revealed that the photographic process involved the formation of colloidal Ag core-shell nanoparticles (30-120 nm). The trailblazing photographic process delivered an unrivaled high sensitivity due to the use of halide mixtures, without Hg common with Daguerre's first photography. Latent images were developed by H_2SO_3. Fixation was done by either KCN or $Na_2S_2O_3$. The first reproduction technology for daguerreotypes consisted of etching to enable printing. A gum arabic treatment enabled the HNO_3 etching of the unexposed areas.

Keywords: Daguerreotypes, heritage science, photochemistry, photography, nanoparticles.

1. Introduction

On August 19, 1839, the French Academy of Sciences presented a revolutionary invention: Louis Jacques Mandé Daguerre (1787-1851) and his lately deceased colleague Joseph Nicéphore Niépce (1765-1833) had developed a method of permanently mapping the world for the first time. This day is officially regarded as the birth of photography. In exchange for a state pension, Daguerre sold the secret of his technique to the French state. The French government made the daguerreotype accessible worldwide (Gröning, Faber 2006).

The daguerreotype was based on the light sensitivity of silver halides. The commonly used silver-coated copper plates were first carefully polished (Dingler 1841a) and then made photosensitive by exposure to iodine vapour in a wooden fumigator box. Ag halogenide was formed on the Ag surface. In the illuminated areas during the subsequent exposure in the camera, the halogenide reduced the silver ions. However, an image only appeared during a development step using Hg vapours. The Hg combined with the metallic silver in the exposed areas, while the areas in shadow remain untouched (Stohman, Kerl 1900). In a final step, the image was fixed in a hot, saturated salt solution so that the unexposed remaining silver halide was removed from the surface.

Thanks to the personal interests of the Austrian chancellor Clemens von Metternich, two daguerreotypes of Daguerre arrived in Vienna before the aforementioned August 19, 1839, and a rapid further development of the procedure and the optical equipment took place in Vienna (Faber

2000). Metternich immediately ordered a study trip of the mathematician and physicist Andreas von Ettingshausen to Paris, where he was instructed directly by Daguerre. Ettingshausen immediately recognised the deficiencies of the optical components on Daguerre's camera. He had a new lens calculated by his colleague Joseph Maximilian Petzval at the University of Vienna. The Petzval lens constructed in 1840 was the first calculated portrait lens in the history of photography. It exhibited 16 times the light intensity of the lens used in the first daguerreotype cameras (Fellner, Holzer, Limbeck-Lilienau 2003). Thus, the Petzval lens allowed exposure times of less than one minute for the first time paving the way to photographic portraits. The Viennese Voigtländer family of opticians manufactured it. They developed their own metal camera for daguerreotypes and sold it equipped with the Petzval lens worldwide (Dingler 1841b).

2. Results and Discussion

2.1. The "new Viennese method"

In 1840/41, the Viennese photo pioneers Franz Kratochwila and the brothers Josef and Johann Natterer developed new sensitisation methods and increased the sensitivity of the silver surface. With such sensitive plates and with Voigtländer's Camera Obscura portraits and other pictures were made within few seconds or less (Dingler 1841b). In order to improve the poor light sensitivity of the plates iodised according to Daguerre, they developed sensitisation methods using mixtures of bromine, chlorine and iodine, which were used in different sequences and compositions (Table 1).

This procedure became known as the "new Viennese method" (Dingler 1841a; Gröning, Faber 2006). Despite the immense improvement of the sensitization method and the resulting reduction of the exposure time, as well as the possibility to photograph moving scenes for the first time, the new Viennese methods did not penetrate to Paris. They were certainly practised by other Viennese photographers (Gröning, Faber 2006), but remained unmentioned in international literature for a long time (Eder 1932).

Table 1. Photographic procedure reconstruction
(Ljubic Tobisch, Kautek 2019)

Process	**Reaction**
Ag coating of the Cu plate	$2\ [AgCl_2]^- + Cu \rightarrow Cu_2^+ + 4\ Cl^- + 2\ Ag$
Sensitization	$2\ Ag + X_2 \rightarrow 2\ AgX$
Exposure	$8\ AgX + 4\ hn \rightarrow 2\ Ag_4 + 4\ X_2$
Development	$2\ AgX + H_2SO_3 + H_2O \rightarrow$ $2\ Ag + 2\ HX + H_2SO_4$
Fixation	$2\ Na_2S_2O_3 + AgX \rightarrow Na_3[Ag(S_2O_3)_2] + NaX$ $4\ KCN + 2\ AgX \rightarrow 2\ K[Ag(CN)_2] + 2\ KX$
Etching	$3\ Ag + NO_3^- + 6\ H^+ \rightarrow 3\ Ag^+ + 3\ H_2O + NO$

In 1841 a new ground-breaking method of the Natterer brothers was reported (Dingler 1841b). They performed the fixation of the developed image and the removal of residual halides by potassium cyanide, KCN, or by sodium thiosulfate, $Na_2S_2O_3$ (Ljubic Tobisch, Kautek 2019) and were able to complete the image directly in the Camera Obscura - without mercury.

2.2. Reproduction by etching of Daguerreotypes

The two techniques - daguerreotype and electroplating, both developed in the late 1830s - were successfully combined in Vienna. Less than half a year after the publication of the daguerreotype procedure, the Viennese anatomy professor Joseph Berres was the first to succeed in etching daguerreotypes (Wiener Zeitung 1840). He quickly recognized the potential of the daguerreotype in the field of (photo) graphic illustration, especially in the field of microscopy. The logical next step was to adapt Daguerre's unique plates for mechanical reproduction by printing (Dingler 1840). Berres applied a gum Arabic solution to the image surface, which preferably wetted the exposed silver amalgam areas so that unexposed areas could be etched with nitric acid (Ljubic Tobisch, Kautek 2019). Berres mentioned a medical student, Erwin Weidele (Berres 1841), who was already involved in daguerreotype and electroplating during his student days (Ponstingl 2011). Theyer, initially undertook photographic studies together with Anton Martin and Franz Kratochwila, but later focused on electroplating (Martin 1873). His experience may also have been the reason for the connection to the young merchant Franz Theyer, with whom Waidele successfully operated the first galvanoplastic-artistic laboratory in Vienna between 1842 and 1845 (Ljubic Tobisch, Weitensfelder, Kautek 2011; Ljubić Tobisch et al. 2020).
One of the tasks of the electroplater ("Galvanoplastiker") in the 19th century was to create a copper deposit on a metal, but once the operation was finished, it could easily be separated from the object that had served as the mould. All contours and details of the object had to be reproduced with exact accuracy. This method was very often used to produce medals or reliefs (Ljubić Tobisch et al. 2020). Also daguerreotypes with their finest details could be duplicated in this way (Ljubic Tobisch, Kautek 2019). The daguerreotype plate was first covered on its backside with an insulating varnish to prevent metal deposition. It was then held horizontally at one corner, and a very dilute KCN solution was applied on it, then washed off with fresh water, and connected at one point with a brass wire so that it could be immersed in a $CuSO_4$ solution. After 6 to 12 hours, the plate was removed from the bath, the edges were cut off with scissors and the two plates were separated with a knife or a fine spatula. In this way, two identical images were obtained, but one was of course mirror inverted. In this method, the raised parts of the mould were deepened, and the depressions were reproduced in a relief. Once a negative form is obtained in this way, it is easy to obtain a large number of copies of the original (Taucher 1893). The facts that on the back of the investigated daguerreotype plate

Fig. 1. The equestrian monument of Emperor Joseph II at the Josefsplatz in Vienna. Today's aspect (Ó Kautek).

Fig. 2. The equestrian monument of Emperor Joseph II at the Josefsplatz in Vienna (127 x 144 x 1 mm). Etched daguerreotype, Inv. No.: 83939/18, Technisches Museum Wien.

there were remnants of a dark insulating layer - presumably asphalt varnish -, and that it was preserved in the only estate of the first Austrian laboratory for electrotyping, are a rather safe indication that copies of this plate were made by electrochemical means in the time period between 1843 and 1845.

2.3. Joseph Monument on Josefsplatz in Vienna

In the course of processing the estate of Franz Theyer and his galvanoplastic-artistic laboratory in the collection of the Technisches Museum Wien, a very unique plate with the view of an equestrian statue was discovered (Figure 2). Obviously, the plate is a daguerreotype, which differs significantly from other, mainly graphic printing plates (Ljubic Tobisch, Kautek 2019). In the collection of the Albertina in Vienna, a print was found that bears remarkable similarities to the plate. The water coloured print called “Das Josephsdenkmal auf dem Wiener Josefsplatz”, is an etched daguerreotype attributed to Joseph Axmann and was produced in 1844. The format and detail of both objects were compared, and it could be confirmed that it is the same scene (Figure 1). However, it is slightly shifted, which confirmed the assumption that the print was made with a different plate. To gain more information about this plate and its production techniques, extensive material analyses were carried out.

Optical microscopy and non-contact profilometry confirmed that the plate represents an etched daguerreotype that was intended for print reproduction. The etched depressions are very flat with a maximum depth of up to 6 µm. Based on a total of 36 X-ray fluorescence (XRF) measuring points, the silver layer thickness varied in the range of 7.3 ± 1.1 µm due to the different etching stages (Ljubic Tobisch, Kautek 2019).

Three different surfaces could be detected on the plate by scanning electron microscope (SEM) (Figure 3). The etched surface (spot no. 3) corresponds to a low light irradiation in contrast to the strongly exposed areas (spot no. 1), which do not exhibit any etching features. Here, Ag nanoparticles with sizes between 30 nm and 120 nm could be detected. In the medium and dark tone range (spot no. 2), the Ag nanoparticles are completely absent. There, the surface is dominated by larger etch pits with diameters of 200-400 nm.

Energy dispersive X-ray spectroscopy (EDX) revealed high contents of silver oxides and silver sulphides besides some AgCl on the strongly exposed regions characterized by the presence of the Ag nanoparticles (Ljubic Tobisch, Kautek 2019). The increased oxygen signal in the dark tone range indicates a stronger oxide formation due to the surface increase caused by etching. The etching process has exposed some copper substrate, which is indicated by a slightly higher

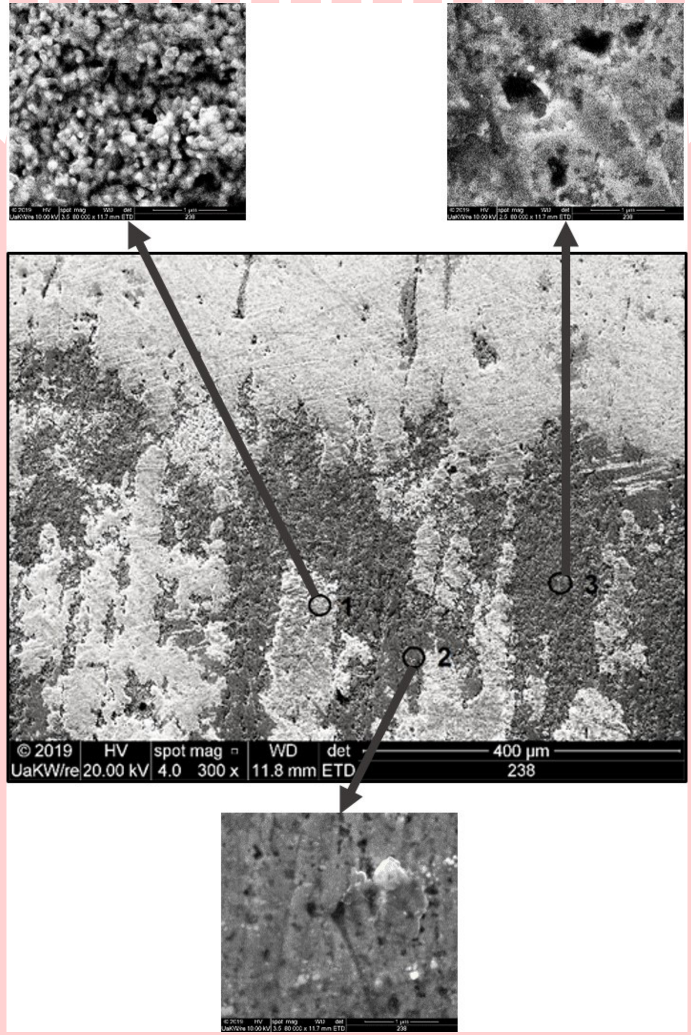

Fig. 3. Scanning electron micrographs of details of the etched daguerreotype (Fig. 2).

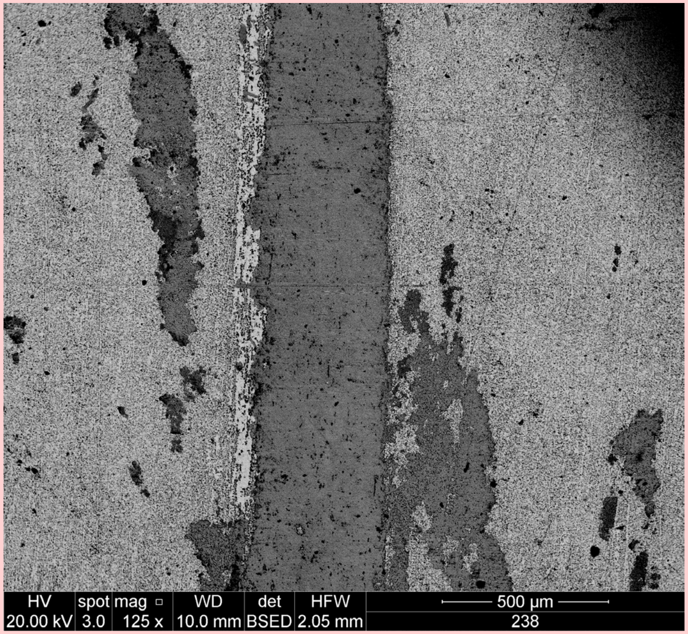

Fig. 4. Scanning electron micrographs of a line feature on the etched daguerreotype in Fig. 2.

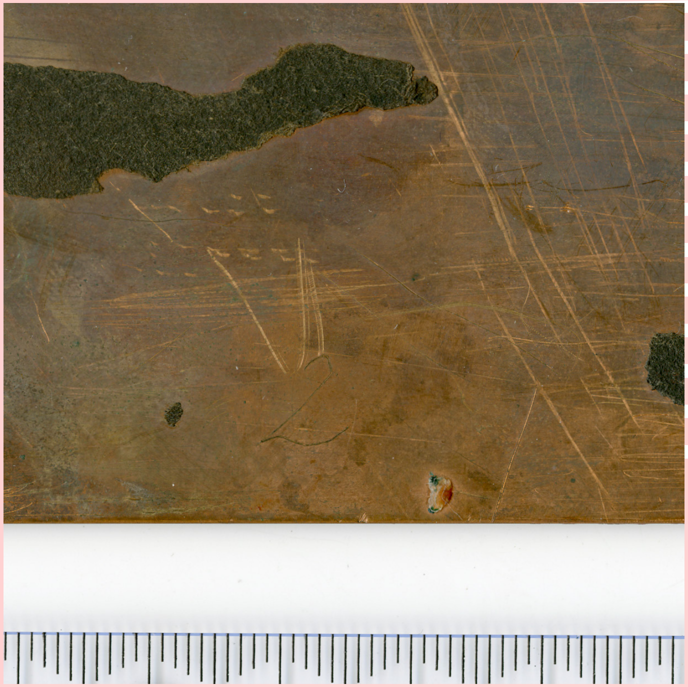

Fig. 5. Reverse side of the plate (Fig. 2) with the remains of a covering varnish.

Cu signal. Hg was not detected at any of the measuring points. Since the plate was kept unprotected over the long period of time, different corrosion processes could be detected microscopically but also with the naked eye. The front of the plate appeared yellow-brownish in the middle and bluish-grey at the blurred edges. Both sides as well as the lower edge are strongly fuzzy. Countless scratches, fingerprints and other wipe marks could be observed on the surface. However, due to the numerous grey tones and blurs, it is difficult to distinguish between physical damage and chemical changes (Figure 4). The back of the plate was protected with a covering varnish, the remains of which are still partially present (Figure 5).

3. Summary

The daguerreotype of Joseph II's equestrian monument raises complex questions that call for a combination of an approach by technical history and natural sciences. Without

intensive examination of historical contexts and technological developments, the questions to the natural sciences could not have been properly addressed. This plate with its so unique surface structures clearly shows the secrets still concealed by the photographic techniques used in Vienna in the early 1840s. It is not easy to define the contributions of individual personalities, for it was precisely in these early years that the pioneers of photography in Vienna cultivated a very lively interaction. Fritz Schuh's (photo) studio on Landstrasse in the Fürstenhof in Vienna was one of the most outstanding of its time. Schuh gathered a circle of scholars and dilettantes around him and thus founded the first photographic society in Vienna - the Fürstenhofrunde (Martin 1873). It was during this period that the most interesting disputes took place about the invention of the brothers Natterer and Kratochwilla to use chlorine and bromine as an accelerating agent in contrast to solely iodine. Also discussed were the etching of silver plates, which professor Berres carried out with the help of the engraver Axmann, as well as the effects of invisible light and galvanoplastic work by Waidele, who, among other things, dealt with the effect of halides and the physico-chemical formation of the latent image (Martin 1848). The small community "die Fürstenhofrunde" as an exchange platform for the promotion of the daguerreotype certainly laid the foundation for the upswing of photography in Austria.
Despite all the gained information, a clear attribution of authorship for the etched daguerreotype plate with the view of the Joseph monument at Vienna's Josefsplatz remains uncertain. After 180 years, the question "How do the pictures differ in their various stages of perfection, as seen from a chemical point of view" (*"Wodurch unterscheiden sich die Bilder in ihren verschiedenen Stadien der Vollkommenheit, vom chemischen Standpunkte aus aufgefasst?"*), once formulated by Anton Martin, still remains to some extent unresolved (Martin 1848). Nevertheless, a far-reaching determination of techniques and production processes, based on the presence or absence of certain characteristic elements, but also of possible process variants, has been achieved based on this single plate.

References

Berres, J., *Polytechnisches Journal* **81** (1841) 149.

Dingler J.G. (ed.), *Polytechnisches Journal* **77** (1840) 159.

Dingler J.G. (ed.), *Polytechnisches Journal* **80** (1841b) 229.

Dingler J.G. (ed.), *Polytechnisches Journal* **82** (1841a) 311.

Eder J.M., *Geschichte der Photographie*, Vol. 1, Halle an der Saale 1932.

Faber M., *Fotogeschichte,* **77** (2000) 15–24.

Fellner M., Holzer A., Limbeck-Lilienau E., *Die Schärfung des Blicks. Joseph Petzval: das Licht, die Stadt und die Fotografie*, Technisches Museum Wien 2003.

Gröning M., Faber M., *Inkunabeln einer neuen Zeit: Pioniere der Daguerreotypie in Österreich 1839-1850*, Wien 2006.

Ljubic Tobisch V., Weitensfelder H., Kautek W.,

Blätter für Technikgeschichte **74** (2011) 135.
Ljubic Tobisch V., Kautek W., *ChemplusChem* **84** (2019) 1730.
Ljubic Tobisch V., Cortea I.M., Ratoiu L., Rãdvan R., Kautek W., *Microchem. J.* **152** (2020) 104320.
Martin A., *Vollständige Anleitung zur Photographie auf Metall nebst den neuesten Fortschritten der Photographie auf Papier*, Wien 1848.
Martin, A., in *Beiträge zur Geschichte der Gewerbe und Erfindungen Oesterreichs von der Mitte des XVIII. Jahrhunderts bis zur Gegenwart*, Vol. I, Exner, W.F. (ed.), Wien 1873, p. 512-530.
Ponstingl M. (ed.), *Die Explosion der Bilderwelt*, Die photographische Gesellschaft in Wien, Wien 2011, p. 1861-1945,
Stohmann, F., Kerl, B., *Encyklopädisches Handbuch der Technischen Chemie* (1900) 93-106.
Taucher, K., *Handbuch der Galvanoplastik*, 5th Ed., Rieger´sche Verlagsbuchhandlung, Stuttgart 1893, p. 183-184.
Wiener Zeitung, April 18 (1840).

*Corresponding authors:
wolfgang.kautek@univie.ac.at; valentina.ljubic.tobisch@gmail.com

Use of 3D laser and optical scanning for monitoring of Cultural Heritage objects

V. PARFENOV
Department of Photonics and Department of laser Measurement & Navigation Systems, St.Petersburg Electrotechnical University, 197376, Russia

Abstract: A novel technique for monitoring of oil paintings is proposed. Experimental results connected with use of optical 3D scanning for monitoring of oil painting with collection of The Military-Historical Museum of Artillery, Engineer and Signal Corps (St. Petersburg, Russia). The scanning of painting was carried out 2 times with time interval of 4.5 years. In both cases computing 3D models of the same painting were created. These models were compared using software GeomagicStudio that allowed to get a precise quantified information about deformations of canvas and wooden frame of the painting.

Keywords: 3D scanning, Cultural Heritage, laser techniques, paintings, monitoring

1. Introduction

This article is devoted to a new little-known application of 3D scanning technology for the preservation of cultural heritage, namely, monitoring of works of art. The data presented in the article are the result of an initiative project implemented by the author's research group, which is one of the few research teams in Russia dealing with use of laser techniques in CH preservation.

The beginning of these works dates back to 2005 and was associated with the development of laser cleaning technology while removing contaminants from the surface of monuments from various materials. Mentioned works were conducted by author in collaboration with Italian scientists with the IFAC – CNR) [1]. The first practical work experience of the research group of the ETU "LETI" connected with the use of lasers in restoration took place in 2006, when laser cleaning of several marble monuments in the XVIII century Necropolis of the Alexander Nevsky Monastery was carried out [2]. Later (in 2007), cooperation began with the State Russian Museum for the cleaning of Italian marble sculptures of the XVIII century in the Summer Garden in St. Petersburg [3]. A total of about 30 sculptures were cleaned with a laser. In the course of these works, the high efficiency and safety (for the state of conservation of the marble surface) of laser cleaning was demonstrated, since even very persistent contaminants were removed with the help of a laser, and without damage to the stone surface. A number of interesting and memorable restoration works were carried out in the framework of c operation with the State Museum-Preserve “Tsarskoye Selo”. Together with the restorers from the company Resstroy Ltd., the specialists of the ETU cleaned several marble sculptures from the collection of this museum, in particular, the sculpture “Zephyr swinging on a branch” (author - sculptor V. P. Brodsky; work done in 1860 in Rome (Italy)).

One more direction of scientific and practical works of the ETU group is the use of 3D laser scanning technology to create electronic passports and high-precision physical copies of works of art. Some case studies are described in [4], but general overview of works is done in [5].

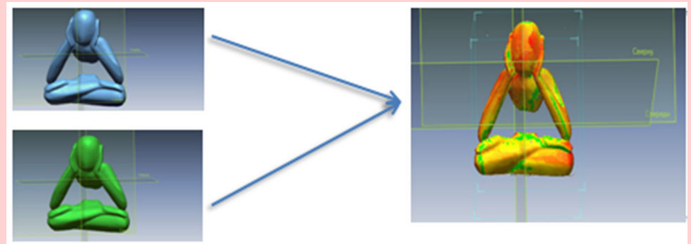

Fig. 1. Reslult of matching two 3D models of the same object created with time interval that corersonds to a control period

Since computer 3D models of CH objects give accurate information about their dimensions and geometrical shape, this allows not only to document the condition of monuments, but also to quantify the degree of damage to their surfaces (for example, to measure the area of the gypsum crusts and biological fouling, depth and width of cracks, etc.) and to track the dynamics of destructive processes by periodic repetition of the scanning the most problematic areas of surface of objects.

In order to detect changes in the state of preservation of the historical monument over a control period of time (for example, 1 year, 2 years, etc.), it is necessary to combine the original 3D model and the newly obtained 3D model in a special computer program. As a result, one can not only visualize the differences that have appeared, but also measure the size of defects (for example, the length and width of cracks, scratches, etc.). As an illustration, Fig.1 shows the result of matching two 3D models of the same object (a small wooden sculpture).

The changes in the shape (topography) of the surface that occurred during the control time interval are shown in different colors in this drawing (red shows the area with the maximum deviation). However, this method of monitoring provides not only visualization of changes, but also allows you to quantify them (the size of defects can be measured with an accuracy of tens of micrometers).

This is the basic principle of monitoring exterior monuments. It should be noted that, despite the potential attractiveness and widespread use of laser technologies in General in the preservation of cultural and historical heritage, 3D scanning has not yet been widely used for monitoring monuments. Only a few case studies connected with its practical implementation are known from the scientific literature [6], [7], and one of works has been carried out by the ETU “LETI” group. Fig. 2 reprsents results of monitoring of marble

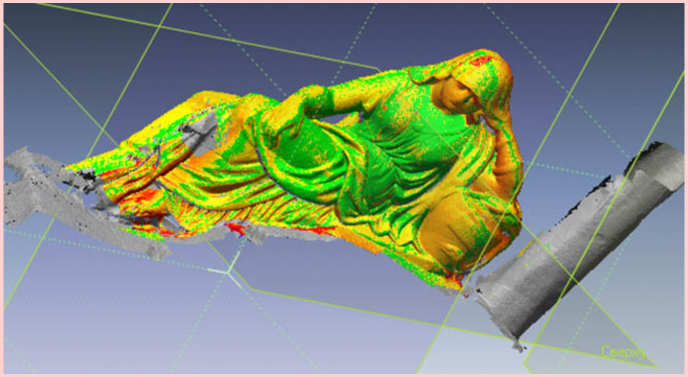

Fig. 2. Result of monitoring of monument to A.Ya.Okhotnikov (marble, Russia, XIX century).

Fig. 3. Painting "Equestrian artillery company No. 13 barrages French columns during the retreat of the "great army".

monument to A.Ya.Okhotnikov (XIX century, Alexander Nevsky monastery, St.Petersburg). Details of this project are described in [8]. Therefore, information about the possibility of using 3D scanning for monitoring paintings, which are absolutely different class of artworks, may be particularly interesting to the reader, since it is a completely new area of application of this technology. The scientific literature describes individual cases of using scanning to monitor wall paintings. In particular, earlier author of this article showed the principal possibility of using 3D scanning to monitor the state of wall paintings to control the "swelling" and the width of the cracks of the plaster layer [9]. However, there is no information on the use of 3D scanning for monitoring oil and tempera paintings in the scientific literature. This suggests a scientific novelty of research conducted in this work describing one of first case studies in the field.

2. Experimental results

Generally speaking, the need for monitoring of paintings is associated with the fact that defects in the paint layer usually occur at the "micro level", and it is very difficult to detect them in a timely manner using photography (including even high resolution one) which is traditionally used in museums to monitor the state of paintings.
Scientific group of the ETU "LETI" carried out in 2014 first experiments on monitoring the painting "Equestrian artillery company No. 13 barrages French columns during the retreat

of the “great army” from Russia” (created by Russian artist P. Karyagin in 1912) with the collection of the Military-Historical Museum of Artillery, Engineer and Signal Corps in St. Peterburg. Its general view is shown in Fig 3.
The choice of this painting as an object of study was connected with that fact its surface has a complex relief. The artist created this painting is characterized by the “volumetric” style of painting technique, which is manifested in the application of the paint layer by separate textured strokes of different thickness and width. It allows one to easily capture the 3D relief of the painting’s surface and track the changes of the paint layer’s state as the relief changes during the reference time interval.
In the experiments, the surface of the painting within a small (of about of 149.3 cm cm2; see Fig. 4) control area was scanned using optical 3D scanner Cronos 3D (manufacturer – Open Technologies Ltd., Italy) in 2014.
The surface geometry capture mode with texture (the surface geometry capture mode with texture was chosen) was used. This scanning mode was used to simplify the process of assembling the scans of the painting into a single computing 3D model at the stage of processing the data obtained in the scanning process. Though the surface of the painting has an individual relief (topography), but its geometry is complicated for aligning the scans in the process of creation of 3D model (the image 3D model of control zone in the computer screen is shown in Fig 5). However, combining the same texture maps may sufficiently simplify the process of assembling 3D model and

Fig. 4. Process of 3D scanning of the painting (white rectangle represents the control area).

increase the accuracy of aligning the scans.
In 2019, we re-scanned the same section of the painting. In the course of this work optical scanner RangeVision Pro5M (manufacturer – RangeVision, Russia) was used.
To verify the possible changes in the geometry of the painting over the past 4.5 years, a specialized computing software Geomagic Studio 2012 was used to proceed the data obtained in the process of 3D scanning. With the help of this program, a comparison of 3D models of the picture obtained in 2014 and 2019 was made. This comparison was made by combining the obtained 3D models, which allowed to visually and quantitatively estimate the deviation of the surfaces of the paint layer

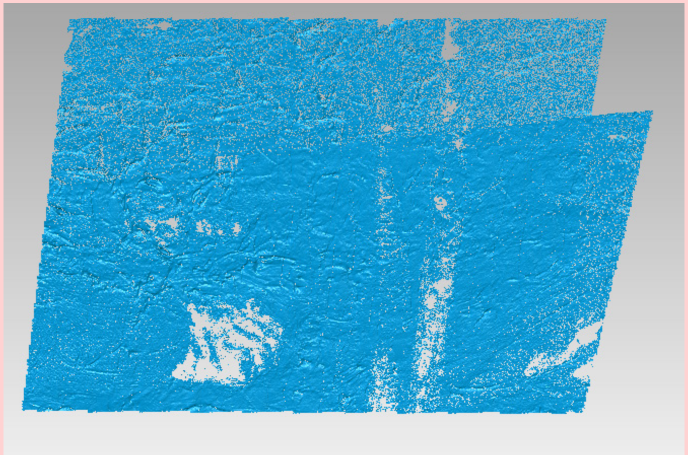

Fig. 5. *3D model of the control zone.*

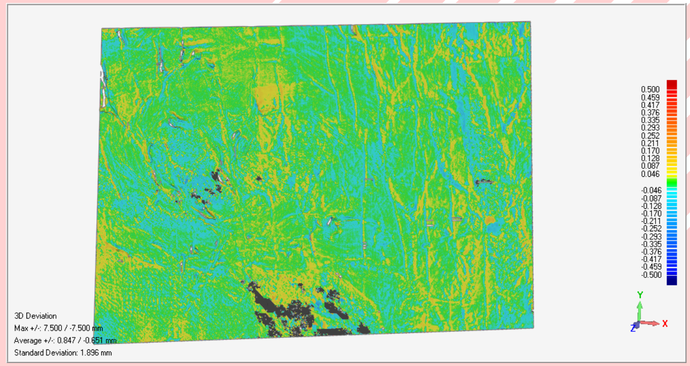

Fig. 6. Result of matching 3D models created in 2014 and 2019.

of the picture fixed in one and the other model. The program allows you to create a color scheme, which displays the value of different colors deviation 2 compared surfaces relative to each other. In this case, one of the surfaces is selected as a reference. In this case, the areas of the said color scheme, represented by shades of blue, are below the reference surface, and areas of red – above the reference surface (see Fig. 6).

To obtain the most correct data, firstly the surface of the paint layer from the 3D model of 2014 and then 3D model of 2019 was chosen as the reference surface. In both cases, similar results were obtained.

As a result of the experimental studies it was shown that the control section of the canvas has 7 zones of yellow and blue colour shades (each of them is an area of about 13.5 cm2, one of them is shown in Fig 3 by red color), which indicates the presence of deviations of the order of 200 micrometres in greater or lesser sides (i. e., there are "swollen" and concave areas. Since these irregularities are distributed throughout the study surface, it can be concluded that the nature of the deformations of the canvas is wavy.

A similar approach was used to monitor the wooden frame of the painting. As a control zone, the lower right corner of the picture was chosen, where there is a crack at the junction of the vertical and horizontal sections of the frame. During the control period of 4.5 years, the gap has increased significantly – when matching 3D models in the Geomagic program along the entire length of the slit, a blue area with a width of about 0.4 mm is clearly visible (see Fig 7). As for the frame itself, it should be

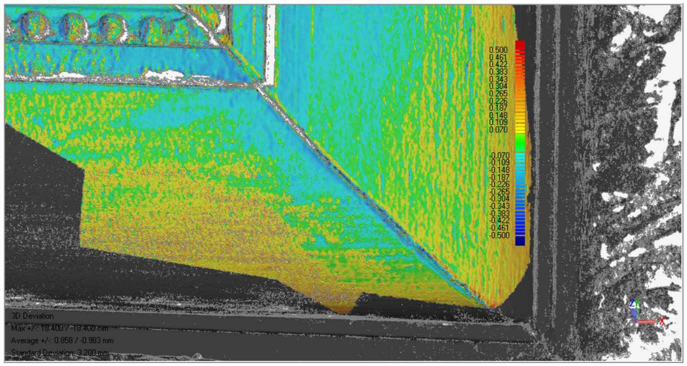

Fig. 7. Result of monitoring the wooden frame.

pointed out that there is a "redness" of the surface of the polygonal grid closer to the edge of the frame as well as presence of a blue area near the joint of the frame and the canvas. Such a distribution of color may be evidence that the edge of the frame began to bend inward – toward the painted layer.

3. Conclusions

Thus, as a result of the experiments, the principal possibility of using 3D scanning for monitoring oil paintings was demonstrated. It was shown that this method allows one to control the state of the surface of the painted layer as well as the wooden frame with high accuracy (fractions of a millimeter). Such information can be useful for the conservators of paintings to decide on the need to change the conditions of storage and exposure of paintings.

Acknowledgements

Author would like o kindly acknowledge the contribution of V.O.Tishkin, A.A.Zhuravlev, I. A. Leonova and who take part in experiments on monitoring of artworks.

References

[1] S Siano, R Salimbeni, A Mencaglia, P Tiano, M Giamello and V Parfenov, ‘Phenomenological characterisation of stone cleaning by different laser pulse duration and wavelength’, Proceedings of the 6th International Congress on Lasers in the Conservation of Artworks (LACONA VI), Vienna, Austria, (2005).
[2] V Rytikova et al, ‘The use of laser technology in the restoration of monuments of the Necropolis of the State Museum of Urban Sculpture’, Relikvia (Restoration. Preservation. Museums), 9, (2006). {in Russian}
[3] O I Ivanov, A V Kazanova, P A Lazarev and V A Parfenov, ‘On the use of laser cleaning technology in the restoration of the sculpture of the Summer Garden in Saint Petersburg: preservation, research, conservation, restoration and examination of museum monuments’, VI International Scientific and Practical Conference, Part 1, National Research and Restoration Center of Ukraine, Kiev, Ukraine (2008) {in Russian}

[4] V.A.Parfenov. Use of 3D laser scanning for digital reconstruction and physical replication of sculptural monuments. SPIE. 11058, (2019).
[5]V.A.Parfenov. Use of laser technologies for restoration, documentation and replication of sculptural monuments in St.Petersburg // Insight - Non-Destructive Testing and Condition Monitoring, 62, 3, (2020).
[6] J.Kottke. An investigation of quantifying and monitoring stone surface deterioration using three dimensional laser scanning: Thesis of Master of Science. Pennsylvania University, (2009).
[7] F.Boochs F., U. Huxhagen U., K.Kraus. Potential of high-precision measuring techniques for the monitoring of surfaces from heritage objects (International Workshop SMW08. (2018).
[8]O.V.Frank-Kamenetskaya, D.Yu.Vlasov, V.V.Manurtdinova, M.Zelenskaya V.A.Parfenov, A.Vlasov, V.G.Grishkin, Monitoring of the State of Stone and Bronze Monuments: Conservation and Management Series (Chapter 6), in "The effect of the environment on Saint Petersburg Cultural Heritage. Results of monitoring of the historical Necropolis monuments", Springer International Publishing (2019).
[9] K.I. Maslov, V.A.Parfenov, F.V.Guzanov. Wall paintings monitoring by laser 3D-scanning Preliminary results. Studies in cultural heritage conservation. Moscow. (2012) {in Russian}

*Corresponding author: Vadim Parfenov
e-mail addresses:
vaparfenov@etu.ru

Overview on the advanced laser techniques for conservation and restoration of The Romanian Traditional Built Heritage

M. DINU, L. GHERVASE, A.I. CHELMUȘ
Center of Restoration by Optoelectronical Techniques CERTO, National Institute of R&D for Optoelectronics INOE 2000

Abstract: The curent article is focused on assessing some of the most important laser techniques applications for restoration, analysis and diagnosis of built heritage, centered on Romanian traditional buildings that are hosted in Open Air Museums. Laser cleaning advantages, particularities and mechanisms were discussed, and Laser Induced Breakdown Spectroscopy (LIBS), Laser Induced Fluorescence (LIF) and Laser Doppler Vibrometry (LDV) were described and exemplified. The laser techniques provide real time, in situ results, that require no sampling or sample preparation – which makes their applications on Cultural Heritage extremely useful, especially whereas the traditional built heritage is concerned.

Keywords: laser cleaning, LIBS, LIF, LDV, cultural heritage.

1. Introduction

One of the most critical issues of our contemporary society is the preservation of the cultural values of the national and universal heritage. In this sense, the laser techniques upraise, their main attraction being a wide range of applicability, in the most diverse fields of science and technology, but also the accuracy of the information obtained.

The conservation and restoration of cultural heritage, regardless of their nature, aims to stop the degradation processes that physically, chemically and/or aesthetically affect the surface and - as much as possible - to restore their original appearance, using materials and techniques that do not harm the originality of the object. In the restoration activity, the "cleaning" process involves the removal of unwanted materials from the surface of the objects. In the restoration process, there are some basic rules that are generally valid, regardless of the material from which the object is made:

- the original parts are fully preserved, even if they are damaged;
- the newly added parts for completing the object must be made of materials compatible with the original ones;
- the materials used in the restoration must be reversible, so as to allow the return to the original form or a new restoration;
- no fillings are made when more than 50% is missing from the object;
- the restoration attempts to bring the object to a state that

expresses its functionality.
After half a century of research in the field of lasers, more than 10,000 types of electronic transitions that generate laser effect are known. A significant number of these have been and are used in practical applications that have led to the emergence of a variety of laser equipment available on the market.
The applications of lasers in the conservation of Cultural Heritage have developed as a result of an extensive research process, which has gone from surface cleaning to methods of investigation and diagnosis. The most advanced laser applications in the field are the following:
- laser cleaning;
- laser spectroscopy techniques (LIBS and LIF) - analysis of the elemental composition;
- laser Doppler vibrometry (LDV) – for identification of hidden defects;
- 3D laser scanning - for high-accuracy digital reconstruction of objects and monuments.

2. Laser cleaning

Laser cleaning is a technique developed in addition to the traditional techniques used by restorers and has been studied for over thirty years, since laser radiation sources became available to a larger number of researchers. Laser cleaning avoids the problems that often occur when using mechanical or chemical cleaning techniques.
This method, through the high degree of control over laser radiation, avoids mechanical damage and eliminates the disadvantage of cleaning with fluids - whether chemicals or water jet - which may cause long-term degradation of the substrate of the material on which the cleaning is performed. Moreover, laser cleaning has the potential to accelerate the conservation work, giving it a better quality through a high degree of control, based on the highly selective interaction of laser radiation with the materials due to its unique properties:[1]
a. <u>Coherence</u> - is the property of a field of waves to be able to cause in a certain region of the space interference bands. We can talk about:
- *spatial coherence* - two rays coming from two different points of a light source, if they can interfere (by overlapping them we obtain fringes of interference), the two radiations are coherent.
- *temporal coherence* - the radiation emitted at a given moment by a certain point of the source can interfere with the radiation emitted at a later moment by the same point of the source, the two radiations are coherent in time. It actually means that the emitted radiation has a single wavelength (or a single frequency).
b. <u>Monochromaticity</u> - is determined by the stimulated emission process, by the mode of oscillation of the resonance in which the amplification phenomenon takes place, as well as by the width of the radiation line compared to the much larger width of the atomic transition. Monochromaticity actually means that the laser emits a single color radiation.
c. <u>Directionality</u> is the property of propagating over long distances with a very low divergency and, consequently, the

ability to focus on a very small area.

d. Radiant intensity is a consequence of spatial coherence. All the energy emitted by a discharge tube is concentrated in a small beam with a very small solid angle. The light intensity of the laser beam must be understood in relation to the narrow spectral range in which the emission is made, the fact that the radiation takes place in an extremely low divergence interval and that in some cases it can also be emitted in pulses. Because atoms are stimulated to emit at a very high speed relative to the rate of spontaneous emission, the probability of stimulated emission is 3-4 orders of magnitude greater than that of spontaneous emission, and the line intensity on the spectral range of laser radiation increases by six to at eight orders of magnitude.

Compared to traditional cleaning processes, laser cleaning introduces the following advantages:

- is a physical process that ceases shortly after the laser irradiation has ended,
- it is a selective process making possible to intentionally remove just certain layers,
- is a non-contact method, having no undesirable effects resulting from direct contact with the substrate,
- it is a process follows closely the profile and the morphology of the surface,
- it is a versatile and controllable process - specific materials can be removed by correctly selecting the operating conditions,
- it is an ecological process - no chemicals are used.

The literature classifies and explains several distinct mechanisms underlying the laser cleaning process. In this context, “laser cleaning” is a generic name that requires a complete definition and specification of the combination of object (substrate) and deposition (adherent layer).[2]

The number of photons absorbed usually depends on the parameters of the source (intensity, angle of incidence) and the characteristics of the irradiated surface. The latter are related to a spectroscopic measure called absorbance which also depends on the material type, its roughness, the degree of adherent deposits, etc. It should be noted that the absorbance of the vast majority of materials is well known and can be used to study the interaction between the laser beam and matter.

The mechanisms of interaction between the laser radiation and matter depend on the parameters of the laser beam, as well as on the physical and chemical properties of the material. Laser parameters are wavelength, intensity, spatial and temporal coherence, polarization, angle of incidence and pulse duration. The material is characterized by the chemical composition and microstructure (the arrangement of atoms and molecules in the solid), which determines the type of the excitation and the interaction.

Cleaning is a particular case of ablation, and the mechanisms of laser cleaning are briefly described below. Following studies involving laser cleaning of stone and various types of marble, *Asmus, 1986* concluded that there are two main mechanisms involved: *ablation* and *spallation*.

Selective vaporization of surface deposition layers depends on the difference between the absorption factors of the

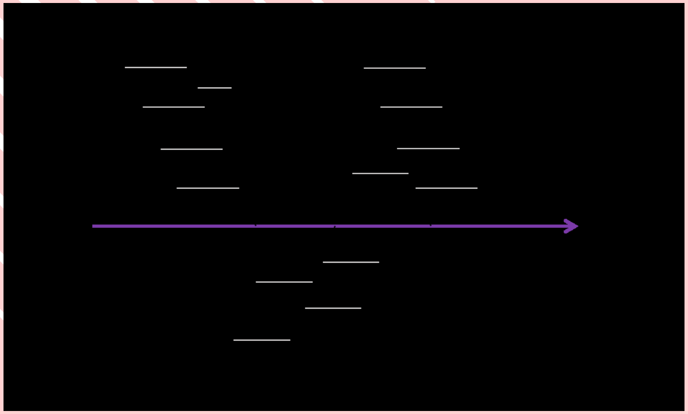

Figure 1: Ishikawa diagram for laser cleaning influences

substrate and the deposition layer, respectively:

$$T_{(0,t)} = \frac{2\beta I_0}{k}\sqrt{\frac{\alpha t}{\pi}} \qquad (1)$$

$T_{(0,t)}$ = surface temperature after time t, k = thermal conductivity coefficient, α = thermal diffusivity coefficient β = absorption coefficient.
It is observed that if all the other variables are kept constant, for different values of the absorption coefficient, β for the substrate and the pollutant layer, it results in significant temperature differences between the two layers.[3, 4]
Hence, the laser irradiation can vaporize the unwanted layer, while keeping intact the original substrate of the object. In practice, the mechanism of selective vaporization is quite limited, mainly being selected in cases that require the removal of adherent deposits of dark colors (usually black) from light color objects, such as stone or marble. It has been observed that the cleaning speed (ablation rate) improves by almost an order of magnitude when using a pulsed laser with a pulse duration of about 5-20 ns.[5]
In the Q-switched mode (pulse duration of about 5-20 ns), it is assumed that the mechanism responsible for cleaning is *spallation* (after Asmus, an *ablation*). At this high level of radiation intensity (~10^7-10^{10} W/cm^2), even surfaces with a relative reflectivity absorb enough energy to reach the vaporization temperature. High temperatures of the order of 10^4-10^5 K are reached in the vaporized material, which becomes partially ionized and absorbs laser energy even more strongly. Thus, the evaporation from the surface of the material stops, becoming “shaded” by the partially ionized vapors (plasma), so the radiation does not reach the substrate. As the pulse continues to be applied, the plasma heats up even more, and the pressure in it reaches very high values (~ 1–100 Kbar), resulting in a shock wave that produces a microscopic compression on the surface of the substrate. After the laser radiation is stopped, the plasma expands from the surface and the material relaxes. This results in the removal of a thin layer of the order of ~ 1-100 µm: spallation.
In addition to the mechanisms proposed by *Asmus*, there are other phenomena that are involved in the laser/material interaction and which result in surface cleaning.
Transient surface heating: when the laser radiation is

applied quickly and absorbed by the surface, instead of the normal heating and contraction processes that usually occur as a result of thermal expansion, the layer of heated material will exert pressure on the adjacent material, and a compressor shock wave will pass through the material.[6] If the magnitude of these stress waves exceeds the stress resistance of the material, there will be a rupture which in terms of laser cleaning can be interpreted as the removal of a surface adherent layer, the total degradation of the substrate being negligible. *White* modeled the effects of transient surface heating produced by repetitive laser pulses. He considered that temperature gradients (normal and parallel to the surface) are formed, resulting in the thermal expansion that produces stress waves in the material, which propagate from the heated surface. The amplitude of the waves produced, for a given absorbed power density, depends on the elastic constraints to which the heated surface is subjected. If the surface is free, the amplitude of the stress waves will be relatively small, but if for example the surface is in contact with another object, the induced stress and the amplitude of the waves can be very large.[7]
Another mechanism that can produce high pressure pulses on the irradiated surface is the *evaporation pressure*. A laser-induced shock wave is generated as a result of the expansion of vapors from the irradiated surface into the ambient gas.[8]. The general idea is that there will be a region of compressed air between the material that evaporates from the object and the ambient air (uncompressed), the shock wave being generated at the compressed air/ambient air interface. This mechanism does not require the absorption of laser energy into a plasma, but simply occurs as a result of the strong impulse given by the evaporation of the material.
Photonic pressure - a small pressure will act on the surface as a result of the impulse of the incident photons. Although the mass of photons is small, focused lasers are able to produce a large flux of photons[9]. This mechanism is mainly considered when removing submicron particles from electrical components, as it is unlikely that sufficient force will be applied to make a difference in laser cleaning.
Photochemical ablation, or “cold” ablation, is a very attractive mechanism for the field of conservation of Cultural Heritage due to the fact that in this case the side effect of surface heating is non-existent (or at extremely low values). In essence, the energy E of a photon depends on the wavelength,

$$E = h\nu = \frac{h}{\lambda} \tag{2}$$

h = Planck’s constant, and *λ* = wavelength.
Consequently, UV lasers are able to have enough energy to directly break C-H bonds in organic materials. Since the integrity of organic materials (including polymers) depends on the presence of carbon-hydrogen bonds, the breaking of these bonds has the effect of breaking the chains resulting in the production of smaller ones that can be easily removed by an air current or a slight mechanical force applied to surface.
Shockwave cleaning involves a plasma shockwave produced

by the penetration of air due to an intense laser pulse. The laser beam is directed parallel to the surface, to avoid direct interaction with the layer of adherent deposits to be removed, carefully focused a few mm above the target area.[10] When the laser beam is applied, the constituents of the ambient gas begin to be ionized and as a result a shock wave is produced which is accompanied by a sound like a crack.[11]

3. Laser spectroscopy techniques

Laser Induced Breakdown Spectroscopy (LIBS) is based on the analysis of the emission of atomic lines produced by focusing laser radiation on the surface of the material, where the very high intensity laser beam begins ionization in the avalanche, thus taking place the phenomenon called *breakdown*. The spectral analysis of the emitted radiation gives us clear and concise information for the identification of the elements, in atomic or ionic state.[12]

The LIBS technique is an extremely efficient spectroscopic technique for the analysis of the chemical structure of materials and provides the following advantages:

- *in situ* measurements (no sampling required)*;*
- rapid results;
- analyses all the chemical elements at once;
- stratigraphy analyses, if necessary;
- no sample/surface preparation is necessary;
- good results on a wide range of materials;
- micro-distructive technique.

If the intensity of the laser radiation is high enough, its interaction with matter produces the ablation of the material, and on the surface plasma is formed, which consists of molecules, atoms, ions and electrons. Plasma phenomena are responsible for: plasma radiation reflection, electronic emission, object heating and phase changes, all of which affect the physical properties of the plasma cloud.

If the intensity reaches a critical value, the number of energetic electrons that can ionize atoms/molecules increases, resulting in an avalanche ionization of the plasma cloud - *breakdown*. Once the plasma has formed, it reaches - within spatio-temporal limits of observation - the Local Thermal Equilibrium. In this case, the effect of re-absorption can be neglected (optically, the plasma is very thin), and the intensity of the spectral lines corresponding to the transition of energy levels E_k and E_i for a specific material can be described by the following relation:

$$I_\alpha = C_\alpha \cdot \frac{g_k \cdot A_k}{U_\alpha \cdot (T)} \cdot \exp(-\frac{E_k}{k_B \cdot T}) \qquad (3)$$

T is the plasma temperature, $U_\alpha(T)$ is the partition function, k_B Boltzmann's constant, A_{ki} is the transition probability between i and k levels, g_k is the degrre of degeneration of the k level, and C_α is the concentration of the chemical element in the plasma.

The major parameters drawn in the time-resolved detection are the gate delay or delay time and the gate width. τd is the time since the laser pulse is triggered until the start of recording, and τw is the time period over which the spectrum is recorded.

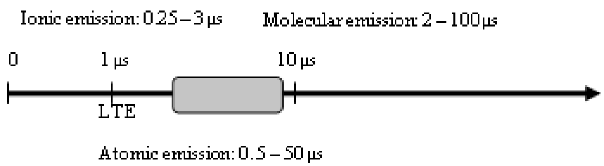

Figure 2. Plasma time-line

The LIBS dp method implements a second laser in the classical LIBS system, synchronizing its irradiation with the first using a pulse generator. The intensity of the spectral lines increases up to 20-30 times. This is essential for the analysis of heritage objects, in which case the microdestructivitness of the method is very important. Also, it has been shown that the matrix effect in the case of double pulse becomes very low, so this method is very suitable for quantitative analysis.
The configurations used for the double pulse are:
- *collinear*, where two laser pulses irradiate the same point of the material at two different times;
- *orthogonal*, where with a laser pulse the surface of the object is irradiated, and with the other the medium is ionized (pre-ablation) or the plasma is heated, depending on whether the pulse parallel to the object of analysis comes before or after the laser pulse perpendicular to the object.
The analyzed objects are irradiated with the laser beam focused on their surface at a regime that induces the plasma cloud formation, thus emitting the spectrum with the atomic and ionic lines characteristic of each chemical element. To intensify the plasma spectral lines, laser beam pre-ablation is performed that passes close to the surface of the analyzed object, a few microseconds before its irradiation, or the plasma is heated by irradiating it a few microseconds after its formation. Plasma heating can be achieved in either of the two configurations. The plasma information is collected and directed into the spectrometer. The scattered radiation from the monochromator is distributed on the *xy* plane of the ICCD. This 2D dispersion is obtained using an Echelle network in combination with two prisms. The identification of the chemical elements is done by attribution of the atomic/ionic lines to the NIST database. For a better analysis of the spectral lines, it is important that the acquired spectrum contains only the pure atomic / ionic lines - without the continuous spectrum from the *Bremsstrahlung* radiation or from the vibrational or rotational spectra. That is why the irradiation and detection process must be timely synchronized.[13].
<u>Laser Induced Fluorescence (LIF)</u> is a process consisting of at least two steps. First an electron is excited by the absorption of a photon. The electron must then shed this additional energy and to the fundamental energy level, emitting a photon of $h\nu_{fluor}$ energy.
Each material has its own characteristic spectrum of absorption and electromagnetic emission. By selective excitation using specific wavelengths, it is possible to identify a variety of materials. Using a laser as an excitatory light source, it is possible to choose a controlled excitation wavelength; thus, even small traces of chemical substances or

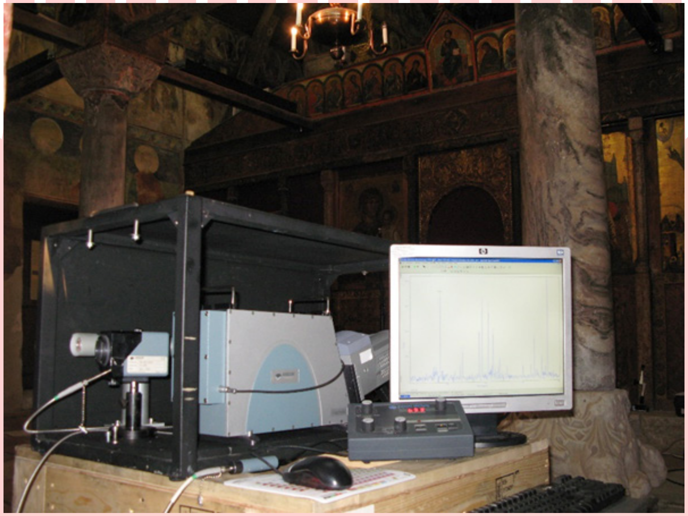

Figure 3: LIBS in situ analyses using an INOE developed portable setup with Echelle type spectrometer

Figure 4: LIBS in situ analyses at Golesti Museum

compounds can be detected.
LIF emissions from painted materials provide information that can be directly related to the molecular structure of pigments or other materials used in painting, both organic and inorganic, such as adhesives, pigments or enamel. Biological layers can also have characteristic LIF emission.[14]
The possibility of using the laser at different wavelengths for excitation increases the versatility and selectivity of this technique.
A distribution map can be generated by selecting the appropriate wavelength bands, which are specific for the detected fluorophores. This, the surface distribution of the selected species can be easily visualized.
This analysis technique is recommended in the study of Cultural Heritage due to the following advantages:
- it is a non-contact and non-destructive technique (it is not necessary to take samples or transport the object for analysis exclusively in the laboratory; this technique does not affect the quality of the interrogated surface, without damaging in any way nor changing the structure of the irradiated material);
- the response time and the efficiency of this technique - not being necessary the process of collecting samples or waiting for the results from a specialized laboratory - providing real-time data resulting from the experiment.
Applied within the Cultural Heritage, LIF is useful in

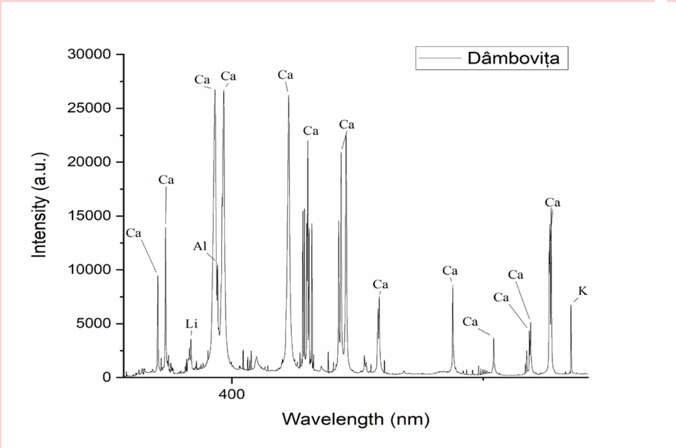

Figure 5: LIBS analysis at Dambovita traditional buiding from Golesti Musem, Arges

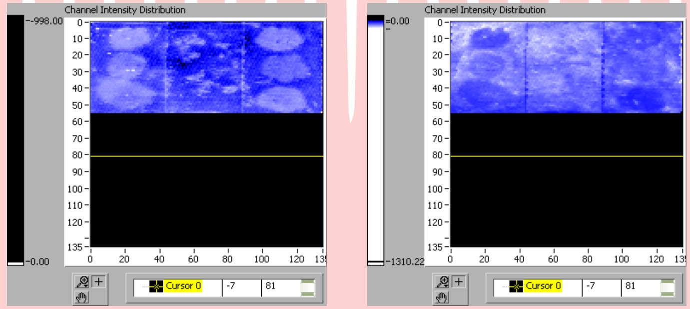

Figure 6: Figure 7: LIF Scanning intensity distribution for 675-685 nm (left) and 395-405 nm (right)

identifying the original component materials, products of the deterioration processes, or added in the restoration activities throughout the life of the object. Excitation of the sample surface with a pulsed laser beam produces the emission of fluorescence, or more generally luminescence, which, for example, may be characteristic of a pigment, and provides information on the aging of an adhesive or enamel, identifies the presence of a protective layer or biological growth on the investigated surface etc.

Due to the versatility of the technique, LIF can also be applied *in situ* as a controlled detection system, using light detection and telemetry (LIDAR).

An optoelectronic device has been developed for the qualitative analysis of the surfaces by scanning with the LIF technique, which allows the point-by-point analysis of the entire surface. This is possible using an automated coaxial system that allows the synchronization of positioning and detection processes.[15]

4. Laser Doppler Vibrometry. Case study: Golesti Museum, Arges

Laser Doppler Vibrometry (LDV) is a non-invasive, non-contact method used to identify hidden defects, such as detachments, gaps, cracks, fissures, etc. in art objects. The working principle is based on the emission of a continuous laser beam on the target surface and the measurement of the surface vibration

Figure 7: LIF Scanning in situ using a customized, portable setup, developed at INOE

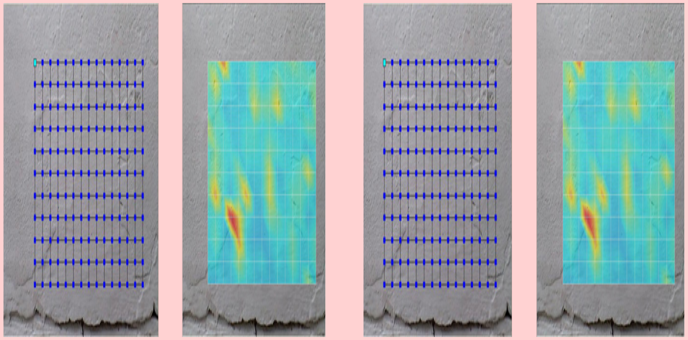

Figure 8: Scan grid and LDV result using Periodic Chirp excitation signal, at Dambovita house, Golesti Museum

by means of the Doppler displacement between the incident beam and the reflected beam. The surface is excited using piezoelectric sensors or other acoustic exciters, depending on the size of the object under investigation. The levels of induced vibrations are very low compared to those normally found in churches and museums. During data acquisition, the equipment emits sounds at well-established frequencies and amplitudes that are repeated for each selected point where the measurements are performed, thus ensuring the same conditions of excitation of the investigated surface. After all the points indicated by the user are covered, the values obtained are interpolated to obtain a colored map. The map represents the 2D plan distribution of the registered values and is perfectly plotted on the investigated area.

This method has many advantages: non-invasive (especially important when used in the field of cultural heritage, due to the international tendency to conduct investigations without affecting the heritage asset); non-contact; no sampling (there is no situation where sampling is necessary for this investigations); requires minimal surface preparation (except for objects with low refraction); usable in the case of uneven surfaces and complex geometries (due to the ability of adjusting the mirrors' focus and alignment, the equipment allows measurements to be made on uneven surfaces, such as stucco, sculptures, etc.); remote measurements (no scaffolding required, the coherent nature of laser radiation allows high-precision measurements from distances of up to 15-20 meters).

The image on the left shows the scanning grid created to perform measurements using the LDV technique on the facade of one of the houses present in the Goleşti Viticulture and Tree Growing Museum. The image on the right presents the result of the investigations based on the Periodic chirp excitation function, as a colored map. The maximum magnitude recorded reached the value of 20µm /s (areas with red), whereas areas with yellow and red are problem areas, respectively areas with detachments.

5. Conclusions

The laser techniques can be the solution to many difficult problems encountered by the restorer, mostly due to their non/micro invasiveness and *in situ* applicability. The heritage science domain is just beginning to unravel new applications of the laser techniques, using complimentary methods in order to create complex profiling methods. Taking into consideration the cases studied and the experiments carried out in recent years, both globally and nationally, several general directions for the use of lasers in cultural heritage applications have been contoured and even included in national road-maps.

There is currently a fairly varied offer on the international market with robust lasers to withstand normal operating conditions. The most popular lasers, are the Nd: YAG solid active medium pumped either by flash lamp or by means of a diode, with a pulse repetition frequency from 0.5 to 40 Hz depending on the model and user requirements.

Two important exceptions should be highlighted as having a separate evolution in recent years. The first category considers laser applications with pulse duration of the order of tens of nanoseconds to microseconds. These lasers emit a higher thermal effect than the aforementioned lasers due to the interaction between the laser beam and the stone, but are considered to have a lower effect in terms of the shock wave propagated inside the material, so a reduction in the chances that would contribute to microcracks. Another exception is the application of femtosecond lasers. These lasers are preferred because they substantially reduce the in-depth thermal effect of the interaction between laser radiation and matter. The laser techniques provide real time, in situ results, that require no sampling or sample preparation – which makes their applications on Cultural Heritage extremely useful, especially whereas the traditional built heritage is concerned.

Acknowledgements:

This work is financed by the Romanian Education and Research Ministry, Sectorial Programme, contract no. 5PS/05.09.2019

References

1. T. Tudor, *Generarea şi propagarea fasciculelor laser*, Editura Academiei Rom., Bucureşti, 2003.
2. J.F.Asmus, *More Light for Art Conservation* IEEE Circuits and Devices Magazine, March, 6-15 (1986).
3. J.F.Asmus, *Light Cleaning - Laser Technology for Surface Preparation in the Arts Technology and Conservation* 13, 14 (1978).
4. J.F.Asmus, *Light for Art Conservation,* Interdisciplinary Science Reviews 12 171 (1987).
5. K.G.Watkins, *A Review of Materials Interaction during Laser Cleaning în Art Restoration Lasers în the Conservation of Artworks,* (W Kautek , Ed) Verlag Mayer, Wien, 1997 pp 7 -16. ISBN 3-901025-68-5.
6. J.F.Ready, *Effects of High-Power Laser Radiation,* Academic Press, New York, 116, 1971.
7. R.M.White, *Generation of Elastic Waves by Transient Surface Heating,* J. Applied Physics, 34, pp. 3559 -3567, 1963.
8. C.Knight, *Theoretical Modeling of Rapid Vaporisation wih Back Pressure,* AIAA Journal, Nr.17, pp.519 – 523, 1979.
9. W.M.Steen, *Laser Material Processing,* Springer, pp. 60, London, 1998.
10. J.M.Lee, W.M.Steen, K.G.Watkins, *Laser Shock Cleaning,* Proc. 19th Intl Congress on Applications of Lasers and Electro-Optics, Dearborn,October 2-5 (ICALEO 2000) Section D, pp. 171 – 178, 2000.
11. K.G.Watkins, W.M.Steen, A*ngular Laser Cleaning for Effective Removal of particles from a Solid Surface,* Journal of Applied Physics A - Materials Science and Engineering, Vol.71, pp.1-4, 2000.
12. D.C.Smith, R.G.Meyerand Jr., *Laser Radiation Induced Gas Breakdown*; Principles of Laser Plasma, ed. G. Bekefi, JohnWiley & Sons, New York,457 -5M,1W6.
13. L.Angheluta, R.Radvan, R.Savastru, M.Simileanu, J.Striber, *Optoelectronic Device/Mounting and Process for the Stratigraphical Analysis of The Chemical Composition of Art Objects Surface Layers Material by LIBS Technique*, Brevet nr. RO125260-A2, 26.02.2010.
14. F.Colao, L.Fiorani, R.Fantoni, A.Palucii, J.Striber, *Diagnostics of stone samples by laser induced fluorescence,* Proceedings - SPIE Int. Soc. Opt. Eng. 5581, 455, ISSN-00913286, 2004.
15. L.Angheluta, R.Radvan, R.Savastru, M.Simileanu, J.Striber, *Optoelectronic Device and Process for the Qualitative Analysis of Art Objects Surfaces by LIF Techique*, Brevet nr. RO125259-A2, 26.02.2010.

*Corresponding author: M. DINU
e-mail addresses:
simileanu@inoe.ro

Good practices, limits and risks of 3D digitization in the continuous documentation of Cultural Heritage

LAURENȚIU ANGHELUȚĂ
National Institute of Research and
Development for Optoelectronics INOE 2000,
409 Atomistilor Street, Măgurele, Ilfov County, Romania]

Abstract: With the explosion of technical possibilities for the 3D digitization of Cultural Heritage elements in the recent years, there are a number of issues that, if not addressed in time, can become real risks in both the long and short term. In this paper, I will address to discussion some questions (still debated in the international community) about the place of 3D digitization in the complete documentation of a Cultural Heritage element, the recommended/ necessary quality for a 3D digitization, the longevity and specific dangers regarding the archiving and preserving digital content, as well as the copyright issues on the results of 3D digitization.

Keywords: 3D digitization, good practices, digital content, scientific documentation, Cultural Heritage

Welcome to the Digital Age

Digital technology's ability to transfer information in large quantities and in so different formats over long distances, almost instantaneously, has never been more necessary than in this period. Today, humanity feels on its skin, at individual level, the limitation of the physical presence given by the extreme conditions and recognizes the importance and value of the possibility to continue the daily activities, both personal and professional, through infinite and invisible strings of 0 and 1. In Cultural Heritage the orientation towards the digital is booming now, but by no means is it a novelty.

Like any other field of activity, Cultural Heritage had to adapt and change many of its ways. Most of the museums had to develop virtual tours and promote their collections in the online medium. During the 2020 lock-down these museums reported a record increase in virtual visitors.

This is not a new trend in Cultural Heritage. Many museums already had a strong online presence: virtual tours of painting collections, online interactive 3D models, public digital libraries etc. The Cultural Heritage community foresaw the need and the advantages of the "way of the Digital". So, before the 2020 lock-down a lot of cultural operators had already made this step. But now, almost all of the players stepped up and went digital, one way or another.

In 2005, the European Commission launched the Digital Libraries initiative, which supported the development of the

Europeana database. Since then, there have been various programs and recommendations for all the Member States on the digitization and online access to the digitized heritage items. I the light of the unfortunate 2018 National Museum of Brasil and the 2019 Notre-Dame de Paris Cathedral devastating fires, on 9th of April 2019, the European Union member states signed a Declaration of Cooperation. This agreement regards the approach of the risks that the European Cultural Heritage is facing, by working on three indicators:

- increasing the European cultural heritage visibility and use;
- improving the involvement of the local communities;
- supporting the interaction with other economic sectors.

We must not imagine that until 2005 no one thought about the importance of passing in digital format the knowledge or visual information of the elements of tangible or intangible heritage. In Romania, the CERTO department (Center of Excellence for Restoration by Optoelectronic Techniques) within INOE 2000, recognized 20 years ago the importance of digitization, researching, in the national projects implemented at that time, various new approaches such as the use of digital data bases for the storage of microclimate data (Bran Castle 2001), development of complex digital packages for the documentation (biological control, multi-spectral imaging, metadata transfer in databases) of audio magnetic tapes and wax cylinders (Ethnography and Folklore Institute of the Romanian Academy, 2003) and the transfer/transformation of the contained information in digital format. In 2003, INOE 2000 also initiated the first international collaborations for the 3D digitization of some historical monuments (the ensemble of small clay churches from Basarabi / Murfatlar, the painted tombs from Constanța etc.). After the pioneering years, today INOE 2000 has become a national and international reference pillar for the development and implementation of new methods for digitization and digitization of heritage elements, in all their complexity and variety.

The concept of '3D digitization'

Going digital involves both digitization and digitalization processes and transformations. Today, these seemingly similar terms are found unchecked in news titles, projects, studies and other activities. In many occasions you will find these terms used in the same contexts to express the same thing. The problem is they are not the same and one does not exclude the other.

Digitization refers to a process of transforming information from analog to digital format. The digitization of the cultural heritage includes historical documents, photographs in physical format (glass, metal, paper, and film), analog film, etc. Digitalization, on the other hand, refers to the transformation of the way an organization is functioning, by 'going digital'. This means basically the use of digital instruments, digital documents, digital signatures, digital databases etc. Banks, public institutions, hospitals and a famous book store (that actually started online) were the first to take this leap into the Digital Age.

Returning to 3D digitization, this of course refers to the process of transforming geometric, spatial and color information of a physical surface, real, in digital format. Not infrequently, in the literature, there will be these small loopholes in which the authors talk about 3D digitization, which is not exactly correct, even if we know that it is actually digitization. A digitalization process automatically involves digitization activities.

Role of 3D digitization in Cultural Heritage

Although for many it might be a simple question with a quite obvious answer, unfortunately there are a lot of misconceptions because 3D digitization' role is often taken lightly. A first statement that might seem surprising for some, is that with 3D digitization we do not preserve the heritage assets. More than that, 3D digitization also does not save the heritage assets.
This clarification is necessary, because we often encounter pompous slogans that use important concepts such as digital preservation of Cultural Heritage, to exaggerate (often for commercial purposes) the importance of an activity, really important, but in no way a life-saving case. Let's take a well-known case: Notre-Dame Cathedral in Paris. This monument is not only one of the most visited sites in Europe, but it is also one of the best documented. But all these documentations could not stop the terrible accident that led to the destruction of the roof of the cathedral. Yes, these meticulous documentations do indeed have a very important role in the restoration of the monument, now, and especially they have, or should have, a decisive role in establishing the policy of preventive conservation in the case of any monument. But once significantly degraded or even destroyed (acts of vandalism, natural disasters, accidents), the elements of heritage lose their identity and the value of age (or authenticity), and in extreme cases they even disappear physically. A digital or physical replica cannot replace the real experience of the historical weight that the original material of a heritage element has.
As I stated before, with 3D digitization we document. A single 3D recording will give us information about the state of conservation of the surface of an element at a certain time (the moment of registration). It is a three-dimensional instance, just as document photography is a two-dimensional instance. For a complete picture, necessary and useful for documenting and preserving a heritage element, it is mandatory to enter the temporal dimension. Repeated digitization (3D or not) at key periods of time can provide really important information about the evolution over time of the monitored surface morphology and will help us understand the degradation mechanisms, approaching prediction and intelligent preventive conservation measures. Following the same idea, without complementary information such as chemical composition, micro-climate data (humidity / temperature / pollutants), chromatic or structural and resistance conditions, 3D digitization (shape, size and color) will not be sufficient to make decisions regarding the conservation / restoration strategy of those elements. In this regard, Dr. Geert Verhoeven pointed out in an invited lecture

that 3D digitization deals only with a narrow, albeit important, aspect, namely the dimensional appearance of the surface of an object (27th edition of the International Conference by the International Committee for Architectural Photogrammetry, CIPA 2019: Documenting the past for a better future).

Methods of implementation

There are many methods for doing 3D digitization in many industries. Today, the main non-contact methods of 3D digitization of the surfaces of tangible heritage elements are: laser scanning, structured light scanning and photogrammetry. The common point of these methods is that the information is transported / collected with the help of light / electromagnetic radiation, thus respecting an important criterion of heritage documentation, namely the non-contact approach.

As we speak, the current digitization methods are constantly being improved, but new methods are also being experimented with (small depth sensors from Intel or LIDAR systems from the new Apple devices). Even if there is a long way to go before these new techniques confirm in a professional way, the direction is clear: miniaturization and automation.

Returning to the currently established methods of 3D digitization, it is difficult to draw a clear line between the three technologies to differentiate where and which of them is more appropriate. The most flexible, as well as

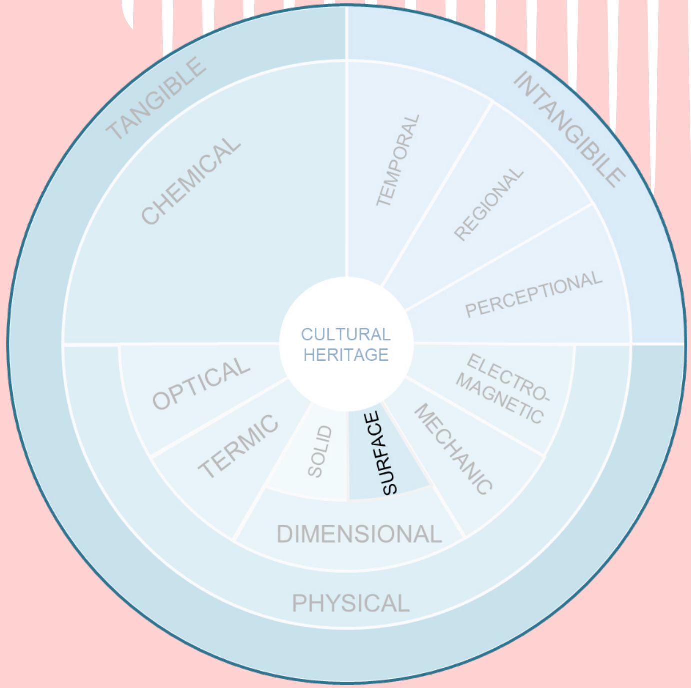

Figure 1 3D digitization's role in the documentation of Cultural Heritage assets [1]

applicability, is photogrammetry. It is also the most accessible. But it requires superior knowledge of photography and 3D processing. Laser and structured light scanning have the advantage of working speed for certain case studies for which those systems have been optimized. The major disadvantage of these two technologies, in addition to the financial aspect, is the lower rendering of real color without complementing with photogrammetry and limiting the use of devices to the case studies for which they were built. One generally accepted point of view is that the best technology is the one you have at your disposal, but it is crucial to know to know the ups and downs of each method before deciding for a specific case study.

Typical deliverables

The types of products or deliverables generated from the digitization methods, cover a wide range of tools. These can be extremely useful to historians, architects, restorers, curators and decision-makers but especially in the long-term strategies for the ongoing documentation and preventive preservation of tangible heritage, of any type or size (small artifacts to architectural ensembles or entire protected areas). These tools generally contribute to highly specialized documentation, which provides information on the technique of realization, originality or history of interventions.
We can list some of the typical raw results, such as point clouds, 3D mesh models (polygons), orthophotos, orthorectified facades, unwrapped surfaces, elevation maps etc. This raw data can be further used for analysis in CAD systems (extraction of sections, surveys, plans) or volumes, areas, elevations, surface erosion determinations or even automatic defect detection (using artificial intelligence) can be calculated.
Modern practices recommends the integration of these data in multi-technical long-term monitoring packages in specialized informatics systems, corroborated with relevant and complementary information obtained using other types of investigation and documentation methods, such as multi-spectral imaging / hyper- spectral / thermal / X-ray, spectroscopic materials analysis techniques, microscopy, ground penetration radar (in the case of monuments and archeological sites) etc. All these different information can be most easily synchronized and exploited with the help of these integrative IT tools, such as GIS (QGIS) or even BIM / HBIM (for built heritage).
A common problem, not only in Romania, but even internationally, is that the direct beneficiaries (administrators of collections, monuments, etc.) do not have enough information about the possibilities and advantages of 3D documentation. For most, these possibilities are limited to the forms of presentation, “the 3D model”. Therefore, not knowing what it can be done, they will not know what they need and will not know what to ask. For this reason, today there is an “ocean” of 3D digital models that are either incomplete, unusable or especially inaccessible.
In order to stop this phenomenon, in a digitization project, three very important good practice aspects must be taken into account:

- training of the beneficiaries (knowledge transfer),
- a clear definition of the purpose of the digitization
- and last but not least, the realization of the digitization by the professionals.

As a form of presentation, 3D digital reconstructions have always had the gift of fascination. The current technological level, still in full development, makes it possible to integrate the visitor in a virtual environment in which we can admire from our home or in specially arranged spaces in museums, the objects and places that either no longer exist or have extremely limited access, or are too fragile for exposure and handling. The virtual environment offers the possibility to observe in detail, from any angle, the museum objects without them being physically exposed to any danger. Of course, it cannot replace the real experience of visiting or viewing certain artistic or architectural masterpieces, just as they cannot really replace destroyed objects. But a conscientiously made digital replica will always be a great experience, especially if the visitor is immersed with the help of virtual glasses.

Digital content conservation

This is a critical topic that needs a proper discussion. Digital is not infallible and not indestructible. To explain, I will refer to three aspects: the transience of storage media, the practice of organizing files on disk and the relevance of the file format over time.

So what do we mean by "digital content"? During a complete 3D scanning workflow we are working with several types of data: raw recordings (scanning system files, RAW image files), pre-processed image files (JPEG, TIFF - corrected colors, corrected white balance, shadows, reflections , corrected brightness), processing projects (in specific software), typical deliverables (dense clouds, meshes, orthomosaics, elevation maps, etc.), post-processed deliverables, integrative deliverables, technical reports.

The first problem that rises up is the file organization on disk. It seems trivial, but working with thousands and tens of thousands of files per year, without a standardization of the file names, the folders' structure to which if we add the personal style of each operator, will certainly lead to duplication, difficulty access, and inability to locate or even permanent loss of digital data. In this respect, an internal policy of standardization for file naming and storage practice is mandatory, preferably compatible with policies of other similar working groups. Another important aspect is the metadata (and even paradata) structure of digitized objects that should coincide with international standards, which will facilitate collaboration with databases and digital libraries.

Digital technology keeps transforming and reinventing itself right before our eyes. 15 years ago appeared the first storage services in the Cloud or online (Amazon, Dropbox). Today we have virtually unlimited online storage services as well as virtual processing machines for any type of system that may be needed. Also fifteen years ago, the main storage methods were still the CDs and DVDs (most of those that were written back then, can no longer be read today). To avoid data loss today there are standards for data storage and back-up. Personnel specially qualified for this activity must manage and update the storage solutions to avoid irrecoverable data loss due to failure or inability to read the storage media.

Another aspect of preserving digital content is the longevity of certain file formats. In particular, certain laser scanning systems have their own file formats for raw data but also for processing projects. They can only be used with the programs dedicated to those systems. These files are endangered if the said programs are discontinued in support for newer operating systems. Luckily, today there is more flexibility in file formats and cross-platform compatibility is encouraged. The digital formats of deliverables, although many, are mostly compatible with most 3D processing, editing and presentation platforms. Even if this is resolved for current technologies, older data should be revisited and updated to compatible formats, and it is important to keep this in mind for the future.

Conclusions

There are several criteria about good practices in 3D digitization that I have highlighted throughout this paper that deserve to be reiterated. An important criteria is to assume and take responsibility for the role of digitizing 3D elements of tangible historical and cultural heritage. This is done by mastering the terminology, theoretical concepts and best implementation practices. Furthermore, without defining a purpose in a context, 3D digitization loses all value and only contributes to the confusion and missing unique opportunities for the documentation of certain monuments or objects before they completely change their structure or appearance (destruction, vandalism). It is also critical that all the players participate collaboratively and integrative in a 3D digitization process (operator, beneficiary, public) and avoid toxic slogans (often for commercial purposes) according to which a single method solves all problems. Last but not least, data in digital format are not immortal, so let's be careful about how we store and manage them, because they can disappear from an unfortunate accident much faster than any other physical form of information. Preservation of digital content is a serious and critical area in the practice of digitization and would deserve a fairly wide space of discussion dedicated only to it.

The good practice of 3D digitization, once it is acknowledged and assumed, it becomes an essential element by saving invaluable information about Cultural Heritage assets, be they monuments, religious or secular art, artistic or historical heritage. A gratifying fact is the increased interest at national level, in recent years, of the authorities and cultural operators alike, compared to the importance of digitization as a whole, but also of 3D digitization. More than ever, today there are financially accessible technologies for 3D digitization, and information, practical guides and models to follow are constantly evolving and increasingly available.

Acknowledgements

Paper published within the project for financing excellence PRO INSTITUTIO - 19 PFE / 2018, funded by the Ministry of Research and Innovation through Program I - Development of the national research and development system, Subprogram 1.2 - Institutional performance - Projects for financing excellence in RDI, Contract No. 19 PFE / 17.10.2018.

This work was also financed by IMPLEMENT - Implementation and exploitation of scientific research results in the practice of restoration and conservation of cultural assets, CCCDI - UEFISCDI, PN-III-P1-1.2-PCCDI-2017-0878 / No. 55, PCCDI / 2018.

References

[1] Verhoeven, G., 2019. The 3D datafication of cultural heritage: more than just a flash in the pan? Keynote at CIPA 2019 Ávila - The 27th CIPA Heritage Documentation international symposium “Documenting the past for a better future”, 02 September 2019, Ávila, Spain. DOI: 10.5281/zenodo.3384881

*Corresponding author: L. ANGHELUȚĂ
e-mail addresses:
laurentiu@inoe.ro

Science, Practice and Public Administration in the Field of Cultural Heritage Protection - the case of IMPLEMENT Project

R. IOSIPESCU, A. CHIRICUȚĂ, A. ȚÎNȚĂREANU,
I. PETRESCU, A. POP, M. CIORNEI, M. DUCA
National Institute of Heritage, Romania

Abstract: The IMPLEMENT research project - Implementation and Exploitation of Scientific Research Results in the Restoration and Conservation Practice of Cultural Goods, initiated and coordinated by the National Institute for Research and Development in Optoelectronics (INOE) refers to the dissemination development of the advanced results of high-level scientific research, with immediate applicability in the complex and vast field of Cultural Heritage. The project builds tools for corroborating experimental data and knowledge handled by scientific research institutes, specialized departments of universities and public institutions responsible for cultural heritage management. The aims of the project are: creating a data-base for scientific research and services in the field of heritage conservation, improvement and dissemination of research knowledge and results, development of new laboratories for areas and functions as aerial or underwater archaeology.

An innovative part of the research project was the collaboration between scientists and public institutions that manage heritage protection in Romania. The National Institute of Heritage developed guidelines, procedures and protocols for a less regulated part of the practice of heritage conservation in Romania, that of monitoring architectural ensembles, archaeological sites or objects belonging to the category of movable heritage. The factors involved in the monitoring processes are not only the heritage specialists but also the owners, administrators, financiers, public authorities, verification and control entities. The guidelines were thus a necessity. Together with the partners, the main stages of the process of shaping a program for monitoring were structured. Regular assessment conditions of monuments and objects, as a systematic action of observing and investigating the impact of environmental factors and human activities, is a long-term process and must meet well-defined objectives related to their conservation. Identification of degradation processes in different stages of evolution, the need to ensure a high degree of operational safety, assessment of the behavior of structures in the action of seismic shocks, evaluation of microclimate changes in relation to interventions of any kind, and last but not least, to know and research the composition of the structures, techniques and composition of the materials used, are the main objectives of monitoring. The timing of the action of monitoring may coincide with the initiation of restoration projects and the preparation of conservation / management plans and other research projects. Unlike the recently built constructions, the interventions on the historical monuments impose special conditions deriving from the respect of the integrity and authenticity of the monument as well as the compatibility between the historical and contemporary materials used, according to the restoration principles and practices. Historic monuments, by their nature and structure, present a number of challenges in making decisions on consolidation that cannot comply with technical standards and regulations in construction. For these reasons, a good understanding of the structure and valuable elements that make up heritage assets and the identification of the physic-chemical characteristics of materials used in relation to the environment, construction techniques and compatibility with contemporary materials and substances are indispensable. An essential condition in any of the stages of monitoring, intervention and control of interventions is the thorough research of the object of the study and the reconstruction of its history as detailed as possible. All actual consolidation, restoration and archaeological research interventions must be preceded by the elaboration of precise documentation.

In the case of archaeological sites, it is ideal that right for the beginning of the actual research program start the monitoring process, and to continue during it, the result being important both for further research and for future conservation or restoration interventions. Archaeological structures discovered, with their partial or total removal from the environment in which they have been preserved for a long time and due to their age, degradation and perishability, as well as the working techniques used, require stabilization interventions, or consolidation prior to an integrated restoration. These interventions must respond exactly to immediate needs and must not replace the restoration process based on in-depth research.

The monitoring of archaeological sites must provide recommendations on the need to take measures to protect short-term discoveries, which are immediately applicable in the event of vulnerable discoveries from the point of view of conservation status, as well as long-term protection measures.

In the case of movable heritage objects, it is also very important to evaluate the microclimate conditions in which the cultural asset is located: determining the temperature (T) and relative humidity (RH) at which the object gained an equilibrium, an assessment of the permitted levels or intervals of T and RH, their rate of change, the duration of the cycles and the frequency at which the cycles are repeated in relationship with the inner environment. Thus, the potential risks to the integrity and authenticity of the movable cultural asset can be predicted.

In each phase of intervention projects, the sets of necessary investigations must be established. Investigations are carried out in order to understand the particularities of the materials of which the monument or object is composed and in order to establish the state of conservation. Investigations must substantiate the decisions that will be made and be the basis for the choice of compatible materials. The results of the investigations must be interpreted in context and thus be found in the intervention proposals. It complements and helps to date or confirm the dating of a monument or an object, to identify and classify previous interventions, to understand the mechanisms of degradation and the possibility of anticipating possible degradations to occur, to establish the intervention methodology and to determine the behavior in time of the newly introduced materials on the work of art. Tests and investigations aim to identify the mechanical, physical and chemical characteristics of materials, deformations or discontinuities of the structure. Test scheduling should be divided into steps, starting with the acquisition of general data, followed by a more detailed examination based on the evaluation of the initial data. Non-invasive or micro-invasive investigations and tests are preferable and when there is no alternative, it is important to assess the need for sampling and whether the answers given by them are of major importance and cannot be obtained by other methods. If possible, the use of several test methods and analysis techniques is recommended and the data obtained should be corroborated. The information presented during the interventions will lead to the modification of the strategy and to the substantiation of the need to carry out new investigations.

The research procedure for the control of the interventions supposes the identification of the interventions and of the newly introduced materials with the consultation of the written, drawn and photographic documentation made during the restoration process, through the in situ inspection and with the help of the investigations. The evaluation of the identified interventions will have to answer the following questions: whether from a structural and technical point of view, the intervention fulfill the initial purpose; if the intervention has other effects on the monument and the constituent materials than those expected and what is their impact on the monument; if the intervention can be removed without degrading the original material, if the changes of a physical or chemical nature are reversible, if it allows another subsequent intervention.

However, it should be noted from the outset that these procedures, protocols and guidelines developed by the National Institute of Heritage represent a first model of good practice in the field, which can be improved and completed as a result of their practical application. At the same time, they do not limit the range of activities that can be carried out in the intervention monitoring processes. The content of the notion of cultural heritage includes an impressive number of entities that can be grouped into families, genera, or, rather, categories, similar to the classification of living organisms, for which common pathologies can be identified, but, like the living world, interventions and monitoring their effectiveness must be adapted to each individual.

Therefore, in order to apply good practice schemes in the field of conservation and restoration of cultural heritage, it is absolutely necessary to identify all entities specialized in research and investigation of cultural assets, identify the services offered and the diversity of categories of cultural assets subject to scientific analysis, as well as the evaluation of the national distribution of both the requests and the possibilities of in situ operation.

Thus, a survey of all existing open source information on public institutions and private operators was a first step in obtaining a summary picture. Based on its analysis, through direct contact with the identified institutes and laboratories and on the basis of a questionnaire, a complete and detailed catalog of the availabilities and services provided will be made. By detailing the specializations within the services offered, the aim is to avoid confusion and the correct evaluation of real skills and availabilities.

The catalog will also allow the evaluation of the distribution in the national territory, by counties and regions, of these services, in order to promote adequate policies for the training of staff in disadvantaged areas but with a significant number of historical monuments.

It was found that the web sites deliver inaccurate information. The public information provided in the virtual environment is not updated: part of the staff is already retired, available equipment is outdated or non-functional and technical language is misused or ambiguous.

Another issue found is that of accreditation at the entity level (laboratory, institution, private operators), or at the personal level. For the movable heritage, accreditations were granted at the level of museums, laboratories and individuals, while for the immovable heritage the attestations of the specialists and experts are obtained only individually. On the other hand, the survey carried out on the conservation laboratories in the museums showed the overwhelming preponderance of certified specialists in the conservation and restoration of movable and archaeological heritage, compared to the number of certified persons in the field of historical monuments.

From the Register of specialists in the field of protection of historical monuments results the attestation of the following professions: engineer, architect, painting restorer, historian, art historian (5), archaeologist (4), urban planner (3), chemical engineer (3), stone restorer, metal restorer, stained glass restorer, timber restorer (4). In a hierarchy of professions is found the preponderance of engineers and architects, historians, followed by painting and stone restorers / metal restorers/ timber restorers. At the same time, the categories of art historians, archaeologists, urban planners, chemical engineers are very poorly represented, which, especially with regard to the latter, raises an alarm.

Regarding the field of attestation, about a third of the specialists have attributions in the inspection and follow-up of the behavior in time of the historical monuments, in the process of consolidation and restoration of the historical structures.

In the Register of experts and technical verifiers in the field of protection of historical monuments the only notable differences refer to the presence of specialists in biology and physics, the areas of attestation being elaboration of studies, research and expertise, inspection and monitoring of historical monuments over time.

Despite these shortcomings, it has been found that many specialized laboratories operate in universities and scientific research institutes benefiting from advanced and competitive facilities, whose involvement in the field of historical monuments and movable heritage is null, insignificant or too little known. This requires greater visibility and openness of these entities, so that it is possible to provide specialized services.

From the public data provided, it was not possible to evaluate the degree of involvement of the analyzed entities in major projects for the restoration of historical monuments. For many of these entities it was difficult to identify their role in researching the following priority topics. Firstly, in terms of detection and evaluation by non-destructive methods of archaeological sites. Secondly, identification and research of sculpted or painted inscriptions from historical monuments with the technical means of electronic optics. Lastly, researching the structure of historical monuments to achieve granular knowledge and identifying construction defects using aforementioned technical means with the scope of preventing degradation and adoption of optimal conservation and restoration solutions.

Din datele publice oferite nu s-a putut evalua gradul de implicare a instituțiilor în proiecte majore de restaurare a monumentelor istorice. De asemenea nu a fost posibil de identificat rolul lor în promovarea unor teme prioritare precum depistarea, evaluarea prin metode nedestructiva a siturilor arheologice; identificarea și cercetarea unor inscripții sculptate sau pictate din cadrul monumentelor istorice cu mijloacele tehnice ale opticii electronice; cercetarea structurii monumentelor istorice pentru cunoașterea amănunțită a acestora, identificarea unor vicii de construcție cu aceleași mijloace spre prevenirea degradării lor și a adoptării soluțiilor optime de conservare-restaurare.

As a good practice example of collaboration in monitoring and control of interventions on historic monuments there can be shown the case of collaboration between the National Institute of Heritage and the National Institute for Research and Development in Optoelectronics INOE 2000 for the preparation of the nomination file of Brâncuşi Monumental Ensemble of Târgu Jiu for inclusion in the World Heritage List. INOE 2000 contributed through the results of a multi-annual research, started in 2015 and continued until 2019, to evaluate and reactive monitoring of the sculptures that make up the Ensemble “Calea Eroilor”: Table of Silence, Alley of Chairs, Gate of the Kiss and Endless Column. The entire documentation was used to prepare parts of the file for the nomination of the Monumental Ensemble made by Constantin Brâncuşi in Târgu Jiu for the World Heritage List.

Acknowledgment

This work is financed by IMPLEMENT - Implementation and exploitation of scientific research results in the practice of restoration and conservation of cultural assets, CCCDI - UEFISCDI, PN-III-P1-1.2-PCCDI-2017-0878 / No. 55, PCCDI ⁄ 2018.

*Corresponding author: R. IOSIPESCU
e-mail addresses:
raluca_iosipescu_arheo@yahoo.com

Study of the picturesque decoration of the State Office of Emperor Nicholas II in the Alexander Palace in Tsarskoye Selo

M. RICCI[A], F. SEBASTIANI[A], M. BECUCCI[AB*],
M. ROGOZNY[C], V. PARFENOV[D]
[a]*Department of Chemistry 'Ugo Schiff', University of Florence, Sesto F.no (FI) 50019, Italy.*
[b]*European Laboratory for Non-Linear Spectroscopy, University of Florence, Sesto F.no (FI) 50019, Italy*
[c]*The St.Petersburg Stieglitz State Academy of Art and Design, St Petersburg 191028, Russia*
[d]*Department of Photonics, St.Petersburg Electrotechnical University, 197376, Russia*

Abstract: The painted decoration found during recent restoration work in the Alexander Palace in Tsarkoye Selo are currently studied by laser spectroscopy methods. We aim to characterize the materials and their degradation on order to support the conservation efforts. We present here the first results on the basic characterization of selected decoration elements carried out by Raman microscopy and by elemental analysis obtained by optical emission following laser plasma formation.

Keywords: Raman, LIBS, Cultural Heritage, laser diagnostics, conservation of mural painting

1. Introduction

The Alexander Palace was the favorite residence of Nicholas II, the last Russian emperor and it is connected to many events in his life. It was his place of birth and here, in March 1917 he was imprisoned with his family under house arrest to be then sent to exile in Tobolsk.

The Alexander Palace in Tsarskoye Selo was commissioned by Catherine II for his grandson, the future Emperor Alexander I, to the Italian architect Giacomo Quarenghi and it was built in 1792-1796. The original interior decoration, still by J. Quarenghi, was designed in the style of classicism. Unfortunately, almost nothing has been preserved from the initial interior decoration. The palace repeatedly changed its owners by inheritance: At different times Nicholas I lived here, both Alexander II and Alexander III spent in the Palace their youth. Interior design changed depending on the tastes and preferences of the owners. Large alterations in the palace were completed during the last emperor Nicholas II. Personal apartments were rebuilt in a fashionable, at that time, Art Nouveau style. The front office Nicholas II was created by the architect R. Meltzer in 1902-1904. The office was connected with a mezzanine to the living room of the wife Alexandra Fiodorovna.

After the palace was nationalized in 1918 and a museum was opened, in the ceremonial halls and personal chambers of the last emperor and empress, which lasted until 1941. Head of the museum V. I. Yakovlev, describing the study, wrote: “The ceiling was lined with mahogany, the walls were painted with mastic oil paint of blue-green color and painted with a stencil with ornamental friezes around the tiled cladding over the fireplace and the niche behind the desk” [1].

During the World War II, Tsarskoye Selo was occupated by the invading army and in the Alexander Palace were located the headquarters of the Spanish Blue Division and the Gestapo branch in the basement of the prison [2]. The palace was badly damaged during the war. The first post-war work was carried out 1946-1951 according to the project of architect L. M. Bezverkhny. The general concept for this project was to restore the interiors to the general style of the palace, for the period of Quarenghi [3]. The remnants of the destroyed interiors, not corresponding to the general style of the building, were dismantled. During this period, the picturesque decoration of the State Office was also destroyed.

More recently, during the 2019 restoration, on the walls of the cabinet, under the late stucco, fragments of a pictorial decoration were found depicting, in the Art Nouveau style, a repeating ornament of stylized bunches of needles and pine cones. The old stucco with the painting was almost completely knocked down, notches were made on firmly held fragments to better fix the new stucco mortar. The paint layer in different areas differs in colour and tone.

A scientific research program was initiated to characterize the materials in use and, possibly, their degradation. Here, we are reporting preliminary results on the distributions of various elements over grounds and paint layers, which allowed us to find similarities and differences of analysed paintings. In the current study, we have concentrated on the comparison of the composition of various layers as obtained by Laser Induced Breakdown Spectroscopy (LIBS), and we focus on the distribution of some specific elements (like Zn, Fe, Pb, Cu, Sn) and tried to classify the paintings according to their content. These studies are complemented by the characterization of materials at a molecular level by means of vibrational spectroscopy methods.

2. The painting and its conservation

The painting was in disrepair, the plaster layer was deformed along the edges of the chips, the paint layer was stratified with persistent, stubborn dirt was spread over the entire surface. Fragments of the painting located on opposite walls differ in colour and tone.

Changes in the paint layer are requiring a detailed research. Instrumental spectroscopic analysis is currently carried out at the University of Florence.

The optical observation of the samples suggests that the surface preparation for painting was done according to the system of putties and primers, with intermediate gluings by intermediate impregnation with drying oil. The putty layer has a thick levelling, beige colour, possibly with a high content

Fig. 1. Fragments of the painting located on opposite walls of the State Office of Emperor Nicholas II in the Alexander Palace in Tsarskoye Selo. Red dots highlight the different sampling points.

of gypsum. The paint layer seems to be realized by the use of mastic-oil painting technique (which includes use of pigments, wax, drying oil and turpentine). The background is blue-green, dense, applied in several layers, and the lower layers are lighter. To give a uniform surface, the last layer of the background is applied by brushing (this method of applying mastic oil paint was common in the late XIX early XX century). The ornament is stencilled, followed by writing with brushes. The texture of the brushstroke is clearly visible on images of pine needles, the paint is applied thickly, the strokes are in the direction of the drawing and the edges are sharp. A characteristic bronze paint was used for some elements of painting. Usually it consists of a very fine copper powder mixed with oil varnish.

3. Experimental methods

The experimental LIBS setup was already described.[4,5] The plasma was generated on the sample surface by laser pulses at 532 nm (approx. 2-5 mJ) from a Q-switched Nd-YAG laser (model CFR 200-GRM, Big Sky Lasers, 8 ns pulse duration, 20 Hz, top hat profile of constant energy density). The emission spectrum was acquired by using a single grating spectrometer (Acton Research Sp2358i, 320mm, equipped with a holographic grating (150 lines/mm, blazed at 500nm) and an intensified CCD camera (Princeton Instruments PI Max-1024/RB-PTG, gated starting 100ns after the laser Q-switching, 1 ms exposure). The small time-delay after laser emission helps to avoid detection of the laser pulse itself and to reduce strongly the continuous background signal given by electrons relaxation in the plasma, the so-called *Bremsstrahlung* process. The reported spectra are obtained by averaging on the CCD detector the emission following 3 consecutive laser pulses applied on the same point of the sample. The grating was set to 450 nm central frequency and in a single data acquisition session the 250-650 nm spectral region was investigated. The spectral resolution was about 1 nm along the spectrum. If needed, the spectra were smoothed by applying the Savitzky-Golay algorithm (second order polynomial function applied on a 5 points window). In some cases, a depth profile of the sample was obtained by repeating the data acquisition session in the same area of the sample a few (3-5) times without any adjustment in the optical system. From optical microscopy measurements we estimate a penetration depth of 10-20 mm per data acquisition session (3 laser pulses). Figure 2 shown a sample with the holes produced during the LIBS experiments after prolonged laser exposure. The distribution of many elements on the surface of samples from the Alexander Palace was monitored by LIBS optical spectroscopy methods. Raman spectra were obtained by using a Renishaw RM2000 Raman microscope, which consists of a single grating monochromator (1200 lines/mm, about 5 cm^{-1} spectral resolution) with a cooled CCD detector optically coupled to a Leica optical microscope. Notch filters were used to decouple Rayleigh and Raman scattering. The laser beam was focused on the sample by using up to 100x microscope objectives that allow for better than 1 mm spatial resolution. Both 514 and 785 nm laser radiation, from an air cooled argon ion laser or a laser diode, respectively, were alternatively used. Laser power on the sample was adjusted between 0.01 and 2 mW. Typical integration time for the acquisition of a Raman spectrum was between 10 and 100 s. In some cases, fragments were prepared for Raman stratigraphic analysis by casting them in a polymer and optically cleaning the surface. An example is shown in Fig.2.

Fourier transform infrared (FTIR) spectroscopy was performed on samples of plasters and pigments using a Spectrum 100 Perkin Elmer with an attenuated total reflectance (ATR) diamond crystal. The detector is FR-DTGS (fast recovery deuterate L-alanina tryglycine sulphate) and the spectral range is 4000–380 cm^{-1} with a spectral resolution of 4 cm^{-1}. The instrument is collecting data from a macroscopic area, as large as 5 mm diameter.

4. Results

The LIBS spectra were analyzed using the sets of atomic transitions calculated from the LIBS data bank which is freely accessible in the NIST web site (under the link https://physics.nist.gov/PhysRefData/ASD/LIBS/libs-form.html), and a calibration-free method. The atomic emission spectra were calculated in the hypothesis of local thermodynamic equilibrium in the plasma and assuming an optically-thin system (i.e. neglecting possible self-absorption phenomena, more likely for the stronger lines).[6] The plasma equilibrium temperature was set to 0.6 eV (about 7000 K), after some initial tests. The calculated transitions were spectrally broadened with a Gaussian function (1 nm FWHM) in order to match the experimental conditions. We adjusted numerically the weight of the different atomic emission sets to match the spectral intensity distribution experimentally observed and to infer the different relative atomic abundances in the samples. The error in the relative intensities can be even larger than 10% in the data reported. However, the presence of the reported atomic species is clearly determined as we mention only the atomic species whose presence is univocally determined by the appearance of characteristic sets of atomic lines with appropriate relative intensities. The most intense bands in the experimental spectrum (Cu bands at 324 and 327 nm and Ca bands at 393, 397, 420 nm) are

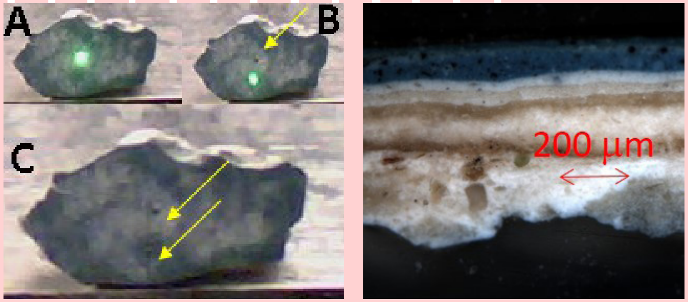

Fig. 2. On the left: a sample under LIBS study (A, B panels) and afterwards (C panel); the bright green dots are the laser beam sampling different points on the surface. The arrows point to the local damage (about 0.1 mm diameter) made by the laser ablation process. On the right: the cross-section of a fragment prepared for Raman stratigraphic characterization.b

possibly attenuated by self-absorption in the plasma. This phenomenon is easily recognized by the large discrepancies between the intensity ratios of the bands assigned to the same atomic species. Therefore, we use only the weak bands to evaluate the relative abundancies of the different atomic species.

An example of experimental LIBS atomic emission spectrum obtained, together with its numerical simulation is reported in Figure 3. The reported relative abundancies a referred only to the atomic species possibly detected in the LIBS experiment, not in the real sample. That is because a LIBS experiment has a very limited sensibility for many atoms (e.g., light atoms (first and second period), halogens and chalcogens) due to their small cross-section in the VIS-UV spectral range. Also, the quantitative information is made sometime problematic by the large difference in the relative cross sections fort the emission lines of different elements. LIBS analysis on the sample shown in Fig. 1(right) are reported in Table 1. Data are taken in the bronze-painted and blue area. Present knowledge on the bronze paint is suggesting that it should be a fine-grained powder of copper alloy (possibly copper could be could present in percentage as large as 70% with presence of zinc and a small amount of aluminum and iron). Our data support this information as copper is only observed in the bronze area. At the same time, the amount of iron and aluminum is larger here with respect to the adjacent blue area. Zinc is present in the bronze area and its presence is even larger in the blue area. That is suggesting the possible use of zinc oxide or lithopone (a $BaSO_4$-ZnS mixture) in the preparation layer or as a pigment.

Table 1. *Most relevant metals found by LIBS experiments in the bronze paint and the adjacent blue area in sample 1. Data reported as percent respect to the total identified components.*

	Al	Ca	Cu	Fe	Pb	Si	Zn
Bronze	6	5	11	7	21	11	35
Blue	3	1	0	3	10	8	75

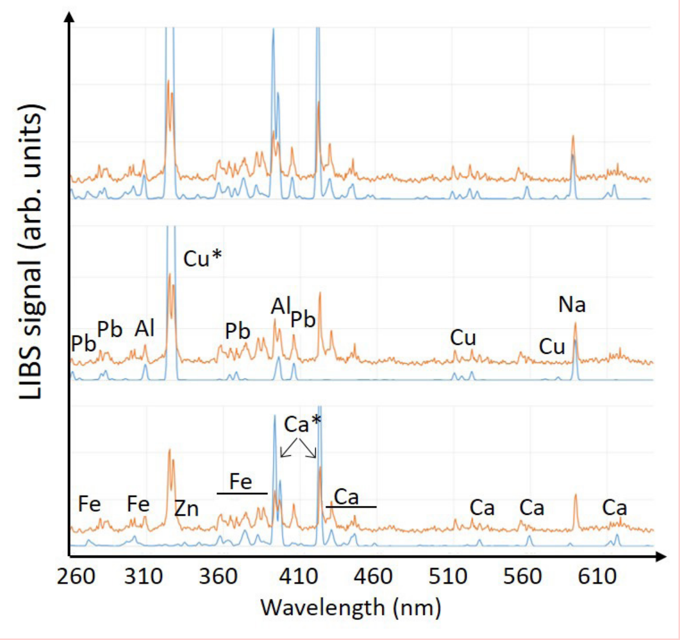

Fig. 3. The LIBS spectrum of a bronze-painted area with its numerical simulation (top panel). The middle and bottom panels show assignment of the main bands to the different atomic species. A few strong bands (*) have a large difference in the experimental and simulated spectra due to self-absorption in the plasma. Experimental spectra are vertically up-shifted with respect to the simulated ones for a better reading.

LIBS data taken in the blue area are compatible either with the use of organic dyes or lapis lazuli (an aluminum silicate of sodium and calcium).

MicroRaman spectra were acquired on both the cross-sections and the surface of the samples to characterize the bronze paint. In all the stratigraphic samples, it is possible to recognize five layers of different thicknesses (sample 1 is shown in Fig. 2). From the bottom to the top, three layers consist of two shades of white paints, the brighter ones, and another one of a light brownish color. Above, a layer of light blue is superimposed on a thick blue layer, where grains of blue pigments are coarsely mixed with dark paint. The two white layers, one bright and the other slightly light brown, are distinguished by the different mixtures of pigments. In the lighter layer, there is white lead with barium sulphate and little calcite, while in the darker one there is calcite and/or gypsum with a small amount of white lead.

The blue pigments are Prussian blue and ultramarine blues. Prussian blue, ($Fe_4[Fe(CN)_6]_3$) is an iron(III) hexacyanoferrate(II) complex, whose color arises from an intervalent charge transfer via a cyano group between iron(II) and iron(III). The ν(CN) vibrations between 2150 and 2160 cm^{-1} are the spectral signature of this pigment. The C≡N group, being coordinated with iron ions of different valence state, exhibits various wavenumber of ν(CN) stretching in this range. The main peak around 2155 to 2160 cm^{-1} refers to the A_{1g} ν(CN) stretching vibration and [Fe(II), Fe(III)] vibrational state. This peak presents a shoulder towards lower wavenumbers at 2123 cm^{-1}, characteristic for CN^-. The second peak is localized at around 2090 cm^{-1} and corresponds to the E_g mode of the ν(CN) stretching vibration of the [Fe(II), Fe(III)] state. Other characteristic peaks are located in the lower part of the spectrum, in the range between 450–620 cm^{-1} and 190–340 cm^{-1}. The group of peaks in the higher spectral window (450– 620 cm^{-1}) is characteristic for all the Fe–C stretching vibrations of the lattice and it is defined by a major peak at 537 cm^{-1} and a second one at 605 cm^{-1}. The lower spectral window (190–340 cm^{-1}) with peaks at 276 cm^{-1} represents the Fe–CN–Fe bond deformation vibrations. (see Fig. 4).[7] The characteristic bands of

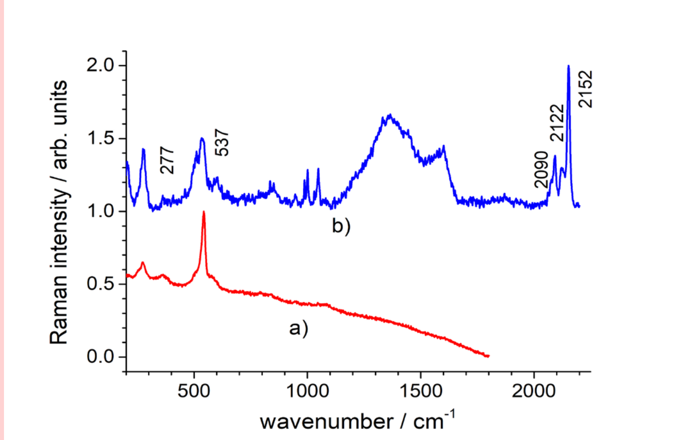

Fig. 4. a) Raman spectrum of ultramarine blue in sample 2; b) Raman spectrum of blue color in sample 1: Prussian blue' vibrations are labeled. The other vibrational bands are due to amorphous carbon, lead white, and barium sulphate.

ultramarine (a pigment originally made of grinded natural lapis lazuli and available as synthetic material since ~1830) are located near 549 cm^{-1} [n_1 (A_1) totally symmetric stretching vibration of S_3^- ions], 259 cm^{-1} [n_2 (A_1) bending vibration of S_3^- ions] and a shoulder near 585 cm^{-1} (stretching vibration of S_2^- ions).[8]

The different hues of blue are obtained by changing the quantity of blue and white pigments. In the dark blue there is more Prussian blue and sometimes amorphous carbon.

The bronze paint was analyzed in the different samples by LIBS and Raman. It is characterized by the presence of Cu and Zn powder (brass) mixed with oil paint. The Raman spectra

of the samples in the bright blue area also show the zinc and potassium chromate pigment in the orange-gold part, and in some places a strong fluorescence is present. In the bronze area of the green-blue part of the paint the oxidation products of copper, such as tenorite, are only observable.
All samples were also analysed with ATR-FTIR spectroscopy. In addition to the presence of the pigments that characterize the blue and white color, bands are visible that can be associated with the presence of the binder or protective. The relevant bands are the stretching vibrations of the C = O group of esters and carboxylic acids, 1732 and 1705 cm^{-1} respectively, and the stretching vibrations CH and CH_2 at 2920 and 2851 cm^{-1}. The sharp bands at 1586 and 1546 cm^{-1} with a double peak at 1536 cm^{-1} shown in Figure 5 are attributed to the metal carboxylates that are the result of saponification processes between drying oil, mainly composed of triglycerides, *i.e.* esters of glycerol linked to three long-chain carboxylic acids, and metal-based pigments.[9]
Drying of the oil predominantly results from photooxidation and autoxidation reactions. The reactivity of the double bonds of the unsaturated fatty acids promotes the initiation of these reactions and it may be catalysed by the presence of metal ions from pigments and driers. The result of this chemical process is a complex three-dimensional polyanionic network based on the glycerol ester with a crosslinked fraction of carboxylate anions stabilised by metal cations. Mono and dicarboxylic acids that are not incorporated in the polyanionic network may migrate to react with metal cations, leading to the formation of an increased proportion of metal carboxylates (metal soaps). The characteristic infrared bands characteristic of metal soap formation are associated with COO group asymmetric stretching vibration for copper (1586 cm^{-1}), lead (1546 cm^{-1}), and zinc (1538 cm^{-1}) carboxylates. The formation of metal soaps in the painting confirms the use of drying oil as the binder. Finally, the spectra show gypsum ($CaSO_4 \cdot 2H_2O$), a common degradation product in wall paintings, since calcite is present both as a pigment and as a binder in the ground layer).

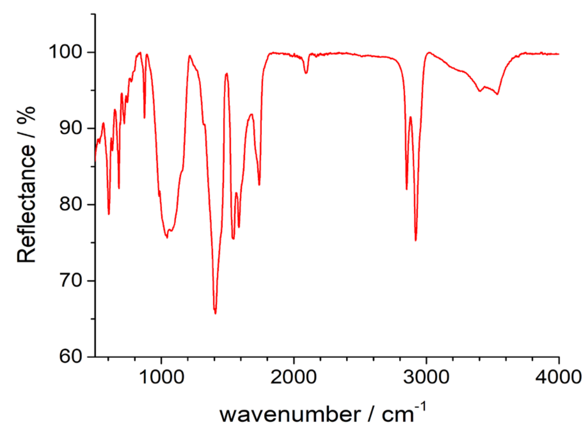

Fig. 5. ATR-FTIR spectrum of sample 1.

5. Further developments

The scientific approach described in the previous Sections is quite universal and easily applicable to different materials. However, it has some limitation, especially when the goal is to determine the presence of organic materials in traces. A relevant example is represented by the identification of organic dyes. That is extremely important for studies of modern wall paintings (where the chromophore molecule is typically a modern synthetic dye) or for materials where natural organics dyes were used (either alone or mixed to inorganic pigments). These organic materials are often used in very limited amounts. Therefore, high sensitivity experimental methods are needed. Electronic spectroscopy (reflectance or fluorescence) has demonstrated a very good sensitivity but, unfortunately, the spectroscopic evidence that provides is not detailed enough to identify the specific substances used. Vibrational spectroscopy can provide detailed molecular information, able to support the chemical identification process but its sensitivity is limited. The development of high sensitivity new methods for vibrational spectroscopy is one of the challenges that lie ahead for significant developments in this field. Surface enhanced Raman scattering (SERS) represents, for some classes of molecules, a very promising new experimental method. It has been shown that the Raman signal of a molecule can be strongly enhanced if it is effectively interacting with a nanostructured metal surface. [10] The enhancement factor can be as large as 10^8, so large that the possibility of single-molecule detection has been demonstrated. We are currently working on the definition of new SERS methods for the identification of organic dyes present in minute amounts on different substrates, like paintings or textile fibers.[11-14] Under this respect, the specificity of the methods devised for the detection of single chemical species (i.e., extraction process from the support, optimization of the nanostructured metal substrate – which includes the use of linkers between the analyte and the SERS active substrate) makes very challenging to define a standard, universal analytical approach.[15] Nevertheless, some application has already been devised.

6. Conclusions

We have obtained new, complementary information on the materials and methods used for the Art Nouveau decoration in the State Office of Emperor Nicholas II (Alexander Palace in Tsarskoye Selo, Russia) by the combined use of different spectroscopic methods. The correlation of data arising from different spectroscopic observables enabled us to provide a deeper understanding of the system. The bronze paint used was identified as a brass powder applied with use of a drying oil as a binder. Also, we are able to make some comments on the degradation products (metal soaps) present on the samples.

Acknowledgements

Support from University of Florence - UNIFI is kindly acknowledged.

References

[1] V. I. Yakovlev. “Alexander Palace Museum in the Children’s Village” (Leningrad: Decoration. 1928) p. 286. {in Russian}

[2] L. V. Bardovskaya, V. F. Plaude, I.G. Stepanenko. Alexander Palace. Album (St. Petersburg: Aurora Publishing House. 2010) p. 42. {in Russian}

[3] L. M. Bezverkhniy. Restoration of the former Alexander Palace and Lyceum in the city of Pushkin. Architecture of Leningrad **1** (12), 23 (1950) {in Russian}

[4] L. Ancillotti, E.M. Castellucci, M. Becucci, Proc. SPIE, **5850**, 182 (2004).

[5] I. Osticioli, N. F. C. Mendes, A. Nevin, A. Zoppi, C. Lofrumento, M. Becucci and E. M. Castellucci, Review of Scientific Instruments **80**, 076109 (2009).

[6] R. Fantoni, L. Caneve, F. Colao, R. Fornarini, V. Lazic, V. Spizzichino, Spectrochim. Acta Part B, **63**, 1097 (2008).

[7] G. Moretti, C. Gervais, J. Raman Spectr. **49**, 1198 (2018).

[8] I. Osticioli, N. F. C. Mendes, A. Nevin, P. S. C. Gild, M. Becucci, E. Castellucci, Spectrochim. Acta A **73**, 525 (2009).

[9] E. Platania. N.L.W. Streeton, A. Vila, D. Buti, F. Caruso, E. Uggerud, Spectrochim. Acta A **228**, 117844 (2020).

[10] E. LeRu, P. Etchegoin. “Principles of Surface-Enhaced Raman Spectroscopy”, Elsevier, Amsterdam (2008).

[11] C. Lofrumento. M. Ricci, E. Platania, M. Becucci, E. Castellucci, J. Raman Spectr. **44**, 47 (2013) .

[12] E. Platania, J.R. Lombardi, M. Leona, N. Shibayama, C. Lofrumento M. Ricci, M. Becucci, E. Castellucci, J. Raman Spectr. **45**, 2014 (2014).

[13] E. Platania, C. Lofrumento, E. Lottini, E. Azzaro, M. Ricci, M. Becucci, Anal. Bioanal. Chem. **407**, 6005 (2015).

[14] C. Lofrumento, E. Platania, M. Ricci, M. Becucci, E. Castellucci, J. Phys. Chem. C **120**, 12234 (2016).

[15] M. Ricci, E. Trombetta, E. Castellucci, M. Becucci, J. Raman Spectr. **49**, 997 (2018).

*Corresponding author: Maurizio Becucci

e-mail addresses:

marilena.ricci@unifi.it

federico.sebastiani@unifi.it

maurizio.becucci@unifi.it

rogozny-misha@mail.ru

vaparfenov@etu.ru

Uncovering Layers of the Past. Spectral Imaging Techniques for Artworks Investigation

L.C. RATOIU

Department of Optoelectronical Methods and Techniques for Artwork Restoration and Conservation, National Institute of R&D for Optoelectronics-INOE 2000, Măgurele, Romania

Abstract

This paper presents a short overview of two non-invasive and versatile spectral imaging techniques used in the field of conservation science. As a part of a complex imagistic model, multispectral and hyperspectral imaging provide complementary data which focus on the top of the surface and the under layers. While multispectral analysis is able to record images from different regions of the electromagnetic spectrum, hyperspectral imaging allows enlarging of the bandwidth area and extracts specific information contained by each recorded pixel. Classification based on the spectral profile of each given material or mixture provides a fresh perspective in the process of investigation and documentation of cultural heritage objects.

Keywords: multispectral imaging, hyperspectral imaging, spectral classification, art conservation

1. Historical and theoretical background

In the process of examination cultural heritage artifacts and especially paintings, five regions of the electromagnetic spectrum (EM) are especially relevant: 1) the Visible radiation (VIS) - ranging from 400-780 nm-used for high accuracy reference images, both greyscale and color; 2) Near- & Far-Ultraviolet radiation (320-400 nm) - for investigations in UV fluorescence and UV reflectance modes. The use of UV radiation in the Medium (280-320 nm) and Short (200-280 nm) region is allowed only in special cases (such as in mineral analysis) because it can cause degradation of art objects; 3) Near-Infrared Radiation (NIR 780-3000 nm) for the analysis of layers and substrates (painting, graphics, textiles, painted ceramics, etc.); 4) Middle Wavelength Infrared (MWIR 3–8 µm) and Long-Wave Infrared (LWIR 8–15 µm) - used exclusively for thermography (a topic not to be addressed here), a very useful technique in historical monument analysis and aerial inspection; 5) X-ray - used in the radiography of opaque objects, from paintings on canvas and wood panel, to metallic or non-metallic artifacts [1].

Articles and studies regarding the use of UV radiation (Rorimer, 1931), X-ray radiation (Burroughs, 1938) or IR reflectography (Van Asperen de Boer, 1968) have been published extensively for decades. The technological development of these techniques has led to a maturity level and to important results which enabled to analyze works of art *layer-by-layer* in a holistic approach. In this sense, more recently hyperspectral cameras managed to combine high-

resolution imaging with spectroscopic analysis [2]. While methods and techniques became more and more advanced in terms of sensibility, accuracy and resolution it remains a mandatory task for researchers to adapt the investigations to the specific structure of each unique artwork.
This paper is focusing on multispectral and hyperspectral imaging as two complementary means to extract relevant data for art history and conservation studies.

2. Spectral imaging techniques in conservation science

Multispectral and hyperspectral imaging, although derive from the same working principle, provide complementary information concerning the successive layers of paintings. If multispectral imaging refers to raster or snapshot images which are obtained with custom filters who allow to record data only on narrow ranges of wavelength, hyperspectral data cubes contains both spatial and spectral information for each pixel of a scanning. In the process of art examination is highly important to define the target areas and the main features that can be extracted according to these targets.

2.1. Multispectral imaging

This technique refers to a portable, non-destructive and non-invasive analysis with real time response that records specialized data on different wavelengths of the electromagnetic spectrum (EM). Initially developed for remote sensing, some 40 years ago, this technique was successfully applied in field of art conservation and art history since the early 1990s [3-4]. Main applications were performed in emphasizing the authenticity of paintings, studying the artist's techniques or underlining the state of conservation.
The interaction of painting materials with the EM is governed by a combination of reflection, absorption, scattering, and emission processes, each dependent on the geometry, refractive index, and physical nature of the surface, and wavelength of the radiation used [1]. Electromagnetic radiation scattering mechanisms in the structure of the paint layers were quantitatively described by the Kubelka-Munk theory.
The multispectral imaging (MSI) system used by CERTO – The Department of Optoelectronical Methods and Techniques for Artwork Restoration and Conservation is an Artist model produced by Art Innovation and is able to record in the range 365 – 1100 nm, covering three regions of the EM: UV - VIS – NIR. For each of these three regions there are two different imaging modes: UV reflection – that records only the reflected radiation, UV fluorescence – enables to emphasize fluorescent materials and to distinguish retouches or other types of recent interventions made at the surface, the Visible Black & White or the Visible Color mode – high accuracy images that are used as reference models, and NIR 1 & NIR 2 – both being images recorded in the near- infrared region (780-1100 nm) – it differs only the range of the wavelengths. Other two types of imaging provided by the camera are False color infrared mode (FCIR 1, 2) – recordings that reunites the information from the visible and near infrared spectrum. These acquisition modes are extremely useful especially when is needed a clear

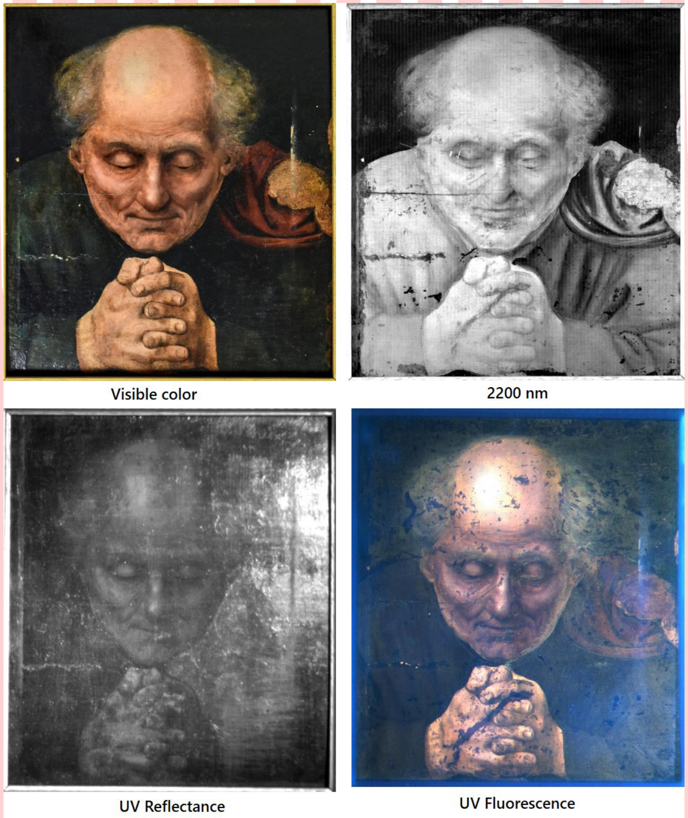

1. Examination of an artwork attributed to Jan Massys "Monk prayin" from the collection of Bucharest Municipality Museum. The UV recordings display later interventions on the surface while the SWIR image highlights the presence of a pentimenti on the portrait.

differentiation between distinct materials, colored in similar tones. The system uses a set of chromatic filters which work as band-pass filters, to produce high-resolution spectral images on different wavelengths. Lighting and environmental conditions are key aspects in recording quality data. As radiation source for NIR and VIS recordings are used two halogen lamps supplied as 12 V DC with a power converter that produce 20 W. The halogen lamps are positioned to form a 90-degree angle with the studied surface, in order to obtain a uniform lightning. For UV imaging modes a black light lamp with LED technology from Karl Deutsch, with a characteristic wavelength at 365 nm, is used as a radiation source. Due to high absorbance of UV radiation these recordings require a controlled environment.

The CCD (charge-coupled device) progressive scan image sensor is a silicon detector able to record in: UV, VIS and NIR. Its main disadvantages are the limited bandwidth in the NIR area and the fact that switching between the acquisition's modes will engage automatically the need to manually adjust the focus and the aperture.

In UV imaging modes the incident radiation is reflected or scattered on the surface while the wavelength is unchanged. UV reflectance renders such areas, depending on their reflectivity, in light shades. In fluorescence recordings they appear black (or dark blue), since UV is absorbed by the barrier filter (See Fig 1). This recording mode is exclusively used for the analysis of superficial layers of an object. Fluorescence is kind of luminescence

2. Icon of Saint Elijah from White Church located in Bucharest. Comparison between visible recordings and SWIR hyperspectral images at different wavelengths. Highlights of the initial composition.

(emission of light exclusive of thermal sources) by which some substance (e.g. pigment) irradiated by electromagnetic radiation – ultraviolet light is emitting light of visible color. Unlike phosphorescence light is emitted only while the UV stimulation continues. The fluorescence of paint layers, which are always complex mixtures, is mainly determined by the binding media in who they are employed (drying oils, resins, egg) or by the (aged) varnish layers and not by pigments. This is due to the poor penetration ability of UV radiation, which is already strongly absorbed in the top layer. The most fluorescent chemical compounds are those of organic nature, while in the case of inorganic compounds fluorescence is a rare phenomenon. These materials of the pictorial layer may exhibit varying colors or intensities of the fluorescence phenomenon, these properties being able to characterize or indicate to a certain degree the present state of conservation. For example, later restoration interventions or retouches can be easily spotted because of the high absorption of UV radiation (these occur in the form of dark areas), while the old varnish layers are highlighted by intense fluorescence [5].
NIR radiation has less energy than visible light and usually excites vibrational overtones rather than electronic transitions [3]. The ability of NIR to penetrate through some pigments has allowed the study of: under drawings, previous compositions, hidden signatures, *pentimenti* or the succession of under layers but also information regarding the actual state of conservation - previous interventions or hidden defects/degradations located in the thickness of the pictorial layer (See Fig 2).
The technique of using NIR photography for detection of under drawings was already in use at the beginning of 1930s, when Ian Rawlins used an NIR camera to improve visual assessment of paintings [3]. Wavelength-specific absorption in pigments are caused by the presence of particular chemical elements or ions, the ionic charge of certain elements, geometry of chemical bonds between elements, and the presence of transition elements in their crystal structures [3]. Van Asperen de Boer, a pioneer of IR-reflectography, was aware that the degree of paint penetration depends on the paint itself, the thickness of the paint and also the exact wavelengths used [6]. A paint layer becomes more transparent with greater wavelength of the incident radiation, smaller thickness of the paint layer, smaller number of particles in the layer, and lesser refractive index difference between pigment and medium. The absorption of infrared radiation of (colored) substances and materials differs very often from their behavior in the visible, so that two pigments in a paint layer of the same hue are rendered differently by means of infrared registration. The same holds for optically alike additions applied to an object during restoration.

2.2. Hyperspectral imaging

Also known as imaging spectroscopy is another non-destructive and non-contact technique, which enables the transition from imaging analysis to spectroscopic/analytical investigations.
In the field of cultural heritage conservation this particular technique provides an *in-depth* analysis that can be linked with other complementary imaging methods for a better understanding of the investigated object [2]. The hyperspectral system available at CERTO is a HySpex SWIR-384, produced by Norsk Elektro Optikk AS, and is able to record in the SWIR

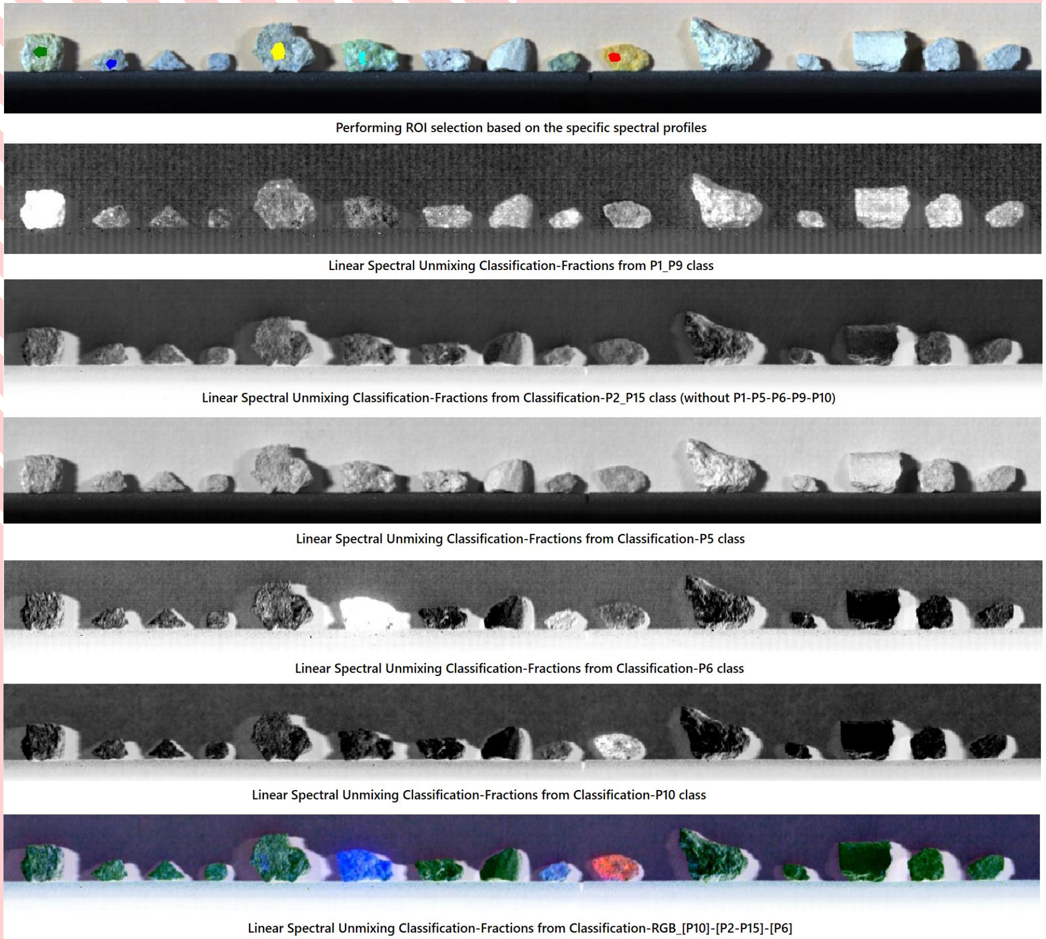

3. LSU classification performed on lime plaster samples. In greyscale images are represented fraction corresponding to the selected endmembers.

(Short Wave Infrared) spectral interval: 950 – 2500 nm. This system is equipped with a state-of-the-art photoconductive detector HgCdTe - Mercury Cadmium Telluride (MCT), with a FOV (Field Of View) of 16 degrees across the track, and an FPA (Focal Plane Array) cooling system which ensures a constant temperature of 150 Kelvin, a characteristic that provides low background noise. For each pixel of a recorded image, the hyperspectral sensor acquires the light intensity for a large number of contiguous spectral bands. Thus, every pixel in the image contains a continuous spectrum expressed as radiance (in our case) or reflectance and can be used in order to characterize any material or mixture with great precision and detail. The acquisition of data are made by line-scan method or push-broom, also known in the literature as along track scanners, which uses a line of detectors, arranged perpendicular on the studied surface. As the translation stage and the camera, mounted on it, moves along a sample, the image is collected one line at a time, with all of the pixels in a line being measured simultaneously. Unlike multispectral images, that capture only single snapshots or raster images, hyperspectral sensors, such as HySpex SWIR-384, simultaneously records up to 288 spectral bands, generating a so-called hyperspectral cube with x, y spatial dimension and λ spectral dimension. The other main feature of the hyperspectral system beside the extraction of well-defined spectral bands is that it enables to identify, component materials (pure or mixtures) of the studied area, by comparing the specific spectral profile with reference or open source spectral database. It also allows to classify and to map component materials based on their characteristic spectral signatures.

3. Research perspectives

Based on the variability of the spectral profiles and by using false color infrared images (FCIR), in which the differences of the spectral profiles are enhanced, recently we were able to discriminate and to select with high accuracy ROI's (Regions Of Interest) for endmembers classification [7-8]. For data processing on various types of artifacts several algorithms for classification were tested. For supervised classification Spectral Angle Mapper and Maximum Likelihood were employed while for unsupervised classification K-means and ISODATA algorithms were applied. Following the structure and heterogeneous distribution of component materials another algorithm, more suitable to detect mixture of signals in the same pixel, was successfully applied on different case studies (See Fig 3).
Linear Spectral Unmixing (LSU) calculation allows also classifying mixtures based on their statistic values. For each endmember selected LSU is capable to extract fractions from the whole recording but also to estimate with high accuracy the errors of classification. The goal of our future research is to corroborate the results of hyperspectral and multispectral analysis with other available imagistic and analytic techniques such as thermal imaging, digital X-ray, FTIR, XRF and LIBS analysis in order to establish a viable digital instrument for complex characterization.

Acknowledgements

Paper published within the project for financing excellence PRO INSTITUTIO - 19 PFE / 2018, funded by the Ministry of Research and Innovation through Program I - Development of the national research and development system, Subprogram 1.2 - Institutional performance - Projects for financing excellence in RDI, Contract No. 19 PFE / 17.10.2018.
This work was also financed by IMPLEMENT - Implementation and exploitation of scientific research results in the practice of restoration and conservation of cultural assets, CCCDI - UEFISCDI, PN-III-P1-1.2-PCCDI-2017-0878 / No. 55, PCCDI / 2018.

References

[1] F. Mairinger, "UV-, IR- and X-ray imaging", Non-Destructive Microanalysis of Cultural Heritage Materials, Eds. K. Janssens , R. Van Grieken, Comprehensive Analytical Chemistry, Volume 42, 2004, pp.15-71.

[2] C. Fischer, I. Kakoulli, Multispectral and hyperspectral imaging technologies in conservation: current research and potential applications", Reviews in Conservation, Nr. 7, pp. 3-16, (2006).

[3] M. Kubik, Hyperspectral Imaging: A New Technique for the Non-Invasive Study of Artworks, Chapter 5 in Physical Techniques in the Study of Art, Archaeology and Cultural Heritage, Vol. 2, Edited by D. Creagh and D. Bradley, Elsevier, Amsterdam, pp. 199-258, (2007).

[4] H. Liang, Advances in multispectral and hyperspectral imaging for archaeology and art conservation", Applied Physics A, , Vol. 106, Issue 2, pp. 309–323, (2012).

[5] R. de la Rie, Fluorescence of Paint and Varnish Layers (Part III), Studies in Conservation, Vol. 27, No. 3 , pp. 102-108, (1982).

[6] J. R. J. van Asperen de Boer, " Infrared Reflectography: a Method for the Examination of Paintings", Applied Optics, Vol. 7, Issue 9, pp. 1711-1714, (1968).

[7] J. C. Morton, Image Analysis, Classification And Change Detection In Remote Sensing, 3rd Edition, CRC Press, (2014).

[8] A. Polak et al., Hyperspectral imaging combined with data classification techniques as an aid for artwork authentication, Journal of Cultural Heritage, No. 26, pp. 1–11, (2017).

*Corresponding author: L. RATOIU
e-mail address:
lucian@inoe.ro

Byzantine coins evaluation using a non-destructive XRF analytical technique

C. TĂNĂSELIA[a], A. TÖRÖK[a], A. ȘTIRBAN[b], D.G. ANGHEL[b,c*]
[a]*INCDO INOE2000 ICIA Cluj-Napoca*
[b]*Union National Museum Alba Iulia*
[c]*1 Decembrie 1918 University of Alba Iulia*

Abstract: X-Ray fluorescence (XRF) analytical technique has been increasingly used for characterization of museum artifacts due to its rapid use and non-destructive nature: samples remain unharmed, while a wealth a data can be obtained about their elemental composition. 48 Byzantine coins belonging to 8^{th}-9^{th} century, originating from the numismatical collection of Union National Museum Alba Iulia have been analyzed trough this technique and the results confirmed their initial origin, but in the same time a possible fake coin, minted in the Byzantine Empire have been identified through these analysis, due to unnatural high amount of Pb that was found in coin's elemental composition.

Keywords: XRF, analytical, byzantine coins

1. Introduction

There are 245 Byzantine numismatical items on the collection of Union Museum of Alba Iulia and of those, 48 are minted between 8^{th} and 9^{th} century by various Byzantine Emperors (Maurice Tiberius, Phocas, Constans II, Heraclius, Basil I, Leon V, Leon VI etc) [1,2]. The coins were minted in Constantinople, as well as in Syracuse, Thessaloniki, Nicomedia, Chersonesus or Cyzicus, as the location is usually specified on the coin itself. 30 coins were selected for this study, 27 are made of bronze, 2 are silver coins and 1 gold coin.
Elemental chemical composition can provide useful metallographic information for conservation and restoration activities, but also as a comparative study with other numismatical items from the same period, present in other collections. Non-destructive investigation technique is crucial for this kind of samples, thus conventional chemical analysis was not suited for this set of investigations [7].
X-Ray Fluorescence (XRF) offers a non-destructive technique to investigate elemental composition of numismatical items without causing any damage to the analyzed items [3,4,6]. The portable nature of the instrument means that it was transported to the museum location, so the items did not even have to leave the museum building.

2. Experimental

2.1. Instrumentation

XRF analysis were performed *in-situ* using an InnovX Alpha-6500 handheld spectrometer, Si-PiN detector, 40 kV voltage, 15 µA intensity, 3 mm filter and Be window. The sample is subjected to an X-Ray bombardment that has enough energy to displace the L-shell electrons out of the atom, thus triggering an electron transition from the K-shell to L-shell, accompanied with the release of a photon, with the energy dependent on the difference between K-shell and L-shell, thus a characteristic to a specific element. The resulted photons are read by a detector, allowing the correct identification of the element it originated from. The integration time for the above-mentioned instrument was set to a total of 60 seconds. Both sides of each coin were measured on 3 different spots and the results listed here are the average of those 6 measurements. The measuring window surface is about 1 cm^2, meaning that the obtained result for one measurement is an average obtained across the window surface area.

2.2 Results

Results are presented for three collections, of various Byzantine Emperors (Phocas, Mauritius Tiberius and Heraclius). Individual coins with their respective inventory number are represented on the y-axis, while their concentration on the x-axis, with different colors for each element in their composition. Data were obtained using a software library that offers alloy identification in real-time for selected samples.

Fig. 1. Phocas gold coin (inv.no. 6075) from 602/610 AD

2.2.1 The Phocas Collection

Flavius Phocas (547-610) was a Byzantine Emperor between 602 and 610 [5].
For the Phocas-era, coins in the studied collection (see Figure 2), one (inventory number 6075, Figure 1) is made from gold (97%) and silver (3%), while the other ones (inv. no. 6063, 5959, 5958, 1208) are from bronze, as expected. Pb is found in all the bronze coins (<1% - 3%), probably being present in natural Cu ore and byzantine techniques at the time were not able to further eliminate it from the refined Cu alloy. Other impurities found in bronze coins were Ni

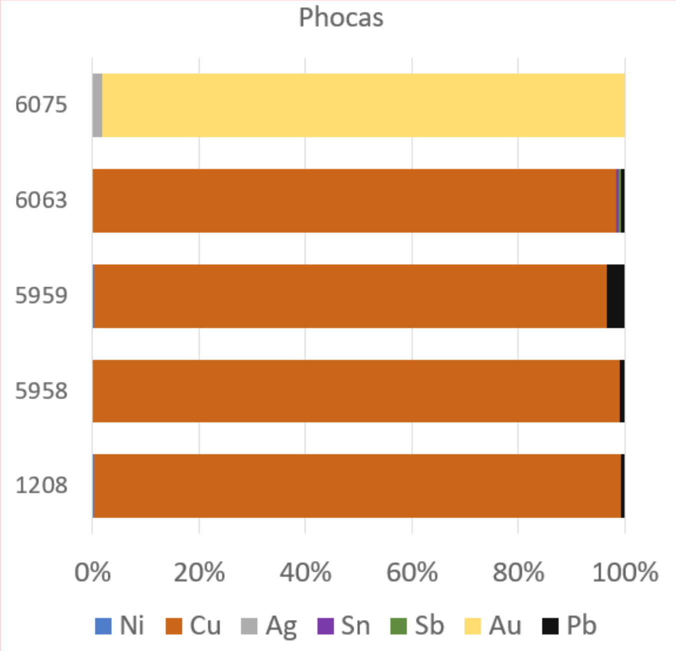

Fig. 2. Graphical representation for Phocas-era coins data. Individual coins are listed on y-axis, while concentration values, in percent, on x-axis

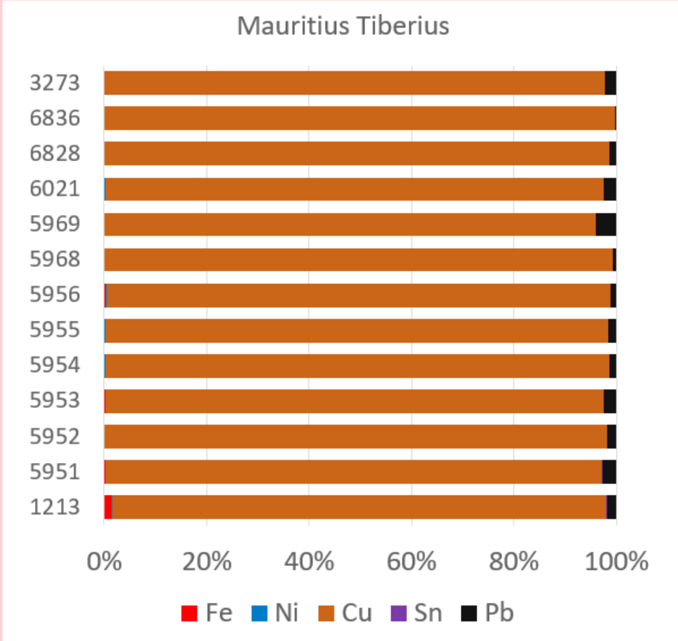

Fig. 3. Graphical representation for Mauritius Tiberius-era coins data. Individual coins are listed on y-axis, while concentration values, in percent, on x-axis

(<1% in inv. no. 1208 and 5959), Sn (<1% in inv. no. 6063) and Sb (<1% in inv. no. 6063).

2.2.2 The Mauritius Tiberius collection

Mauritius Tiberius (539-602) ruled the Byzantine Empire between 582 and 602, when his throne was usurped by Flavius Phocas, leading to his execution [5].

The Mauritius Tiberius collection is much more homogenous than the previous one in this study, with Cu concentrations varying from 96.5% (inv. no. 1213) to 99.7% (inv. no. 6836), as represented in Figure 3.

Pb is once again present in concentrations from <1% (inv. no. 5968) to a maximum of 3.9% (inv. no. 5969), but it's

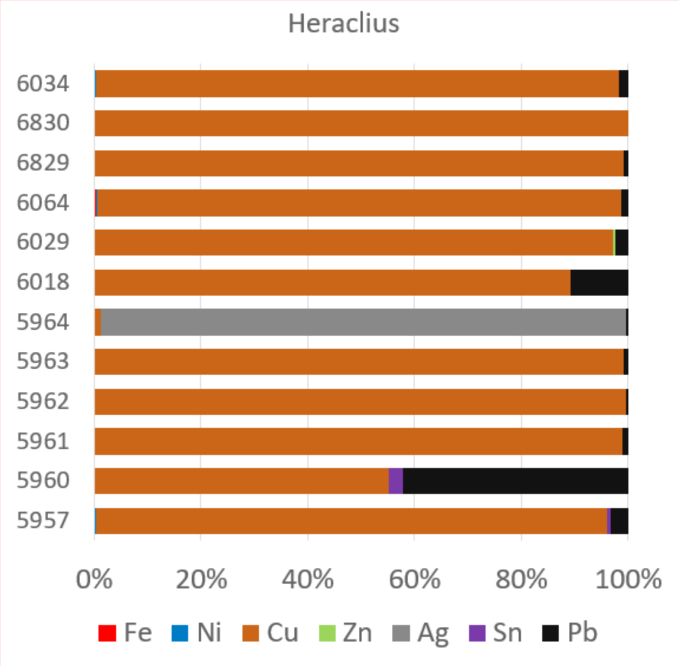

Fig. 4. Graphical representation for Mauritius Tiberius-era coins data. Individual coins are listed on y-axis, while concentration values, in percent, on x-axis

speculated that its presence is either a by-product of Cu metallurgy or a left-over from original ore.
The concentration results fall within expected range for the era and geographic location of the coins. Fe was found in 5 coins, but only in one (inv. no. 1213) its concentration was above 1%, while the rest of the items in the collection (item no. 5951, 5953, 5956, 6021) have <1% Fe composition. Ni and Sn were all below 1%, in 6 items (inv. no. 1213, 5954, 5955, 5956, 6021 and 3273), respectively
2 items (inv. no. 1213, 5951).

2.2.3 The Heraclius collection

Heraclius (575-641) was a Byzantine emperor between 610 and 641 (his rule started with the assassination of Flavius Phocas, who ruled before him)[5].
The Heraclius era coins offer some unexpected results, compared with other sets in this study. It is worth mentioning that the origin of these coins is not very clear, as it's the case with the other two sets mentioned above. There is one coin made from Ag (inv. no. 5964) with traces of Pb (<1%) and Cu (1.1%). One item (inv. no. 6029) contains Zn, but it is below 1% in concentration, while the expected traces of Fe, Ni and Sn were found, almost all in concentrations below 1% (with the exception of inv. no. 5960 that has a Sn concentration of 2.5%).
The high Pb concentration in item with inv. no 5960 (as seen in Figure 5) does not fit the expected Pb concentration range for this historical era and geographical region. Pb is 42.3%, while Cu concentration is only 55.2% (with Sn as impurity, at 2.5%) and this could mean that the coin is part of a fake series of coins that were minted during Heraclius reign, with or without the emperor's knowing.

Fig. 5. Heraclius coin (inv.no. 5960) from probably 629 AD, with a higher than expected Pb concentration

Fig. 6. Heraclius(?)silver coin (inv.no. 5964) from after 615 AD

3. Conclusions

Data for elemental concentration of the coins that took part in this study revealed that most of the items fall in the general pattern for so-called bronze coins of the specified Byzantine era [7,8], where Cu concentration is known to vary from 89%-99%, most of the coins being a binary alloy Cu/Pb or ternary allows Ag/Cu/Pb with impurities like Ni, Fe, Sn and Zn being present in concentrations usually below 1%.

If Pb concentration is below 3%, it's believed that Pb is present as a trace component in main Cu ore, while if Pb concentration is over 3%, then it's believed that it's presence in the alloy is intentional.

The XRF handheld device is a suited analytical tool to characterize the metallography of numismatical items in museum collection, since it offers fast alloy data about the samples. Further method development could bring the analysis in the domain below 1% concentration for most of identified elements, but for the purposes of identifying main alloy elements and item comparison, current detection limits are proved to be sufficient.

Further applications of this analytical technique could expand the studied items to a more detailed range of samples, like ancient or medieval jewellery, weapons or ceramics, that could further expand the historical significations of such items.

Acknowledgements

This work was supported by a grant of the Romanian Ministry of Research and Innovation, CCCDI-UEFISCDI, project number 352PED/2020 (GLAZEX) within PNCDI III.

References

[1] D. Anghel, O. Oargă, M. Ursu, C. Tănăselia, M. Chintoanu, M. Șenilă, Terra Sebus. Acta Musei Sabesiensis, **7** (2015)

[2] S. Shackley, An Introduction to X-Ray Fluorescence (XRF) in Geoarcheology, LLC, 2011, p. 6.

[3] V. Felix, M. Pereira, R. Freitas, P. Arahna, P. Heringer, M. Anjos, R. Lopes, Applied Radiation and Isotopes, **166** (2020)

[4] A. Bolewski, M. Matosz, W. Pohorecki, J. Melendez, Radiation Physics and Chemistry, 171 (2020)

[5] G. Ostrogorsk, History of Byzantium, Sibirskaya Blagozvonnitsa, Moscow, 2011

[6] A. Gueli, S. Pasquale, D. Tanasi, S. Hassam, V. Garro, Q. Lemasson, B. Moignard, C. Pacheco, L. Pichon. G. Stella, G. Politi, Measurement, **129**, 677-685 (2018)

[7] M. Crosera, E. Baracchini, E. Prenesti, A. Giacomello, B. Callegher, P. Oliveri, G. Adami, Microchemical Journal, **147**, 422-428 (2019)

[8] K. Melessanaki, M. Mateo, S.C. Ference. P.P. Betancourt, D. Anglos, Applied Surface Science, **197-198** (2002)

*Corresponding author: Dan George Anghel, dnanghel@yahoo.com